Exchange of water masses between the southern Weddell Sea continental shelf and the deep ocean

Kjersti Birkeland Daae

Thesis for the Degree of Philosophiae Doctor (PhD)
University of Bergen, Norway
2018

UNIVERSITY OF BERGEN

Exchange of water masses between the southern Weddell Sea continental shelf and the deep ocean

Kjersti Birkeland Daae

Thesis for the Degree of Philosophiae Doctor (PhD)
at the University of Bergen

2018

Date of defence: 13.06.2018

Year: 2018

Title: Exchange of water masses between the southern Weddell Sea continental shelf and the deep ocean

Name: Kjersti Birkeland Daae

Print: Skipnes Kommunikasjon / University of Bergen

Exchange of water masses between the southern Weddell Sea continental shelf and the deep ocean

Kjersti Birkeland Daae

Dissertation for the degree of Philosophiae Doctor (PhD)
at the University of Bergen

2018

Scientific environment

This study is carried out at the Geophysical Institute, University of Bergen. The work is supported by the Centre for Climate Dynamics at the Bjerknes Centre for Climate Research and by the Norwegian Research councils FRINATEK program through the project WARM (231549) and through the NARE program under the project WEDDELL (211415). I have been enrolled in the ResClim Research School in Climate Dynamics, who provided many relevant courses.

ResClim
RESEARCH SCHOOL IN CLIMATE DYNAMICS

UNIVERSITAS BERGENSIS

BJERKNES CENTRE
for Climate Research

Abstract

The exchange of water masses between the shallow Weddell Sea continental shelf and the deep ocean is of climatic importance. Firstly, on-shelf transport of warm oceanic water masses, contributes to basal melting of ice shelves, which affects the stability of the Antarctic Ice Sheet. Secondly, export of dense Weddell Sea shelf water, contributes to production of Antarctic Bottom Water (AABW), which feeds into the lower limb of the global thermohaline circulation.

This thesis considers processes related to both on-shelf heat transport, and to export of dense shelf water. Based on a combination of idealized numerical model experiments and observations of hydrography and current at various locations in the southern Weddell Sea, the thesis discusses pathways and variability of the oceanic circulation along the continental slope, on the continental shelf and inside the Filchner Trough (FT), a deep trough across the continental shelf. The response to wind forcing is assessed, along with mechanisms contributing to mixing and transformation of water masses.

The Antarctic Slope Front (ASF) protects the Weddell Sea continental shelf from the saline Warm Deep Water (WDW) offshore. Most of the on-shore transport occurs in the summer season, when the thermocline is shoaling at the shelf break, and through the FT, where the sill depth is 200 m below the shelf depth. However, on-shelf transport of warm water may also occur when dense shelf water is present on the shelf. An isopycnal connection between the dense shelf water and the WDW offshore creates a pathway for WDW to access the shelf without doing work against the buoyancy forces.

The southward transport of heat into the FT is sensitive to the slope current properties, and to the characteristics of the dense shelf water. The slope current is associated with the ASF, and flows westward along the continental slope. The core of the slope current is found to migrate shoreward onto shallower isobaths under strong wind forcing, leading to different inflow regimes in the FT. In the weak wind regime, the slope current core is located over deep isobaths, and does not interact with the FT topography. In this regime, the southward heat transport into the FT is dominated by eddies, and is sensitive to dense shelf water properties. In the strong wind regime, the slope current is topographically steered southward into the Filchner sill region. However, potential vorticity constraints at the sill edge force the slope current to turn and exit the Filchner sill, without reaching the deeper part of the trough. The recirculating slope current efficiently advects eddies out of the Filchner sill area, and limits the southward heat transport.

A recirculation of the slope current across the Filchner sill could influence the export of dense Ice Shelf Water (ISW) from the FT. The slope current is mainly wind-driven, and responds to monthly scale variability in the along-slope wind stress. Here, it is shown that the variability of the ISW overflow velocity is also connected to the up-

stream wind stress, which could result from interaction between the ISW overflow and the recirculating slope current.

New insight is gained regarding the ISW pathway from the Filchner Ice Shelf (FIS) front toward the continental slope. The ISW is flowing northward as a mid-depth jet along the eastern side of the FT. An eastward turning of the ISW across the FIS front could be related to potential vorticity constraints associated with the large increase in water column depth at the FIS front. The dense ISW overflows the Filchner sill and continues westward along the continental slope as a bottom intensified plume. The plume thickness fluctuates strongly on time scales of a few days. High shear and mixing is observed during the early stage of a thick plume event, and indicate efficient entrainment of WDW, which is essential for production of AABW. The efficient mixing is, at least partly, related to topographic vorticity waves.

In summary this thesis discusses key elements of the current circulation and its variability in the southern Weddell Sea. The thesis demonstrates the inter-connection between the cold water masses on the continental shelf and the warmer off-shelf water masses. Today, the ASF is an important barrier which protects the Weddell Sea continental shelf from the warm water off-shore. However, the stability of the ASF is vulnerable to climate change, and is not well resolved in global climate models. This study highlights the need for improved understanding of the processes related to the slope front system, and the importance of the exchange and interaction between water masses in the Filchner Trough.

List of abbrevations and water masses

- ACoC: Antarctic Coastal Current
- ASF: Antarctic Slope Front
- ENSO: El-Niño/Southern Oscillation
- FT: Filchner Trough
- FIS: Filchner Ice Shelf
- FRIS: Filchner-Ronne Ice Shelf
- RIS: Ronne Ice Shelf
- PV: Potential Vorticity
- SAM: Southern Annular Mode
- SAO: Semi-Annual Oscillation
- TVW: Topographic Vorticity Waves

Table 1: Overview of water masses and their characteristics. salinities are given for both practical salinity units (S, PSS-78) and converted to Absolute Salinity (S_A, TEOS 10) (McDougall and Barker, 2011)

Acronym	Name	Θ (°C)	S	S_A (g kg^{-3})
ESW	Eastern Shelf Water	$-1.9 \leq \Theta \leq -1.7_d$	$S < 34.44_a$	$S_A < 34.60$
WSW	Western Shelf Water	$\Theta < -1.9$	$34.56 < S < 34.84_a$	$34.72 < S_A < 35.00$
CDW	Circumpolar Deep Water	$\Theta > 0.5_c$		
WW	Winter Water	$\Theta \sim -1.9$	$34.28 \leq S \leq 34.52_a$	$34.44 \leq S_A \leq 34.68$
WDW	Warm Deep Water	$0 \leq \Theta \leq 0.8$	$34.64 \leq S \leq 34.72_a$	$34.80 \leq S_A \leq 34.88$
MWDW	Modified Warm Deep Water Mix of WDW and WW/ESW$_{a,d}$	$-1.7 \leq \Theta \leq 0.2$	$34.45 \leq S \leq 34.64_d$	$34.61 \leq S_A \leq 34.80$
HSSW	High Salinity Shelf Water	$-1.9 \leq \Theta \leq -1.7$	$S > 34.65_d$	$S_A > 34.81$
ISW	Ice Shelf Water	$\Theta < -1.9_b$		
WSBW	Weddell Sea Bottom Water	$\Theta < -0.8^o C_a$		
AABW	Antarctic Bottom Water, Mix of WDW and WSBW$_b$	$-0.8 \leq \Theta \leq 0$		

[a] *Foster and Carmack* (1976a)
[b] *Carmack and Foster* (1977)
[c] *Gammelsrød et al.* (1994)
[d] *Grosfeld et al.* (2001)

Outline

This thesis consists of an introductory part and four scientific papers. Chapter 1 gives an introduction to the Weddell Sea circulation system and bottom water production. Objectives, data and methods, as well as a detailed description of the idealized numerical model are provided in chapter 2. A brief summary of the papers is given in chapter 3, before perspectives and outlooks are presented in chapter 4. The manuscripts included in this thesis (chapter 5) are:

1. Daae, K., T. Hattermann, E. Darelius, and I. Fer, (2017) *On the effect of topography and wind on warm water inflow An idealized study of the southern Weddell Sea continental shelf system*, J. Geophys. Res. Oceans **122**

2. Darelius, E., K. Makinson, K. Daae, I. Fer, P. R. Holland, and K. W. Nicholls, (2014) *Hydrography and circulation in the Filchner Depression, Weddell Sea, Antarctica*, J. Geophys. Res. Oceans **119**.

3. Daae, K., E. Darelius, I. Fer, S. Østerhus, S. Ryan, (2018) *Wind stress mediated variability of the Filchner Trough overflow, Weddell Sea*, J. Geophys. Res. Oceans (Accepted, March 2018)

4. Daae, K., I. Fer, E. Darelius, *Variability and mixing of the Filchner overflow plume descending the continental slope west of Filchner Trough, Weddell Sea*, Prepared for submission to J. Phys. Oceanography

Contents

Chapter 1

Introduction

The Antarctic continent holds the largest ice sheet on Earth. The average thickness is 2.7 km with maximum thickness of about 4.8 km. The ice sheet takes up 90 % of the Earth's total ice masses, and 70 % of the fresh water content, which is equivalent to a sea level rise of more than 60 m. In order to obtain realistic predictions on future sea level rise, it is important to understand the underlying mechanisms which influence the Antarctic ice sheet stability, and the interactions between the ice sheet and the ocean.

The Antarctic region is also important for the Earth's climate through production and export of dense Antarctic Bottom Water (AABW), which feeds into the lower limb of the Global Thermohaline Circulation (*Orsi*, 1999). Understanding the formation and transformation of AABW is therefore a key to improved knowledge of the climate system, and how the climate will respond to changes in the forcing.

This chapter provides a summary of the oceanic circulation in the Weddell Sea, with focus on the relevant processes governing the exchange of water masses between the continental shelf and the deep ocean.

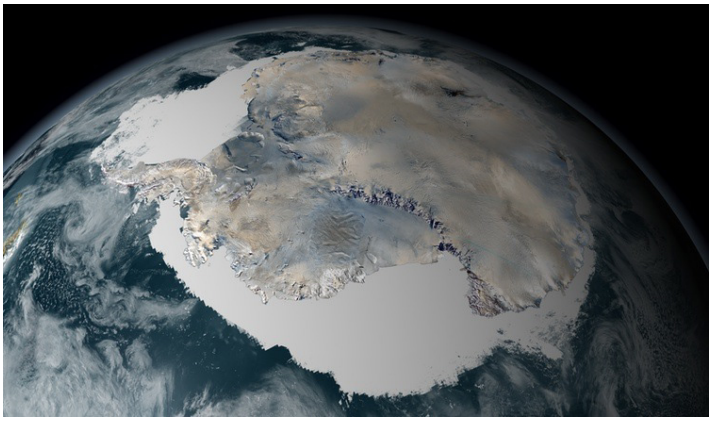

Figure 1.1: The Antarctic continent and its surrounding ice shelves and sea ice, derived from AVHRR data. Image courtesy: NASA/GSFC Scientific Visualization Studio

1.1 Ice sheet stability

Glacial ice from the Antarctic Ice Sheet flows toward the coast. The equilibrium of the ice sheet depends on the amount of accumulation of snow and the loss of ice into the sea, through calving and melting of the ice shelves (Figure 1.2). Ice shelves, which are floating extensions of the ice sheet, fringe the continent and contribute to buttress, or slow down the advance of land ice into the ocean (*Dupont and Alley*, 2005). Recent observations of thinning ice shelves along western Antarctica (Bellingshausen and Amundsen Sea) (*Paolo et al.*, 2015; *Pritchard et al.*, 2012) raise concerns on the stability of the ice sheet in a warmer climate. Although the West Antarctic Ice shelves cover less than 10 % of the total ice shelf area, they contribute to roughly half of the observed ice shelf mass loss (*Rignot et al.*, 2013). The observed ice shelf thinning is a result of the oceanic circulation. In the Amundsen and the Bellingshausen Sea, warm Circumpolar Deep Water (CDW), of oceanic origin, enter the ice shelf cavities and melt the ice shelves from below. The inflow of warm water is facilitated through bottom corrugations and troughs across the continental shelf (*Arneborg et al.*, 2012; *Moffat et al.*, 2009; *Walker et al.*, 2007).

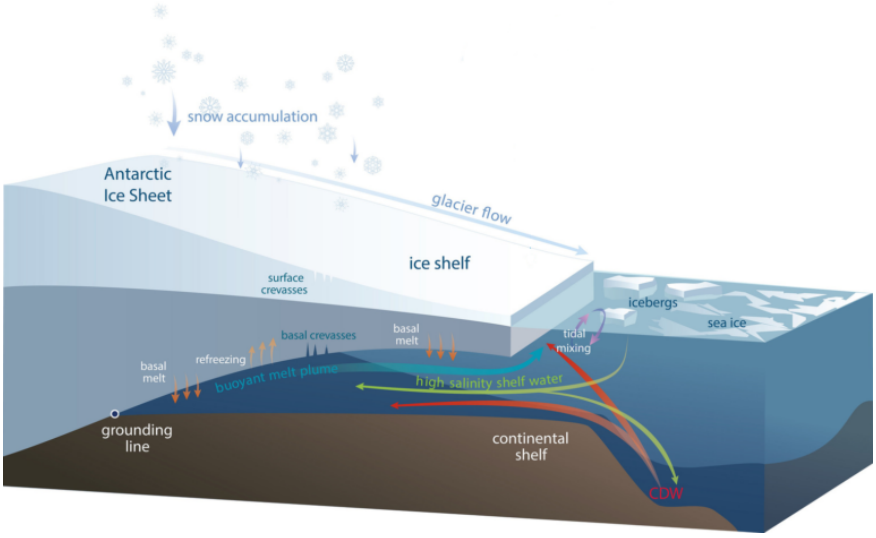

Figure 1.2: Sketch of a typical Antarctic Ice shelf. Snow is accumulated on the surface, and is transformed to ice that flows toward the coast where calving occurs. Nut more important, warm water under the floating ice shelf contributes to thinning through basal melting. Image courtesy: H.A. Fricker, Scripps Institution of Oceanography, UC San Diego.

The oceanic conditions in the Weddell Sea are different from those in the Amundsen and Bellingshausen Sea (west Antarctica). In the Weddell Sea, the Antarctic Slope Front (ASF, section 1.2) limits the on-shelf transport of Warm Deep Water (WDW), a slightly cooler and fresher derivative of CDW (*Heywood et al.*, 1998). The water temperatures on the continental shelf and inside the Filchner-Ronne Ice Shelf (FRIS) cavity are close to the surface freezing point ($\sim 1.9^{o}$C) (*Nicholls et al.*, 2009; *Orsi and Wiederwohl*, 2009), and the basal melt rates are low (~ 0.3 m yr^{-1}, *Rignot et al.*, 2013). However, both observations (*Darelius et al.*, 2016; *Foldvik et al.*, 2001) and numerical model results (e.g. *Hellmer et al.*, 2012) show that the FRIS is vulnerable to changes in the mechanisms that bring warm water onto the continental shelf.

Numerical model experiments suggest that substantial increase in the basal melt rates (up to 4 m y^{-1}) may occur within this century (*Hellmer et al.*, 2012; *Timmermann and Hellmer*, 2013). The increased melt rates in the model study result from changes in the oceanic circulation and in the on-shelf transport of warm water, related to future atmospheric changes. *Hellmer et al.* (2017) further suggest a tipping point behavior. Once warm water flushes the Filchner Ice Shelf (FIS) cavity, a positive melt water feedback enhances the shelf circulation and the onshore transport of heat. In their numerical model, the process is irreversible unless they prescribe basal melt rates back to today's level.

This thesis is part of a large project, *Inflow of Warm Deep Water on the Antarctic Continental Shelves (WARM)*, which aims to quantify the on-shelf heat flux and to identify the dominant mechanisms for on-shelf heat transport. The FRIS comprises an area of 450 000 km^2, and is the largest ice shelf by volume (*Fox et al.*, 1994). Increased oceanic heat fluxes, and basal melt rates of the FRIS will have consequences not only for the water mass transformation and ocean circulation in the Weddell Sea, but also for the stability of the inland ice and for the global sea level rise.

1.2 The Antarctic Slope Front system

The Antarctic Slope Front (ASF) separates the warm and saline WDW, found at mid-depth north of the continental slope, from the colder and fresher surface water (*Gill*, 1973; *Jacobs*, 1991). The ASF is mainly driven by the prevailing easterly winds, which lead to on-shore Ekman transport and downwelling at the coast (*Deacon*, 1937; *Sverdrup*, 1953). The downwelling causes a southward depression of the isopycnals toward the continental slope, which is a characteristic feature of the ASF. A transect across the Weddell Sea continental slope, showing the ASF, is presented in Figure 1.3. The transect was obtained roughly along 18°W in 2009 (*Chavanne et al.*, 2010). In the Weddell Sea, dense water formation over the continental shelf leads to formation of a second, on-shore part of the front, which separates the lighter offshore surface water from the dense shelf water (*Foster and Carmack*, 1976a; *Nicholls et al.*, 2009). The combined front system, with V-shaped isopycnals over the continental slope (*Gill*, 1973; *Jacobs*, 1991), protects the continental shelf from inflow of WDW.

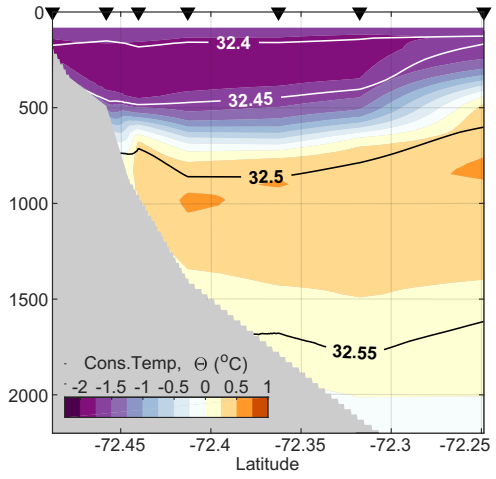

Figure 1.3: Conservative Temperature (Θ, colors), and density anomalies referenced to 1000 dbar (σ_1, contours) across the continental slope at roughly 18°W (Chavanne et al., 2010). Two transects obtained 8 days apart are combined. Triangles indicate the location of the CTD profiles.

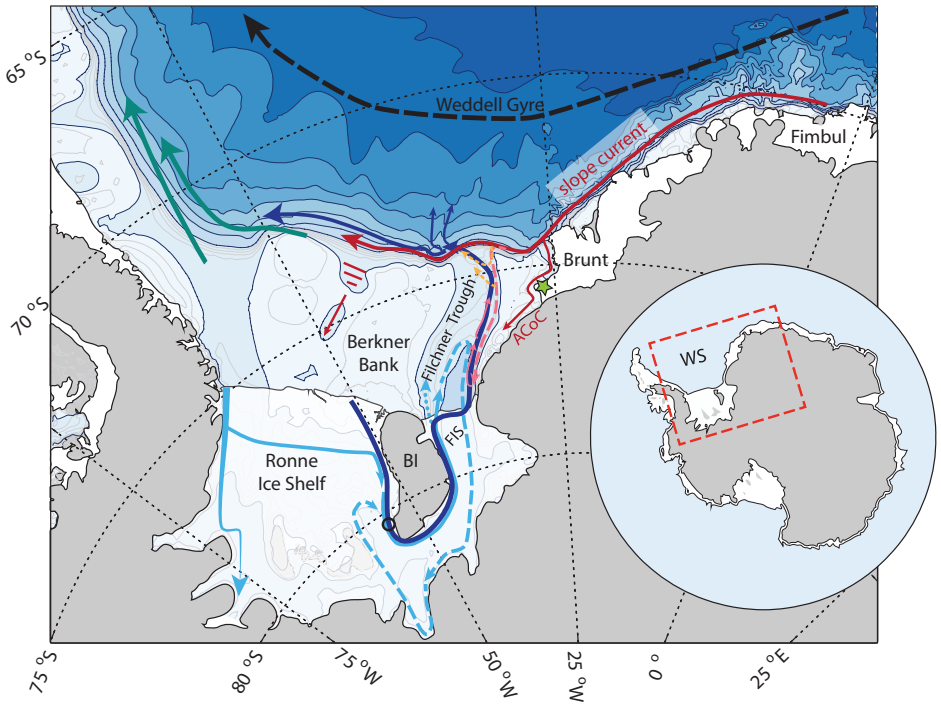

Figure 1.4: Map of the southern Weddell Sea, with bathymetry from Bedmap2 (Fretwell et al., 2013). Colored arrows indicate the circulation pattern, where the dashed lines represent seasonal flow. The circulation under the FRIS is from Nicholls and Østerhus (2004), and is based on measurements made from bore-holes in the ice shelf at five sites, ship-based measurements made along the ice front, and glaciological measurements of the ice shelf. Halley Research station is indicated by a green star, and the black circle indicate the location of site 5, near the southern tip of Berkner Island (BI).

The on-shore Ekman transport associated with the ASF leads to increased sea surface elevation toward the coast, resulting in a geostrophic current westward along the slope. This current has frequently been referred to as the Antarctic Coastal Current (e.g., *Fahrbach et al.* (1992); *Foster and Carmack* (1976a); *Gill* (1973)). Here, we follow *Heywood et al.* (1998), and use the term slope current to describe the current as it flows along the continental slope. A schematic of the circulation pattern in the southern Weddell Sea, with the thick red arrow representing the slope current, is presented in Figure 1.4. The slope current bifurcates at roughly 27^oW, where the continental shelf widens. Here, the term Antarctic Coastal Current (ACoC) refers to the slope current branch that flows southward along the coast after the bifurcation (thin red line along the Brunt Ice Shelf, Figure 1.4).

The slope current is influenced by several forcing mechanisms such as local wind speed, sea ice drag, wind stress curl, variability of the Weddell Gyre, and surface related processes (*Núñez-Riboni and Fahrbach*, 2009). Existing estimates of the volume transport associated with the slope current range from 7 Sv (based on year-long moored instruments, *Graham et al.*, 2013) to 14 ± 3 Sv (based on a wider transect of ship-borne hydrography profiles, *Heywood et al.*, 1998). The slope current responds to the seasonal variability of the wind forcing and the sea ice drag (*Fahrbach et al.*, 1992; *Graham et al.*, 2013; *Jensen et al.*, 2013; *Núñez-Riboni and*

Fahrbach, 2009). The maximum current velocity is observed between May and August, when the Ekman transport is high due to increased along-slope wind stress. This thesis discusses the co-variability of the slope current and the wind stress further, with emphasize on the monthly time scales (Paper III), and the on-shore migration of the slope current core under strong wind forcing (Paper I).

The slope current crosses the Filchner Trough (FT) opening (Figure 1.4). There exist many open questions regarding the interaction between the slope current and the FT. To what degree is the slope current affected by the trough geometry? How much warm water associated with the slope current is transported southward into the trough? What is the role of eddy formation through breaking topographic waves and mesoscale baroclinic and barotorpic instabilities at the trough opening? Could the slope current be redirected southward into the trough as suggested by *Hellmer et al.* (2012, 2017, Section 1.1).

Model studies indicate that the interaction between a shelf break jet, like the slope current, and a trough across the shelf depends on the trough geometry, the stratification, and the strength and direction of the slope current (*Allen and Durrieu de Madron*, 2009; *Klinck*, 1996; *Williams et al.*, 2001; *Zhang et al.*, 2011). Although inflow of warm water into the FT occurs seasonally (Section 1.3), most of the warm water carried by the slope current continues westward along the slope. Based on an idealized model of the Weddell Sea, this thesis addresses the questions above, and study the interaction between the slope current and the FT for different combinations of wind and water mass properties (Paper I). The results indicate that Potential Vorticity (PV) constraints, related to the trough topography, may limit the southward heat transport into the trough.

The ACoC branch of the slope current follows the coast line southward along the Brunt Ice Shelf. The ACoC is fast and narrow, and contributes to renewal of the Weddell Sea shelf waters by transporting low-salinity water onto the shelf (*Heywood et al.*, 1998; *Jacobs*, 1991). Observations of the ACoC are sparse, but strong currents at mid-depth (mean speed of 0.1 m s^{-1} at 194 m) are observed close to the Brunt Ice Shelf (75.81°S) in 2003-2004 (*Nicholls*, 2005). This thesis describes the variability of the ACoC on both seasonal and monthly time scales (Paper III). It is shown that increased wind stress along the continental slope leads to an increased current speed within the ACoC. A combination of strong wind forcing and a shallow thermocline at the shelf break could lead to increasing heat transports onto the shelf and contribute to basal melting of the ice shelves. However, the southward extent of the ACoC is not yet known. In order to quantify the southward heat flux associated with the ACoC, and its contribution to basal melting, new observations are needed along the southeastern Weddell Sea continental shelf.

1.3 Seasonal inflow of Modified Warm Deep Water

Modified Warm Deep Water (MWDW), a slightly cooled version of WDW enters the FT seasonally, from January to May, when weaker wind forcing allows for a shoaling of the thermocline (*Årthun et al.*, 2012). MWDW with a core at roughly 400 m depth has been observed along the eastern flank of the FT in several hydrographic surveys (Paper II, *Årthun et al.*, 2012; *Carmack and Foster*, 1977; *Darelius et al.*, 2016; *Foldvik et al.*, 1985a; *Ryan et al.*, 2017). The inflow is indicated by a pink, dashed line in Figure 1.4. In summer, the ISW in the FT reaches the lower layers of the eastern shelf (flat shelf east of the FT). The southward warm inflow is maintained by an east-west density gradient between the warm inflow and the ISW (*Ryan et al.*, 2017). During winter, the ISW retreats from the eastern shelf and the temperature of the inflow decreases. This leads to a weaker density gradient and a reversed flow along the eastern

FT.

The southern extent of the warm inflow varies from year to year. Observations near the FIS front show that MWDW was present in 2013, but not in 2011 (*Darelius et al.*, 2016). This thesis presents observations suggesting that the MWDW associated with the seasonal inflow, to some extent recirculates and returns northward away from the ice shelf cavity (Paper III). Year-to-year variations of the southward extent of the MWDW recirculation could explain the lack of MWDW near the FIS front in 2011. The finding has implications for monitoring and quantifications of the southward heat flux associated with the inflow of MWDW. Either, the recirculation of the MWDW must be quantified, or the mooring arrays must be located so far south that recirculation is negligible.

1.4 Production and export of AABW

AABW is a mixture of cold shelf water and the warmer and more saline oceanic water masses (CDW/WDW), which surround the Antarctic continent (*Carmack and Foster*, 1977). A major part of the AABW is formed through mixing between WDW and Weddell Sea Bottom Water (WSBW), formed in the southern Weddell Sea (*Carmack and Foster*, 1975a; *Foldvik et al.*, 2004; *Orsi*, 1999). WSBW consists of roughly 25% shelf water, and 70 % WDW, with the remainder being surface waters (*Foster and Carmack*, 1976b; *Weppernig et al.*, 1996). Estimates of the total production of WSBW range from 2-5 Sv (*Gordon*, 1998, and references therein).

High Salinity Shelf Water (HSSW) is the source water mass for WSBW. HSSW is formed over the continental shelf during winter, as a result of atmospheric cooling and brine rejection from sea ice formation (*Nicholls et al.*, 2009). Polynyas along the ice front maintain high production rates of HSSW throughout the winter (*Foldvik et al.*, 2001). The properties of the HSSW varies with respect to the formation site. The most dense and saline version of HSSW, is produced over the western part of the continental shelf, near the Ronne Ice Shelf (*Nicholls and Østerhus*, 2001, 2004). HSSW from this region has also been referred to as Western Shelf Water (*Gammelsrød et al.*, 1994).

HSSW contributes to production of WSBW in two ways. HSSW produced over the western Weddell Sea continental shelf may descend the continental slope directly (turquoise arrows in Figure 1.4) and form WSBW through mixing with the ambient offshore water masses (*Foster and Carmack*, 1976b; *Gordon*, 1998). Alternatively, the HSSW flows into the FRIS cavity, where it is transformed into Ice Shelf Water (ISW) which eventually overflows the Filchner sill, mixes with WDW, and forms WSBW(*Foldvik et al.*, 1985b). This thesis discusses different aspects of the ISW flow. A detailed description of the water mass transformation taking place under the FRIS, and the ISW pathways is given below.

The freezing point of sea water decreases with depth. Deep into the cavity, the HSSW entering from the continental shelf is warmer than the *in situ* freezing point. Glacial ice is melted and entrained into the HSSW, which is transformed into Ice Shelf Water (ISW). The ISW is potentially super-cooled, and is slightly fresher than the HSSW (*Gammelsrød et al.*, 1994). ISW formed under the FRIS circulates around the Berkner Island (BI) toward the Filchner trough (FT). The coldest ISW ($\Theta < -2.4^oC$) is observed near the Berkner Island, from bore-holes through the ice shelf (*Nicholls and Østerhus*, 2004). In Figure 1.4, ISW formed from the saline Ronne-sourced HSSW (ISW_{Ronne}) is indicated by light blue arrows, and ISW from the Berkner Bank sourced HSSW (ISW_{BB}) is indicated by dark blue arrows. *Nicholls and Østerhus* (2004) suggest that most of the ISW_{Ronne} is too dense to escape the 600 m deep FT sill, and instead recirculates under the FRIS, where it becomes fresher and lighter, due to entrainment of more glacial melt water (dashed blue arrow in Figure 1.4).

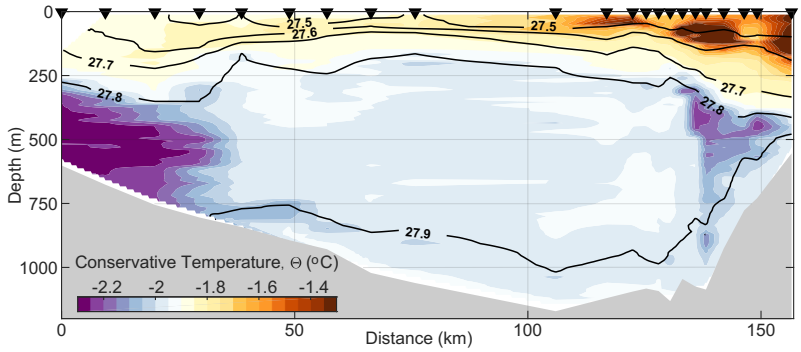

Figure 1.5: Conservative Temperature section along the FIS front in 2017. The section is a reprint from Darelius and Sallée (2018) and was obtained during the cruise JR16004 (Sallée, 2017)

A temperature transect along the FIS front from 2017 (Figure 1.5; reprint from *Darelius and Sallée* (2018)) shows two cores of ISW between 300 and 700 m depth. The western core consists of cold ($\Theta < -2.2°C$) ISW_{Ronne}, while the eastern core is slightly warmer.

Prior to this study, few observations existed from the FIS front, except from single hydrographic profiles obtained during summer cruises. It was assumed that the ISW emanating from under the FIS front was flowing northward along the western flank of the FT toward the Filchner sill (*Nicholls et al.*, 2009). The project *WARM*, which this thesis is a part of, has contributed to increased knowledge of the ISW flow in the FT. Rather than flowing northward along the western side of the FT, the ISW flows northward in a mid-depth jet along the eastern side of the FT (Paper II). It is suggested that the ISW turns eastward and crosses the FT upon reaching the FIS front, due to potential vorticity constraints (Paper II). Recent moored observations near the FIS front agrees with these findings, and brings further insight to the dynamics of the ISW flow (*Darelius and Sallée*, 2018; *Darelius et al.*, 2016). Along the western FT a northward flowing core of ISW_{Ronne} is present seasonally, from February to May/June. During the rest of the year, the ISW is warmer (lighter) and flows eastward along the FIS front. The northward flow across the FIS front is suggested to be facilitated through a decoupling of the lower part of the water column, which reduces the effect of the PV barrier (*Darelius and Sallée*, 2018).

On the eastern side of the FT, the ISW is flowing northward throughout the year (*Darelius et al.*, 2016). Intermittent traces of ISW_{Ronne} is observed, but the dominating source salinity of the ISW is fresher, and is more likely associated with ISW_{BB} (*Darelius and Sallée*, 2018). The ISW continues northward, and crosses the Filchner sill toward west. Estimates of the ISW volume transport range from 0.7 Sv (*Foldvik et al.*, 1985c) to 1.6 ± 0.5 Sv (*Foldvik et al.*, 2004). The ISW spills over the Filchner sill, and veers westward under the effect of rotation. In this thesis, the plume is referred to as the Filchner overflow plume, or just the plume. A temperature transect across the continental slope (east of the ridge at 36°W) is shown in Figure 1.6. Here, the cold Filchner overflow plume is roughly 200 m thick, with a core near the 1300 m isobath. In addition to the westward plume pathway along the continental slope, two northward and down-slope plume pathways are supported through topographically steering along two ridges near 36 and 37°W, respectively (*Darelius and Wåhlin*, 2007; *Foldvik et al.*, 2004). The Filchner overflow plume descends into the deep Weddell Sea. En route, the plume water mixes with the ambient water masses and forms WSBW (*Foster and Carmack*, 1976b), which is ultimately transformed into AABW.

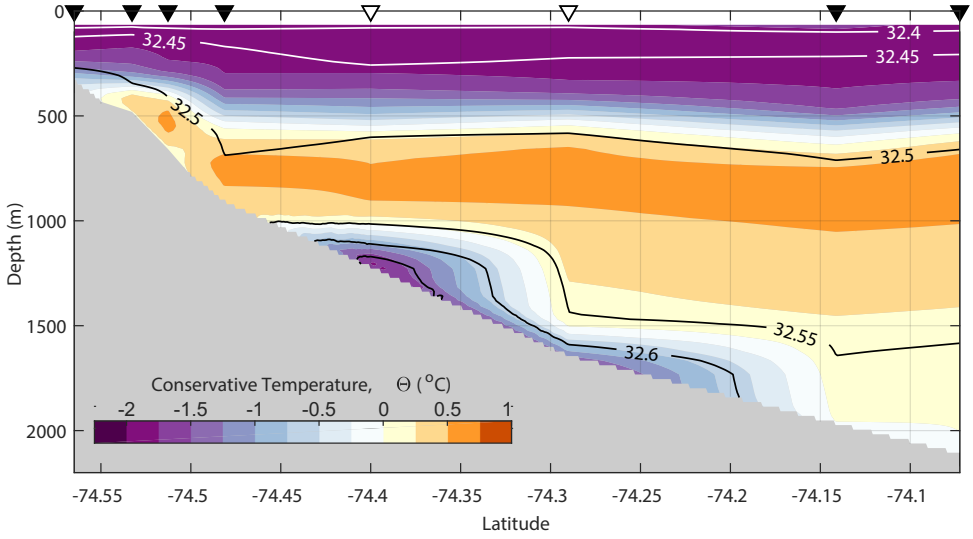

Figure 1.6: Conservative Temperature (Θ, colors), and density anomalies referenced to 1000 dbar (σ_1, contours) across the continental slope, obtained from cruise ANT XVI/2 in 1999 (Fahrbach and el Naggar, 2001). The transect was originally presented in Foldvik et al. (2004). Here, the temperature is converted to conservative temperature, Θ, and the horizontal axis represent latitude instead of distance. The section is obtained roughly along a northeast oriented ridge at 36°W. Triangles indicate the location of the CTD profiles. The latitudinal position of the white triangles are adjusted (see paper IV). Note that the color scale is different from that in Figure 1.5.

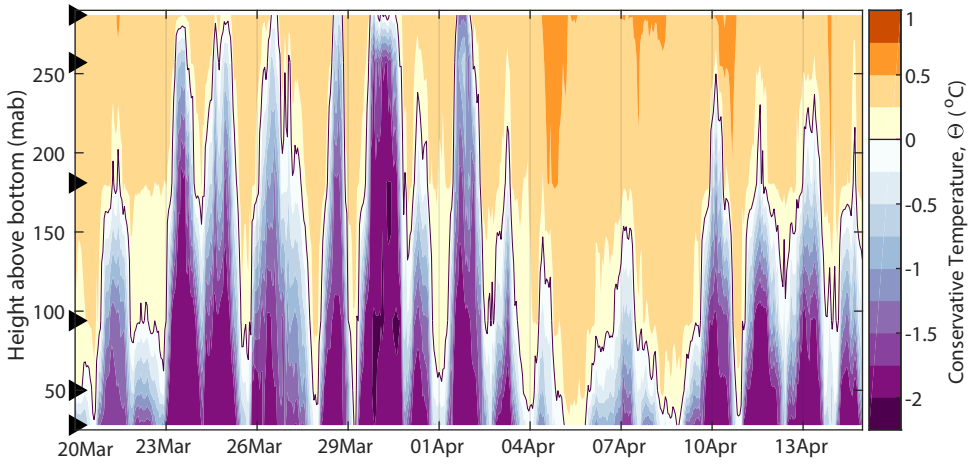

Figure 1.7: Time series of Conservative Temperature (Θ,) from a mooring located within the Filchner overflow plume along the continental slope, downstream of the FT (Paper IV)

This thesis discusses several aspects of the ISW flow across the Filchner sill and along the continental slope. Existing ISW transport estimates are discussed and compared to recent observations (Paper II, Paper IV). The variability of the ISW overflow velocity across the Filchner sill is discussed on both interannual and monthly time scales (Paper III). A somewhat unexpected co-variability between the monthly scale ISW overflow velocity and the upstream along-slope wind stress is presented, along with a suggested mechanism that could explain such co-variability. New observations of the Filchner overflow plume are presented, which indicate large fluctuations of the plume thickness and strong mixing (Figure 1.7, Paper IV). Different mechanisms that could explain the variability are discussed, and new insight governing the plume thickness variability and mixing is provided.

1.5 Mixing and variability on shorter time scales

Mixing processes over the continental shelf break and slope are important for both water mass transformation (section 1.4), and cross-shelf exchange of water masses over the continental shelf and in the FT (section 1.2). This section summarizes different mixing processes, such as internal waves and eddy-induced mixing, as well as eddy transports, which are different from mixing as they transport water masses adiabatically, rather than mixing them.

1.5.1 Internal tides

Barotropic tidal currents can generate internal waves, known as internal tides. Internal tides are typically generated over topographic features such as sea mounts, ridges and continental slopes. Steep bottom slopes, such as the Weddell Sea continental slope, are favorable for generation of internal tides. Here the bottom slope is similar to the internal wave slope from the horizontal, known as critical slope. When the internal waves meet the sloping topography, they are reflected, and the reflected waves interact with the incident wave, leading to enhanced shear and turbulence (*Eriksen*, 1985).

In addition to having a critical slope, the southeastern Weddell Sea continental slope is roughly co-located with the critical latitude for the semi-diurnal tidal wave (*Daae et al.*, 2009). Linear semi-diurnal internal tides cannot propagate freely poleward of the critical latitude. Instead, the waves are exponentially damped (*LeBlond and Mysak*, 1978; *Vlasenko*, 2005), which lead to thickening of the bottom boundary layer and enhanced mixing near the bottom (*Daae et al.*, 2009; *Fer et al.*, 2016; *Furevik and Foldvik*, 1996). The Filchner Overflow plume crosses the shelf break and continues westward along the upper continental slope. Enhanced mixing in this region has consequences for the entrainment of WDW and the final properties of the WSBW.

The enhanced semi-diurnal tidal currents in the southern Weddell Sea also lead to uncertainties in estimates of volume transports across the FT based on ship-borne profiles of hydrography and currents (Paper II). Obtaining a transect across the FT (or just parts of it) typically takes up to 12 hours. This means that the stations within a transect are obtained at different tidal phases. The tidal contribution to the observed currents must be removed prior to calculating the volume transports. The detiding procedure requires careful attention, since the transport estimates are highly sensitive to the choice of detiding scheme.

1.5.2 Topographic vorticity waves

Conservation of PV causes trapping of waves along coastal walls or over sloping topography (e.g. *Mysak*, 1980; *Rhines*, 1970). These waves are often referred to as coastal trapped waves, continental shelf waves, or topographic Rossy waves, but here the term Topographic Vorticity Waves (TVW) is used. The waves are forced by a PV gradient across the sloping bottom. The conservation of PV is expressed by

$$\frac{d}{dt}\left(\frac{\zeta+f}{H}\right)=0,$$

where $\zeta=\partial v/\partial x-\partial u/\partial y$ is the vertical component of the relative vorticity, $f=2\Omega\sin\phi$ is the vertical component of the planetary vorticity (Coriolis frequency), and H is the bottom depth. If a fluid parcel is moved upslope toward shallower isobaths, H decreases and the water column is squeezed vertically. Conservation of PV then requires a reduction of $\zeta+f$. If we assume f is constant, ζ must decrease, which means that the parcel gains anticyclonic (negative) relative vorticity. The opposite is true when a fluid parcel moves downslope toward deeper isobaths. In the southern hemisphere, the net effect of the changes in relative vorticity is a westward propagating wave along the sloping topography. Different modes of TVW reflects the dominating effects of a coastal wall or a sloping topography. Mode zero waves, are predominantly forced by a coastal wall, and are also referred to as Kelvin waves. Mode one waves are mainly forced by a sloping topography, whereas mode two waves are affected by both, although the effect of the coastal wall is dominating (*Wang and Mooers*, 1976).

In the Weddell Sea, TVW may increase the heat exchange across the continental shelf break and affect the dense water production rates. Observations show that excitation of zero mode barotropic TVW at the diurnal frequency leads to enhanced eddy kinetic energy (EKE) and mixing at the diurnal frequency (*Foldvik et al.*, 1990; *Middleton et al.*, 1987; *Semper and Darelius*, 2017). Energetic oscillations with periods of 35 hours, 3 days and 6 days are also observed along the continental slope. These oscillations have properties that agree with westward propagating TVW (*Jensen et al.*, 2013). The 35 hour oscillation is consistent with mode one TVW where the wavelength is less than 200 km, and where the group speed and phase speed are opposing each other, i.e. the group speed (energy) propagates eastward. The 3 and 6 days oscillations are consistent with mode two TVW, with wavelengths of 100 and 1000 km, respectively, and westward propagation of energy. *Marques et al.* (2014) show that TVW may be generated by the dense Filchner overflow. Westward propagation of TVW, i.e. in the same direction as a dense overflow, affects the mixing between the overflow and the ambient water masses, which in turn, influence both the volume flux and the properties of the AABW (*Jensen et al.*, 2013; *Marques et al.*, 2014).

Here, it is shown that alignment of counter-rotating TVW with periods of 24 and 72 contribute to enhanced mixing and thickness fluctuations of the Filchner overflow plume (Paper IV).

1.5.3 On-shelf transport by eddies

Recent studies indicate that eddies contribute largely to the on-shore transport of CDW (*Hattermann et al.*, 2014; *Nøst et al.*, 2011; *Stewart and Thompson*, 2016). Eddies formed by baroclinic instability may cause overturning and mixing of the ASF, and convert the available potential energy (APE) associated with the front into EKE (*Nøst et al.*, 2011). Eddies act to reduce the APE in the water column as a whole. However, the APE may increase locally

within the water column, and cause upward sloping isopycnals near the bottom. Upward sloping isopycnals combined with presence of dense water on the shelf may create an isopycnal connection between the dense shelf water and the warm CDW. The isopycnal connection favors on-shelf transport of CDW, since the CDW may flow onto the shelf along the isopycnal, without doing work against the buoyancy force (*Stewart and Thompson*, 2016).

In order to obtain realistic estimates of on-shore heat transport in numerical simulations, it is essential to have a high lateral resolution ($\mathcal{O}$(1 km)) in order to resolve eddies (*Hattermann et al.*, 2014; *St. Laurent et al.*, 2013; *Stewart and Thompson*, 2015).

This thesis studies the on-shelf transport by eddies, by means of a high-resolution idealized model of the southern Weddell Sea (Paper I). In agreement with *Stewart and Thompson* (2016) it is shown that eddy induced on-shelf transport of warm water is facilitated when dense shelf water is present on the shelf. In addition, the on shore transport and eddy kinetic energy responds to variations in the off shelf upper ocean density, which enhances eddy overturning during summer.

1.6 Variability on annual and inter-annual time scales

Observations on the continental slope and on the Filchner sill show large year-to-year variability. The variability is linked to the Weddell gyre and how it responds to large scale atmospheric circulation patterns such as the Southern Annular Mode (SAM), the Semi-Annual Oscillation (SAO), and the El-Niño/Southern Oscillation (ENSO). Long term variability of the ISW overflow from the Filchner sill is discussed in Paper III. This section introduces the large scale atmospheric variability and its impact on the Weddell Sea circulation system.

The SAM-index is calculated from the difference in mean circumpolar sea level pressure between 40 and 65°S. A positive SAM-index indicates a large pressure gradient which, in the Weddell Sea, leads to increased cyclonic wind stress curl and spin-up of the Weddell gyre (*Jullion et al.*, 2010; *Lefebvre and Goosse*, 2004). *Gordon et al.* (2010) show that a positive SAM-index leads to depression of the pycnocline and to enhanced export of WSBW from the northwestern Weddell Sea. The SAM-index has been increasing since the late 1970s (*Marshall*, 2003). The increase has been attributed to stratospheric ozone depletion and greenhouse gas emissions (*Gillett and Thompson*, 2003; *Polvani et al.*, 2011).

The annual temperature cycles in the mid-latitude ocean and the Antarctic regions are out of phase. The phase difference causes a semi-annual poleward shift of the circumpolar pressure trough in spring (September) and autumn (March), and is known as the SAO (*Meehl*, 1991; *Simmonds and Jones*, 1998; *Van Loon*, 1967). When the circumpolar through shifts southward, the meridional pressure gradients become stronger and the surface wind stress increases (*Hurrell and Loon*, 1994). The phase of the SAO is consistent from year to year, while the SAM-index varies. *Hurrell and Loon* (1994) suggest that, due to the persistence of the SAO, SAO influences the long-term mean sea level pressure more strongly than the SAM. The SAO was particularly strong in the late 1970s, but has been declining during the last decades. The decline is likely caused by seasonal temperature changes in connection with SAM (*Van Loon et al.*, 1993).

ENSO is a periodic fluctuation in sea surface temperature and air pressure across the equatorial Pacific Ocean. ENSO is a strong source of variability in the Pacific sector of the Southern Ocean (*Turner*, 2004, and references therein). In the Weddell Sea, ENSO is mainly found to influence the atmospheric pressure in the northwestern part, due to pressure differences on either side of the Antarctic Peninsula (*Gordon et al.*, 2010). During warm El Niño events, the northward wind increases in the western Weddell Sea, while cold La Niña events lead to re-

versed winds. However, the effects of ENSO can be difficult to disentangle from the combined effects of ENSO and SAM. When SAM and ENSO have the same sign, they tend to counteract each other. The variability induced by ENSO is therefore most pronounced when SAM is in a neutral phase, or SAM and ENSO are of opposite signs (*Gordon et al.*, 2010; *Jullion et al.*, 2010). In the western Weddell Sea, the export of WSBW was larger in years following warm El Niño events (*Gordon et al.*, 2010; *McKee et al.*, 2011). The production of HSSW over the western Weddell Sea continental shelf is also related to ENSO. During El Niño events, strong northward winds increase the sea ice export and the production of HSSW (e.g. *Nicholls and Østerhus*, 2004). The opposite is true in La Niña events.

Chapter 2

This study

2.1 Objectives

Processes related to the Filchner-Ronne Ice Shelf (FRIS) in the Weddell Sea are of climatic importance. The main objective of this study has been to explore mechanisms related to the exchange of water masses between the continental shelf and the deep ocean. The study is based on available hydrography and current observations from the region (Paper II-IV), and on idealized numerical model experiments (Paper I). The thesis discusses mechanisms for on-shelf transport of heat inferred from idealized model experiments (Paper I). A thorough description of the idealized model is given in section 2.3. The thesis further assess the variability in the Weddell Sea current circulation on sub-seasonal time scales based on moored observations of hydrography and current over the continental slope, over the continental shelf, and in the Filchner Trough and Sill region (Paper III). Finally, the ISW pathway in the FT (Paper II) and the dense water overflow and mixing processes related to formation of AABW along the continental slope (Paper IV) are being addressed. A schematic overview of the current circulation, showing what part of the circulation is discussed in each paper is given in Figure 2.1.

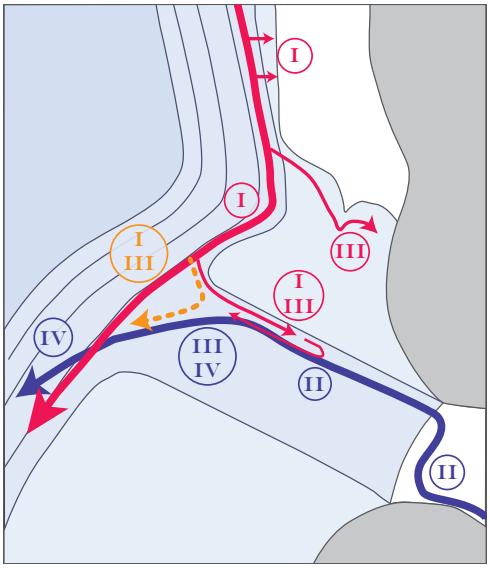

Figure 2.1: Schematic illustration of the current circulation in the southeastern Weddell Sea. The annotations indicate which papers included in this thesis discuss the different aspects of the circulation.

2.2 Data

2.2.1 Atmospheric data

Atmospheric data are obtained from the ERA-Interim reanalysis data set with 0.75° resolution (named ERA hereinafter; *Dee et al.*, 2011). The ERA data set has a time resolution of 6 hours, and is available from 1979 to present. Wind stress is calculated from ERA wind velocity at 10 meter above sea level and Sea Ice Concentration (SIC), following the procedure by *Andreas et al.* (2010), where the drag coefficient is a function of the SIC.

Observed wind velocity from the Halley Research station (turquoise star in Figure 2.2) is compared to the ERA dataset. The Halley record dates back to 1957, and allow for evaluation of long-term trends as well as comparison with current observations prior to 1979 when the ERA record starts.

2.2.2 Sea Ice Concentration

Time series of SIC from 1978 to 2017 are extracted from the National Snow and Ice Data Center (*Cavalieri et al.*, 1996). The data set is a satellite product generated from brightness temperature on a 25 km $\times$ 25 km grid. While SIC from ERA is based on different datasets of sea surface temperature prior to 2009 (*Dee et al.*, 2011), the NSIDC SIC product is consistent throughout the time series.

2.2.3 Moored observations

Hydrography and current velocity from 16 moored instruments form the basis of this thesis. An overview of the mooring locations and measurement periods is given in Table 2.1, and Figure 2.2. Here we report original mooring names. In paper II, we renamed the moorings according to geographic locations. These names are given in brackets, where the acronyms are as follows: the Continental Slope (CS), the Coastal Current inflow (CC), the shelf area east of FT (ES), the Filchner Trough (FT), and the Filchner Sill (FS).

2.2.4 Ship-borne observations

Paper I is based on vertical profiles of hydrography and velocity obtained during a cruise with RRS Ernest Shackleton in 2013. The data are collected using a conductivity-temperature-depth (CTD, SBE9111) package equipped with down and upward-looking lowered acoustic Doppler current profilers (LADCPs, 300 kHz RD Instruments Workhorse).

The data set from 2013 is compared with profiles obtained during cruises in 1973 (USCGC Glacier *Carmack and Foster*, 1975a), 2005 and 2009(JR97 and ES033 *Nicholls et al.*, 2009), and single stations from the FIS front in 1977 (*Foldvik et al.*, 1985a), 1980 (*Foldvik and Gammelsrød*, 1985), 1984, 1993 (*Gammelsrød et al.*, 1994), 1995 (*Grosfeld et al.*, 2001), and 2011 (JR244 *Larter*, 2011). The hydrographic sections and repeat time stations are indicated on the map in Figure 2.2, and detailed information is given in Table 2.2.

Table 2.1: Overview of the mooring records. Mooring names used in paper II are given in brackets.

Mooring Name	**Year deployed**	**# days**	**Lat** (°S)	**Lon** (°W)	**Bottom depth** (m)	**Reference**
S2 (FS1)	1977	411	74° 40′	33° 56′	558	*Foldvik et al.* (1985c)
S2 (FS1)	1985	371	74° 40′	33° 56′	545	*Foldvik et al.* (2004)
S2 (FS2)	2003	747	74° 40′	33° 28′	597	*Darelius et al.* (2014a)
S2 (FS2)	2010	364	74° 38′	33° 30′	602	*Darelius et al.* (2014a)
S2E (FS3)	2014	1124	74° 40′	33° 00′	593	
FR1 (FS4)	1995	837	75° 01′	31° 46′	610	*Woodgate and Schröder* (1998)
FR2	1995	828	75° 02′	31° 33′	574	*Woodgate and Schröder* (1998)
M78$_{7E}$ (FT1)	2013	376	77° 45′	36° 09′	705	*Darelius et al.* (2016)
M77$_{7}$ (FT2)	2013	371	77° 00′	34° 28′	705	*Darelius et al.* (2016)
M77$_{5}$ (ES1)	2013	371	77° 00′	34° 03′	505	*Darelius et al.* (2016)
M$_{31W}$ (ES2)	2014	746	76° 00′	31° 00′	457	*Ryan et al.* (2017)
M1 (CS1)	2009	386	72° 29′	17° 28′	273	*Graham et al.* (2013)
M2 (CS2)	2009	386	72° 27′	17° 38′	487	*Graham et al.* (2013)
M3 (CS3)	2009	361	74° 31′	30° 10′	725	*Jensen et al.* (2013)
B3 (CC)	2003	746	75° 49′	26° 52′	392	*Nicholls* (2005)
W2	2010	362	74° 21′	36° 1′	1411	Paper IV
W3	2010	360	74° 13′	35° 55′	1844	Paper IV

Table 2.2: Overview of the CTD/LADCP sections and time series.

Name	**Year**	**Start**	**End**	**Reference**
Section 1	2013	77°43'S, 35°28'W	77°43'S, 36°19'W	*Darelius et al.* (2014b)
Section 2		78°05'S, 43°25'W	77°52'S, 41°28'W	
Section 3		77°50'S, 43°43'W	77°42'S, 35°23'W	
Section 4		77°15'S, 33°40'W	76°54'S, 35°39'W	
Section 5		75°59'S, 30°42'W	75°50'S, 33°15'W	
Section 6		75°50'S, 33°15'W	75°10'S, 31°44'W	
Section05	2005	76°33'S, 33°18'W	76°41'S, 31°57'W	
Section09	2009	75°24'S, 30°29'W	74°59'S, 32°00'W	
Section73	1973	77°59'S, 43°29'W	74°45'S, 35°50'W	*Carmack and Foster* (1975b)
Time series:				
TS1	2013	77°52'S, 41°28'W		*Darelius et al.* (2014b)
TS2		77°40'S, 36°16'W		
TS3		76°00'S, 30°30'W		
TS4		75°05'S, 30°52'W		

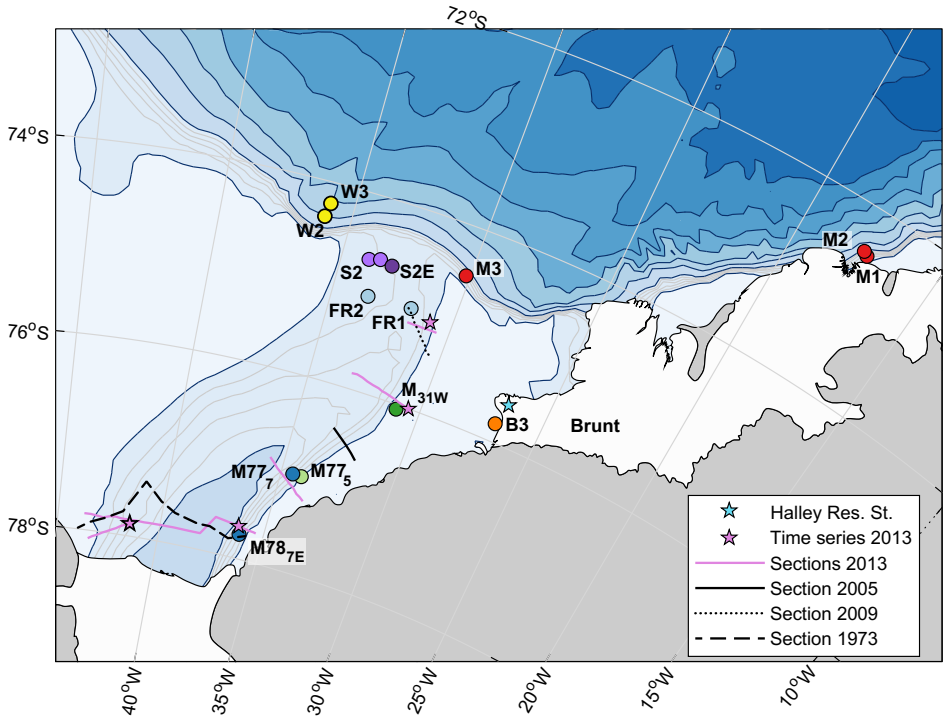

Figure 2.2: Map of the southern Weddell Sea, with bathymetry from Bedmap2 (Fretwell et al., 2013). Several records exist from the S2 location, represented by two light purple circles on the Filchner sill. The left circle indicates the S2 location in 1977, 1985 and 1987, and the right circle indicates the location in 2003, 2009 and 2010. CTD sections and time series are indicated according to the legend. The Halley Research station is indicated by a turquoise star.

2.3 An idealized model of the Weddell Sea

Idealized models are effective tools for testing ideas and hypotheses on various processes. By changing the driving forces systematically in different experiments, the model simulations may provide insight on isolated effects of each driving force or a combination of different driving forces. In addition, the cost of running idealized models are much lower than obtaining observation data. This is especially true for the Weddell Sea region. Both the remoteness and the severe sea ice conditions in the Weddell Sea make observations expensive and difficult. Models cannot replace the value of observations. However, results from idealized models may contribute to improved design of the observational surveys, especially regarding the temporal and spatial resolution needed to resolve the different processes.

To improve the understanding of the processes which control access of warm water onto the Weddell Sea continental shelf, a process oriented idealized numerical ocean model was set up. Idealized model studies based on channel models have contributed to understanding of some of the processes related to on-shelf transport (e.g. *Nøst et al.*, 2011; *Stewart and Thompson*, 2015), and to the effect of canyons and trough across the continental shelf (e.g. *Allen and Hickey*, 2010; *St. Laurent et al.*, 2013; *Williams et al.*, 2001). This study focuses on special features regarding the Weddell Sea geometry and processes, and is motivated by questions such as: How does the ASF respond to various wind forcing and surface water properties? How does the transition from a narrow to a wide continental shelf affect the on-shelf eddy transport? What is the effect of dense water formation over the wide shelf? How much warm water enters into the FT, and is the inflow to the FT sensitive to the properties of the dense shelf water in the deep trough?

This section gives a detailed technical description of the idealized model set-up applied in paper I, as well as motivation and a brief summary of the different sets of model experiments.

2.3.1 The Regional Ocean Model System (ROMS)

Idealized numerical simulations are conducted using the Regional Ocean Modeling System (ROMS, version 3.6, *Shchepetkin and McWilliams*, 2009). ROMS is a free-surface, terrain-following, hydrostatic primitive equations ocean model. The momentum equations are solved using a split-explicit time-stepping scheme, which reduce the computation cost by separating the slow (baroclinic) and the fast (barotropic) modes. Within each baroclinic time step, a finite number of barotropic time steps are carried out. ROMS applies orthogonal coordinates on a staggered Arakawa C-grid. In the vertical, the primitive equations are discretized over variable topography using stretched terrain-following coordinates (*Song and Haidvogel*, 1994). Stretched coordinates allow for increased resolution near the sea bed, which is needed to study eddy-mediated transport across the steep Weddell Sea continental slope. ROMS has various options for advection schemes. Here, the third order upwind scheme with no explicit mixing is applied, along with baroclinic time steps of 3 minutes, with 25 barotropic sub-steps.

2.3.2 Model grid

The interior Weddell Sea is large, with the wider continental shelf being roughly 950 $\times$ 450 km. In order to have a grid domain that is feasible to run, the model domain is reduced to 500 $\times$ 1500 km, which includes a 700 km long narrow channel upstream of the wide continental shelf (Figure 2.3). The model geometry is simplified to represent the main features that are important for the circulation along the Weddell Sea continental slope. A 400 m deep continental

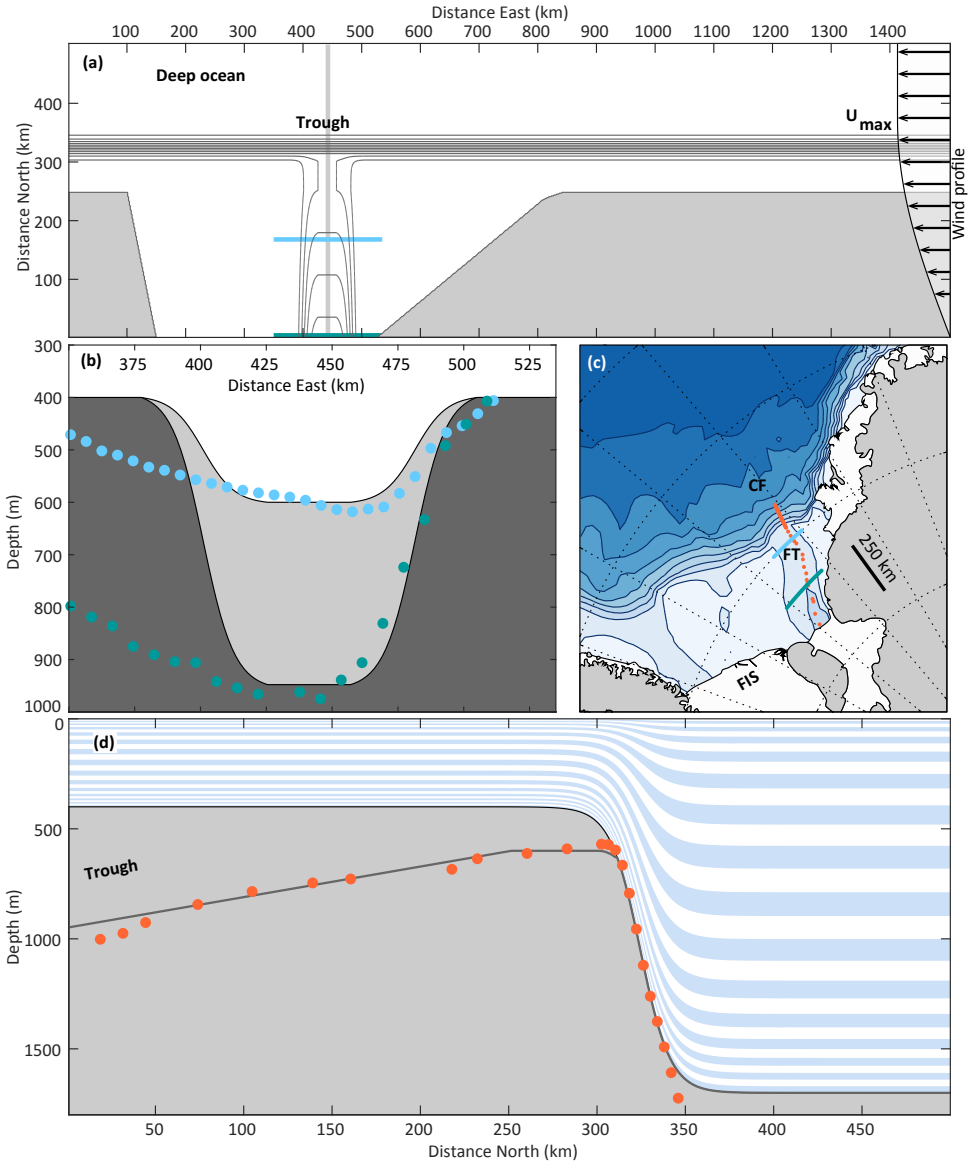

Figure 2.3: (a) Model domain seen from above. Bathymetric contours are drawn every 100 m, yielding a diffuse line over the steep continental slope. Arrows along the eastern boundary indicate the wind forcing profile. The green/yellow patches indicate averaging areas for the wide/narrow shelf respectively. (b) zonal transects showing the model trough geometry at the southern boundary (dark gray) and over the trough sill (light gray) together with real trough geometry from Bedmap (blue/petrol) at comparable distance from the sill, indicated on the map in (c). (d) Meridional transect showing the continental shelf and slope and vertical layers (blue/white). The depth profile along the center of the trough is drawn as a thin black line together with Bedmap topography (orange dots).

shelf is connected to a deep ocean through a continental slope. The maximum bottom depth in the open ocean is limited to 1700 m, which is assumed to cover the dynamically active part of the water column. The slope steepness ($\alpha \sim 0.016$) is similar to the Crary Fan (CF) region north of the FT, and is calculated from a hyperbolic tangent function (Figure 2.3 c-d).

In the Weddell Sea, wind and currents roughly follow the continental slope. The calculations are therefore simplified by making the continental slope purely zonal in the idealized set-up. The continental shelf is narrow in the east (similar to the eastern Weddell Sea coast) and widens toward west. A 125 km wide trough with a 600 m deep sill is cross-cutting the wide shelf region. The depth and the width of the trough is similar to the FT. The trough depth increases linearly from 600 m at the sill to 950 m at the southern boundary (Figure 2.3 d). The side walls are symmetric with a steepness representative of the eastern flank of FT, ranging from $\alpha \sim 0.0043$ at the sill to $\alpha \sim 0.0109$) near the southern boundary (light and dark gray shaded areas, respectively in Figure 2.3 b).

The horizontal resolution is 1.5 km, which is required to resolve mixing by eddies (*Hattermann et al.*, 2014; *St. Laurent et al.*, 2013; *Stewart and Thompson*, 2015). Vertically, the model is discretized into 30 terrain-following layers, with enhanced resolution near the surface and near the sea bed. The layer thickness varies from less than 3 m in the surface layer over the continental shelf, up to 110 m in the deep ocean interior.

2.3.3 Initialization

The shallow continental shelf is initially filled with a uniform water mass, having a salinity of 34.4 and a temperature at the freezing point ($\theta = -1.9^oC$). Over the continental slope, the stratification is constructed from 26 conductivity-temperature-depth (CTD) profiles, obtained across the eastern Weddell Sea continental shelf break at 17^o W in 1997 (*Nøst and Østerhus*, 1998). WDW resides in the deep water, and the isopycnals slope down over the continental slope, which is characteristic for the ASF (Section 1.2). Fresh surface water is removed to obtain a typical winter stratification with a well-mixed upper layer (Figure 2.4a-c). Apart from a geostrophically balanced current over the continental slope, the velocity fields are initially at rest.

In the reference simulations, the trough is filled with Dense Shelf Water (DSW) with $\theta_{DSW} = -2^oC$ and $S_{DSW} = 34.65$ below shelf depth. These values fall within the range of observed ISW properties (Figure 2.4g-i). In order to test the sensitivity to the DSW density, additional experiments were performed, where the model was initialized with higher and lower DSW salinity (S=34.5 and S=34.8), as well as no DSW (S=34.4). All these values are extremes compared to the available observed salinity profiles (Figure 2.4h).

2.3.4 Summer and winter climatologies

The experiments are sorted in two seasonal categories (winter and summer) to study how the eddy transports are affected by upper ocean stratification. The seasonal forcing is applied to the model runs through climatology fields at the open boundaries and at the surface. The winter climatology is the same as the initialization described in section 2.3.3, with a homogeneous well mixed upper layer. The summer climatology includes a fresh off-shelf surface layer, and is constructed from hydrographic observations obtained by instrumented Elephant seals (*Nøst et al.*, 2011) (Figure 2.4d-f), as described in *Hattermann et al.* (2014). Over the wide continental shelf (east of 800 km East in Figure 2.3a), the climatology is the same in the winter and summer scenarios (i.e. always winter). In the summer scenarios, there is a linear transition

in hydrography between the winter conditions over the wide shelf and the summer conditions over the continental slope.

2.3.5 Atmospheric forcing

The ASF is mainly wind-driven (Section 1.2). Each set of model configurations (combinations of water mass properties and season) were forced with a suite of westward along-slope wind stress corresponding to wind speeds of 3, 6, and 9. The wind stress is calculated from $\tau = \rho_{air} C_D U^2$, where $\rho_{air} = 1 kg m{-}3$ and the drag coefficient $C_D = 0.001$. The reference winter run was, in addition, forced with wind stress corresponding to 0 and 12 m s^{-1}. The wind field is constant north of 375 km North and decays sinusoidally toward zero at the southern boundary (Figure 2.3a).

Sea ice is not included directly in the idealized model. The effects of sea ice are instead mimicked by restoring the SST to $-1.9^o C$ and SSS to 34.4, with a restoring time scale of 3 days. The restoring is uniform for the winter simulations. In summer, the surface restoring over the wide shelf is the same as for winter conditions, while the restoring toward SST$=$ $-1.5^o C$ and SSS$=$ 33.7 is applied over the narrow shelf and the deep ocean. To assess how presence of dense water over the shelf affect the on-shelf transport of warm water, experiments with increased SSS restoring (SSS=34.5), leading to denser shelf water were conducted. A contrasting scenario, with reduced SSS restoring (SSS=34.3) was also tested.

2.3.6 Boundary conditions

At first, the model was run as a re-entrant channel model, similar to e.g. (*Hattermann et al.*, 2014; *Stewart and Thompson*, 2015). The motivation for doing so, was to keep a fully developed eddy field along the continental slope, and to ensure a closed model domain, which is required to separate eddy fluxes into purely rotational and purely divergent parts (*Fox-Kemper et al.*, 2003; *Marshall and Shutts*, 1981). However, the re-entrant model did not work satisfactorily due to flow of DSW from the trough. In order to guarantee that changes in the DSW properties did not lead to upstream changes in the flow (due to re-entrant water masses), it was decided to use open boundaries in the east and in the west. The northern and southern boundaries are treated as closed walls. A series of tests were performed to find a suitable configuration for open boundary conditions and sponge zones without spurious reflections.

The open boundary conditions for the hydrography and the 3-D momentum fields are defined by a radiation scheme with restoring toward the initial conditions (*Marchesiello et al.*, 2001). A radiation condition similar to Flather (*Flather*, 1976), but adjusted for staggered grids (named Shchepetkin in ROMS) is applied for the 2-D momentum fields, accompanied by the Chapman explicit condition for the free surface (*Chapman*, 1985). At all boundaries, there is a 30 km sponge zone, where the diffusivity and viscosity increase smoothly from 1 $m^2 s^{-1}$ in the interior to 3 $m^2 s^{-1}$ at the boundary.

To avoid drift in the water mass properties, temperature and salinity are restored at all boundaries using smoothly increasing relaxation time scales (*Nycander and Döös*, 2003). The 3D momentum is also restored to maintain the geostrophically balanced slope current. The restoring zone is 24 km at the southern boundary, and 30 km at the other boundaries. An extended 350 km eastern boundary restoring zone is applied for the 10 deepest layers, in order to reduce piling up of DSW. The restoring time scale is 30 days at the western and northern boundaries. Along the eastern boundary the restoring time scale is 60 days. To ensure that the DSW properties do not drift over the 5 years model run, the restoring time scale at the southern

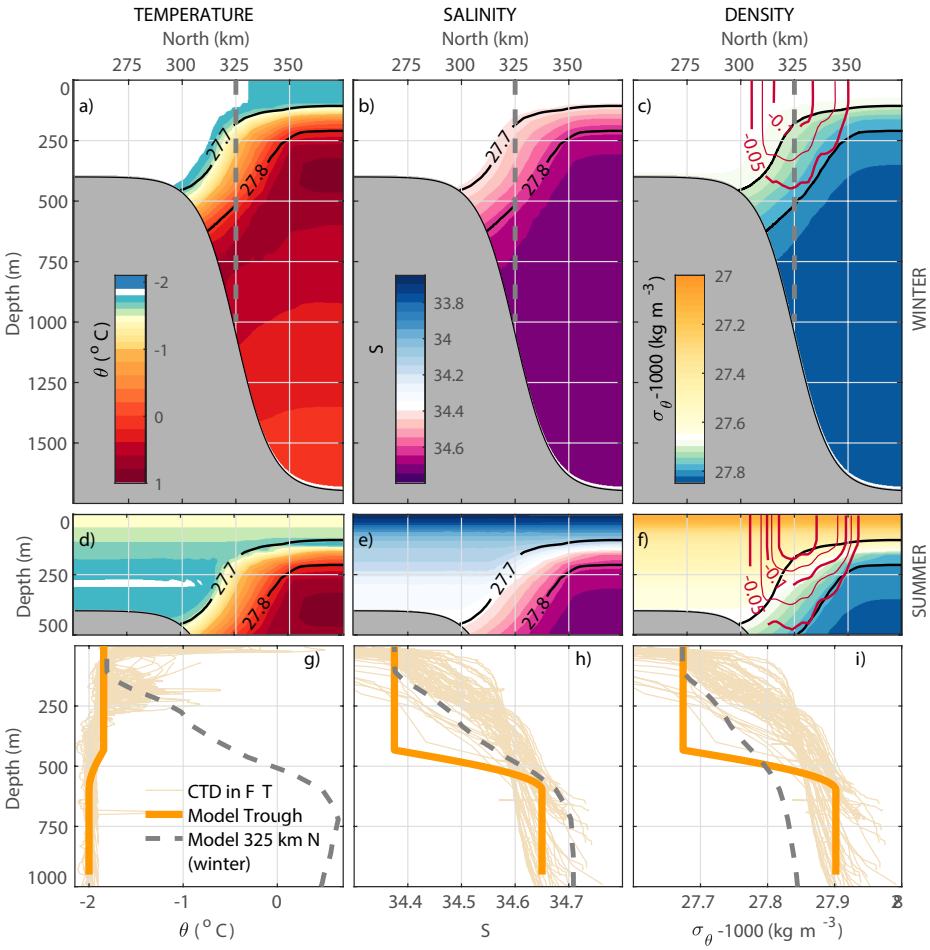

Figure 2.4: Initial temperature (a), salinity (b) and density (c) for the idealized model over the continental slope in winter. Surface summer climatology for temperature, salinity and density are shown in (d-f), respectively. The summer climatology is only differing from the winter condition above the $\sigma_\theta = 27.7$ isopycnal. Black contours in (a-f) show isopycnals at $\sigma_\theta = 27.7$ and 27.8. Red contours in (c) and (f) indicate the geostrophically balanced slope current. Panel (h-i) show hydrographic profiles of temperature, salinity and density from 58 historical CTD casts in the central Filchner Trough (light orange), as well as the model hydrography in the trough (dark orange) and over the continental slope at 325 km N (gray dashed).

boundary is shorter (5 days above 400 m and only 1 hour below 400 m), and a northward flux of ($\sim 1\,Sv$) is imposed by restoring the northward velocity, V_{north} to 0.025 m s^{-1} below 430 m at the southern boundary.

2.3.7 Experiments

I order to address the different research questions outlined in the beginning of section 2.3 (and repeated below), a set of 35 experiments were conducted, where wind stress, surface stratification (summer and winter), DSW properties and the SSS restoring value were systematically varied. A schematic overview of the different sets of experiments and links to the research questions is given in table 2.3.

All experiments are run in pairs of winter and summer scenarios. The model is spun up by running for five years with continuous winter forcing and various combinations of wind, DSW and SSS restoring. Reference scenarios are based on a DSW salinity of S=34.65 and a Sea Surface Salinity restoring of SSS=34.4. The output after the spin-up period is used as starting conditions for both winter and summer experiments. Each experiment is run for five years with constant climatology. Daily averaged fields are saved for the last model year. The southward volume transports are estimated from the daily fields prior to averaging over the model year. Other parameters are calculated from temporal averages over the last six months.

1. How does the ASF respond to various wind forcing and seasonal surface stratification?
2. How does the transition from a narrow to a wide continental shelf affect the on-shelf eddy transport?
3. What is the effect of dense water formation over the wide shelf?
4. How much warm water enters into the FT
5. Is the inflow to the FT sensitive to the SSS restoring or to the properties of the dense shelf water in the deep trough?

Table 2.3: Overview of the idealized model experiments, with references to the research questions they are designed to assess. Reference values are indicated by bold face characters

Parameter	Value	Res. question
Season	Winter, Summer	1-5
Wind	(0,12[a]) 3,6,9	1-5
SSS restoring	33.3, **33.4**, 33.5	2, 3, 5
DSW salinity	33.4[b], 33.5, **33.65**, 33.8	5

[a] Only for winter reference runs

[a] No DSW, only for winter runs with reference SSS

Chapter 3

Introduction to the papers

Paper I: **On the effect of topography and wind on warm water inflow - An idealized study of the southern Weddell Sea continental shelf system**

Daae, K., T. Hattermann, E. Darelius, and I. Fer (2017), J. Geophys. Res Ocean, 122(3)

Paper I investigates processes related to on-shelf transport of WDW. The results are based on experiments with an idealized numerical ocean model (Section 2.3). The idealized model geometry resembles the Weddell Sea Continental shelf and slope, and includes a trough similar to the Filchner Trough across the continental shelf. A suite of experiments with varying zonal wind speed and water mass properties are conducted.

Inflow of warm water onto the shelf is limited due the presence of the ASF. More warm water enters the shelf during summer, when fresh surface water is present. A shallower eddy overturning associated with the upper ocean stratification partially balances the Ekman downwelling, such that the WDW interface is relaxed. We further show that the inflow of warm water is sensitive to along-shelf salinity gradients. Presence of denser water over the wide shelf favors up-slope eddy transport along isopycnals of the V-shaped slope front.

Inflow of warm water in the trough is sensitive to the wind forcing. In experiments with weak wind forcing, the slope current is not influenced by the trough topography and crosses the FT. The southward transport is dominated by eddies, and is highest in experiments with denser shelf water. In experiments with strong wind forcing, the wind-driven component of the slope current moves up-slope to shallower isobaths, and is topographically steered into the FT. Due to PV constraints, the slope current cannot cross the sill, but is forced to turn and leaves the trough. The recirculation of the slope current suppresses the southward heat transport by eddies, since eddies are being advected out of the trough along with the current.

Paper II: **Hydrography and circulation in the Filchner Depression, Weddell Sea, Antarctica**

Darelius, E., K. Makinson, K. Daae, I. Fer, P. R. Holland, and K. W. Nicholls (2014),J. Geophys. Res Ocean, 119

Paper II investigates ship-born observations of hydrography and currents from the Filchner Trough in January 2013. The northward flow of cold and dense ISW has traditionally been associated with the western flank of the Filchner Trough, but here we show that the northward flow of ISW occurs in a mid-depth jet along the eastern flank of the trough. Numerical model

results support the findings and further suggest that ISW flowing along the eastern coast of the Berkner Island turns eastward and crosses the Filchner Trough upon reaching the Filchner Ice Shelf front. The eastward turning of the ISW flow is likely a result of potential vorticity constraints. The ice shelf front represents a sudden change in the thickness of the water column, and thus a potential vorticity barrier which the flow cannot cross.

A northward ISW transport of 0.2 to 1 Sv is estimated based on several transects across the eastern side of the FT. The large uncertainties in the transports reflect the strong tidal currents in the area, and the difficulties to remove the tidal signal from the observed current profiles in a consistent way.

My main contribution to this paper was processing and analyzing of current records from the lowered Acoustic Doppler Current profiler (LADCP), as well as testing and refining different schemes for de-tiding of the current velocity data.

Paper III: **Wind stress mediated variability of the Filchner Trough overflow, Weddell Sea**

Daae, K., E. Darelius, I. Fer, S. Ryan, and S. Østerhus (2018), J. Geophys. Res Ocean (Accepted March 2018)

Paper III explores the relationship between monthly scale variability of wind and current velocity associated with the ISW overflow and the ASF processes in the southeastern Weddell Sea. The paper shows that the current variability over the slope and along the ACoC pathway is strongly linked to the along-slope wind forcing on monthly time scales. Both the slope current and the ACoC current speed increases during periods of high along-slope wind stress.

Paper III further describes occurrence of high correlation between the ISW overflow velocity in the FT and the along-slope wind stress over the continental slope upstream of the FT. We propose that recirculation of the slope current, as described in paper I, may occur during periods with strong along-slope wind forcing. Interaction between the wind-driven recirculating slope current and the ISW overflow could increase the ISW overflow speed and thereby explain the co-variability of the wind and the ISW overflow. Although the existing data set is insufficient to prove the recirculation mechanism, a few threads of evidence for the proposed mechanism are presented. The results merit further investigation over the Filchner Sill, to improve the understanding of the water exchange and the proposed interaction between the slope current and the ISW overflow.

Paper IV: **Variability and mixing of the Filchner overflow plume descending the continental slope west of Filchner Trough, Weddell Sea**

Daae, K., I. Fer, and E. Darelius, manuscript in preparation

Paper IV describes the flow of ISW over the Filchner Sill and along the continental slope downstream, based on moored instruments. The paper demonstrates that the monthly scale plume properties at the two sites are related, and discusses the transport of ISW over the Filchner sill and along the continental slope. The paper further describes the characteristics of the Filchner overflow plume. The plume thickness fluctuates strongly on daily time scales. The thick plume events contribute with a large portion of the dense water transport. We show that the thickening of the plume, and the associated strong mixing, is related to alignment of counter-rotating oscillations with periods of 24 and 72 hours. We discuss the source of the oscillations, and the implications of the mixing associated with the alignment.

Chapter 4

Perspectives and Outlook

Based on available observations and idealized numerical model experiments, this thesis addresses key processes governing the exchange of water masses between the Weddell Sea continental shelf and the deep ocean. The thesis illustrates how the Antarctic Slope Front (ASF) protects the continental shelf from on-shore heat transport, and hence contributes to maintaining low basal melt rates in the Weddell Sea.

The ASF is forced by prevailing easterly winds (*Sverdrup*, 1953) and varies seasonally as a response to the wind forcing, the Weddell Gyre, and the hydrography of the surface water (*Fahrbach and el Naggar*, 2001; *Gordon et al.*, 2010; *Graham et al.*, 2013; *Núñez-Riboni and Fahrbach*, 2009). This thesis demonstrates that the co-variability of the slope current and the wind stress also occurs on monthly time scales. It is further shown that other parts of the Weddell Sea circulation, including the Filchner overflow, respond to the upstream monthly scale wind variability. Results from the idealized model experiments suggest that the slope current core moves upslope to shallower isobaths during strong wind forcing. This shift leads to stronger interaction between the slope current and the trough topography.

The Filchner overflow consists of ISW formed under the FRIS. Observations from the FT are sparse, especially from the western side of the FT, where sea ice is present year-round. The thesis presents observations suggesting that the ISW emanating from the FIS is flowing northward along the eastern side of the FT as a mid-depth jet. The finding contrasts the traditional view that ISW flows northward along the western side of the FT (*Nicholls et al.*, 2009). The ISW crosses the Filchner sill and veers westward along the continental slope under influence of the Earth's rotation (*Foldvik et al.*, 2004). The thesis describes strong fluctuations of the Filchner overflow plume thickness (Paper IV). The monthly scale variability is related to the upstream conditions on the Filchner sill, which is modulated by the monthly scale co-variability between the overflow and the wind. New insight is gained concerning the sub-inertial plume thickness fluctuations. Alignment of counter-rotating oscillations associated with topographic vorticity waves leads to strongly increased shear across the plume interface, plume thickening and enhanced mixing with the ambient water masses. The thick plume events contribute with a large portion of the total dense water transport, and are important for the AABW production.

4.1 The Antarctic Slope Front response to a changing climate

The long-term variability of the ASF is related to the surface stress, which is regulated by the strength of the easterly wind and the presence of sea ice. The Southern Annular Model (SAM)

is a strong driver of long-term climate variability. During the past few decades, a trend toward the positive state of the SAM is observed (*Marshall*, 2003; *Thompson and Solomon*, 2002), which results in spin-up of the Weddell gyre and stronger easterly winds along the Weddell Sea continental slope (*Jullion et al.*, 2010; *Lefebvre and Goosse*, 2004). Based on regional Ice-Ocean models, forced with outputs from a global climate model, *Hellmer et al.* (2012, 2017) and *Timmermann and Hellmer* (2013) studied the ASF system in the present day climate and in future scenarios with higher carbon emissions and a warmer atmosphere. They show that the ASF and the slope current is vulnerable to future atmospheric changes. In their experiments, the increased surface stress, resulting from reduction of the sea ice cover, lead to irreversible changes to the ASF, and a southward redirection of the slope current into the Filchner Trough. A redirection of the slope current could fill the FRIS cavity with warm oceanic water, and strongly increase the basal melt rates.

Results from the idealized model experiments presented in this thesis suggest a slightly different response to increased wind stress. Instead of being redirected southward, the slope current recirculates over the trough opening due to conservation of potential vorticity. The recirculating of the slope current effectively reduces the southward transport of warm water by eddies, as the eddies are being advected out of the trough along with the current. The results emphasize the role of potential vorticity conservation in the FT sill region. In order to obtain realistic predictions of the slope current response to future climate warming, the model resolution must be adequate to resolve the potential vorticity dynamics in the Filchner sill area.

4.2 Future freshening of the dense shelf waters

The sea ice production over the Weddell Sea continental shelf has reduced substantially during the past 30 years, with subsequent reduction in both formation of HSSW and transport of HSSW under the FRIS (K. W. Nicholls, P. Holland, S. Østerhus and K. Makinson, unpublished manuscript). These changes may impact the exchange of water masses between the continental shelf and the deep ocean.

Firstly, eddy-mediated transport of WDW (CDW) across the ASF and onto the continental shelf is facilitated when dense water is present on the shelf (Paper I; *Stewart and Thompson*, 2016). The establishment of an isopycnal connection between the dense shelf water and the WDW, creates a pathway for WDW to access the continental shelf without doing work against the buoyancy force. This process strongly relies on the density of the shelf water. A freshening of the dense water may weaken this mechanism for on-shelf transport of WDW. Based on idealized model experiments conducted in this study, it is shown that a freshening of $\mathcal{O}(0.1)$ is sufficient to suppress the on-shelf eddy-mediated WDW transport.

Secondly, the presence of dense ISW in the FT can reduce the southward transport of WDW into the trough (*Hellmer et al.*, 2012, 2017). *Hellmer et al.* (2012, 2017) suggest that a combination of ISW freshening and a shallower thermocline, could reduce the ISW density enough to allow intrusions of WDW into the FT beneath the ISW. However, the presented strong co-variability between the Filchner overflow and the upstream wind stress, illustrates the complexity of the water exchange across the Filchner sill. In order to assess the effect of ISW freshening, and the proposed interaction between the ISW overflow and the slope current, an array of moorings across the Filchner sill is needed. Several moorings were deployed on the continental slope and in the FT in early 2017 (*Sallée*, 2017), and may cast light to the processes discussed here.

4.3 Future monitoring of the Weddell Sea

Several aspects of this study would have benefited from a better coverage of observations. The severe sea ice conditions in 2010, when moorings were deployed on the Filchner Sill and across the continental slope downstream (Paper IV), resulted in too few observational points across the continental slope to capture the width of the Filchner Overflow plume. With a better coverage of the plume, it would have been possible to estimate the volume transport of the plume, and to better assess the mixing processes. Along with the two moorings that were deployed on the continental slope in 2010, a third mooring, was deployed further west, on the other side of the ridge at 36° W. Unfortunately, this mooring was never recovered. Despite multiple year efforts, the sea ice conditions has prevented a recovery.

Paper III highlights a co-variability between the ISW overflow velocity and the wind stress upstream. However, the proposed mechanism leading to the co-variability - slope current recirculation and interaction with the ISW overflow - could not be tested firmly owing to few joint observational sites. New observations from the Filchner sill and the continental slope, upstream, are underway (*Sallée*, 2017). These data may provide sufficient coverage of the ISW plume to study the suggested interaction with the slope current. In addition, they may contribute with improved estimates of the ISW volume transport from the FT.

It is not an easy task to plan and conduct field campaigns to the southern Weddell Sea. Field campaigns are typically quite expensive due to long transit times and high risks involved with mooring deployment and recovery. Severe sea ice conditions, ice bergs threatening to destroy the moorings, and steep topography are among the elements which limit the available mooring locations and the vertical extent of the moorings. Although a certain region might be accessible one year, it is never certain if, or when, the same region can be revisited to recover the moorings. International partners (from e.g. the United Kingdom, Germany, France, and Norway) are collaborating on field campaigns to the southern Weddell Sea. With the coming of the new Norwegian ice breaker research vessel *Kronprins Haakon*, the Norwegian contribution to the collaboration may advance, and open up for new exciting research projects.

Emerging technology may facilitate observations and monitoring of the Weddell Sea in the near future. Several ongoing research projects in the southern Weddell Sea are testing out available new technology. The use of autonomous vessels, such as gliders and floats, may contribute to facilitate observations under the sea ice. Today, observations from large parts of the sea ice covered Weddell Sea continental shelf are lacking. In addition to observations made from instrumented seals (e.g. *Årthun et al.*, 2013), floats may provide access to previously unreachable areas. In the ongoing project WAPITI (*WAPITI*, 2018), several APEX profiling floats have been deployed in the FT and along the Weddell Sea continental slope (*Sallée*, 2017). The floats can travel under the sea ice, and are equipped with hydrophones which can communicate with sound sources attached on several moored arrays on the Weddell Sea continental shelf and slope. The floats can also be programmed to follow the bottom topography, and hence provide new *lagrangian* observations of the Filchner overflow plume.

Two joint projects (the Filchner Ice Shelf System project (FISS, *FISS*, 2018) and the Filchner Ice Shelf Project (*FISP*, 2018)) have made advances in monitoring of the water column below the FIS. Moorings are deployed through hot water drilling holes at several locations (*Hattermann et al.*, 2017), and provide new insight into the ISW circulation and formation processes under the ice shelf (*Hattermann et al.*, 2018). In January and February this year (2018), pioneering experiments with an autonomous underwater vehicle (Autosub Long Range) took place under the FRIS (*FISS*, 2018), reaching a largely unknown environment. The combined data set from the Autosub and the moorings underneath the FIS may contribute to increased un-

derstanding of the processes controlling the water mass exchange across the FIS front, which might change significantly in the near future.

Chapter 5

Scientific results

Paper I

On the effect of topography and wind on warm water inflow - An idealized study of the southern Weddell Sea continental shelf system

K. Daae, T. Hattermann, E. Darelius, and I. Fer
J. Geophys. Res. Oceans, **122** (2017)

AGU PUBLICATIONS

JGR

Journal of Geophysical Research: Oceans

RESEARCH ARTICLE

10.1002/2016JC012541

Key Points:
- PV constraints impede warm inflow to a coastal deep trough
- Warm inflow along the trough decreases with stronger wind
- Dense water formation increases on-shelf transport of WDW

Supporting Information:
- Supporting Information S1
- Movie S1
- Movie S2
- Movie S3

Correspondence to:
K. Daae,
kjersti.daae@uib.no

Citation:
Daae, K., T. Hattermann, E. Darelius, and I. Fer (2017), On the effect of topography and wind on warm water inflow—An idealized study of the southern Weddell Sea continental shelf system, *J. Geophys. Res. Oceans*, *122*, 2622–2641, doi:10.1002/2016JC012541.

Received 8 NOV 2016
Accepted 28 FEB 2017
Accepted article online 2 MAR 2017
Published online 31 MAR 2017

On the effect of topography and wind on warm water inflow—An idealized study of the southern Weddell Sea continental shelf system

K. Daae[1], T. Hattermann[2,3], E. Darelius[1], and I. Fer[1]

[1]Geophysical Institute, University of Bergen and Bjerknes Centre for Climate Research, Bergen, Norway, [2]Akvaplan-niva AS, High North Research Centre, Tromsø, Norway, [3]Helmholtz Centre for Polar and Marine Research, Alfred Wegener Institute, Bremerhaven, Germany

Abstract An idealized eddy-resolving numerical model, with topographic features common to the southern Weddell Sea, is constructed to study mechanisms through which warm deep water enters a wide continental shelf with a trough. The open ocean, represented by a 1700 m deep channel, is connected to a 400 m deep shelf with a continental slope. The shelf is narrow (50 km) in the east but widens to 300 km at the center of the model domain. Over the narrow shelf, the slope front is balanced by wind-driven Ekman downwelling and counteracting eddy overturning, favoring on-shelf transport of warm water in summer scenarios when fresher surface water is present. Over the wide shelf, the Ekman downwelling ceases, and the mesoscale eddies relax the front. Inflow of warm water is sensitive to along-shelf salinity gradients and is most efficient when denser water over the wide shelf favors up-slope eddy transport along isopycnals of the V-shaped slope front. Inflow along the eastern side of the trough cannot penetrate the sill region due to potential vorticity constraints, while along the western trough flank, eddy-induced inflow crosses the sill and reaches the ice front. The warm inflow into the trough is sensitive to the density of the outflowing dense shelf water. For weaker winds, absence of the dense water outflow leads to a reversal of the trough circulation and a strong inflow of warm water, while for stronger winds, baroclinic effects become less important and the inflow is similar to experiments including dense water outflow.

1. Introduction

The observed thinning of the floating ice shelves in West Antarctica has been attributed to increased basal melt caused by increased flow of warm (>−1.9°C) Circumpolar Deep Water (CDW) into the ice shelf cavities [*Pritchard et al*., 2012]. Ice shelf thinning reduces buttressing of the ice sheet upstream, resulting in accelerated ice flow and ice sheet mass loss [*Dupont and Alley*, 2005]. The ice shelf thinning is strongest in the Bellingshausen and Amundsen Sea [*Pritchard et al*., 2012; *Paolo et al*., 2015], where CDW has direct access to the ice shelf cavities [*Jacobs et al*., 2011].

In other regions, such as the Ross Sea and the Weddell Sea, water temperatures on the continental shelf and inside the ice shelf cavities are close to the surface freezing point (−1.9°C) [*Nicholls et al*., 2009; *Orsi and Wiederwohl*, 2009], and the basal melt rates are low (∼ 0.13 m yr^{-1}) [*Rignot et al*., 2013]. The warm CDW (>1.25°C) is decoupled from the shelf circulation by a front system over the continental slope, often referred to as the Antarctic Slope Front (ASF), and characterized by a southward depression of the isopycnals toward the continental slope [*Gill*, 1973; *Jacobs*, 1991]. Dense water formation over the continental shelf in the southern Weddell Sea [*Nicholls et al*., 2009; *Foster and Carmack*, 1976], where the large Filchner-Ronne Ice Shelf (FRIS) resides (Figure 1), furthermore leads to a second, on-shore front separating the lighter water in the north from the dense shelf water. The isopycnals over the shelf break and the continental slope thus exhibit a V-shape [*Jacobs*, 1991; *Gill*, 1973].

In the Weddell Sea, the ASF impedes on-shore transport of warm deep water (WDW), a slightly cooler and fresher derivative of CDW [*Heywood et al*., 1998]. However, future climate model simulations [*Hellmer et al*., 2012; *Timmermann and Hellmer*, 2013] suggest circulation changes in which WDW will access the FRIS cavity and increase melting from 0.2 to almost 4 m/yr within this century. The predicted increase in the flow of WDW toward the FRIS is linked to the Filchner Depression (FD) and changes in the momentum transfer from the atmosphere to the ocean, which causes a redirection of the slope current.

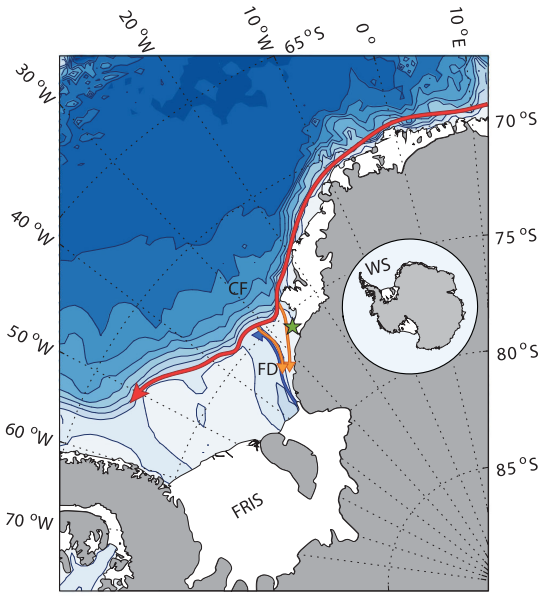

Figure 1. Map of the southern Weddell Sea. Bathymetric contours are drawn every 500 m. The Crary Fan (CF), Filchner-Ronne Ice Shelf (FRIS), and Filchner Depression (FD) are indicated by bold letters, and Halley Research Station is marked by a green star. The red arrow shows the slope current, the orange arrows show the coastal current and the inflow through the depression, while the blue arrow shows the overflow. An inset shows the Antarctic continent, with the Weddell Sea (WS) in the top left sector.

The slope current is associated with the offshore part of the ASF [*Gill*, 1973] and flows westward along the continental slope. In the eastern Weddell Sea, where the continental shelf is a few kilometers wide, the slope current coincides with the Antarctic Coastal Current (red arrow in Figure 1), but as the continental shelf widens at 27°W and the coast separates from the continental slope, the current bifurcates into a coastal current (orange arrow in Figure 1) and the slope current [*Whitworth et al.*, 1985; *Heywood et al.*, 1998]. Downstream of the bifurcation, the Filchner Depression, a 100 km wide and 1000 m deep coastal trough with a sill depth of about 600 m, crosscuts the wide continental shelf. The FD is filled with dense Ice Shelf Water (ISW) that emerges from the FRIS cavity and spills over the FD sill at a rate of 1.6 Sv (blue arrow in Figure 1) [*Foldvik et al.*, 2004].

Existing climate model simulations do not fully resolve the relevant dynamics nor provide clear answers on the processes being responsible for the predicted circulation changes. The on-shore heat transport across the ASF can potentially be controlled by several mechanisms. This includes flow instability of the slope current [*Klinck and Dinniman*, 2010], thermocline response to surface wind stress and near-surface hydrographic conditions [*Hattermann et al.*, 2014], mesoscale eddies [*Nøst et al.*, 2011; *Stewart and Thompson*, 2015], and flow interaction with bottom corrugations and troughs crosscutting the shelf break [*Klinck and Dinniman*, 2010; *St. Laurent et al.*, 2013]. A better understanding of these mechanisms and the interplay between them is needed in order to improve future predictions of ice shelf-ocean interaction and ice sheet mass loss in a warming climate.

Model resolution is an important issue in studies of water exchange across the Antarctic continental slope, where the internal Rossby radius of deformation typically is less than 10 km. High resolution is required in order to properly resolve the steep topography and the water transport associated with mesoscale eddies [*St. Laurent et al.*, 2013; *Stewart and Thompson*, 2015], but are yet too computationally expensive to be applied over large areas and/or time scales. High-resolution idealized models, such as the one being used in this study, are therefore important tools to study mechanisms for on-shelf transport of warm water.

We investigate a shelf region similar to the southern Weddell Sea, using an eddy-resolving regional ocean model with idealized topography, hydrography, and forcing conditions. The geometry represents the essential features of the region; a steep continental slope (α=0.016) connecting the deep ocean (1700 m) to a shallow (400 m) continental shelf, which is narrow in the east and opens up and widens toward the west. A deep coastal trough (sill depth 600 m), representing the FD (Figure 1), cuts across the wide shelf (Figure 2a). We study the slope front stability and the mechanisms which transport warm water on-shore over three bathymetric regions (narrow shelf, wide shelf, and trough opening).

It has been hypothesized that on-shelf transport of heat across the ASF, along the Weddell Sea continental slope, is controlled by a balance between the wind-driven Ekman overturning and a counteracting eddy

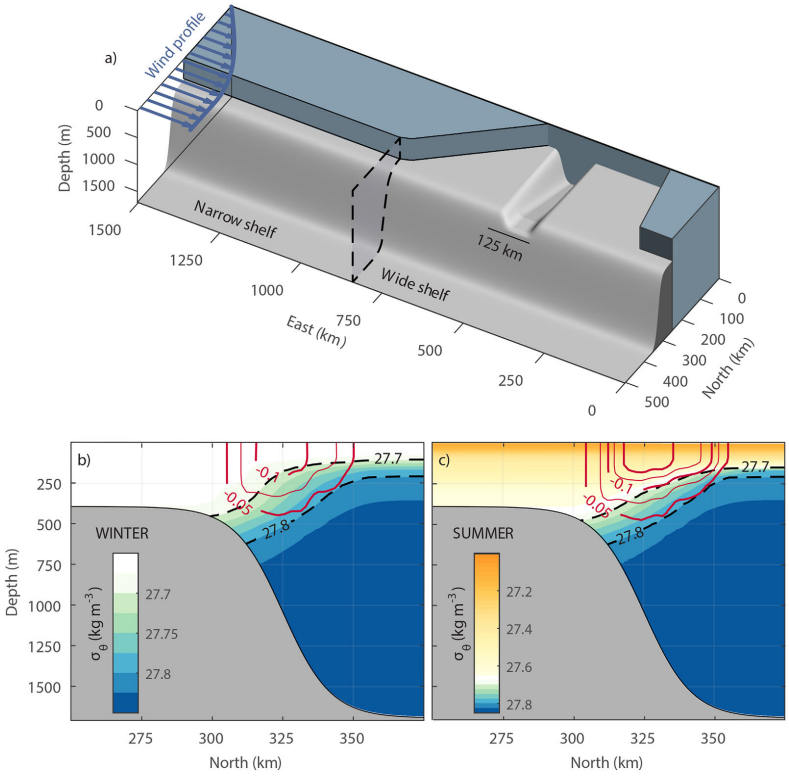

Figure 2. (a) Idealized model configuration. The shaded transect at 850 km East marks the transition from the narrow to the wide shelf. A 125 km wide trough cuts across the wide shelf region, with a sill depth of 600 m. The depth of the trough increases linearly to 900 m at the southern boundary. The zonal wind profile is shown with blue arrows. Potential density climatology for (b) winter and (c) summer, with geostrophic current velocity displayed as red contours. The winter climatology is also the same as the initial condition. $\sigma_\theta = 27.7$ and 27.8 isopycnals are shown with black dashed contours.

overturning [*Nøst et al*., 2011]. However, previous modeling studies have mainly focused on zonally uniform, near equilibrium configurations [*Stewart and Thompson*, 2015]. We explore how this balance changes when the shelf widens. We perform a series of sensitivity tests to study the effect of (I) the magnitude of westward wind stress, (II) the shelf salinity, and (III) the surface hydrography.

Troughs across the continental shelf break offer pathways for shoreward transport of warm water. Observations from the FD show inflow of warm water with a core at 400 m depth along the eastern flank [*Carmack and Foster*, 1977; *Foldvik et al*., 1985; *Årthun et al*., 2012] during summer, which at least occasionally reaches as far south as the Filchner Ice Front and which appears to be wind driven [*Darelius et al*., 2016]. Interactions between a shelf break jet and cross-shelf trough will depend on the trough geometry, stratification, and the strength and direction of the flow [*Williams et al*., 2001; *Klinck*, 1996; *Allen and Durrieu de Madron*, 2009; *Zhang et al*., 2011a].

We investigate how the southward transport of warm water in a trough, with characteristics similar to FD, responds to changes in forcing conditions I–III above. In addition, we explore (IV) how the presence of dense shelf water (DSW), a mixture of ISW and High Salinity Shelf Water, in the trough, and also the DSW density, affects the WDW inflow. *Hellmer et al.* [2017] suggested that the density of the ISW is an important regulator of the warm inflow. This work provides an assessment of the mechanisms they proposed.

The paper is organized as follows. Section 2 introduces relevant concepts of mesoscale eddy transports and potential vorticity constraints that are used to analyze the model results. The model results are presented in section 3, and a discussion of the model performance and limitations is given in section 4. Finally, a summary of the main findings is provided in section 5.

2. Methods

2.1. Model Setup

We conduct idealized numerical simulations using the Regional Ocean Modeling System (ROMS, version 3.6) [*Shchepetkin and McWilliams*, 2009]. The model domain is 1500 km × 500 km, with a horizontal resolution of 1.5 km, which has previously been found to be sufficient to resolve cross-shelf transport by eddies [*Hattermann et al*., 2014]. In the vertical, the model is discretized into 30 terrain-following layers with enhanced resolution near the surface and near the sea bed. The layer thickness varies from less than 3 m in the surface layer over the continental shelf up to 110 m in the deep ocean interior.

The idealized model geometry is shown in Figure 2a, resembling the prominent features of the southern Weddell Sea (Figure 1). The deep ocean is connected to a 400 m deep shelf with a continental slope, represented by a hyperbolic tangent function. The slope steepness ($\alpha = 0.016$) is similar to the Crary Fan region north of the FD (Figure 1). The maximum bottom depth in the open ocean is limited to 1700 m, which is assumed to cover the dynamically active part of the water column, while optimizing model performance, which is limited by the barotropic wave speed $\sqrt{gH}$. A 125 km wide trough, with geometry similar to FD, is crosscutting the continental shelf and the upper part of the continental slope. The trough deepens linearly from 600 m at the shelf break sill to 900 m at the southern boundary. The side walls are symmetric with steepness ($\alpha_{trough} = 0.0043$–0.0109 from the sill to the southern boundary) representative of the eastern flank of FD.

Horizontal advection of tracers and momentum are computed using a third-order upwind scheme with no explicit mixing being applied. The model is stepped forward in time with a split-explicit scheme, using a baroclinic time step of 3 min, and 25 barotropic substeps.

Initial and climatology hydrographic forcing (Figures 2b and 2c) are constructed from 26 conductivity-temperature-depth (CTD) profiles, taken across the eastern Weddell Sea continental shelf break at 17°W [*Nøst and Lothe*, 1997], and from more than 2000 CTD profiles from instrumented southern Elephant seals [*Nøst et al*., 2011]. The dataset is described in *Hattermann et al*. [2014] and is adapted to the idealized setup, where we apply zonally homogeneous conditions. For our reference simulations, the trough is initially filled with DSW with temperature $\theta_{DSW} = -2$°C and salinity $S_{DSW} = 34.65$. These values fall within the range of observed DSW properties (Figure 3). At the southern boundary, we restore temperature and salinity to the initial values. We further impose a northward flux (∼1 Sv), by restoring the velocity in the deep trough to $V_{north} = 0.025$ m s^{-1} below 430 m, to ensure that the DSW properties do not drift over the 5 years we run the model. The restoring velocity is kept constant in all experiments, including those where DSW is absent.

A geostrophically balanced slope current, relative to the pressure level at 1700 m depth, is calculated from the hydrographic fields and is imposed along the eastern model boundary (Figures 2b and 2c). Apart from that, the initial momentum fields are at rest. We apply an idealized westerly wind stress over the deep ocean with a sinusoidal decay to zero from $y = 375$ km to the southern boundary (Figure 2). We conduct simulations with wind stress maxima corresponding to wind speeds of 0, 3, 6, 9 and 12 m s^{-1}. From 1957 until present, the average wind speed along the main direction (260°) at Halley Research Station is 3.6 m s^{-1} with a standard deviation of 6.5 m s^{-1} [*British Antarctic Survey*, 2013].

We do not include sea ice in the simulations, but restore sea surface temperature (*SST*) and salinity (*SSS*) to mimic the effects of ice. We do not consider tides in the model, but a discussion on the effects of tides is given in section 4. Further details on the forcing and boundary conditions are given in Appendix A.

For each scenario, the model is run for 5 model years (1 year is 360 days) applying constant winter (no fresh surface water) surface stratification, and then for 5 years applying constant summer (including fresh surface water) surface stratification (see Figures 2b and 2c). Average fields from the last model year of winter and summer are used for analysis of hydrography and currents as well as depth-integrated Mean and Eddy Kinetic Energy (MKE/EKE). Eddy fluxes are computed using daily mean fields of velocity and hydrography and are averaged over 1 year.

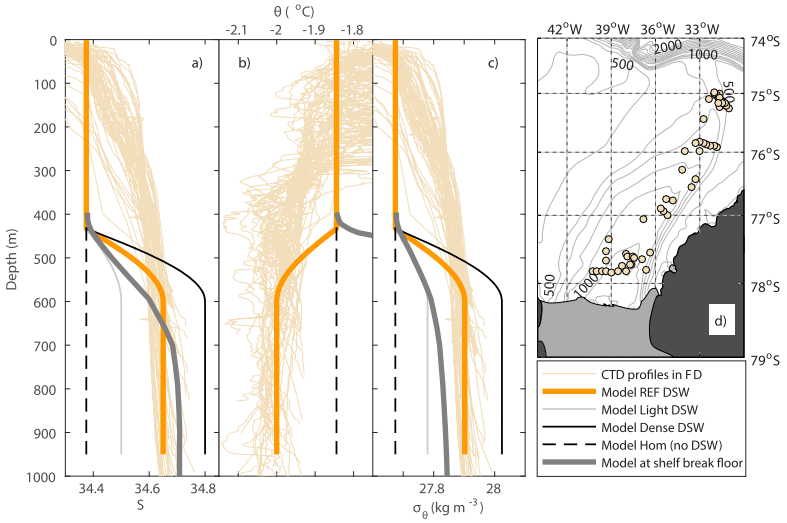

Figure 3. Hydrography from 58 historical CTD profiles in the central, deep Filchner Depression. Thin orange lines show profiles of (a) salinity, (b) potential temperature, and (c) potential density from the locations marked in (d) the map. Modeled trough hydrographic profiles for the REF experiments are shown with thick orange lines. Hydrographic profiles for experiments with perturbed trough density are shown for Light/Dense trough water (thin gray/black lines) and for the Hom experiments with no dense DSW (black dashed lines). The thick, gray lines show the model hydrography at the bottom over the shelf break. The temperature at the shelf break is much warmer than the trough region and exceeds the displayed temperature range.

In addition to the suite of reference simulations, which covers winter and summer scenarios with varying wind forcing, a number of five sensitivity experiments were conducted, where we perturb the trough hydrography (θ_{DSW} and S_{DSW}, Figures 3a–3c) and the wide shelf *SSS*. An overview of the different experiments and their short names is summarized in Table 1.

2.2. Mesoscale Eddies and Vertical Reynolds Fluxes

To diagnose the effects of eddies in on-shelf heat transport, we follow the methods outlined by *Marshall and Shutts* [1981]. The steady state Eddy Available Potential Energy (EAPE) equation, neglecting sources/sinks of heat and advection of EAPE by eddy velocity, is

$$\overline{\mathbf{v}} \cdot \nabla \frac{\overline{\mathbf{T}'^2}}{2} + \overline{\mathbf{v}'\mathbf{T}'} \cdot \nabla \overline{\mathbf{T}} + \overline{w'T'} \frac{\partial \overline{T}}{\partial z} = 0. \quad (1)$$

The overbar represents a time average, long compared to the eddy life time, and the prime represents the deviation from the average. The first term is advection of EAPE by the mean flow. The second term includes horizontal Reynolds fluxes and represents conversion of mean Available Potential Energy (APE) to EAPE. The third term includes the vertical Reynolds fluxes and represents the conversion of EAPE to Eddy Kinetic Energy (EKE).

In baroclinically unstable regions, away from boundaries, eddies act to reduce the large scale APE related to, e.g., geostrophic currents, by transferring the APE into EKE, and hence, redistribute the water masses toward a less energetic

Table 1. Overview of the Model Runs[a]

	Wind Speed x (m s^{-1})	*DSW* Salinity	Wide Shelf *SSS*	Short Name
REF	0, 3, 6, 9, 12	34.65[b]	34.4[b]	WxREF
SSS Sensitivity	3, 6, 9	34.65[b]	34.3	WxLowSSS
	3, 6, 9	34.65[b]	34.5	WxHighSSS
DSW Sensitivity	3, 6, 9	34.40	34.4[b]	WxHom
	3, 6, 9	34.50	34.4[b]	WxLight
	3, 6, 9	34.80	34.4[b]	WxDense

[a]All runs are in pairs of winter and summer. The stars denote reference values. The *x* in the short names are to be replaced by the wind speed.
[b]Reference value.

state. The loss of EAPE from conversion to EKE and from advection downstream (positive term 1 and 3 of equation (1)) leads to down-gradient transfer of heat ($\overline{\mathbf{w}'\mathbf{T}'} < 0$). *Gent and Mcwilliams* [1990] have suggested that the eddy fluxes in essence work as an along-isopycnal diffusion operator which tends to make the isopycnals more parallel.

In regions of eddy decay, however, the conversion to EKE is small, or even negative, which can lead to upgradient transfer of heat [*Marshall and Shutts*, 1981]. Similarly, in proximity to boundaries, such as the continental slope, the slope current is restricted to follow *f/H* contours due to potential vorticity conservation. Here eddies can interact with topography and cause local up-slope transport of denser water (in our case WDW) and hence increase the APE locally [*Nøst et al*., 2011; *Hattermann et al*., 2014].

Diagnosing eddy fluxes is not trivial. Ideally, eddy fluxes can be separated into purely rotational and purely divergent parts in order to better understand effects of mesoscale eddy activity [*Marshall and Shutts*, 1981]. However, *Fox-Kemper et al*. [2003] asserted that such a decomposition is only possible in infinite domains. For an open-bounded finite domain, the divergent and rotational fluxes cannot be observed individually, and without using additional constraints these fluxes and their boundary conditions cannot be uniquely determined.

Here we use the vertically integrated, and hence uniquely determined, Reynolds fluxes that represent the conversion of EAPE to EKE (third term in equation (1)), assuming that EAPE is essentially provided by the second term in equation (1). Principally, the vertical Reynolds fluxes are general measures of the transient vertical buoyancy advection and are not related to eddies or any particular mechanism. However, considering that the constant mean model forcing does not introduce any transients, as well as assuming that the interior circulation is nearly adiabatic, i.e., that the grid scale mixing should be small compared to the resolved tracer advection, we can assume that the diagnosed covariance is mainly determined by the internal model variability arising from instability of the forced mean flow. Then, given the temporal (1–360 day band) and spatial ($L \geq 1.5$ km, $H \geq 10$ m) scales taken for the fluctuating terms, we are filtering for what would be a typical signal of mesoscale eddies, although any other type of fluctuations or waves may also be present.

The total vertical flux can be written as the sum of a mean and a fluctuating part (Reynolds flux). For example, for temperature we have

$$\overline{wT} = \bar{w}\bar{T} + \overline{w'T'}. \tag{2}$$

The vertical Reynolds flux is computed as the residual between the two first terms of equation (2). We calculate depth-integrated fluxes of temperature and salinity, and also a linearized density flux, using the approximation:

$$\overline{w'\rho'} = \rho_0(-\alpha\overline{w'T'} + \beta\overline{w'S'}), \tag{3}$$

where ρ_0 is the reference density, α is the thermal expansion coefficient, and β is the saline contraction coefficient. The linearized density aids the understanding of which water masses are involved in the density flux.

Negative Reynolds fluxes for density mean lowering of the APE by lifting light water or lowering dense water. This is expected in most areas of the model, especially away from the steep topography. Positive Reynolds fluxes for density show us where the APE is increased by, e.g., lifting dense water up-slope.

2.3. Potential Vorticity

In order to interpret the interaction of the slope current with the topography of the trough, we will follow the procedure described by *Magaldi et al*. [2011], and calculate the Ertel PV according to equation (4):

$$\mathrm{PV} = -\frac{2\Omega + \nabla\times\mathbf{v}}{\rho_0}\cdot\nabla\boldsymbol{\sigma_\theta} \simeq -\frac{f}{\rho_0}\frac{\partial\sigma_\theta}{\partial z} - \frac{1}{\rho_0}\left(\frac{\partial v}{\partial x} - \frac{\partial u}{\partial y}\right)\frac{\partial\sigma_\theta}{\partial z} - \frac{g}{\rho_0^2 f}\left[\left(\frac{\partial\sigma_\theta}{\partial x}\right)^2 + \left(\frac{\partial\sigma_\theta}{\partial y}\right)^2\right]. \tag{4}$$

We only consider the vertical component of the planetary vorticity, $2\Omega \simeq (0, 0, 2\omega\sin\phi) = f$. We have further applied the thermal wind balance, and neglected the vertical velocity terms [*Hall*, 1994]. The first term on the right-hand side relates to stretching and compression of isopycnals. The second term is related to the relative vorticity, $\zeta = \frac{\partial v}{\partial x} - \frac{\partial u}{\partial y}$, and the last term is connected to tilting of isopycnals.

The model fields have terrain-following vertical coordinates and are interpolated to regularly spaced Cartesian depth levels with $dz = 5$ m before calculation of PV. Finally, the PV is averaged within the isopycnal layer $\sigma_\theta = 27.7-27.8$, which contains the warm inflow.

3. Results

We will first give an overview of the general model performance (section 3.1). We will then focus on inflow of WDW over the shelf (section 3.2) and into the trough (section 3.3).

3.1. Model Performance

The idealized model approaches a stable state, where the total KE is no longer increasing, after 3–4 years of spin-up for both winter and summer stratification. The circulation pattern agrees with observations in the southern Weddell Sea. A strong, westward slope current is associated with the slope front, with current velocities in the same range as observations from moored instruments [*Fahrbach et al.*, 1992; *Jensen et al.*, 2013] and geostrophic estimates from hydrographic profiles [*Heywood et al.*, 1998]. The slope current and the eddy fields are fully developed ~200 km from the eastern boundary. A combination of radiation and nudging along the western boundary efficiently advects the slope current out through the western boundary, and no spurious return flow is seen. In the trough, DSW flows along the eastern flank, crosses the sill to the western flank and leaves the trough (Figures 4a and 4c). The circulation in the trough is similar to recent observations and regional modeling of FD [*Darelius et al.*, 2014], lending some credibility on the idealized model configuration.

In winter scenarios, no warm water is transported onto the shelf, and the shelf water stays homogeneous with temperatures near the surface freezing point (Figure 4a). In summer scenarios, where fresh surface water is present, on-shelf transport of warm water causes increased bottom temperature over the shelf (Figure 4c). The warmest water ($\theta \sim -1.5$°C) is found in the narrow shelf region, and depth-integrated EKE over the shelf (both narrow and wide) increases by a factor of 10–100 compared to the winter conditions (Figures 4b and 4d).

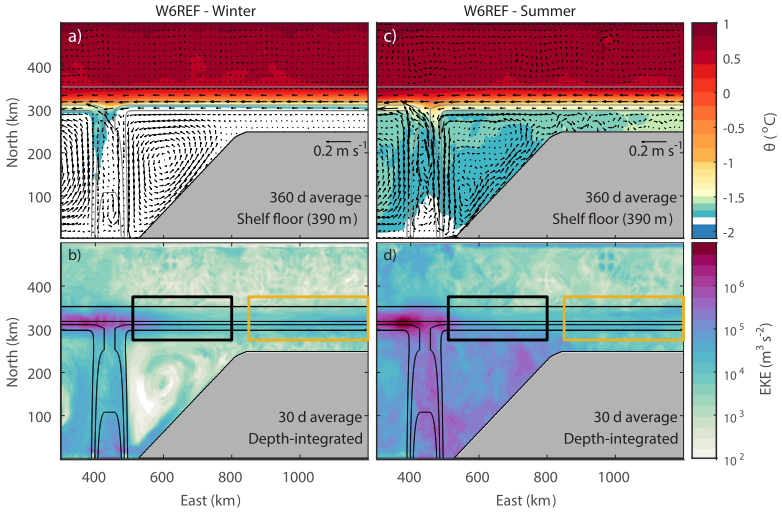

Figure 4. Average temperature and velocity at shelf floor depth (390 m) for W6REF in (a) winter and (c) summer conditions. (b, d) Thirty day averages of depth-integrated EKE during winter and summer conditions, respectively. Isobaths are shown at 450, 600, 800, and 1650 m. Boxes in Figures 4b and 4d indicate the regions for wide (yellow) and narrow (black) shelves discussed in section 3.2.1.

For weak wind scenarios (W0REF and W3REF), the slope current flows westward, along the 850 m isobaths (~320 km North), with a core of 0.15 m s^{-1} (Figure 5a). Observations of current velocity across the ASF are limited but reported long-term means range from 0.1 to 0.2 m s^{-1} at slope depths of 400–1000 m [*Fahrbach et al.*, 1992; *Heywood et al.*, 1998; *Jensen et al.*, 2013]. In agreement with observations from *Fahrbach et al.* [1992], the model also shows increasing westward transports associated with the slope current when the wind stress increases. At 900 km East, the westward transport is, relative to W0REF, 100%, 107%, 121%, and 166%, for W3REF, W6REF, W9REF, and W12REF, respectively.

In weak wind scenarios, the core of the slope current follows the 850 m isobath until it reaches the trough mouth region. Here the current crosses the trough mouth while shifting southward, continuing along the 600 m isobath (310 km North, Figure 5a). In scenarios with stronger wind, an additional westward wind-driven current, associated with the Ekman circulation, develops and combines with the initial slope current, to form a broader current with a dual core and weaker maximum velocities (Figures 5c and 5e). The northern core along the 850 m isobath crosses over the trough mouth region similar to scenarios with weak wind. The wind-driven, southern core shifts on-shore for stronger wind. At 500 km East, this core is located over the 525 m isobath (305 km North, Figure 5c) in W9REF. The vertical structure of the current is similar for weak and strong wind scenarios, but as the current shifts south toward shallower isobaths, the current

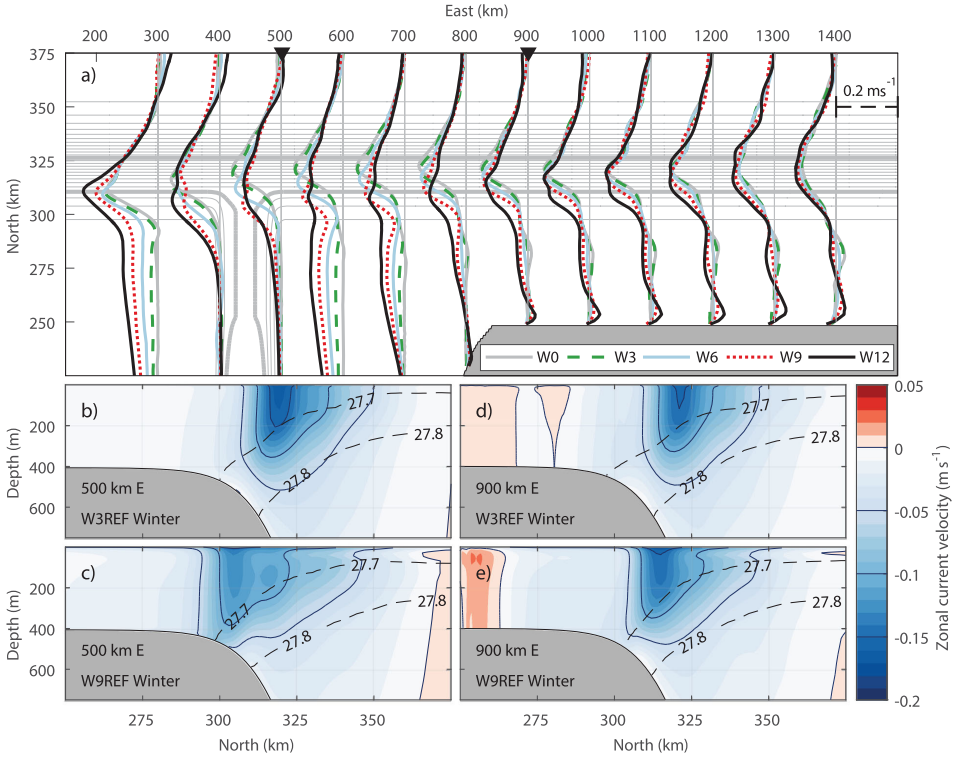

Figure 5. (a) Relative strength of westward slope current for five different wind speed scenarios (see legend for color interpretation) during winter stratification. The distance between the vertical gray lines corresponds to a velocity scale of 0.2 m s^{-1}. Isobaths are shown with increments of 50 m starting at 450 m, where the thick lines correspond to the 500 and 1000 m isobaths, respectively. The black triangles indicate the locations of the vertical transects of zonal velocity shown in (b, c) 500 km East and (d, e) 900 km East. Negative velocities are directed westward. The displayed vertical range is limited to the upper 750 m. The dashed, black lines show the isopycnals $\sigma_\theta = 27.7$ and $\sigma_\theta = 27.8$.

takes up the whole water column and becomes barotropic. The wind-driven part of the current is affected by the trough topography, which affects the inflow of WDW that will be described in section 3.3.

During summer (not shown), the slope current velocity exceeds the winter values near the surface, with maximum velocity ~0.3 m s^{-1}. Comparing to the respective winter wind forcing scenario, the summer transports are 148%, 144%, and 173% for W3REF, W6REF, and W9REF. Over the narrow shelf, a westward coastal current, related to the convergence of fresher surface water along the coast, is found in strong wind scenarios.

In addition to the nonlinear eddy field, the model shows westward propagation of topographic waves along the continental slope. Band-pass filtered Hovmüller diagrams of along-slope currents (not shown) yield waves propagating westward along the continental slope with periods of ~42 h, wavelengths between 80 and 110 km, and with phase speeds between 0.55 and 0.75 m s^{-1}. We do not see wave propagation in the trough, although other model studies indicate that waves can cause considerable onshore heat transport within troughs [*St. Laurent et al.*, 2013]. The waves follow the continental slope and cross the trough mouth region. In the weak wind scenario (W3REF), when the eddy field is weak, the waves account for 95% of the EKE in the model (calculated from EKE frequency spectra in the frequency band 38–51 h). For stronger wind, nonlinear eddy processes and current instabilities become increasingly more important and the wave contribution to the EKE reduces to 50% in W9REF.

To summarize, the modeled flow pattern agrees with observations in the area. The location and the shape of the slope current depend on the strength of the zonal wind stress. A wind-driven component of the slope current, related to the Ekman dynamics, develops for strong winds. In summer, the surface current is stronger and the EKE level is higher over the continental shelf. In section 3.3, we will look further into how the location of the slope current influences the inflow of WDW into the trough region. We will also explore how the density of the DSW within the trough affects the cross-slope exchanges. But before doing so, we examine the role of eddies for the cross-slope exchange over the narrow and wide shelf region.

3.2. Interaction of the Slope Current and the Continental Shelf Break

3.2.1. Eddy Transports Over the Narrow and Wide Shelf Regions

In this section, we will study the balance between the wind-driven Ekman overturning and the counteracting eddy overturning. We will use the Reynolds flux calculations (section 2.2) to examine the cross-slope exchange in a narrow shelf region, and how it changes downstream, when the shelf widens. In the following, the narrow and wide shelf regions will be referred to as narrow/wide regions. We will apply zonal averages over the narrow (yellow) and wide (black) regions identified in Figure 4c. The narrow region is dominated by a convergence of southward Ekman transport at the coastline/ice front, whereas the downwelling is less pronounced in the wide region, where the coastal wall is further away, and the zonal wind stress decays gradually in the wide region (Figure 2a). We will focus on the effect of surface stratification, which changes from winter to summer, and also comment on the effect of wind stress.

The slope current (> 0.075 m s^{-1}) occupies the water column down to ~400 m, corresponding to the shelf depth, and the location of the slope current core varies with the wind stress as described in section 3.1. In summer, the current becomes more baroclinic with higher surface velocities. We find EKE maxima, coinciding with the slope front in both regions and for both summer and winter stratification (Figures 6a–6d). The EKE is amplified near the surface and the bottom. In summer, higher EKE is also seen near the surface over the flat shelf and upper slope, shoreward of the front.

Being consistent with the EKE structure, the Reynolds fluxes indicate different eddy transports over the wide and narrow shelf in the two seasons. In winter, the vertical density fluxes are always negative across the slope front in the narrow region (Figure 6e). Eddies, dominated by the salt fluxes, act to move fresher water up and more saline water down, suggesting that their main role is to reduce APE by balancing the wind forcing that depresses the isopycnals in this region. In the wide region, the Ekman downwelling ceases and eddy transports will cause a transient response of the weakly forced front, as opposed to a quasi steady state that may be reached in the narrow region. While the integrated net eddy transport is still negative, i.e., reducing total APE, this locally leads to positive density fluxes, as this aids to relax the front (Figure 6f). Also, the total eddy transport is weaker, and the front approaches a more stable

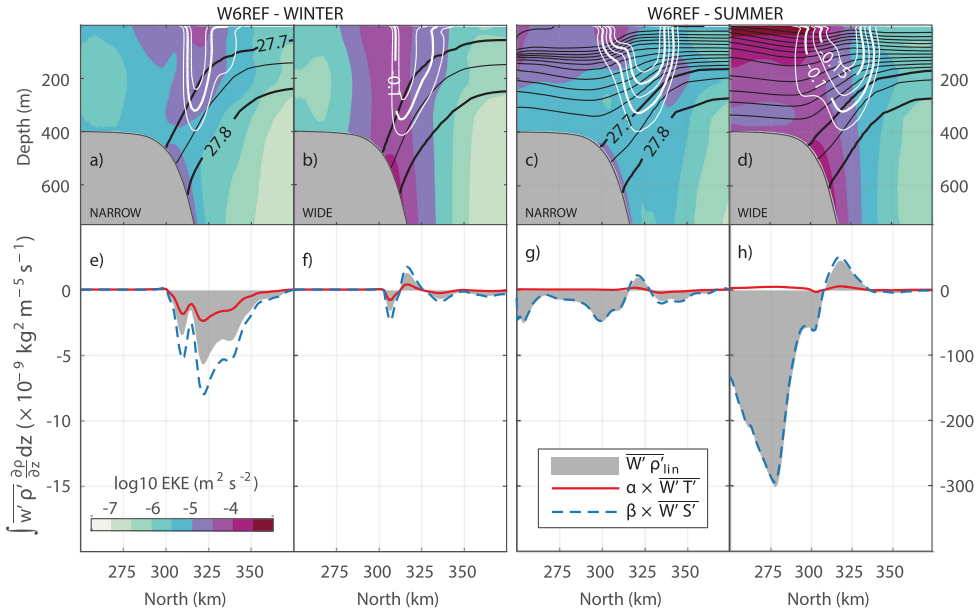

Figure 6. (a–d) Zonally averaged EKE for (a, c) the narrow and (b, d) the wide regions during (a, b) winter and (c, d) summer surface stratification and medium wind stress (W6REF). Black contours show isopycnals with increments of 0.05 kg m^{-3}, and white contours show zonal current velocity in increments of 0.025 m s^{-1}. (e–h) Corresponding depth-integrated vertical Reynolds fluxes (third term in equation (1)) for density (gray filled area), temperature (red), and salinity (blue, dashed). The narrow and wide regions refer to the yellow and black squares in Figure 4c.

configuration with reduced vertical shear of the slope current between 300 and 325 km North in Figure 6f compared to Figure 6e.

In winter, EKE is weak over the flat continental shelf and the Reynolds fluxes vanish accordingly, with no density gradients shoreward of the slope front. In summer, when lighter surface water is present, a second, shallower front develops associated with the near-surface stratification and leads to significant downward density fluxes over the continental shelf. As a result, the Ekman downwelling is balanced by a shallower eddy overturning cell, allowing the deep slope front to relax. This is evident from the vanishing temperature contribution in the Reynolds fluxes (as temperature differences between the fresh surface water and the Winter Water are small) but can also be seen by the shoaling of the $\sigma_\theta = 27.7$ and $\sigma_\theta = 27.8$ isopycnals in (Figure 6d compared to Figure 6b), which leads to warmer water on the shelf in summer, as seen in Figure 4.

3.2.2. Effect of Varying Shelf Salinity

In addition to changes of the surface flow convergence, the shelf water mass properties will also change as the slope current passes from the narrow region, with the less saline Eastern Shelf Water, to the wide region, where more saline and denser waters are observed on the shelf [*Gill*, 1973]. We will now analyze the effect of along-slope salinity changes on the eddy driven transports. For this purpose, the shelf salinity is modified by increasing/decreasing the *SSS* restoring value south of 250 km North over the wide shelf region. The narrow region is unaffected by these modifications, since the shelf, in this region, is located north of 250 km North.

In experiments with higher shelf salinity (HighSSS), dense water is exported from the shelf (negative $\overline{W'S'}$ > and $\overline{W'\rho'}$ in Figure 7f). The $\sigma = 27.7$ isopycnal is lifted over the slope (Figure 7d) and forms a V-shape, which connects the cold, dense shelf water to the warmer CDW at middepths over the slope [*Stewart and Thompson*, 2016]. Eddies transport warm water onto the shelf (positive $\overline{W'T'}$), and the shelf-depth temperature increases by 0.1–0.2°C (Figures 7b and 7f).

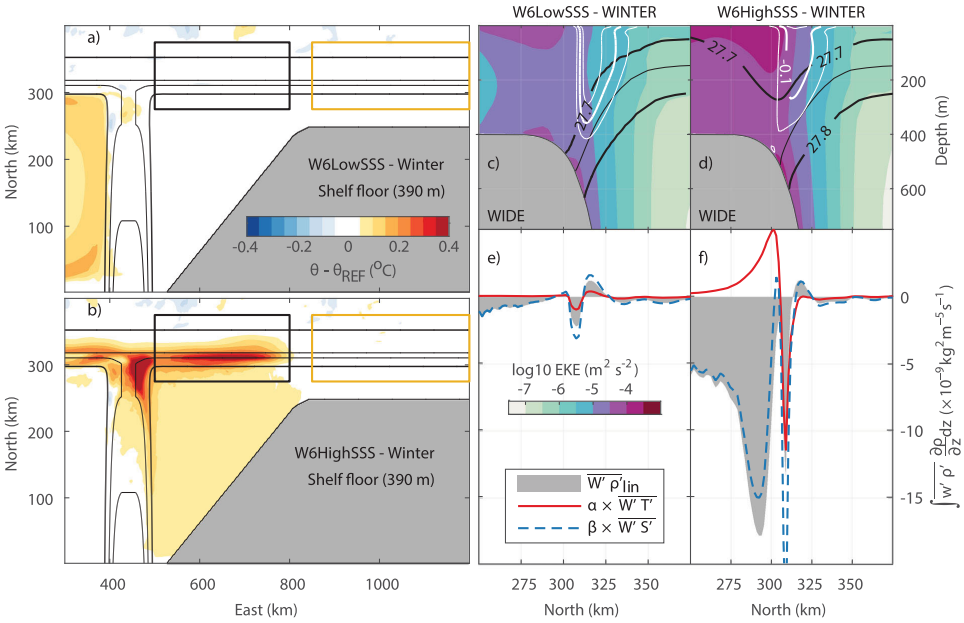

Figure 7. Winter time temperature difference between (a, b) W6LowSSS/W6HighSSS and REFSSS at shelf floor depth (390 m). The yellow and black squares mark the narrow/wide regions, respectively. Isobaths are shown at 450, 600, 800, and 1650 m. (c, d) Zonally averaged EKE for the wide region with (c) lower and (d) higher shelf salinity. Isopycnals are shown with black contours, and white contours show zonal current velocity, where the thicker line is $U = -0.1$ m s^{-1}. (e, f) Corresponding depth-integrated vertical Reynolds fluxes for density (gray filled area), temperature (red) and salinity (blue, dashed). The negative salt flux peak (blue line) in Figure 7f is exceeding the axis, with a peak value of $\sim -25 \times 10^{-9}$ kg^2 m^{-5} s^{-1}.

In experiments with lower shelf salinity (LowSSS), we find no transport of warm water onto the shelf (Figures 7a and 7e). The shelf water advected from the narrow region is more saline, and negative Reynolds salt fluxes indicate that eddies export this water downslope, reducing the steepness of the σ=27.7 isopycnal compared to the reference experiment (Figures 6b and 7c).

The effect of changing the shelf salinity is strongest in winter scenarios, when the water mass over the shelf is initially homogeneous. In summer, high eddy activity is connected to the surface stratification as explained above, and the presence of fresh water over the shelf, north of 250 km North, dampens the effect of modifying the water mass salinity over the southern portion of the shelf. Experiments with weaker and stronger wind speed give similar results to the medium wind speed experiment (6 m s^{-1}) shown in Figures 6 and 7.

3.3. Warm Inflow in the Trough

Most observations of warm water entering the Weddell Sea shelf are from areas where bottom corrugations or troughs crosscut the continental slope [*Foldvik et al.*, 1985; *Nicholls*, 2003; *Nicholls et al.*, 2008; *Årthun et al.*, 2012; *Darelius et al.*, 2016]. In this section, we will study the WDW inflow in an idealized trough with similar geometry to FD.

We will first look at the response to wind stress in the reference scenarios. We will then compare the results to scenarios with modified shelf salinity, to see the effect of the increased shelf-depth temperatures found in the HighSSS scenario (Figure 7b). Finally, we will study how the density of the DSW in the deep trough affects the circulation and inflow of WDW into the trough (Hom/Light/Dense scenarios).

3.3.1. Sensitivity to Wind and Slope Current

In section 3.1, we showed that increased wind stress leads to a stronger and broader slope current. The core of the current is also shifted toward shallower isobaths for stronger wind, and the flow is more affected

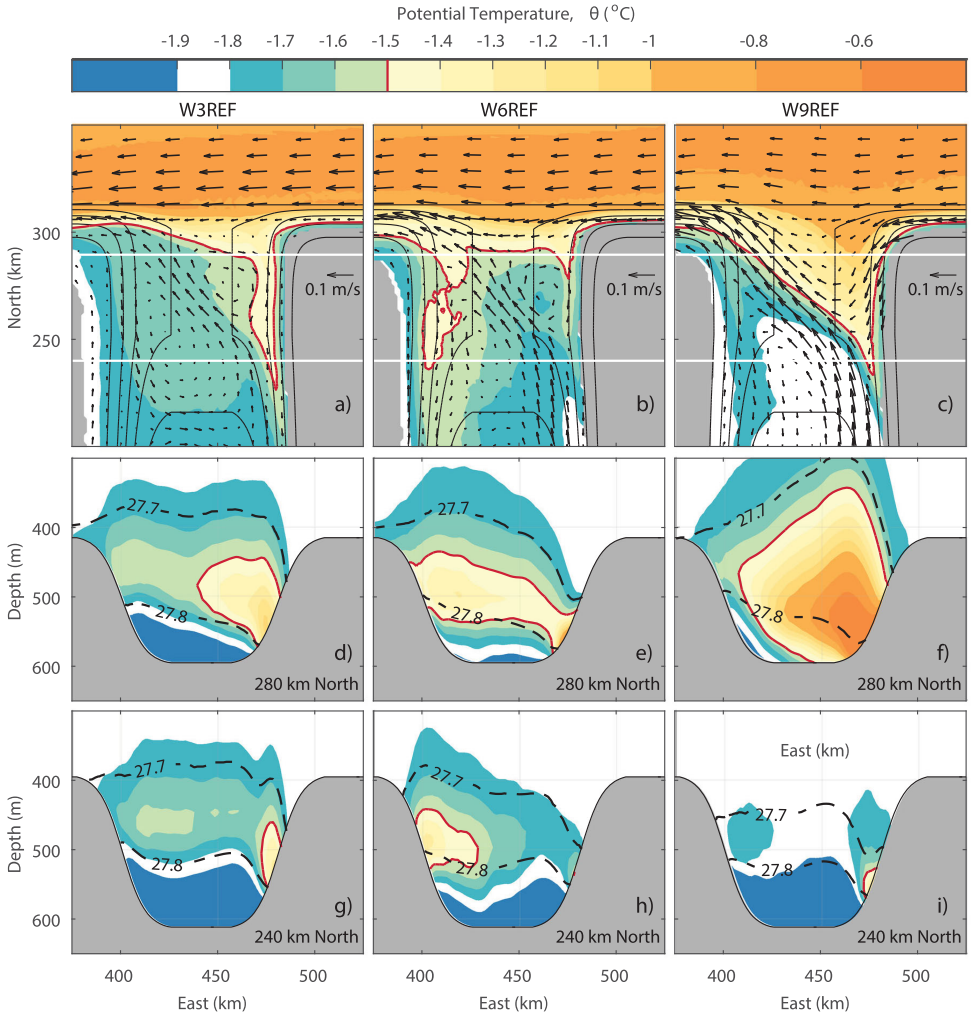

Figure 8. (a–c) Winter temperatures and current vectors in the trough region averaged over densities $\sigma_\theta = 27.7-27.8$, and vertical sections across the trough at (d–f) 280 km North and (g–i) 240 km North. The transect locations are indicated in Figures 8a–8c by white horizontal lines, and isobaths are shown with 50 m increments from 450 to 650 m. The −1.5°C isotherm is shown with red contours in all plots, and black dotted lines in Figures 8d–8i show the $\sigma_\theta = 27.7-27.8$ layer.

by the trough topography. In relation to the effect of trough topography and current location, we identify three different regimes of WDW transport into the trough.

The first regime occurs for scenarios with weak wind (W0REF and W3REF). Here the core of the slope current is following the 850 m isobath across the trough and is not affected by the trough bathymetry (Figure 8a). A standing cyclonic vortex on the eastern side of the trough opening draws filaments of warm water south along the eastern side of the trough (Figures 8d and 8g).

The second regime occurs for medium wind (W6REF) when the core of the slope current is following the 620 m isobath. At this location, the current is located at the very corner of the trough opening. The current is deflected at the corner, but the trough topography is weak and the current crosses the trough at 300 km North (Figure 8b). We find that in this regime, a warm inflow into the trough is caused through eddy shedding, as the topographic shelf waves described in section 3.1 interact with the trough opening. From movies of the flow (supporting information I), it can be seen that the waves approximately follow the 650 m isobath and break toward the center of the trough (~460 km East). Examination of the current and the density field shows that those waves cause undulations in the PV field that leads to eddy formation, as described by *Zhang et al.* [2011b]. Being advected by the mean flow, these eddies propagate southwestward across the trough mouth, and into the deep trough, causing warm inflow on the western side of the trough (Figure 8h); a mechanism that appears to be most efficient for intermediate winds.

The third regime occurs during strong wind (W9REF and W12REF), when the trough topography interacts more strongly with the slope current. The wind-driven component of the slope current flows along shallower isobaths and is deflected southward into the trough. Due to PV constraints, the current cannot cross the sill and leaves the trough, along the same path as the outflow of DSW from the deep trough (Figure 8c). The slope current brings large amounts of warm water onto the sill region (Figure 8f), but only a very small amount of this warm water is found south of the sill (Figure 8i). Similar to the second regime, topographic waves break at the trough opening and generate eddies. However, the waves break further east, near the 500 m isobath, and the eddies are mostly being advected out of the trough by the mean current.

The flow pattern described for the three regimes above is also reflected in the time-mean PV fields shown in Figure 9. The PV is low in the slope region for all scenarios and increases over the trough. In the eastern sill area, weaker PV coincide with filaments of WDW inflow. At the southern edge of the sill, where the trough starts to deepen, higher PV forms a barrier which the warm water cannot penetrate. The water column is stretched and conservation of PV leads to gain of cyclonic vorticity, which turns the flow westward over the flat trough bottom. The flow leaves the trough roughly following the topography around the western corner of the trough. In the medium wind scenario (W6REF), the PV barrier appears to be located further north than for the weak and strong wind scenarios (Figure 9b), and the reduced PV along the western side of the trough agrees with more WDW inflow here.

The slope currents response to varying wind strength is similar in winter and summer. However, since the current is wider and less stable in summer scenarios (see EKE in Figures 4 and 6d), eddies interact stronger with the mouth of the trough, such that the first regime is absent, and we find generally more warm inflow than during winter for the comparable wind forcing.

In order to quantify and compare the amount of WDW flowing into the trough, we estimate net mass transports, with positive numbers indicating southward transport, for water masses with $\theta > -1.5$°C and $\sigma_\theta > 27.7$ across a transect at 240 km North. Transports are calculated, within the $\theta - \sigma_\theta$ limits, from daily mean

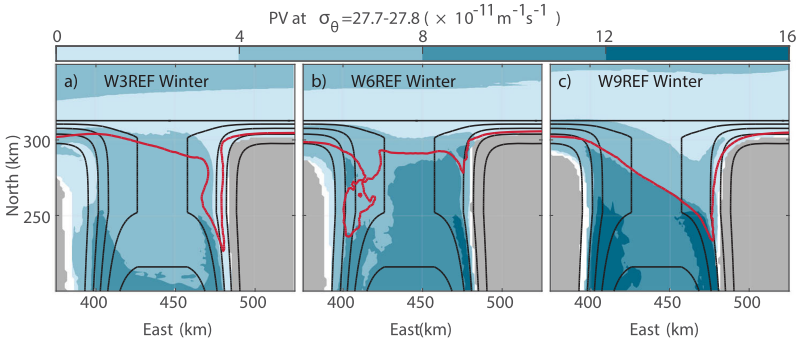

Figure 9. Ertel PV averaged over densities $\sigma_\theta = 27.7 - 27.8$ for the same wind speed scenarios as in Figures 8a–8c. Isobaths at 450–650 m are shown on all plots with increments of 50 m, and the red contour show the −1.5°C.

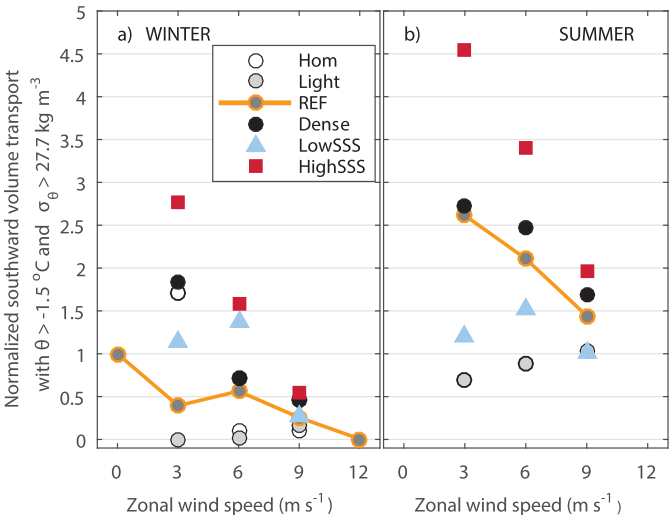

Figure 10. Net southward volume transport across 240 km North for water masses with $\theta > -1.5$°C and $\sigma_\theta > 27.7$ for all scenarios, normalized with respect to the W0Ref scenario. Reference scenarios are displayed with orange lines. Different DSW densities are shown with gray-scaled circular markers ranging from white in scenarios without DSW (Hom) to gray and black for increasing DSW densities (Light/REF/Dense). Scenarios with lower (higher) shelf salinity are shown with blue triangles (red squares).

fields to capture transient features, and were then averaged over the last 360 days of the respective model run. For comparison, all estimates are normalized by the transports in the W0REF winter scenario.

Except from the increase in the medium wind winter scenario, which is related to the regime change described above, the southward transport of WDW decreases with increasing wind (orange line in Figure 10) for both winter and summer conditions. The transports are higher in summer compared to winter. In summer, the EKE level is higher (Figure 4d), and we also find increased temperatures for the $\sigma_\theta > 27.7$ water mass (not shown).

3.3.2. Sensitivity to Shelf Salinity and DSW Density

The southward transport of WDW in the trough increases for denser DSW (Dense) and for higher shelf salinity (HighSSS) (Figure 10). The changes are large for the weak wind scenarios, where HighSSS(Dense) bring $\sim 7(5)$ times more WDW into the trough during winter, respectively. For strong wind, changes to the southward transport of WDW are modest, potentially because the strong barotropic flow crossing the trough mouth area prevents weaker baroclinic responses to variations in the hydrography.

In section 3.2, we showed that higher shelf salinity leads to larger Reynolds fluxes and more on-shelf transport of WDW. The $\sigma_\theta = 27.7$ isopycnal was lifted and bent upward over the shelf, forming a V-shape (Figures 7b and 7d). Associated with these changes, the WDW reaches higher up in the water column near the trough opening, and more warm water is hence transported into the trough. For LowSSS, the southward transport of WDW is higher than the reference scenarios in winter and lower than the reference scenarios in summer, for respective wind forcing. Consistent with this result, we find that the EKE levels and Reynolds fluxes increase for LowSSS in winter and decrease in summer (not shown).

In weak wind scenarios (W3), the circulation in the trough amplifies for higher DSW densities and brings more WDW into the trough (Figure 11). The southward transport of WDW is close to zero for W3Light, but is ~5 times higher in W3Dense compared to W3REF (Figure 10a). The larger density difference between the DSW and the shelf water sets up a baroclinic flow field that favors the warm inflow (as seen in Figure 11).

When DSW is present in the deep part of the trough, the circulation in the trough is characterized by outflow along the eastern flank and inflow along the western flank (Figures 11i–11l). When the DSW is absent

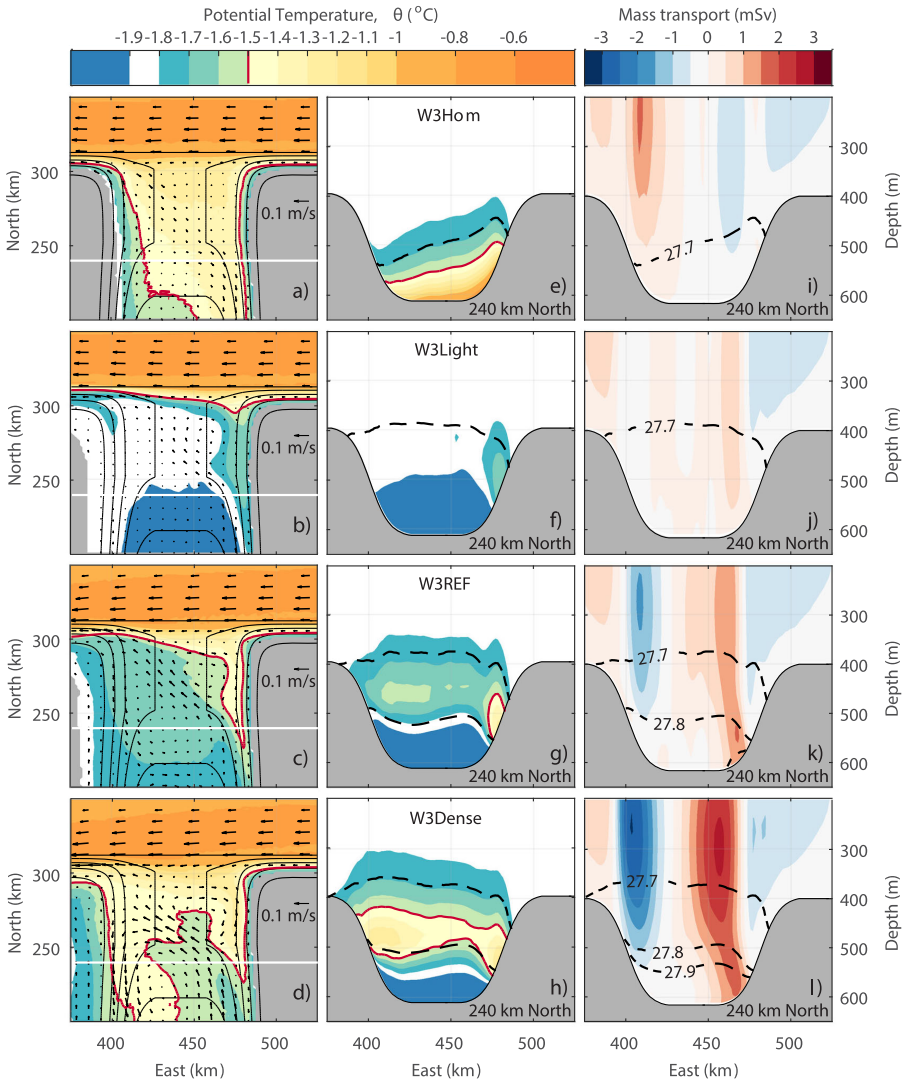

Figure 11. Winter temperatures and current vectors in the trough region averaged over densities σ_θ=27.7–27.8 for (a–d) four different DSW densities. Vertical sections of (e–h) temperature and (i–l) mass transport across the trough at 240 km North. The transect location is indicated by white horizontal lines in Figures 11a–11d. The −1.5°C isotherm is shown with red contours in Figures 11a–11h, and black dashed lines in Figures 11d–11l show isopycnals, with increments of 0.1.

(homogeneous shelf and trough), a fundamental circulation change is seen in the trough. In this case, WDW is the most dense water mass in the system and enters the shelf as a gravity current that flows along the bottom of the trough. In the weak wind scenario (W3Hom), the density driven flow in the trough reverses (Figure 11i) leading to warm inflow along the eastern flank. For stronger wind (W6Hom and W9Hom), the circulation pattern is not altered, and there is only small amounts of WDW south of the sill.

4. Discussion

As discussed in section 3.1, our idealized model reproduces the main circulation pattern observed over the continental slope in the Weddell Sea and in FD. The comparison of the different model scenarios has identified several processes that interact to control the access of WDW to the continental shelf and into the trough.

Observations from moored instruments on the Weddell Sea shelf show that warm inflow occurs during the summer season when the thermocline depth is shallower than during winter [*Årthun et al*., 2012]. *Semper and Darelius* [2016] found changes in thermocline depth on the order of 200 m between winter and summer, upstream of FD, on the narrow continental shelf. Modeled transport of WDW toward the shelf is low for both seasons (summer/winter). We find that the establishment of an upper eddy overturning cell in summer leads to a relaxation of the ASF isopycnals at depth. Since it can be assumed that this process occurs over the entire eastern Weddell Sea, this will lead to a larger shoaling of the thermocline (as observed) than seen in our model results, where the thermocline depth is fixed at the eastern boundary. This is consistent with *Hattermann et al*. [2014] and *Zhou et al*. [2014] who find larger thermocline displacements as a response to surface hydrographic forcing in a periodic (and hence infinite) domain. Running the model with a more realistic summer climatology would likely increase the on-shelf transport of WDW. The increased southward transport of WDW we find during summer scenarios is linked to a dynamic response, rather than to changes in the depth of the thermocline.

Eddy-mediated transport of WDW to the wide continental shelf is most efficient when dense water on the shelf (HighSSS) is transported offshore, creating V-shaped isopycnals across the continental slope. The result agrees with *Stewart and Thompson* [2016], who find that the establishment of an isopycnal connection between the dense shelf water and the CDW, creates a pathway for CDW to access the continental shelf without doing work against the buoyancy force. For the other scenarios, the main role of eddies is to balance the wind-driven downwelling, which influence the thermocline depth and the temperature of the WDW interacting with the trough topography.

The trough, with characteristics similar to FD, contributes to southward transport of WDW in the model. We identify three flow regimes, related to the degree of interaction between the slope current and the trough topography. The response to concurrent effects of mean PV conservation and eddy shedding at the trough opening, is different in the three regimes, and leads to a nonlinear relationship between the wind speed and the southward transport of WDW (Figure 10). In the weak wind regime, there is no interaction between the slope current and the trough topography, and the southward transport of WDW is dominated by eddies. In the medium wind regime, the core of the slope current is located at the edge of the trough opening and is only weakly affected by the topography. However, this regime seems to be optimal for southward transport of WDW by eddies along the western side of the trough. We associate the eddy formation to the blocking of westward propagating topographic waves at the trough opening, as described by *Zhang et al*. [2011b]. The waves propagate westward along the continental slope, supported by the PV jump along the slope. In the strong wind regime, the flow pattern resembles that described by *Williams et al*. [2001], for a shelf break jet flowing over a wide channel topography. The current is deflected southward into the trough but crosses the trough due to PV conservation (compensating vortex stretching and the gain of relative vorticity). The southward transport of WDW is low, but filaments of warm water are transported south along the eastern flank of the trough. Similar to the medium wind regime, eddy formation due to topographic waves and PV undulations occur, but the eddies form closer to the eastern side of the trough, and seem to be efficiently advected out of the trough by the mean current. Movies showing the propagating waves and eddy formation are included in the supporting information.

In summer, the southward transport of WDW in the trough is higher than for winter scenarios with similar forcing. The thermocline response is small (<50 m), as described above, but we do find higher temperatures within the density layer $\sigma_\theta = 27.7-27.8$, which leads to larger inflow within the $\theta-\sigma_\theta$ limits in Figure 10. Furthermore, the EKE level is higher during summer and the southward transport by eddies formed through instabilities in the slope current and breaking of continental shelf waves at the trough mouth is higher. Observations of topographic Rossby waves along the continental slope of the Weddell Sea [*Jensen et al*., 2013; *Semper and Darelius*, 2016] also show more wave activity and higher EKE in the summer season, compared to the winter season.

Hellmer et al. [2012] suggested that stronger atmospheric stress from a reduced sea ice cover, combined with lower DSW densities can cause a redirection of the slope current into FD, bringing large amounts of WDW into the ice shelf cavities and increasing the basal melt rates. Our process oriented model does not support such a scenario. Instead, we find that for strong wind, the WDW cannot penetrate the sill due to PV constraints, and the WDW leaves the trough regardless of the DSW density. In experiments with lighter DSW the trough circulation is weaker, and less WDW is transported south. For weak wind, however, we find strong southward transport of WDW when DSW is absent (W3Hom), and the circulation in the trough reverses (Figure 11a), supporting the tipping point behavior suggested by *Hellmer et al.* [2017].

The changes in warm water properties and circulation in the trough and their effect on the ice shelf system merit further studies. In this respect, the idealized numerical model results encourage further experiments on the tipping point behavior and sensitivity to suggested future changes in sea ice production, DSW source waters, and imposed fluxes of DSW at the southern model boundary.

In scenarios with strong wind, we find a convergence of the southward transport of WDW. The barotropic flow, steered by the PV conservation, over the trough sill dominates the flow pattern, and modifications of the hydrographic forcing have little effect. In scenarios with weak wind, we find large differences in the southward transport of WDW, where higher salinity on the shelf (HighSSS) and higher DSW density (Dense) favor southward transport of WDW.

Inclusion of tides is beyond the scope of this study. Our focus has been to study isolated forcing mechanisms. Nevertheless, including tides would increase the general level of mixing along the slope, as the upper continental slope is suggested to be a generation site for semidiurnal internal tides, which are trapped by the critical latitude and dissipate their energy along the bottom [*Fer et al.*, 2016]. Enhanced near-bottom tidal mixing at the M2-frequency could also affect the stability of the slope front and the amount of warm inflow over the shelf.

Darelius et al. [2016] suggested that certain combinations of wind (storm events), sea ice concentration, shelf salinity, and summer preconditioning of the slope front and stratification favor on-shelf transport of WDW. They specifically point to the importance of the wind. Warm water, which is episodically lifted onto the outer shelf during summer, can be advected south by the wind-driven coastal current. The southward transport of warm water increases during storm events with wind from NW (favors southward water transport). In this study, we only consider the effect of constant wind forcing. During constant winter or summer forcing, the effect of storms, or a seasonal hydrological cycle, on the inflow will be the subject for a future study.

5. Conclusions

This study presents results from an eddy-resolving, idealized high-resolution ocean circulation model that resembles the circulation in the southern Weddell Sea shelf and slope region, including the interaction of the coastal current with the Filchner Depression.

Warm inflow over the continental shelf is limited by the presence of the ASF. In agreement with *Stewart and Thompson* [2016], we find that on-shelf transport of CDW mainly occurs when dense water formation over the shelf connects the density surfaces between the oceanic CDW and the cold shelf water, and the CDW can access the shelf without doing work against the buoyancy forces.

We find more warm water on the shelf when fresh surface water is present (summer scenarios). A shallower eddy overturning associated with the upper ocean stratification partially balances the Ekman downwelling, such that the WDW interface is relaxed. Future predictions suggest that a warmer and wetter atmosphere will generally lead to a freshening of the upper ocean. Also, reduced sea ice production will weaken the convection, allowing upper ocean stratification to persist during winter. Both effects will favor more warm water onto the shelf through a relaxation of the thermocline.

We study the ASF balance in a transient configuration that includes along-shelf changes of the shelf width. Reduced Ekman downwelling over the wide shelf, compared to the narrow shelf, affects the Reynolds fluxes but does not impose large changes on the cross-slope exchange unless along-flow variations of the shelf water density are included.

Southward transport of warm water in the trough is controlled by several processes: (I) the thermocline depth, regulating the temperature of the water at the depth of the trough sill, (II) the interaction between the slope current and the trough topography, (III) eddy formation through breaking topographic waves at the trough opening, and (IV) density of the water masses in the trough and on the shelf region upstream of the trough. In our results, (II) is dominant for high wind speed, where we find low southward transport of warm water in all scenarios as the WDW will not cross the sill. (III) is important in scenarios with medium wind speed (6 m s^{-1}), causing high transports of warm water into the western side of the trough. For weak and medium wind speed, the inflow is also sensitive to (IV), with greater inflow for denser DSW and for more saline shelf water upstream. The seasonal changes in the depth of the thermocline are small in the model, but the temperature at shelf depth (390 m) increases in summer, and we conclude that the higher trough inflow in summer is a combined response of the processes (I–III).

The sensitivity experiments based on our idealized model have provided new insights on the response of the warm inflow to changing atmospheric forcing and to modifications of DSW properties. *Hellmer et al*. [2012] and *Timmermann and Hellmer* [2013] suggested a future scenario where the slope current is redirected southward along FD, as a consequence of more mobile sea ice and higher momentum transfer between the atmosphere and the ocean. *Hellmer et al*. [2017] further describe a tipping point behavior, where a warm water flushing of the ice shelf cavity leads to a melt water feedback that enhances the shelf circulation and the southward transport of warm water along the trough. Our results suggest a slightly different response to increased wind stress, where the wind-driven part of the slope current is directed southward along the trough opening, but conservation of PV causes the current to turn at the sill and leave the trough. The current is strong and barotropic and reduces the southward transport of warm water by eddies, as the eddies are being advected out of the trough along with the current. This mechanism occurs for strong wind scenarios regardless of the density of the DSW in the trough. Instead, we find an optimal configuration for medium strength wind forcing, where warm inflow related to eddy-shedding appears to be most efficient. In the simulation with weak wind and no DSW present in the trough (W3Hom), we find a reversed circulation pattern in the trough and increased warm inflow. Although we do not include ice shelves or fresh water input from basal melting, the results support the suggested tipping point behavior. If the DSW production is cut off, a continuous inflow of warm water occurs along the bottom of the trough, reaching the southern boundary of the model. However, we did not find similar results in scenarios with stronger wind. Our work therefore emphasizes the need for further studies of these processes and how they are affected by transient changes in the wind pattern and the DSW properties.

Appendix A: Model Boundary Conditions and Surface Forcing

The northern and southern boundaries are treated as closed walls. Along the eastern and western open boundaries, we apply a radiation boundary scheme with restoring toward the initial hydrography and 3-D momentum fields [*Marchesiello et al*. 2001]. For the 2-D momentum, we apply a radiation condition similar to Flather [*Flather*, 1976], but adjusted for staggered grids (named Shchepetkin in ROMS) and for the free surface we apply Chapman explicit conditions *Chapman* [1985]. We restore temperature, salinity, and velocities at all boundaries, using smoothly increasing relaxation time scales [*Nycander and Döös*, 2003]. An overview of the restoring zones and time scales is given in Table A1. At all boundaries, we apply a 30 km sponge zone, where the diffusivity and viscosity increase smoothly from 1 m^2 s^{-1} in the interior to 3 m^2 s^{-1} at the boundary.

Table A1. Restoring Zones and Inverse Time Scales

	East	West	North	South	Deep West	Deep Trough
T,S						
Restoring zone (km)	30	30	30	24	345	24
Time scale (days)	60	30	30	5	30	1/24
U,V						
Restoring zone (km)	30	30	30	24		
Time scale (days)	60	30	30	5		

In order to reduce piling up of cold and saline DSW overflow west of the trough (downstream), we increased the restoring zone for temperature and salinity in the 10 deepest terrain-following layers west of 350 km East. At the shelf break, this corresponds to water depths below 400 m, increasing to 1300 m over the deeper ocean.

In the deeper part of the trough (>400 m), a reduced restoring time scale maintains the property of the DSW in the southern trough.

We restore *SST* and *SSS* to mimic the effects of sea ice. The restoring time scale is 3 days. For winter simulations, we restore to $SST = -1.9$°C and $SSS = 34.4$ over the whole domain. For summer simulations, we keep the winter conditions over the wide shelf but restore to $SST = -1.5$°C and $SSS = 33.7$ over the narrow shelf and deep ocean.

The wind stress is calculated from $\tau = -\rho_{air} C_D U^2$, where $\rho_{\text{air}} = 1$ kg m^{-3} and the drag coefficient $C_D = 0.001$. We apply an idealized westerly wind stress, with $\tau_{\text{max}} = -\rho_{air} C_D U^2_{\text{max}}$ over the channel and sinusoidal decay to zero from $y = 375$ km to the southern boundary (Figure 2a).

Acknowledgments

This work is supported by the Centre for Climate Dynamics at the Bjerknes Centre and by the Norwegian Research council's FRINATEK program through the project WARM and through the NARE program under the project WEDDELL. Helpful comments and discussions with P.E. Isachsen were greatly appreciated. We thank T. Birkeland for technical support on computing resources. We also thank K. Makinson and one anonymous reviewer for constructive comments that improved this paper. The model output files used for analysis in this paper is available at https://archive.norstore.no/, doi: 10.11582/2017.00003.

References

Allen, S. E., and X. Durrieu de Madron (2009), A review of the role of submarine canyons in deep-ocean exchange with the shelf, *Ocean Sci. Discuss.*, *6*(2), 1369–1406, doi:10.5194/osd-6-1369-2009.

Årthun, M., K. W. Nicholls, K. Makinson, M. A. Fedak, and L. Boehme (2012), Seasonal inflow of warm water onto the southern Weddell Sea continental shelf, Antarctica, *Geophys. Res. Lett.*, *39*, L17601, doi:10.1029/2012GL052856.

British Antarctic Survey (2013), *UK Antarctic Surface Meteorology; 1947–2013, Database, Version 1.0*, Polar Data Cent, Cambridge, U. K.

Carmack, E. C., and T. Foster (1977), Water masses and circulation in the Weddell Sea, in *Polar Oceans, Proceedings of the Polar Oceans Conference, Montreal, 1974*, pp. 151–165, Arctic Inst. of North Am., Calgary, Canada.

Chapman, D. C. (1985), Numerical treatment of cross-shelf open boundaries in a Barotropic Coastal Ocean Model, *J. Phys. Oceanogr.*, *15*(8), 1060–1075, doi:10.1175/1520-0485(1985)015<1060:NTOCSO>2.0.CO;2.

Darelius, E., K. Makinson, and K. Daae (2014), Hydrography and circulation in the Filchner Depression, Weddell Sea, Antarctica, *J. Geophys. Res. Oceans*, *119*, 1–18, doi:10.1002/2014JC010225.

Darelius, E., I. Fer, and K. W. Nicholls (2016), Observed vulnerability of Filchner-Ronne Ice Shelf to wind-driven inflow of warm deep water, *Nat. Commun.*, *7*, 1–7, doi:10.1038/ncomms12300.

Dupont, T. K., and R. B. Alley (2005), Assessment of the importance of ice-shelf buttressing to ice-sheet flow, *Geophys. Res. Lett.*, *32*, L04503, doi:10.1029/2004GL022024.

Fahrbach, E., G. Rohardt, and G. Krause (1992), The Antarctic Coastal Current in the southeastern Weddell Sea, *Polar Biol.*, *12*(2), 171–182, doi:10.1007/BF00238257.

Fer, I., E. Darelius, and K. Daae (2016), Observations of energetic turbulence on the Weddell Sea continental slope, *Geophys. Res. Lett.*, *43*, 760–766, doi:10.1002/2015GL067349.

Flather, R. (1976), A tidal model of the northwest European continental shelf, *Mem. Soc. R. Sci. Liege*, *10*(6), 141–164.

Foldvik, A., T. Gammelsrød, and T. Tørresen (1985), Hydrographic observations from the Weddell Sea during the Norwegian Antarctic research expedition 1976/77, *Polar Res.*, *3*, 177–193.

Foldvik, A., T. Gammelsrød, S. Østerhus, E. Fahrbach, G. Rohardt, M. Schröder, K. W. Nicholls, L. Padman, and R. A. Woodgate (2004), Ice shelf water overflow and bottom water formation in the southern Weddell Sea, *J. Geophys. Res.*, *109*, C02015, doi:10.1029/2003JC002008.

Foster, T., and E. C. Carmack (1976), Temperature and salinity structure in the Weddell Sea, *J. Phys. Oceanogr*, *6*, 36–44.

Fox-Kemper, B., R. Ferrari, and J. Pedlosky (2003), On the indeterminacy of rotational and divergent Eddy fluxes, *J. Phys. Oceanogr.*, *33*(2), 478–483, doi:10.1175/1520-0485(2003)033<0478:OTIORA>2.0.CO;2.

Gent, P. R., and J. C. Mcwilliams (1990), Isopycnal mixing in ocean circulation models, *J. Phys. Oceanogr.*, *20*(1), 150–155, doi:10.1175/1520-0485(1990)020<0150:IMIOCM>2.0.CO;2.

Gill, A. (1973), Circulation and bottom water production in the Weddell Sea, *Deep Sea Res. Oceanogr. Abstr.*, *20*(2), 111–140, doi:10.1016/0011-7471(73)90048-X.

Hall, M. (1994), Synthesizing the Gulf Stream thermal structure from XBT data, *J. Phys. Oceanogr*, *24*, 2278–2287.

Hattermann, T., L. H. Smedsrud, O. A. Nøst, J. Lilly, and B. Galton-Fenzi (2014), Eddy-resolving simulations of the Fimbul Ice Shelf cavity circulation: Basal melting and exchange with open ocean, *Ocean Modell.*, *82*, 28–44, doi:10.1016/j.ocemod.2014.07.004.

Hellmer, H. H., F. Kauker, R. Timmermann, J. Determann, and J. Rae (2012), Twenty-first-century warming of a large Antarctic ice-shelf cavity by a redirected coastal current, *Nature*, *485*(7397), 225–228, doi:10.1038/nature11064.

Hellmer, H. H., F. Kauker, R. Timmermann, and T. Hattermann (2017), The fate of the southern Weddell Sea continental shelf in a warming climate, *J. Clim.*, doi:10.1175/JCLI-D-16-0420.1, in press.

Heywood, K. J., R. A. Locarnini, R. D. Frew, P. F. Dennis, and B. A. King (1998), Transport and water masses of the Antarctic Slope Front system in the eastern Weddell Sea, in *Ocean, Ice, and Atmosphere—Interaction at the Antarctic Continental Margin*, vol. , edited by S. S. Jacobs and R. F. Weiss, pp. 203–214, AGU, Washington, D. C.

Jacobs, S. (1991), On the nature and significance of the Antarctic Slope Front, *Mar. Chem.*, *35*(1–4), 9–24, doi:10.1016/S0304-4203(09)90005-6.

Jacobs, S., A. Jenkins, C. F. Giulivi, and P. Dutrieux (2011), Stronger ocean circulation and increased melting under Pine Island Glacier ice shelf, *Nat. Geosci.*, *4*(8), 519–523, doi:10.1038/ngeo1188.

Jensen, M. F., I. Fer, and E. Darelius (2013), Low frequency variability on the continental slope of the southern Weddell Sea, *J. Geophys. Res. Oceans*, *118*, 4256–4272, doi:10.1002/jgrc.20309.

Klinck, J. M. (1996), Circulation near submarine canyons: A modeling study, *J. Geophys. Res.*, *101*(95), 1211–1223, doi:10.1029/95JC02901.

Klinck, J. M., and M. S. Dinniman (2010), Exchange across the shelf break at high southern latitudes, *Ocean Sci.*, *6*(2), 513–524, doi:10.5194/os-6-513-2010.

Magaldi, M. G., T. W. N. Haine, and R. S. Pickart (2011), On the nature and variability of the East Greenland Spill Jet: A case study in summer 2003, *J. Phys. Oceanogr.*, *41*(12), 2307–2327, doi:10.1175/JPO-D-10-05004.1.

Marchesiello, P., J. C. McWilliams, and A. Shchepetkin (2001), Open boundary conditions for long-term integration of regional oceanic models, *Ocean Modell.*, *3*(1–2), 1–20, doi:10.1016/S1463-5003(00)00013-5.

Marshall, J., and G. Shutts (1981), A note on rotational and divergent Eddy fluxes, *J. Phys. Oceanogr.*, *11*(12), 1677–1680, doi:10.1175/1520-0485(1981)011<1677:ANORAD>2.0.CO;2.

Nicholls, K. W. (2003), Water mass modification over the continental shelf north of Ronne Ice Shelf, Antarctica, *J. Geophys. Res.*, *108*(C8), 3260, doi:10.1029/2002JC001713.
Nicholls, K. W., L. Boehme, M. Biuw, and M. A. Fedak (2008), Wintertime ocean conditions over the southern Weddell Sea continental shelf, Antarctica, *Geophys. Res. Lett.*, *35*, L21605, doi:10.1029/2008GL035742.
Nicholls, K. W., S. Østerhus, K. Makinson, T. Gammelsrød, and E. Fahrbach (2009), Ice-ocean processes over the continental shelf of the southern Weddell Sea, Antarctica: A review, *Rev. Geophys.*, *47*, RG3003, doi:10.1029/2007RG000250.
Nøst, O. A., and T. Lothe (1997), The Antarctic Coastal Current-physical oceanographic results from NARE 1996/97, *Norsk Polarinst. Meddelelser 148*, edited by J. G. Winther, pp. 51–57, Norsk Polarinstitutt, Tromsø, Norway
Nøst, O. A., M. Biuw, V. Tverberg, C. Lydersen, T. Hattermann, Q. Zhou, L. H. Smedsrud, and K. M. Kovacs (2011), Eddy overturning of the Antarctic Slope Front controls glacial melting in the eastern Weddell Sea, *J. Geophys. Res.*, *116*, C11014, doi:10.1029/2011JC006965.
Nycander, J., and K. Döös (2003), Open boundary conditions for barotropic waves, *J. Geophys. Res.*, *108*(C5), 3168, doi:10.1029/2002JC001529.
Orsi, A. H., and C. L. Wiederwohl (2009), A recount of Ross Sea waters, *Deep Sea Res., Part II*, *56*(13–14), 778–795, doi:10.1016/j.dsr2.2008.10.033.
Paolo, F. S., H. A. Fricker, and L. Padman (2015), Volume loss from Antarctic ice shelves is accelerating, *Science*, *348*(6232), 327–331.
Pritchard, H. D., S. Ligtenberg, H. Fricker, D. Vaughan, M. van den Broeke, and L. Padman (2012), Antarctic ice-sheet loss driven by basal melting of ice shelves, *Nature*, *484*(7395), 502–505, doi:10.1038/nature10968.
Rignot, E., S. Jacobs, J. Mouginot, and B. Scheuchl (2013), Ice-shelf melting around Antarctica, *Science*, *341*(6143), 266–270, doi:10.1126/science.1235798.
Semper, S., and E. Darelius (2016), Seasonal resonance of diurnal continental shelf waves in the southern Weddell Sea, *Ocean Sci. Discuss.* *13*, 1–25, doi:10.5194/os-2016-36.
Shchepetkin, A., and J. C. McWilliams (2009), Computational Kernel algorithms for fine-scale, multiprocess, longtime oceanic simulations, in *Handbook of Numerical Analysis*, edited by P. G. Ciarlet, vol. 14, pp. 121–183, Elsevier B. V., doi:10.1016/S1570-8659(08)01202-0.
St. Laurent, P., J. M. Klinck, and M. S. Dinniman (2013), On the role of coastal troughs in the circulation of warm Circumpolar Deep Water on Antarctic shelves, *J. Phys. Oceanogr.*, *43*(1), 51–64, doi:10.1175/JPO-D-11-0237.1.
Stewart, A. L., and A. F. Thompson (2015), Eddy-mediated transport of warm Circumpolar Deep Water across the Antarctic Shelf Break, *Geophys. Res. Lett.*, *42*, 432–440, doi:10.1002/2014GL062281.
Stewart, A. L., and A. F. Thompson (2016), Eddy generation and jet formation on the Antarctic continental slope, *J. Phys. Oceanogr.*, *46*(12), 3729–3750, doi:10.1175/JPO-D-16-0145.1.
Timmermann, R., and H. H. Hellmer (2013), Southern Ocean warming and increased ice shelf basal melting in the twenty-first and twenty-second centuries based on coupled ice-ocean finite-element modelling, *Ocean Dyn.*, *63*(9–10), 1011–1026, doi:10.1007/s10236-013-0642-0.
Whitworth, T., A. H. Orsi, S.-J. Kim, W. D. Nowlin Jr., and R. A. Locarnini (1985), Water masses and mixing near the Antarctic Slope Front, in *Ocean, Ice, and Atmosphere: Interactions at the Antarctic Continental Margin*, edited by S. S. Jacobs and R. F. Weiss, AGU, Washington, D. C., doi:10.1029/AR075p0001.
Williams, W. J., G. G. Gawarkiewicz, and R. Beardsley (2001), The adjustment of a shelfbreak jet to cross-shelf topography, *Deep Sea Res., Part II*, *48*(1-3), 373–393, doi:10.1016/S0967-0645(00)00085-0.
Zhang, Y., J. Pedlosky, and G. R. Flierl (2011a), Cross-shelf and out-of-bay transport driven by an open-ocean current, *J. Phys. Oceanogr.*, *41*(2004), 2168–2186, doi:10.1175/JPO-D-11-08.1.
Zhang, Y., J. Pedlosky, and G. R. Flierl (2011b), Shelf circulation and cross-shelf transport out of a bay driven by Eddies from an open-ocean current. Part I: Interaction between a barotropic vortex and a steplike topography, *J. Phys. Oceanogr.*, *41*, 889–910, doi:10.1175/2010JPO4496.1.
Zhou, Q., T. Hattermann, O. A. Nøst, M. Biuw, K. M. Kovacs, and C. Lydersen (2014), Wind-driven spreading of fresh surface water beneath ice shelves in the eastern Weddell Sea, *J. Geophys. Res. Oceans*, *119*, 3818–3833, doi:10.1002/2013JC009556.

Paper II

Hydrography and circulation in the Filchner Depression, Weddell Sea, Antarctica

E. Darelius, K. Makinson, K. Daae, I. Fer, P. P. Holland, and K. W. Nicholls
J. Geophys. Res. Oceans, **119** (2014)

AGU PUBLICATIONS

JGR

Journal of Geophysical Research: Oceans

RESEARCH ARTICLE

10.1002/2014JC010225

Hydrography and circulation in the Filchner Depression, Weddell Sea, Antarctica

E. Darelius[1], K. Makinson[2], K. Daae[1], I. Fer[1], P. R. Holland[2], and K. W. Nicholls[2]

[1]Geophysical Institute, University of Bergen and Bjerknes Centre for Climate Research, Bergen, Norway, [2]British Antarctic Survey, Natural Environment Research Council, Cambridge, UK

Key Points:
- New detailed CTD and LADCP sections from the Filchner Depression are presented
- Observations and modeling suggest a new circulation scheme for the depression
- The outflow of ISW in the Filchner Depression occurs along its eastern flank

Correspondence to:
E. Darelius,
darelius@gfi.uib.no

Citation:
Darelius, E., K. Makinson, K. Daae, I. Fer, P. R. Holland, and K. W. Nicholls (2014), Hydrography and circulation in the Filchner Depression, Weddell Sea, Antarctica, *J. Geophys. Res. Oceans*, *119*, doi:10.1002/2014JC010225.

Received 10 JUN 2014
Accepted 11 AUG 2014
Accepted article online 20 AUG 2014

Abstract Cold and dense ice shelf water (ISW) emerging from the Filchner-Ronne Ice Shelf cavity in the southwestern Weddell Sea flows northward through the Filchner Depression to eventually descend the continental slope and contribute to the formation of bottom water. New ship-born observations of hydrography and currents from Filchner Depression in January 2013 suggest that the northward flow of ISW takes place in a middepth jet along the eastern flank of the depression, thus questioning the traditional view with outflow along the western flank. This interpretation of the data is supported by results from a regional numerical model, which shows that ISW flowing northward along the eastern coast of Berkner Island turns eastward and crosses the depression to its eastern side upon reaching the Filchner ice front. The ice front represents a sudden change in the thickness of the water column and thus a potential vorticity barrier. Transport estimates of northward ISW flux based on observations ranges from 0.2 to 1.0 Sv.

1. Introduction

Cold ice shelf water (ISW) emerging from the Filchner-Ronne Ice Shelf (FRIS) in the southern Weddell Sea (see Figure 1) flows northward through the Filchner Depression and crosses its sill to eventually descend the continental slope and contribute to the formation of Weddell Sea deep and bottom water [*Foldvik et al.*, 2004]. These cold, dense water masses leave the Weddell Sea, e.g., through gaps in the South Scotia ridge, and are major contributors to Antarctic Bottom Water (AABW) formation [*Orsi et al.*, 1999].

The outflow of ISW—commonly referred to as the Filchner overflow—was discovered in 1977 [*Foldvik et al.*, 1985a] and the flux of cold ISW across the sill has been estimated to 1.6±0.5 Sv (1 Sv ≡ $10^6 m^3 s^{-1}$) resulting in 4.3±1.4 Sv Weddell Sea Bottom Water [*Foldvik et al.*, 2004]. After crossing the Filchner sill, the relatively dense ISW forms a gravity plume that flows westward along the continental slope, partly being steered downslope by two ridges cross cutting the slope [*Darelius and Wåhlin*, 2007]. The outflow has been monitored sporadically since 1977 and continuously since 2009 with a mooring at the sill (S2, see Figure 1) and the data reveal a seasonal signal in the temperature and salinity of the outflowing water. The seasonality is partly caused by admixture of high salinity shelf water (HSSW) from the Berkner Bank [*Darelius et al.*, 2014].

HSSW is formed through cooling of modified warm deep water (MWDW) and additional brine rejection from sea ice formation during winter [*Nicholls et al.*, 2009] and it enters the FRIS cavity west of the Berkner Island and through the Ronne depression (see Figure 1). The depression of the freezing point with increasing pressure allows the HSSW ($\theta = T_{f,surface}$) which is here in contact with ice at great depth (the grounding line is as deep as 1800 m) to be transformed into potentially supercooled ($\theta < T_{f,surface}$) ISW: it is cooled, as its heat is used to melt ice, and freshened, as it mixes with the fresh melt water. Since a given amount of heat is associated with a given amount of freshwater, the HSSW-ISW transformation will cause the θS-characteristics (S is salinity) of the water to change along a straight line in θS-space; the Gade line [*Gade*, 1979; *Jenkins*, 1999]. The gradient of the Gade line is 2.4–2.8°C depending on the amount of heat conduction into the ice [*Nicholls et al.*, 2009]. The source salinity can be found by extrapolating the Gade line to the point where it intersects the surface freezing point. Following this argument, the HSSW precursor to the overflowing ISW has been found to originate at the Berkner Bank, while the ISW resulting from the slighty more saline Ronne HSSW-inflow is too dense to escape across the Filchner sill and is forced to recirculate within the cavity [*Nicholls et al.*, 2001].

The Filchner Depression is filled with ISW up to a depth of about 200–300 m [*Carmack and Foster*, 1975], above which is found winter water or, along the coast, eastern shelf water (ESW). The circulation in the

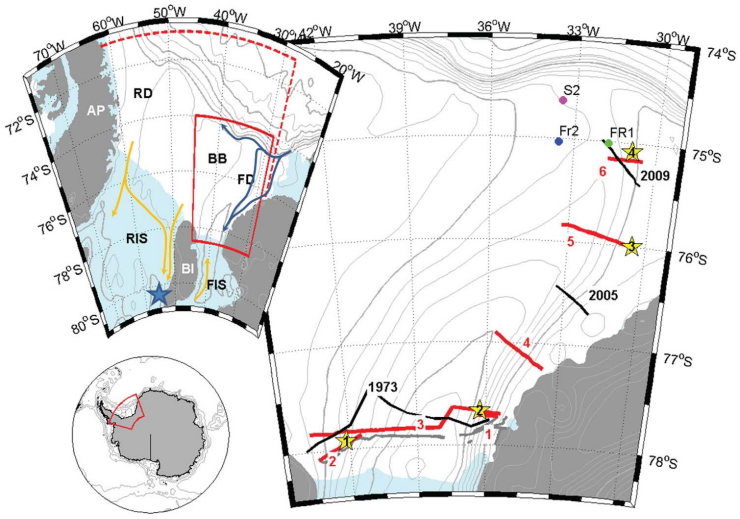

Figure 1. Map of the study region showing the position of the CTD-sections (labeled lines) and time series (labeled yellow stars) occupied in 2013 (red), 2009, 2005, and 1973 (black) and of the moorings Fr1 (green circle), Fr2 (blue circle) and S2 (magenta circle). Isobaths (Bedmap) [*Fretwell et al*., 2013] are shown every 100 m (gray lines) with every 500 m in dark gray. Land and grounded ice is shown in dark gray and floating ice shelves (from Bedmap) in light blue. The position of the ice shelf front (or heavily ridged fast ice in the east) observed during the cruise is included (thin gray line). The upper inset shows the location of the study area (red box) and the Ronne ice shelf (RIS), the Filchner ice shelf (FIS), Berkner Island (BI), Filchner Depression (FD), Ronne depression (RD) and Berkner Bank (BB). The limits of the model domain are indicated by dashed, red lines. The blue arrows show the path of the coastal current/Antarctic slope current and yellow arrows show inflow and circulation below FRIS, from *Nicholls et al.* [2009]. The blue star shows the location of Site 5. The lower inset shows the location of the region (red box) shown in the upper inset.

upper layer in the depression region is described by *Nicholls et al.* [2009] and sketched in the upper inset of Figure 1. Just east of the depression the Antarctic slope current branches off to form a coastal current carrying ESW onto the shelf. Below the surface layer, there is a summer inflow of MWDW toward the ice shelf [*Årthun et al*., 2012], which reaches the Filchner ice front in late summer or early winter [*Foldvik et al*., 1985b; *Årthun et al*., 2013]. While basal melt rates below FRIS are low (0.2–0.34 m yr^{-1}) today [*Nicholls et al*., 2009; *Rignot et al*., 2013], numerical modeling suggest that they will increase significantly (to 4 m yr^{-1}) in a warmer future as changing wind and ice conditions cause more warm water to flow onto the shelf [*Hellmer et al*., 2012]. Based on hydrographic data and geostrophic calculations from the first scientific cruises to the region (USCGC Glacier 1968–1973), *Carmack and Foster* [1975] inferred a cyclonic gyre circulation at depth in the depression. Accordingly, the flow of ISW from the FRIS cavity toward the Filchner sill is commonly believed to follow the topography on the western side of the Filchner Depression [see e.g., *Foldvik and Gammelsrød*, 1988; *Foldvik et al*., 2001; *Nicholls et al*., 2001] although there are no direct observations of the flow as the western part of the depression is often ice-covered even during summer. In this paper, we present detailed sections of hydrography and velocity obtained during a cruise to the Filchner Depression in January 2013 that question the traditional view of the circulation within the depression, and suggest that the core of the ISW outflow is located above the eastern flank of the depression. The observations are compared to results from a regional numerical model, which supports our interpretation of the data.

2. Data and Methods

Data were collected in the Filchner Depression during ten days, 1–11 January 2013, onboard *RRS Ernest Shackleton*. The obtained data set includes vertical profiles of hydrography and velocity from 116 casts with a conductivity-temperature-depth (CTD, SBE911+) package equipped with down and upward-looking lowered acoustic Doppler current profilers (LADCPs, 300 kHz RD Instruments Workhorse). Stations were

Table 1. Information on CTD/LADCP Sections and Time Series Occupied During Cruise ES060, 2013[a]

Stations		Start	End	Time (UTC)	Duration (h)	Angle B (°)	Sta_T
Section 1	6–10	77°43′S, 35°28′W	77°43′S, 36°19′W	3/1 01:30	5	28	
Section 2	12–21	78°05′S, 43°25′W	77°52′S, 41°28′W	3/1 20:40	9	28	
Section 3	29–61	77°50′S, 43°43′W	77°42′S, 35°23′W	5/1 3:50	43	28	
Section 4	70–80	77°15′S, 33°40′W	76°54′S, 35°39′W	7/1 20:50	12	37	73–78
Section 5	90–102	75°59′S, 30°42′W	75°50′S, 33°15′W	9/1 9:10	12	25	93–97
Section 6	103–109	75°50′S, 33°15′W	75°10′S, 31°44′W	10/1 3:50	6	0	105–107
Time Series							
TS1	23–28	77°52′S, 41°28′W		4/1 13:40	10	28	
TS2	62–69	77°40′S, 36°16′W		7/1 02:00	13	28	
TS3	81–89	75°60′S, 30°30′W		8/1 17:30	13	25	
TS4	110–116	75°05′S, 30°52′W		10/1 13:10	12	0	

[a]For location of the sections and time series, see Figure 1. β is the angle that the coordinate system is rotated to be aligned with the slope and Sta_T ares the stations included in the transport estimate (see section 3.2.1., stations are also marked in Figure 6). Time gives the time the first stations in the section/time series was occupied and dates are given in the format day/month.

occupied along six sections: one along the Filchner ice front, one on the western and four on the eastern flank of the depression, and in addition time series (12–14 h long) were obtained at four locations, see Figure 1. The CTD was equipped with double conductivity and temperature sensors and a single oxygen sensor (not shown) which were calibrated by the manufacturer directly after the cruise. In addition, water samples for monitoring of the conductivity sensor were collected using two Niskin bottles attached to the CTD-rosette. The CTD system included an altimeter, allowing for data collection to within 10 m from the bottom. Positions from a Garmin handheld GPS were incorporated directly into the data stream, while data from the positioning system of the ship were recorded separately.

The velocity profiles are calculated at 8 m vertical resolution using the inverse method [*Visbeck*, 2002] constrained by navigation from the GPS and bottom tracking by the LADCP. The error velocity is typically 3 cm s^{-1}. The coordinate system at sections 4–6 and time series 3 and 4 were rotated locally (see Table 1), in order to align the y axis with the isobaths, and velocities are henceforth referred to as along and cross slope. Positive along-slope flow thus has a northeastward direction, i.e., flow toward the sill of the Filchner Depression.

Tides in the region are relatively strong (up to 10–15 cm s^{-1}) and transport calculations based on the LADCP profiles are highly sensitive to errors related to detiding. Attempts were made to detide the LADCP profiles using (1) the tidal model results from the CATS2008b (an update to the circum-Antarctic inverse barotropic tidal model described by *Padman et al*., [2002]), while correcting for errors in the bathymetry of the tidal model using observed depths and conserved volume flux (i.e., $u' = u_{model} h_{model} h_{observed}^{-1}$, where h is the depth and u the tidal current) and (2) harmonic fits to the depth-integrated observed velocities (i.e., volume flux per unit width) at sections and time series, see Appendix A. Observations from the upper and lower 150 m of the profiles were neglected to remove boundary layer effects, as were stations with strong currents above the slope. It is not obvious to draw a conclusion regarding what detiding routine is more correct, see further discussion in Appendix A, and transport estimates are therefore given as an interval spanning the results given by the different detiding procedures. Velocity sections shown in Figures 2, 5, and 7 are detided using CATS.

In addition to the CTD and LADCP data collected during the cruise, sections obtained in the depression in 2005 (JR97) [*Nicholls et al*., 2009] and 2009 (ES033) [*Nicholls*, 2009], at the Filchner ice front in 1973 (USCGC Glacier) [*Carmack and Foster*, 1975] and single stations from 1977 [*Foldvik et al*., 1985a], 1980 [*Foldvik et al*., 1985c], 1984, 1993 [*Gammelsrød et al*., 1994], 1995 [*Grosfeld et al*., 2001], and one station from 2011 (JR244) [*Larter*, 2011] are included in the analysis. Records from ~500 m depth at moorings Fr1 and Fr2 [*Foldvik et al*., 2004] deployed south of the sill in 1995–1996 (see Figure 1 for location) are also included. The data from 1973 have low (10–100 m) vertical resolution.

The transports are calculated using the detided along-slope component of the current velocity. The sections are divided into segments centered at each station and the width of each segment corresponds to half the distance from adjacent stations. For the first and last station segments, the width is set equal to either side of the station. The −1.9°C isotherm is taken as the upper boundary for the ISW in transport calculations. To

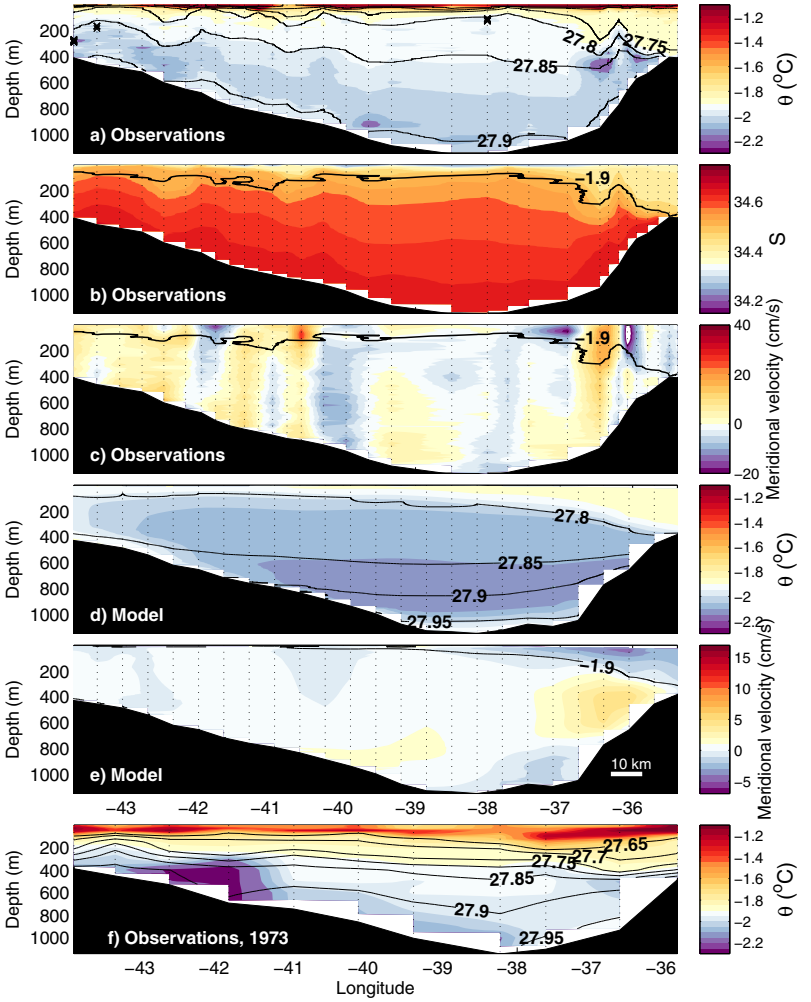

Figure 2. Sections of (a) Potential temperature (color) and isopycnals (labeled black lines) referenced to surface pressure, (b) salinity, and (c) meridional velocity (cm s^{-1}) observed in January 2013 across the Filchner Ice Front (section 3). Mean, modeled sections of (d) potential temperature (color) and isopycnals (labeled black lines) and (e) meridional velocity at 78°S. Section of (f) Potential temperature (color) and isopycnals (labeled black lines) referenced to surface pressure observed in February 1973 [*Carmack and Foster*, 1975]. Observations of in situ supercooled water are marked with black crosses in Figure 2a. The horizontal length scale is shown in the lower right corner of Figure 2e.

limit the error introduced by erroneous detiding, only stations with a baroclinic northward flow are included. The stations included in the transport calculations are given in Table 1 and marked in Figure 5.

The geostrophic shear is calculated using the dynamic height anomaly approach in the Gibbs Seawater Oceanographic Toolbox [*McDougall and Barker*, 2011]. Data from the upper 25 m at each station were ignored to remove surface effects and errors, i.e., the reference level of no motion was effectively set to 25 m. Given the uncertainty in detiding of the LADCP (see Appendix A), absolute geostrophic currents were not calculated. The method gives profiles of relative velocity only above the depth of the shallowest of the two CTD stations used to obtain the profile. In a section across a sloping bottom the geostrophic transport

in what is often referred to as the "bottom triangle," i.e., the area closest to the bottom, is not included unless profiles are somehow extrapolated. This has not been done and transport in the bottom triangle is hence ignored.

The observations are compared with results from an isopycnic coordinate ocean circulation model (MICOM) [*Bleck et al.*, 1992] applied to a region including the FRIS cavity and the Filchner Depression (see Figure 1) and adapted to include a thermodynamically active but static ice shelf as well as tidal forcing [*Holland and Jenkins*, 2001]. Following *Jenkins et al.* [2004] the model is forced by restoring the surface salinity over the open ocean to an annually repeating seasonally and spatially varying field [*Makinson et al.*, 2011] which is designed to represent the effect of sea ice growth and decay. With the largest tides around Antarctica found in the southern Weddell Sea, the model is also forced along its northern and eastern boundaries by restoring the surface elevations to those predicted by the CircumAntarctic Tidal Simulation (CATS) [*Padman et al.*, 2002] utilizing 10 tidal constituents. In the vertical, the model consists of 15 isopycnic layers and a surface mixed layer (with a freely evolving density) while the horizontal resolution increases from 12.5 km in the north to 4.5 km in the south. Explicit vertical mixing in the model occurs through mixed-layer entrainment or detrainment, see *Holland and Jenkins* [2001] for details. After a 13 years spin up, seven years of model data are available as monthly mean fields. The data fields are interpolated to depth coordinates and averaged to a time mean field. The seasonality in the modeled ISW circulation is small and results including only summer months are similar. For further details on the model setup the reader is referred to *Makinson et al.* [2011].

3. Results

3.1. The Filchner Ice Front

3.1.1. Observations

Section 3 was occupied along the entire Filchner ice front at a distance of about 6–30 km from the ice front. Fast ice on the eastern side of the depression forced the ship to move farther north to finish the section. Potentially supercooled ISW is found at depth across the entire Filchner Depression. On the eastern side of the depression, the ISW resides below 300–400 m depth, separated from the ESW above it through relatively sharp gradients in both salinity and temperature (Figures 2a and 2b). The eastern flank is further characterized by low temperatures (down to -2.2°C) in a distinct layer between 350 and 600 m depth. On the western side of the depression, vertical gradients—with the exception of the surface thermo and halocline located at about 50 m depth—are much weaker, and there is little trace of ESW. The internal Rossby radius, $\lambda=(g\Delta\rho h)^{1/2}(\rho_0 f)^{-1}$, where g is gravity, $\Delta\rho = 0.1$ kg m^{-3} the density difference between ESW and the ambient water, $h=100$–300 m the thickness of the ESW layer and f the Coriolis factor, is about 2–4 km. A coastal current carrying ESW westward along the ice front would hence be trapped south of section 3, since the stations were occupied >6 km from the ice front. As discussed below, the ice front section from 1973 which was occupied 1–3 km from the ice front (A. Foldvik, personal communication, 2014) does show a 300–400 m thick layer of ESW below a thin layer of surface water.

Unlike the two stations occupied at the ice front in 1993 [*Gammelsrød et al.*, 1994; *Nicholls et al.*, 2001] the ISW observed in 2013 does not in general fall on one Gade line, but appears to be a layered mixture of ISW with different source salinities, see e.g., station 32 in Figure 3a. While the larger part of the water column can be expected to have source salinities between 34.68 and 34.70, there are a few cold intrusions (e.g., on station 45, see Figure 3a) indicating higher source salinities. Below the temperature minimum, there is a tendency for stations on the eastern side of the depression to be shifted about 0.05°C downward in θS-space compared to the western stations (i.e., for the same salinity water is 0.05°C colder in the east than in the west). This corresponds to an increase in source salinity of about 0.02.

The lowest temperatures are typically observed 100–300 m above the bottom, and bottom temperatures are generally lower (by about 0.1°C) on the eastern side than on the western side of the depression (Figure 2a). The ISW is by definition potentially supercooled, i.e., its temperature is below the surface freezing point $\theta(z) < T_f(S,0)$. In a few locations on the western flank of the depression, especially in section 2 (not shown) we also observed water that was *in situ* supercooled (i.e., $T(z) < T_f(S,z)$, Figure 2a). These locations are characterized by upward doming isotherms and low temperatures in the surface but they do not necessarily coincide with locations of flow directed away from the cavity. No *in situ* supercooled water was observed on the eastern flank, possibly because the fast ice forced us to place stations further away from the ice front. *In situ* supercooled ISW in the vicinity of an ice front have been observed previously by e.g., *Fer et al.* [2012].

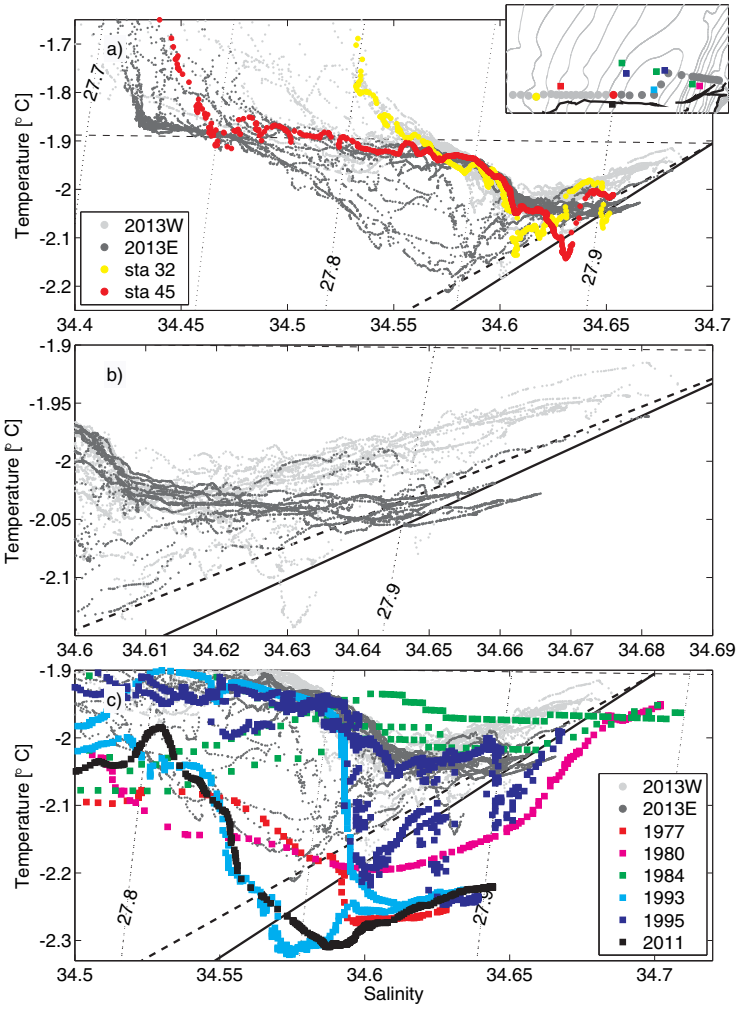

Figure 3. *θS*-diagram showing (a) data from the Filchner Front in 2013 (section 3) where "eastern" stations are colored dark gray and "western" stations light gray, (b) the same data but zoomed in on the ISW, and (c) selected historic stations occupied in the vicinity of the front according to legend. Dotted, labeled lines are isopycnals referenced to surface pressure, the thin, dashed line is the surface freezing point and thick black lines are Gade lines with a gradient of 2.4 (dashed) and 2.8°C. The inset shows the location of the stations occupied in 2013 (circles) and the historical stations (squares), colored according to the legends in Figures 3a and 3c.

The velocity field at the front is characterized by high variability with lateral length scales of about 10 km and amplitudes reaching 20 cm s^{-1} (Figure 2c), possibly related to instabilities or meanders in a potential (but unobserved) coastal current. Ignoring these mesoscale features, which can be expected to vary in time and space, we note that isopycnals generally are bowl-shaped below about 27.85 kg m^{-3}, while shallower isopycnals deepens from west to east, especially above the eastern flank, i.e., below the southward flowing ESW. The shape of the isopycnals along the ice front indicate a weak (relative geostrophic velocities on the order of a few cm s^{-1}) cyclonic circulation of the densest water in the depression, as suggested by *Carmack*

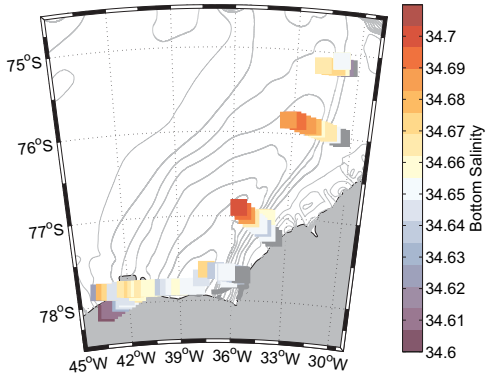

Figure 4. Map showing the bottom salinity at all CTD-stations occupied during cruise ES060, 2013. Stations with a bottom salinity lower than 34.6 are colored equally gray.

and Foster [1975]. On the eastern flank, there is the potential for a northward undercurrent below the southward coastal current, which, if present, would be shadowed by the strong mesoscale variability.

3.1.2. Numerical Model

The modeled ice front section (78°S, Figures 2d and 2e), with the exception of the mesoscale variability, shows features similar to the observations. The depression is filled with ISW up to 50–100 m, with a deepening of the thermocline on the eastern side due to the presence of the southward flowing coastal current and ESW. The isopycnals show the same bowl shape as the observations at depth, and the same eastward deepening at shallower depth. The associated velocity field manifests the deep cyclonic circulation, i.e., outflow on the western flank and inflow on the eastern flank, as identified by *Carmack and Foster* [1975], and supports the idea of a northward flowing undercurrent on the eastern flank as suggested by the tilting isopycnals in the observations. Mean velocities are on the order of a few cm s^{-1} giving a total northward transport of 1.0 Sv, about 0.2 Sv of which returns southward within the deep cyclonic circulation. The model thus has a net northward flow of ISW of 0.8 Sv.

3.1.3. Comparison With USCGC Glacier Section From 1973

The observations warrant a closer comparison with e.g., the ice front section obtained by *USCGC Glacier* in 1973 [*Carmack and Foster*, 1975, Figure 4]. Comparing Figure 2f with Figures 2a and 2b, one notes the following:

(A) The lowest temperatures were observed on the western side in 1973 (and in 1980, 1995) [*Foldvik et al*., 1985c; *Grosfeld et al*., 2001] and on the eastern side in 2013 (and in 1993) [*Gammelsrød et al*., 1994].

(B) Densities below 400 m were higher in 1973 than in 2013. The 27.90 kg m^{-3} isopycnal was found at around 500 m depth in 1973 while it is generally about 50 m above bottom in 2013. No densities above 27.95 were observed in 2013.

(C) The density at sill depth (600 m) was 27.90 kg m^{-3} in 1973 and 27.85 kg m^{-3}, i.e., about 0.05 kg m^{-3} lighter less dense in 2013.

Differences in the upper layer—e.g., the density and the upper limit of the ISW—are most likely related to seasonality and to differences in the distance between the section and the ice front and possibly also to the shape of the ice front itself, which was pointed in 1973 (the stations shown in Figure 1 follows the position of the ice front) while it was relatively straight in 2013.

The comparison suggests changes in the Filchner Depression hydrography that would directly influence the properties of the ISW flowing over the sill and ultimately the deep water masses formed. Figure 3c shows data collected from stations occupied in the vicinity of the Filchner ice front during the period 1977–2013, suggesting that the changes are the result of interannual variability rather than a long-term trend. Large changes in the FRIS-circulation linked to the southern annular mode (SAM) and HSSW production on the Berkner Bank have been suggested by *Timmermann et al*. [2002] for example, and observations from the ice shelf cavity show interannual variability [*Nicholls and Østerhus*, 2004].

Figure 4 shows the bottom salinity observed in 2013. The highest bottom salinities—reaching up to 34.71—were observed at the deepest stations at 76–77°S (sections 4 and 5). At the ice front (sections 1–3) bottom salinities were generally lower with the highest values occurring in the deep, central part of the

depression and at relatively shallow (400–700 m) depths on the western flank of the depression, adjacent to Berkner Bank. The large difference between section 2 and section 3 on the western flank of the depression suggests high temporal and/or spatial variability here. Extrapolating the HSSW-ISW mixing line from stations at the eastern flank (sections 4–6) to the surface freezing point gives a HSSW salinity of 34.72 (Figure 6b), while the western stations in section 3 suggest slightly less saline HSSW.

The observations are consistent with those presented by [*Carmack and Foster*, 1975] and with HSSW formed on Berkner Bank entering the depression and circulating cyclonically along its rim, but not yet having reached the ice front. Observations in 1995 show HSSW presence at the eastern side of the ice front [*Grosfeld et al*., 2001].

3.2. Sections on the Eastern Flank

3.2.1. Observations: Section 4–6

Figure 5 shows the observed hydrography and currents at sections 4–6 on the eastern flank of the depression. The Filchner Depression is filled with ISW up to 100–300 m depth, with the interface depth generally being shallower toward the south. There are clear intrusions of MWDW ($\theta > -1.7$ °C, S $<$34.6) [*Foster and Carmack*, 1976] at section 6, which are found at shelf-level (400–500 m) in the east and at shallower levels—above the ISW—in the depression. The MWDW signal at section 5 is similar but weaker, and at section 4 there is no trace of MWDW. The MWDW intrusions and the erosion of its properties between sections 5 and 6 are evident in θS-space (Figure 6a). Focusing on the ISW, the stations can be divided into two main groups: an eastern group where the θS-relation aligns with a Gade line (slope 2.4) with a source salinity of 34.70 for 34.64 $<$S $<$34.68 and a western group where temperatures in the same salinity range are about 0.05°C higher (Figures 6b and 6c). In addition, there exist a number of "mixed" stations, with "eastern" water at the bottom and "western" water above. The "eastern" and "western" water correspond to water found in the east and the west at the Filchner ice front (Figure 6b). For salinities above 34.68, and more so on the deeper western stations, the θS-relation deviates from the Gade line suggesting admixture of HSSW [*Nøst and Østerhus*, 1998] with a salinity of about 34.72 (Figure 6b).

As observed in the eastern part of section 3 at the ice shelf front, the depth of the densest isopycnals ($\sigma > 27.85$ kg m^{-3}) in section 4–6 generally increase westward, while the depth of the lighter isopycnals decrease westward. The steeply sloping isopycnals at middepth are associated with a relatively strong—maximum observed velocities are 30–40 cm s^{-1}—outflow of ISW located near the 600 m isobath (see Figure 5). The northward transport of ISW above the slope is estimated from the detided LADCP data to be 0.3–0.9, 0.6–1.0, and 0.2–0.3 Sv at section 4–6 respectively. On the shallow shelf in the east, the currents are generally weak with southward flow of ESW and warmer MWDW along the bottom. Currents in section 5 suggest a surface intensified eddy toward the center of the depression (32.25–33°W). Sections 4 and 5 show relatively strong (5–10 cm s^{-1}) barotropic currents with northward flow above the slope and southward flow in the western part of the section and consequently a large barotropic shear. The direction of the flow agrees with the phase of the tidal currents at the time of occupation and are potentially related to tides (see discussion and alternative detiding procedures in Appendix A). Figures 5g–5i show the relative geostrophic currents estimated from the observed hydrography and the thermal wind equation. The strong (up to 20 cm s^{-1}), northward baroclinic current above the slope agrees well with the shear in the observed absolute currents. The baroclinic transport of ISW over the eastern flank of the depression estimated from the geostrophic shear is 0.4, 0.6 and 0.3 Sv at sections 4–6 respectively.

3.2.2. Observations: Sections From 2005 and 2009

Hydrographic sections across the eastern flank of the Filchner Depression have also been occupied in 2005 and 2009 (Figure 7, see Figure 1 for location). They show similar characteristics as the sections discussed above: (A) The depression is filled with ISW up to about 300 m depth, (B) The depth of the shallow isopycnals ($\sigma <$27.85 kg m^{-3}) tilt upward away from the slope while dense isopycnals tilt downward, and (C) MWDW is found at a depth around 350 m in the east and above the ISW, around 250 m depth, in the depression. In addition, the detided LADCP section from 2009, shows an outflow above the 550 m isobath at about 30.9°W.

3.3. Circulation in the Model

Figure 8 shows the modeled mean velocity across three sections: one in the cavity, south of the ice front, one north of the ice front (roughly corresponding to section 3 in ES060) and one perpendicular to the ice

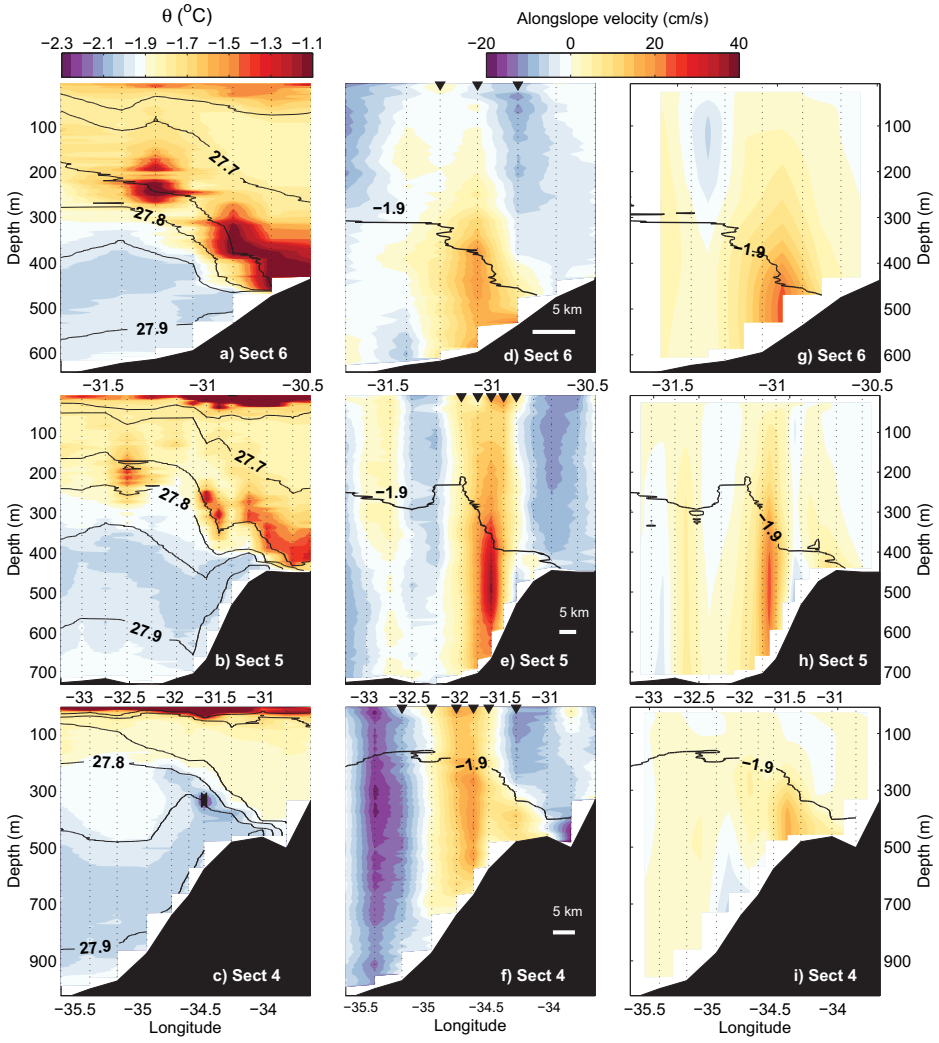

Figure 5. (a–c) Potential temperature (color) and isopycnals (labeled, black lines) referenced to surface pressure, (d–f) along-slope velocity (cm s^{-1}) observed with LADCP in January 2013, and (g–i) Geostrophic shear currents relative to the surface calculated from the observed hydrography. (a, d, g) section 6, (b, e, h) section 5, and (c, f, i) section 4. See Figure 1 for location. Black triangles in Figures 5d–5f mark stations included in ISW transport estimates. The white bar in the lower right corner of Figures 5d–5f is 5 km long. The vertical, dashed lines mark the position of the stations.

front (see inset in Figure 9 for location). Within the cavity at 78.5°S (Figure 8a) approximately 0.9 Sv of ISW flows northward toward the ice front along the eastern side of Berkner Island while there is a weaker 0.3 Sv inflow on the eastern side of the cavity. The core of the northward flow is located between the 27.85 and the 27.90 kg m^3 isopycnal with velocities on the order of 5 cm s^1, while the core of the inflow is slightly denser. North of the ice front (Figure 8b), the core of the northward flow has shifted to the eastern side of the depression, where it is centered between the 27.80 and the 27.85 kg m^3 isopycnal, beneath the southward flowing

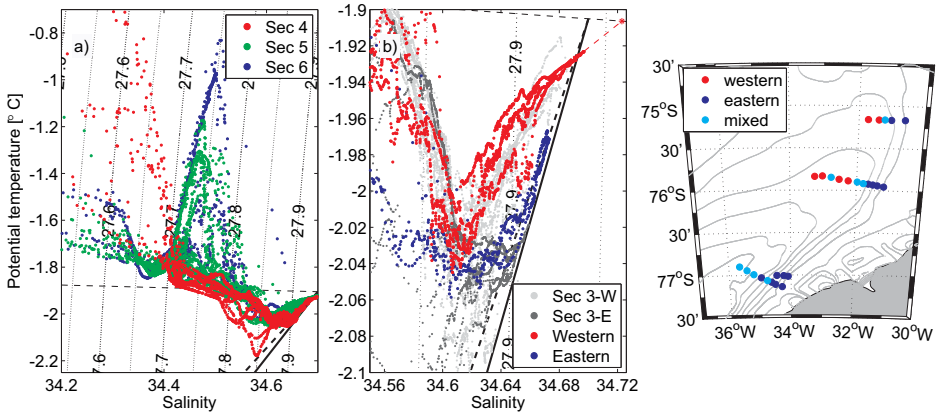

Figure 6. *Θ*/*S*-diagram showing data from (a) the eastern flank of the depression in 2013 (sections 4–6) and (b) 76°S (section 5) and stations from the Filchner Front (section 3). For location of sections, see Figure 1. Note the different scales in Figures 6a and 6b. Dotted, labeled lines are isopycnals referenced to surface pressure, the thin, dashed line is the surface freezing point and thick black lines are Gade lines with a gradient of 2.4 (dashed) and 2.8°C. The red, dashed line shows the extrapolation of the ISW-HSSW mixing line and the red star indicates the inferred properties of the HSSW. (c) Map showing the location of stations in Figure 6a where the color of the dot indicates if the station can be characterized as "eastern," "western," or "mixed" (see text and Figure 6b).

coastal current and over a denser southward undercurrent. Apart from the relatively strong currents in the east, there is a general slow northward motion across the larger part of the depression.

The section normal to the ice front (Figure 8c) shows a relatively narrow zone of high shear separating the westward flowing coastal current from an eastward flowing core of ISW that resides just south of the ice front. By the time the shallower coastal current reaches 39.9°W, its density has been changed significantly through mixing along the length of the ice front and no longer has ESW characteristics. The eastward flow of ISW is located just south of the ice front and extends from the ice shelf base at about 500 m down to 900 m depth.

The transport across the sections shown in Figure 8, divided in density classes, is shown in Figure 9. We note that (A) the density of the northward flowing water has significantly decreased between the two zonal sections (78.5°S and 77.9°S), suggesting intensive mixing at the ice front (B) north of the ice front, the northward transport on the eastern and western side is of roughly equal magnitude (Figure 9b) (C) northward flowing ISW with densities equal to the main northward flow observed in the cavity (27.90 kg m^3, 78.5°S) are observed mainly on the western side of the depression (77.9°S west) suggesting minimal mixing as it crosses this part of the ice front, (D) the fresher and lighter ESW ($<$ 27.77 kg m^3) in the coastal current, which is prominent in eastern part of the section north of the ice front (77.9°S east), has disappeared in the section perpendicular to the ice front (39.9°W) as a result of the intense mixing along the ice front, (E) the deep southward flow has a slightly greater density resulting from the input of HSSW originating from Berkner Bank, and (F) the southward flow at 78.5°S south of the ice front, which does not include any ESW, is roughly two times larger than the southward transport north of the ice front (77.9°S) meaning that about half of the recirculating water remains within a cyclonic gyre that straddles the ice front.

North of the ice front, the middepth outflow of ISW flows northward, gathering into a focused current that occupies the water column from about 300 m to 600 m depth along the eastern flank of the depression until reaching the Filchner Sill. The modeled velocity field agrees well with the mean currents observed at mooring Fr1–2 and explains why, contrary to what was expected from the traditional circulation scheme, no northward flow was observed at Fr2 (Figure 10).

3.4. Potential Vorticity and Ice Front Dynamics

The draft of the ice shelf is about 400–600 m at the ice front [*Lambrecht et al.*, 2007], and compared to the total water depth of up to 1200 m the ice front represents a large step in the thickness of the water column (H) and a discontinuity in the fH^{-1} contours (Figure 11a), suggesting that the ice front constitutes a

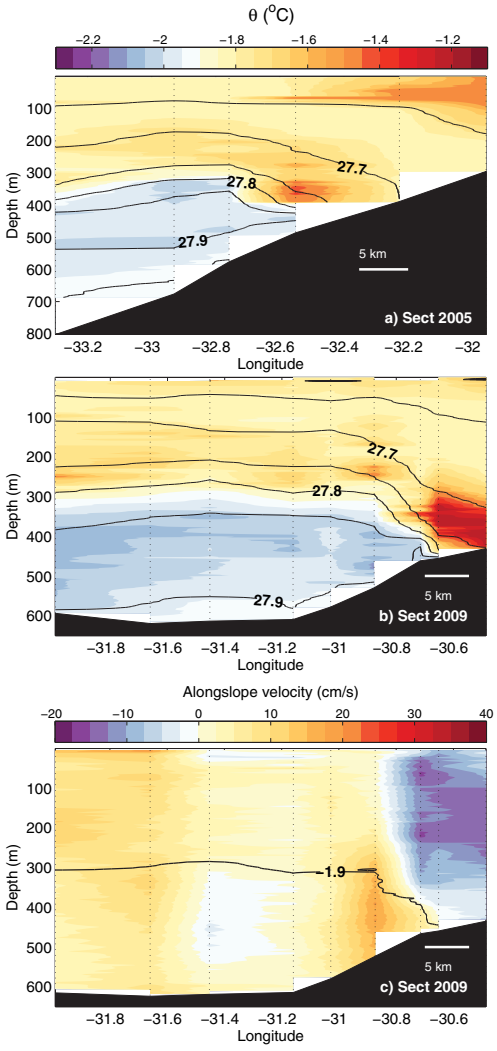

Figure 7. Sections of potential temperature (color) and isopycnals (labeled, black lines) referenced to surface pressure from sections across the eastern flank in (a) 2005 and (b) 2009. (c) Along-slope velocity (cm s^{-1}) observed in 2009. The upper limit of ISW (given as the −1.9°C isotherm) is marked with a thin, black line in Figure 7c. The horizontal white bar in the lower right corner of each subplot is 5 km long.

potential vorticity (PV) barrier. The components of the Ertel potential vorticity [*Pedlosky*, 1986] were calculated using the mean velocity and density fields while neglecting the vertical velocity component. The PV field is dominated by the planetary stretching term, slightly modified at the ice front by the relative vorticity term while the tilting term is negligible. A simpler expression for the PV, $((\rho_2-\rho_1)\rho_0^{-1}fH_\rho^{-1}$, where H_ρ is the thickness of the layer delimited by the ρ_1 and ρ_2 isopycnals) also gives a PV-field similar to that depicted in Figure 11b, which shows the Ertel PV-field at the 27.87 kg m^{-3} isopycnal, which is within the density class with maximum eastward flow at 39.9°W. A region with constant Ertel PV extends along the eastern side of Berkner Island, bifurcating at the ice front with one branch crossing the ice front along the western flank (i.e., no cross ice front gradient in Ertel PV) and the other branch extending eastward, running parallel to the ice front. Along the eastern part of the ice front, where the core of the northward flow is observed, there is a strong cross ice front Ertel PV gradient.

4. Discussion

New, detailed *in situ* observations from the Filchner Depression and results from regional numerical modeling using MICOM suggest a circulation pattern that challenges—or at least complements—previously proposed circulation schemes from the region [*Foldvik and Gammelsrød*, 1988; *Foldvik et al.*, 2001; *Nicholls et al.*, 2001]. A revised circulation pattern is presented in Figure 12. The core of the northward flowing ISW which eventually crosses the Filchner sill and contributes to bottom water formation is found along the *eastern* flank of the depression and not—as previously proposed—along the western flank (Figure 12). Below the outflow, there is a relatively weak cyclonic circulation, as observed by *Carmack and Foster* [1975]. Previous circulation schemes are based on interpretation of very limited data sets in which the relatively narrow current above the eastern flank

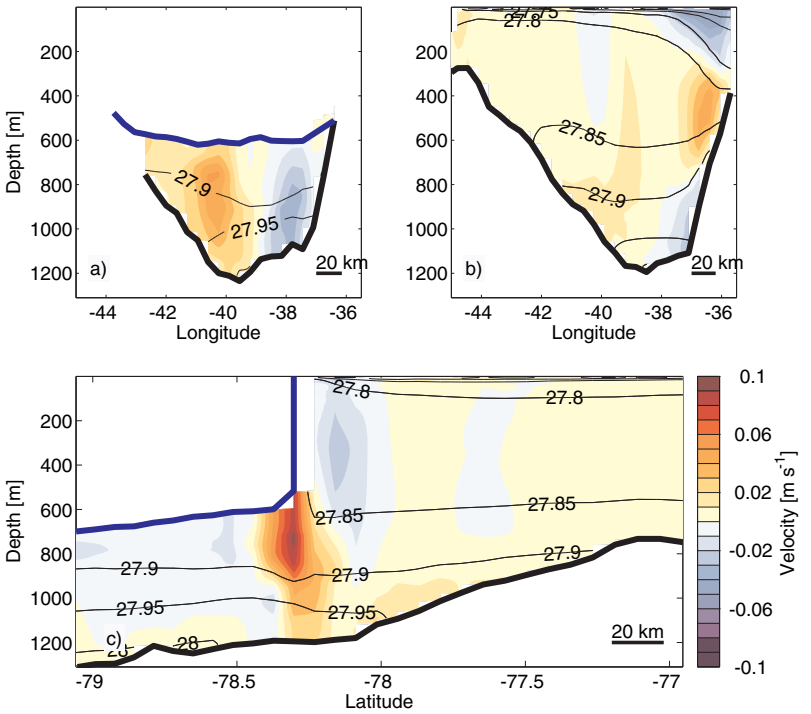

Figure 8. Sections of modeled mean velocity perpendicular to the section at (a) 78.5°S (b) 77.9°S, and (c) 39.9°W. Positive velocities are northward, i.e., in to the paper in Figures 8a and 8b and eastward, i.e., out of the paper in Figure 8c. The position of the sections is shown in the inset in Figure 9. The velocity scale given in Figure 8c is valid for all plots. Labeled, thin, black lines show isopycnals referenced to surface pressure, the thick, black line indicates the bottom and the thick, blue line the draft of the ice shelf. The horizontal, black bar in the lower right corner of each subplot is 20 km long.

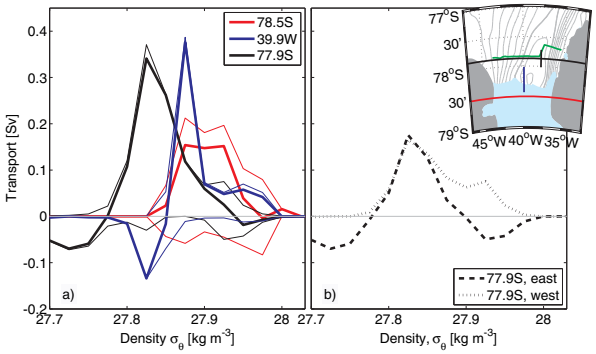

Figure 9. Modeled transport in density classes (a) through sections parallel and perpendicular to the front according to the legend and (b) through the eastern and western part of the section at 77.9°S. Thin lines show total in and outflow and thick lines show net flow. Positive transports are northward for the zonal sections and eastward for the meridional section. The inset in Figure 9b shows the location of the sections, including CTD section 3 from ES060 which is shown in green. The black, vertical line in the middle of section 77.9°S indicates the division between "77.9°S east" and "77.9°S west" shown in Figure 9b.

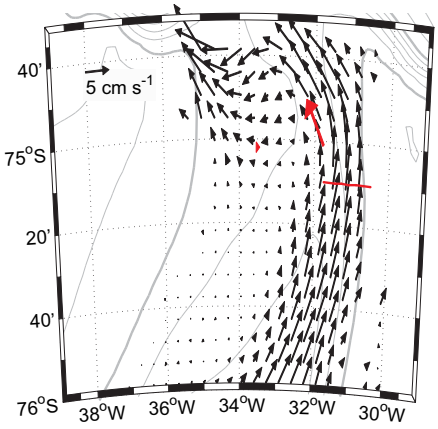

Figure 10. Modeled mean currents at 460 m depth (black lines). The velocity scale is given in the upper left corner. The mean current observed at Fr1 (480 m depth) and Fr2 (450 m depth) [*Foldvik et al.*, 2004] is shown as red arrows and the red line indicates the location of section 6.

was not captured. The revised circulation scheme proposed here results directly from improved station coverage and insight gained from the regional modeling, giving a better understanding of the system, rather than to a change in the physical system itself. The new circulation scheme also agrees well with the existing mooring observations (Fr1–2, Figure 10) and previous hydrographic surveys (Figure 7).

The transport estimates based on the LADCP sections are highly sensitive to the detiding and the uncertainty in the transport estimates are relatively high. Unfortunately, the current data set and the available tidal models do not allow for a better quantification of the transport and current strength. A northward flow along the eastern flank of the depression is however present in all sections from 2013 as well as two sections from 2005 and 2009 and its existence is not compromised by detiding errors. While the difference in transport between sections 4 and 5 is within the error bars, the transport at section 6 near the sill is significantly lower. This might be related to temporal variability, but it is also possible that the section did not capture the entire outflow. As suggested by the modeled currents in Figure 10, the outflow in the vicinity of the sill occurs on both sides of the Depression with comparable magnitude. At the location of section 6 however, the flow in the model is still concentrated on the eastern flank.

The northward flow of ISW is thus occurring on the eastern and not, as previously thought, on the western side of the Depression. This means that the dense water to a higher degree is in contact with lighter ESW, but also with the seasonal inflow of warm MWDW [*Årthun et al.*, 2012] compared to an outflow situated on the western flank of the Depression. The seasonality of the outflow observed at the sill is however not related to the admixture of ESW or MWDW, but to HSSW from the Berkner Bank [*Darelius et al.*, 2014]. While it is beyond the scope of this study, the presence of a northward flow of ISW along the eastern flank is likely to influence the dynamics of the inflow of warm MWDW toward the cavity.

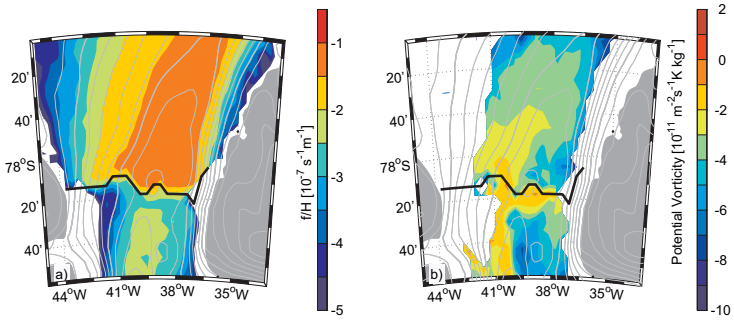

Figure 11. Map showing (a) fH^{-1} contours, where H is the thickness of the water column and (b) mean Ertel potential vorticity at the mean 27.87 kg m^{-3} isopycnal surface. Isobaths are shown every 100 m (gray lines) and the Filchner ice front is indicated in black.

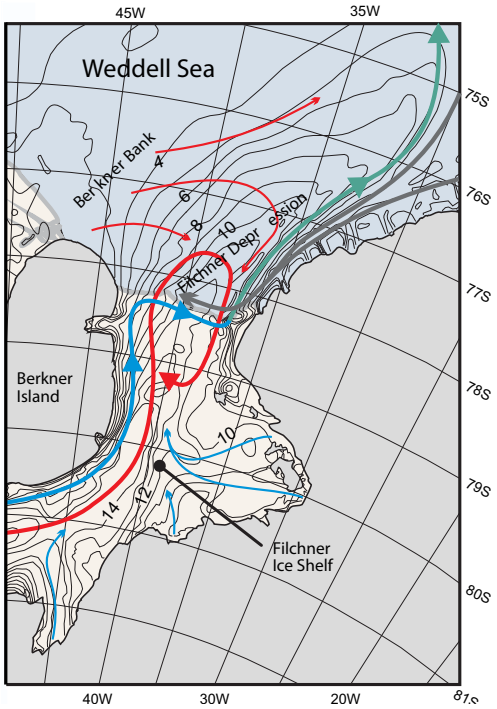

Figure 12. Map showing a schematic of the proposed circulation beneath Filchner Ice Shelf (light gray shading) and within the Filchner Depression. The thick colored arrows beneath the ice shelf show the main circulation originating from the western (red) and eastern (blue) ends of the Ronne Ice Front. The thin colored lines show minor flows of ISW (blue) from deeper ice and HSSW flowing into Filchner Depression from Berkner Bank (red). The coastal currents are shown in dark gray, with main ISW outflow on the eastern flank of Filchner Depression in dark green. Bathymetric contours are labeled in hundreds of meters.

The deep cyclonic circulation can be expected to entrain the HSSW descending into the depression from the Berkner Bank [*Carmack and Foster*, 1975; *Nøst and Østerhus*, 1998] and carry it into the FRIS cavity (as schematically shown by the thin red lines in Figure 12). This is observed in the numerical model. The observations from January 2013 show—much like the observations from 1973—that the bottom salinity north of the ice front (section 4) is higher than the bottom salinity at the ice front, suggesting that a seasonal pulse of HSSW from the Berkner Bank has descended into the Depression but not yet reached the Filchner ice front. The seasonality of the HSSW drainage into the depression is supported by CTD-profiles obtained between 75 and 76°S above the eastern flank of the depression: profiles from February to April 2011 show presence of HSSW while profiles obtained in May–September the same year do not [*Darelius et al*., 2014]. With a length scale of about 200 km and velocities of a few cm s^{-1}, the advective time scale for the flow of HSSW in the Depression would be on the order of 2–7 months. Seasonal pulses of HSSW entering the depression can thus be expected to be "flushed out" before the arrival of next season's HSSW. This is in accordance with the results by *Nøst and Østerhus* [1998] suggesting that the residence time for water in the Filchner Depression is shorter than two years.

Results from the numerical model imply that part of the northward flow of ISW, which follows the western flank of the depression within the cavity, shifts over to the eastern flank while following the Filchner ice front across the depression. The draft of the ice front is about 400–600 m [*Lambrecht et al*., 2007], and compared to a total depth of the depression of about 1000 m, it represents a significant and sudden change in the thickness of the water column. We thus hypothesize—supported by Figure 11—that the behavior of the ISW in the ice front region is governed by vorticity dynamics, and that part of the ISW is unable to cross the step in topography but is forced to follow the ice front eastward. The situation is to a large extent analogue (but up-side down) to a coastal current encountering a sudden change in bathymetry—an escarpment—upon which it bifurcates in two branches, one leaves the coast to flow parallel to the escarpment and the other continues along the coast [see e.g., *Carnevale et al*., 1999; *Cenedese*, 2005]. The ice front has previously been suggested to act as a PV-barrier to HSSW inflow [see e.g., *Grosfeld et al*., 1997]. A region of constant Ertel PV (Figure 11b) extends northward along the eastern side of Berkner Island and divides in two: one part continuing northward along the western flank of the depression, one part flowing eastward

parallel to the ice front. It was shown in Figure 9 that water leaving the ice shelf cavity along the eastern flank of the depression is exposed to intensive mixing at the ice front (since the density of the northward flow north of the ice front is reduced compared to the flow within the cavity) and the Ertel PV signal is lost. The absence of a continuous Ertel PV-field across the ice front does not mean that water is not crossing the ice front. On the western side of the depression Ertel PV-contours cross the ice front, and the model results show northward flow of unmodified cavity water (i.e., water north of the ice front has similar density and Ertel PV as water within the cavity).

The observations suggest that the depression in 2013 was filled with ISW having variable source salinities and Figure 3 suggests even larger variability in source salinity on interannual timescales. For example, the very cold ISW observed at the ice front in 2011—which suggests source salinities of 34.75 – is not seen in 2013, when source salinities are lower (34.68−34.7) and temperatures higher. The large differences between 2011 and 2013 support the finding by *Nøst and Østerhus* [1998] that the residence time of the ISW in the Filchner Depression is shorter than two years. Differences in source salinities can be due to either (A) spatially variable sources, i.e., a shift from source water originating from Berkner Bank to water originating from the Ronne Depression and/or (B) temporal variability of source waters from one location, due either to seasonal or interannual changes in ice production and preconditioning. It seems likely that the small variability observed between and at stations in 2013 is due to (B), especially when taking into account that the ISW emanates from several different deep, high melt, locations (and thus different paths and residence times) of melt below FRIS [*Holland et al*., 2007; *Makinson et al*., 2011] while the larger interannual variability e.g., between 2011 and 2013 would be caused by (A). CTD-profiles obtained through access holes drilled southwest of Berkner Island (Site 5, see large inset in Figure 1) in 1999 [*Nicholls et al*., 2001] show a two layered structure with high (34.77) source salinity ISW at the bottom and lower source salinity (S=34.66) water at the top. The high source salinity water originates from the Ronne Depression [*Nicholls et al*., 2001] and corresponds to the ISW found in the Filchner Depression in 1977, 1993, and 2011 while the low salinity source water originates from the Berkner Bank and corresponds more closely to the ISW filling the depression, e.g., in 2013 and partly in 1995. Interestingly, the two stations occupied at the western side of the ice front in 1995 show Ronne source water, while the two western stations are dominated by ISW originating at the Berkner Bank [*Grosfeld et al*., 2001] suggesting an ongoing transition from Ronne source water, which dominated the water column in 1993, to Berkner source water, which dominated the Filchner outflow in 1998 [*Nicholls et al*., 2001]. The changes observed in the Filchner Depression suggest a reorganization of the circulation beneath FRIS, which is likely to be linked to atmospheric forcing as proposed e.g., by *Timmermann et al*. [2002], but its origin and the mechanisms involved is beyond the scope of this study. Changes in the circulation beneath FRIS can be expected to influence the circulation in the depression, and consequently the volume flux and properties of the Filchner overflow and the bottom waters generated.

Appendix A: Detiding of LADCP Velocity Profiles

Tidal currents in the Filchner region are relatively strong (10–15 cm s^{-1}) and transport estimates based on LADCP velocity profiles are highly sensitive to errors in detiding. Attempts were made to detide the LADCP profiles using (1) the tidal model results from the CATS2008b (an update to the circum-Antarctic inverse barotropic tidal model described by *Padman et al*. [2002]) and (2) harmonic fits to the depth-integrated

Table A1. Northward Transport of ISW Across Sections 4–6 Calculated Using Different Detiding Procedures

		ISW flux (Sv)		
	Detiding	Section 4	Section 5	Section 6
1	CATS2008b	0.9	1.0	0.3
2a	Time series[a]		0.7	
2b	Time series + Section, excluding stations with strong currents[b]		0.9	
2c	Time series + Section, excluding stations with very strong currents[b]		0.6	
2d	Section, excluding stations with strong currents[c]	0.7		0.3
2e	Section, excluding stations with very strong currents[c]	0.3		0.2

[a]Including constituents M2, M4, S2.
[b]Including constituents M2/S2/M4/K1/O1.
[c]Including constituents M2.

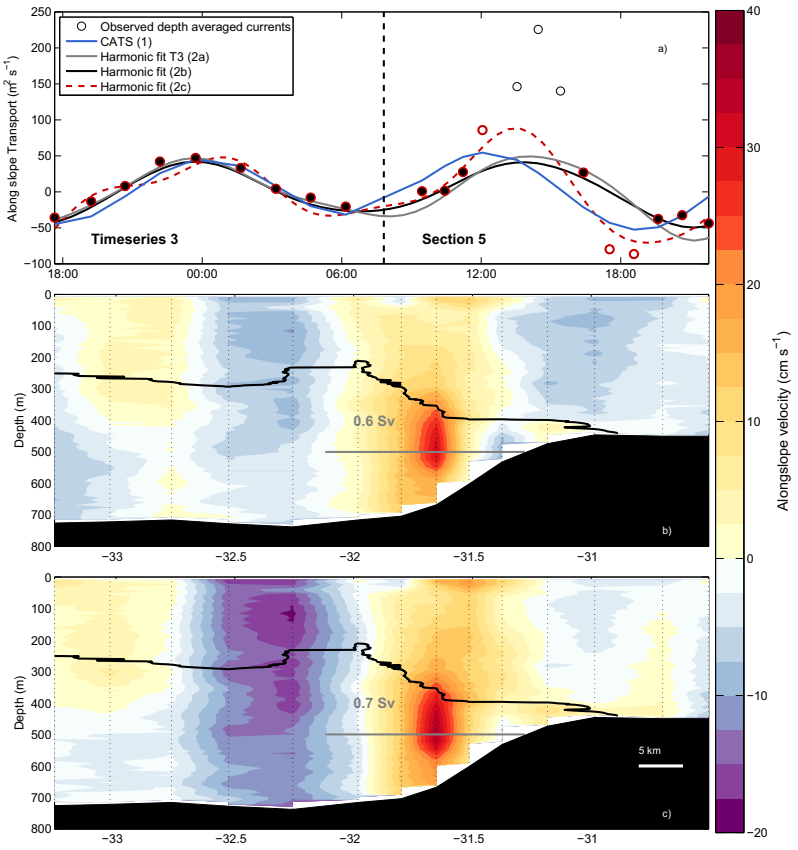

Figure A1. (a) Observed, depth integrated along-slope current (circles; stations included in 2b are colored black, stations included in 2c have red border) from time series 3 and section 5 (see Figure 1 for location) and tidal predictions from tidal model (blue line) and harmonic fits to stations from T3 (2a: gray line) and section 5 + T3 (2b: black line, 2c dashed red line). The dashed black line marks the end of T3. Observed along-slope current at section 5 detided using harmonic fit Figure A1b) 2a (gray line in Figures A1a and A1c) 2c (dashed red line in Figure A1a). The gray lines in Figure A1b and A1c marks the stations included in the transport estimate and the number gives the along slope transport of ISW. The horizontal white bar in the lower right corner of Figures A1b and A1c is 5 km long and the black line is the −1.9°C isotherm.

observed fluxes. Observations from the upper and lower 150 m of the profiles were neglected to remove boundary layer effects, as were stations with strong currents above the slope. Harmonic analysis were carried out including stations from time series and/or sections (see Table A1). Figure A1 shows the observed depth integrated fluxes and tidal predictions from TS3 and section 5, which were occupied consecutively, and two examples of detided currents.

In general, predictions from the tidal model (CATS2008b) agree well with the time series, especially for TS 1 and 3 where the rms error is <1.5 cm s^{-1}. However, when predictions from the tidal model were applied to the sections, or when the harmonic fits derived from the time series are extrapolated and used to detide a nearby section, the residual depth integrated currents are relatively strong (up to 10 cm s^{-1}) above the slope and in the deeper part of the depression. The currents are in phase with the tides, suggesting that tidal currents here are stronger than predicted by the model. When combining stations from the time series and the nearby section in harmonic analysis, the tidal predictions for the time series appear less good

(Figure A1a). The occupation of sections 4 and 5 are "in phase" with each other: it took roughly 12 h to occupy the sections (Table 1) and tidal currents were directed northward above the slope and southward in the deeper part of the depression during the occupation of both sections.

Estimates of northward transport across sections 4–6 were calculated as outlined in section 2 using the different detiding procedures and the results are presented in Table A1. Transport estimates in section 3 are given as an interval using the lower and upper transport estimate from Table A1. Figures presented in section 3 are detided using the tidal model.

Acknowledgments

The authors are grateful to A. Wåhlin and Göteborg University, Sweden for kindly providing CTD, Rosette and sensors, to T. Aspen, M. Reigstad and J. T. Eiliertsen at University of Tromsø, Norway for kindly providing the CTD-winch during cruise ES060 in 2013 and to C. Chavanne for sharing his Matlab routines for tidal calculations. Assistance during cruise ES060 from the crew of RRS Ernest Shackleton, H. Bryhni, K. Vaage and M. Jensen was much appreciated. This work was carried out under the project WEDDELL with funding from the Norwegian Research Council, and the study is also part of the British Antarctic Survey Polar Science for Planet Earth Programme funded by The Natural Environment Research Council. Data availability: Model results, data from cruise ES060 and older data from Norwegian cruises are available from the authors upon request while data from cruise ES033, JR97 and JR244 are available at www.bodc.ac.uk and observations from 1973 at www.nodc.noaa.gov/OC5/WOD13.

References

Årthun, M., K. W. Nicholls, K. Makinson, M. A. Fedak and L. Boehme (2012), Seasonal inflow of warm water onto the southern Weddell Sea continental shelf, Antarctica, *Geophys. Res. Lett.*, *39*, L17601, doi:10.1029/2012GL052856.

Årthun, M., K. W. Nicholls, and L. Boehme (2013), Wintertime water mass modification near an Antarctic Ice Front, *J. Phys. Oceanogr.*, *43*(2), 359–365, doi:10.1175/JPO-D-12-0186.1.

Bleck, R., C. Rooth, D. Hu, and L. T. Smith (1992), Salinity-driven thermocline transients in a wind-and thermohaline-forced isopycnic coordinate model of the North Atlantic, *J. Phys. Oceanogr.*, *22*, 1486–1505, doi:10.1175/1520-0485(1992)022¡1486:SDTTIA2.0.CO;2.

Carmack, E. C., and T. D. Foster (1975), Circulation and distribution of oceanographic properties near the Filchner Ice Shelf, *Deep Sea Res. Oceanogr. Abstr.*, *22*(2), 77–90, doi:10.1016/0011-7471(75)90097-2.

Carnevale, G., S. G. L. Smith, F. Crisciani, R. Purini, and R. Serravall (1999), Bifurcation of a coastal current at an escarpment, *J. Phys. Oceanogr.*, *29*, 969–985.

Cenedese, A. (2005), Effects of a topographic gradient on coastal current dynamics, *J. Geophys. Res.*, *110*, C09009, doi:10.1029/2004JC002632.

Darelius, E., and A. Wåhlin (2007), Downward flow of dense water leaning on a submarine ridge, *Deep Sea Res., Part I*, *54*(7), 1173–1188, doi:10.1016/j.dsr.2007.04.007.

Darelius, E., K. O. Strand, S. Østerhus, T. Gammelsrød, M. Årthun and I. Fer (2014), On the seasonal signal of the Filchner Overflow, Weddell Sea, Antarctica, *J. Phys. Oceanogr.*, *44*, 1230–1243, doi:10.1175/JPO-D-13-0180.1.

Fer, I., K. Makinson, and K. W. Nicholls (2012), Observations of thermohaline convection adjacent to Brunt Ice Shelf, *J. Phys. Oceanogr.*, *42*(3), 502–508, doi:10.1175/JPO-D-11-0211.1.

Foldvik, A., and T. Gammelsrød (1988), Notes on Southern Ocean hydrography, sea-ice and bottom water formation, *Palaeogeogr. Palaeoclimatol. Palaeoecol.*, *67*, 3–17.

Foldvik, A., T. Gammelsrød, and T. Tørresen (1985a), Hydrographic observations from the Weddell Sea during the Norwegian Antarctic research expedition 1976/77, *Polar Res.*, *3*, 177–193.

Foldvik, A., T. Gammelsrød, and T. Tørresen (1985b), Circulation and water masses on the southern Weddell Sea shelf, in *Oceanology of the Antarctic Continental Shelf, Antarct. Res. Ser.*, vol. 43, edited by S. S. Jacobs, pp. 5–20, AGU, Washington, D. C.

Foldvik, A., T. Gammelsrød, and T. Tørresen (1985c), Oceanographic conditions on the Weddell Sea shelf during the German Antarctic Expedition 1979/80, *Polar Res.*, *3*, 195–207.

Foldvik, A., T. Gammelsrød, E. Nygaard, and S. Østerhus (2001), Current measurements near Ronne Ice Shelf: Implications for circulation and melting, *J. Geophys. Res.*, *106*(C3), 4463–4477, doi:10.1029/2000JC000217.

Foldvik, A., T. Gammelsrød, S. Østerhus, E. Fahrbach, G. Rohardt, M. Schröder, K. W. Nicholls, L. Padman and R. A. Woodgate (2004), Ice shelf water overflow and bottom water formation in the southern Weddell Sea, *J. Geophys. Res.*, *109*, C02015, doi:10.1029/2003JC002008.

Foster, T. D., and E. C. Carmack (1976), Frontal zone mixing and Antarctic Bottom Water formation in the Southern Weddell Sea, *Deep Sea Res. Oceanogr. Abstr.*, *23*, 301–317.

Fretwell, P., et al. (2013), Bedmap2: Improved ice bed, surface and thickness datasets for Antarctica, *Cryosphere*, *7*(1), 375–393, doi:10.5194/tc-7-375-2013.

Gade, H. (1979), Melting of ice in sea water: A primitive model with application to the Antarctic ice shelf and icebergs, *J. Phys. Oceanogr.*, *9*(1), 189–198.

Gammelsrød, T., A. Foldvik, O. A. Nøst, Ø. Skagseth, L. Anderson, E. Fogelqvist, K. Olsson, T. Tanhua, E. Jones, and S. Østerhus (1994), Distribution of water masses on the continental shelf in the southern Weddell Sea, in *The Polar Oceans and Their Role in Shaping the Global Environment, Geophys. Monogr. Ser.*, vol. 85, edited by O. M. Johannessen, R. D. Muench, and J. E. Overland, pp. 159–176, AGU, Washington, D. C.

Grosfeld, K., R. Gerdes, and J. Determann (1997), Thermohaline circulation and interaction between ice shelf cavities and the adjacent open ocean, *J. Geophys. Res.*, *102*(C7), 15,595–15,610, doi:10.1029/97JC00891.

Grosfeld, K., M. Schröder, E. Fahrbach, R. Gerdes, and A. Mackensen (2001), How iceberg calving and grounding change the circulation and hydrography in the Filchner Ice Shelf-Ocean system, *J. Geophys. Res.*, *106*(C5), 9039–9055.

Hellmer, H. H., F. Kauker, R. Timmermann, J. Determann, and J. Rae (2012), Twenty-first-century warming of a large Antarctic ice-shelf cavity by a redirected coastal current., *Nature*, *485*(7397), 225–228, doi:10.1038/nature11064.

Holland, D., and A. Jenkins (2001), Adaptation of an isopycnic coordinate ocean model for the study of circulation beneath ice shelves, *Mon. Weather Rev.*, *129*, 1905–1927.

Holland, P. R., D. L. Feltham, and A. Jenkins (2007), Ice Shelf Water plume flow beneath Filchner-Ronne Ice Shelf, Antarctica, *J. Geophys. Res.*, *112*, C05044, doi:10.1029/2006JC003915.

Jenkins, A. (1999), The impact of melting ice on ocean waters, *J. Phys. Oceanogr.*, *29*(3), 2370–2381.

Jenkins, A., D. M. Holland, K. W. Nicholls, M. Schröder, and S. Østerhus (2004), Seasonal ventilation of the cavity beneath Filchner-Ronne Ice Shelf simulated with an isopycnic coordinate ocean model, *J. Geophys. Res.*, *109*, C01024, doi:10.1029/2001JC001086.

Lambrecht, A., H. Sandhäger, D. G. Vaughan, C. Mayer (2007), New ice thickness maps of FilchnerRonne Ice Shelf, Antarctica, with specific focus on grounding lines and marine ice, *Antarct. Sci.*, *19*, 521–532, doi:10.1017/S0954102007000661.

Larter, R. D. (2011), Cruise report RRS James Clark Ross JR244, Marine geoscience and physical oceanography, southern Weddell Sea and South Orkney continental shelf, January-March 2011, technical report number JR244, British Antarctic Survey, Cambridge, U. K.

Makinson, K., P. R. Holland, A. Jenkins, K. W. Nicholls, and D. M. Holland (2011), Influence of tides on melting and freezing beneath Filchner-Ronne Ice Shelf, Antarctica, *Geophys. Res. Lett.*, *38*, L06601, doi:10.1029/2010GL046462.

McDougall, T. J., and P. M. Barker (2011), *Getting Started With TEOS-10 and the Gibbs Seawater (GSW) Oceanographic Toolbox*, 28pp., SCOR/IAPSO WG127, S-10.org.

Nicholls, K., S. Østerhus, K. Makinson and M. Johnson (2001), Oceanographic conditions south of Berkner Island, beneath FilchnerRonne Ice Shelf, Antarctica, *J. Geophys. Res.*, *106*(C6), 11,481–11,492.

Nicholls, K. W. (2009), Cruise report RRS Ernest Shackleton ES033, Second ACES-FOCAS cruise to the southern Weddell Sea 22 January-7 March 2009, technical report, ES033, Br. Antarct. Surv., Cambridge.

Nicholls, K. W., and S. Østerhus (2004), Interannual variability and ventilation timescales in the ocean cavity beneath Filchner-Ronne Ice Shelf, Antarctica, *J. Geophys. Res.*, *109*, C04014, doi:10.1029/2003JC002149.

Nicholls, K. W., S. Østerhus, K. Makinson, T. Gammelsrød and E. Fahrbach (2009), Ice-ocean processes over the continental shelf of the southern Weddell Sea, Antarctica: A review, *Rev. Geophys.*, *47*, RG3003, doi:10.1029/2007RG000250.

Nøst, O. A. and S. Østerhus (1998), Impact of grounded icebergs on the hydrographic conditions near the Filchner Ice Shelf, in *Ocean, Ice, and Atmosphere—Interaction at the Antarctic Continental Margin*, vol. 75, edited by S. S. Jacobs and R. Weiss, pp. 267–284, AGU, Washington, D. C.

Orsi, A. H. H., G. C. Johnson, and J. L. Bullister (1999), Circulation, mixing, and production of Antarctic Bottom Water, *Prog. Oceanogr.*, *43*(1), 55–109, doi:10.1016/S0079-6611(99)00004-X.

Padman, L., A. Fricker, R. Coleman, S. Howard, and S. Erofeeva (2002), A new tidal model for the Antarctic ice shelves and seas, *Ann. Glaciol.*, *34*, 247–254, doi:10.3189/172756402781817752.

Pedlosky, J. (1986), *Geophysical Fluid Dynamics*, 2nd ed., 710 pp., Springer, N. Y. and Berlin.

Rignot, E., S. Jacobs, J. Mouginot, and B. Scheuchl (2013), Ice-shelf melting around Antarctica, *Science*, *341*(6143), 266–70, doi:10.1126/science.1235798.

Timmermann, R., H. H. Hellmer, and A. Beckmann (2002), Simulations of ice-ocean dynamics in the Weddell Sea 2. Interannual variability 1985–1993, *J. Geophys. Res.*, *107*(C3), 3025, doi:10.1029/2000JC000742.

Visbeck, M. (2002), Deep velocity profiling using lowered acoustic Doppler current profilers: Bottom track and inverse solutions*, *J. Atmos. Oceanic Technol.*, *19*, 794–807.

Paper III

Wind stress mediated variability of the Filchner Trough overflow, Weddell Sea

K. Daae, E. Darelius, I. Fer, S. Ryan, and S. Østerhus

J. Geophys. Res. Oceans, (Accepted, March 2018)

Wind stress mediated variability of the Filchner Trough overflow, Weddell Sea

K. Daae,[1] E. Darelius,[1] I. Fer,[1] S. Østerhus,[2] S. Ryan,[3]

[1]Geophysical Institute, University of Bergen and Bjerknes Centre for Climate Research, Bergen, Norway

[2]Uni Research Climate, and Bjerknes Centre for Climate Research, Bergen, Norway

[3]Alfred Wegener Institute, Helmholtz Centre for Polar and Marine Research, Bremerhaven, Germany

Key Points:

- Ice Shelf Water overflow is related to wind variability along the continental slope upstream of Filchner Trough
- Monthly scale variability in the slope current and Antarctic Coastal Current is strongly linked to the along-slope wind variability

Corresponding author: K. Daae, kjersti.daae@uib.no

Abstract

The Filchner Trough (FT) is a key site for exchange of water masses between the Weddell Sea continental shelf and the deep ocean. Cold and dense Ice Shelf Water (ISW), a precursor for Antarctic Bottom Water, flows north along the FT and overflows the Filchner Sill. Although access of warm water to the Weddell Sea continental shelf is limited due to the presence of the Antarctic Slope Front, southward transport of warm water is facilitated through the FT. We use moored current meters from the Filchner Sill region to show that the monthly scale variability of the ISW overflow is connected to the variability of the along-slope wind stress upstream. Periods with significant correlation between the wind and ISW overflow are characterized by (I) wind directed along the continental slope, (II) high ISW overflow speed, and (III) high variability in the 16-64 day period band for wind and current. We propose that a recirculation of the slope current, associated with the Antarctic Slope Front, may occur in the FT during periods of strong wind-forcing, and that such recirculation could explain the correlation between the wind stress and the ISW overflow. We further show that an increased wind stress along the continental slope leads to an increased current speed within the slope current and the Antarctic Coastal Current, with possible implications for the on-shore heat transport.

1 Introduction

The southeastern Weddell Sea is a site of climatic importance, where exchanges of water masses between the shallow continental shelf and the deep ocean occur. In deeper layers, cold and dense Ice Shelf Water (ISW), formed through interaction between High Salinity Shelf Water (HSSW) and the Filchner-Ronne Ice Shelf cavity, exits the Filchner Trough (FT, map in Figure 1) and contributes to the formation of Antarctic Bottom Water [*Foldvik et al.*, 2004; *Darelius et al.*, 2009], which is an important driver of the global thermohaline overturning circulation. In the upper layers, Warm Deep Water (WDW), a slightly cooler and fresher derivative of the Circumpolar Deep Water [*Heywood et al.*, 1998], enters the shelf and may contribute to increasing the mass loss of the floating ice shelves through basal melting [*Hellmer et al.*, 2012]. At present climate, the water temperature on the Weddell Sea shelf is low (near freezing point) and the ice shelf melt rates are low compared to e.g., the Amundsen Sea [*Pritchard et al.*, 2012; *Rignot et al.*, 2013].

The access of WDW onto the shelf is limited by the Antarctic Slope Front (ASF), which separates the WDW from the cold and fresh Eastern Surface Water [*Gill*, 1973; *Jacobs*, 1991].The ASF is largely wind-driven. The slope current, associated with the ASF, carries WDW westward along the continental slope. On interannual time scales, the variability of the slope current is connected to the wind-driven Weddell gyre [*Gordon et al.*, 2010], and on seasonal time scales the slope current corresponds well with easterly wind along the continental slope [*Fahrbach et al.*, 1992; *Graham et al.*, 2013]. Maximum slope current transport is found during austral winter (May to July) when the wind forcing is strong and the slope current is barotropic [*Núñez-Riboni and Fahrbach*, 2009].

Modified Warm Deep Water (MWDW, $\theta > -1.7°C$), a slightly cooled version of WDW, crosses the shelf break and enters the continental shelf seasonally (January to May) [*Årthun et al.*, 2012; *Ryan et al.*, 2017], when weaker wind forcing allows for a shoaling of the thermocline. Recent observations near the Filchner Ice Shelf (FIS) front [*Darelius et al.*, 2016] show that when WDW is present on the shelf, strong wind from northeast can advect this water mass southward toward the FIS front. Furthermore, numerical modeling results [*Hellmer et al.*, 2012; *Timmermann and Hellmer*, 2013; *Hellmer et al.*, 2017] predict that the slope current carrying warm water could be redirected southward, in the near future.

The cross-shelf FT plays a key role in facilitating the transport of MWDW toward the FIS. Warm water ($\theta > -1.9°C$), with a core at 400 m depth, is observed along the eastern flank of the FT in several hydrographic surveys [*Carmack and Foster*, 1977; *Foldvik et al.*, 1985a; *Årthun et al.*, 2012; *Darelius et al.*, 2014a; *Ryan et al.*, 2017]. Interactions between a shelf break jet and a cross-shelf trough depend on the trough geometry, stratification, and the strength and direction of the flow [*Williams et al.*, 2001; *Klinck*, 1996; *Allen and Durrieu de Madron*, 2009; *Zhang et al.*, 2011]. Results from an idealized numerical model, showed that the inflow of warm water in the FT strongly depends on the wind forcing, due to associated changes in the slope current [*Daae et al.*, 2017]. A sketch of the slope current based on the idealized model results for weak and strong wind forcing is given in Figure 2. During weak winds, the slope current crosses the FT opening, and the water exchange between the slope and the FT is dominated by eddies. During strong winds, a shoreward, wind-driven branch of the slope current is steered south into the FT, bringing warm water into the region. Due to potential vorticity constraints near the southern sill edge (where the FT is getting deeper), the current recirculates and exits the FT toward the west.

Here, we explore the connections between wind and current circulation associated with the ISW overflow and the ASF processes in the southeastern Weddell Sea on a monthly time scale. We use several year-long current records from moored instruments on the continental slope and shelf region, as well as from the FT (Figure 1).

We present new findings of a high correlation between the ISW overflow from FT and the along-slope wind upstream. We propose a mechanism that could explain such high correlation. If the wind-forced slope current recirculates at the mouth of the FT, as suggested by the idealized model results [*Daae et al.*, 2017] (Figure 2), interactions between the slope current and the ISW overflow could increase the overflow speed. Although the existing data set is insufficient to prove the mechanism, we present measurements at different locations which are consistent with the proposed recirculation of the slope current.

2 Data and Methods

2.1 Atmospheric data

Atmospheric data are obtained from the ERA-Interim reanalysis data set with 0.75° resolution [*Dee et al.*, 2011] (named ERA hereafter). The ERA data set has a time resolution of 6 hours, and is available from 1979 to present. We extract ERA wind velocity at 10 meter above sea level (mabsl). Wind stress is calculated following the procedure by *Andreas et al.* [2010], where the drag coefficient is a function of the Sea Ice Concentration (SIC). We use the SIC available in ERA to be consistent with the data set and grid for wind velocity. The coordinate system for wind stress is rotated, with the along-flow component directed toward 245°, roughly along the continental slope. Hereafter, this wind direction is referred the as the along-slope wind.

At monthly time scales, the pressure system governing the winds over the Weddell Sea is larger than our study region, yielding a similar wind pattern in the FT and over the continental slope. To illustrate this, a video of 15 days low-passed mean sea level pressure and wind vectors from 1995 is included in SI. We expect that the wind driven slope current variability affects the on-shelf transport of water, and possibly the recirculation in the FT. Thus, we compare observed current speed to mean along-slope wind stress from an area over the continental slope, upstream of the FT, from 10-30°W and 69-75°S, limited by the 3500 m isobath and the coastline (indicated by the red line in Figure 1). We refer to this region as

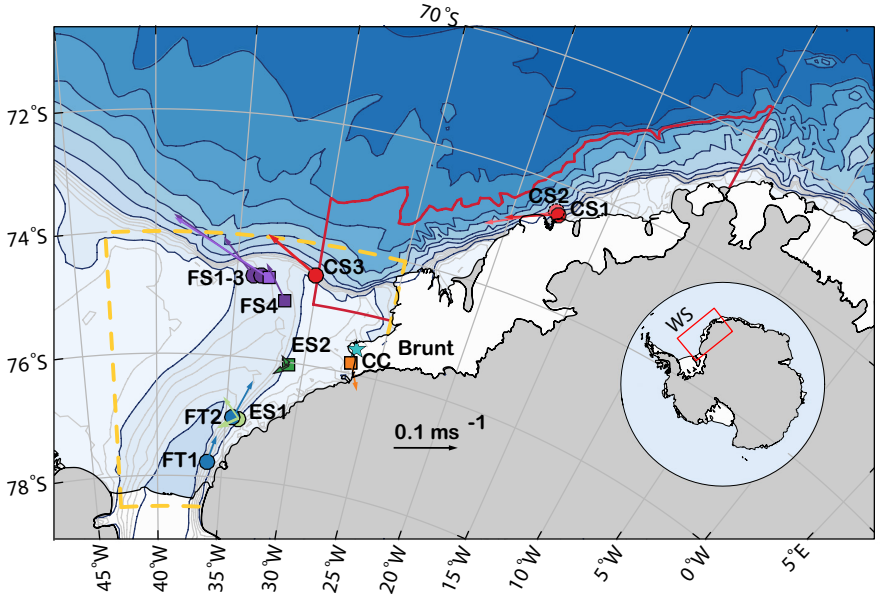

Figure 1. Map showing the Southeastern Weddell Sea (WS) bathymetry and the mooring locations. Color coding and mooring names refer to Continental Slope (CS, red), Coastal Current (CC, orange), Eastern Shelf (ES, green), Filchner Trough (FT, blue) and Filchner Sill (FS, purple). Squares indicate mooring records of two to three years duration, while circles indicate year-long records. Colored arrows from each mooring location show vector mean currents. At FS1 and FS2 we show mean currents from 1977/2010, respectively. At ES1-2 the current direction changes seasonally, and we show two vectors, representing mean currents during inflow and cross-flow periods. The star on the Brunt Ice Shelf shows the location of the Halley Research Station. ERA upstream Wind and SIC are extracted from the region bounded by the red line and the coast. Additional SIC is extracted from the Filchner region delineated by the yellow dashed line.

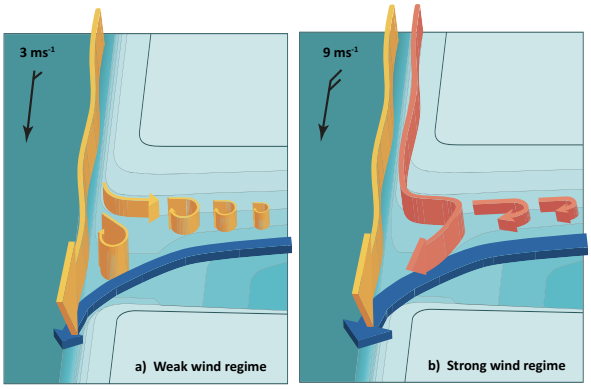

94 **Figure 2.** Sketch of the circulation over the Filchner Sill from idealized numerical simulations [*Daae et al.*,
95 2017] (a) with weak wind along the slope, and (b) with strong wind along the slope. The continuous yellow
96 arrows indicate the background slope current. During weak wind, the slope current flows across the FT open-
97 ing, and eddies carrying moderately warm water (-1 to -1.5°C) enter the FT on its eastern flank. In the strong
98 wind regime, a wind-driven slope current (red arrow) adds to the background current. We refer to this current
99 as the Recirculating Slope Current (RSC). RSC circulates over the Filchner sill region, and leaves the Sill
100 along with the dense Filchner overflow (blue arrow).

the upstream region hereafter. Maps of correlation between along-flow current speed and wind speed (not shown), showed highest correlation for the continental slope region upstream along 245°, and support our choice of area and direction of wind stress used in further analysis.

The first current record from the Filchner Sill is from 1977, when neither ERA data nor SIC is available. To include this data set in our analysis, we instead compare the current speed with observed alongslope (245°) wind speed from the Halley Research station [*British Antarctic Survey*, 2013], located on the Brunt Ice Shelf (star in Figure 1). 15 day low-passed along-slope wind speed from ERA (upstream region) and Halley agree well ($R = 0.82$, above the 99% confidence limit, see section 2.4 for description of low-pass filtering and correlation analysis). For current records where ERA is available, correlations between the current speed and the ERA wind stress/Halley wind speed are similar.

There is a bias in the ERA and Halley time series. Low-passed, along-flow mean wind speed from Halley and ERA (1979 to 2017) are 3.3 and 1.9 m s^{-1}, respectively. However, we focus on the variability of the wind, and the difference in mean wind speed should not impact the results. To facilitate comparison of results from moorings on the Filchner Sill, all figures from these locations show results for both Halley wind speed and ERA wind stress.

Correlation between current speed and wind from Halley is performed using wind speed, and not wind stress, since SIC is not available for all record years. From ERA data, correlations with current speed were similar using either wind speed or wind stress. We therefore assume that correlation values obtained using the Halley wind speed is representative for wind stress.

The sampling interval for Halley data was 3 hours prior to 1986, and then increased to 1 hour. Short periods of missing data are linearly interpolated prior to frequency analysis and low-pass filtering.

2.2 Sea Ice Concentration

Time series of SIC from 1978 to 2017 are extracted from the National Snow and Ice Data Center, *Cavalieri et al.* [1996]. The data set is a satellite product generated from brightness temperature on a 25 km × 25 km grid. While SIC from ERA is based on different datasets of sea surface temperature prior to 2009 [*Dee et al.*, 2011], the NSIDC SIC product is con-

sistent throughout the time series. We calculate daily (every two days prior to July 1987) mean SIC for the upstream area (same as for ERA wind), as well as for the Filchner region (marked by red/yellow in Figure 1, respectively). Mean summer SIC is calculated for the period Dec-Feb every year. The year 1988 is left out of the summer mean calculation due to missing SIC data in December 1987 and January 1988.

2.3 Moored Instruments

We analyze current records of one to three years duration from 14 moored instruments in the southern Weddell Sea (Figure 1). To facilitate the reading and the discussion of the moorings, we rename the moorings according to their locations: the Continental Slope (CS), the Coastal Current inflow (CC), the shelf area east of FT (ES), the Filchner Trough (FT), and the Filchner Sill (FS). An overview of the current records and measurement depth used in this document is given in Table 1. Mooring names used in earlier publications are given in brackets. A complete table of the moorings with available depths and instrument types is given in the SI.

The coordinate system at each mooring is rotated to the main flow direction, calculated from vector averaged currents (see Table 1). For moorings where the current changes seasonally (ES1-2 and FT1-2), we rotate the coordinates according to the bathymetry, roughly correspond to NE direction. The current along this direction is referred to as outflow. The defined along-flow direction at each current meter, is given in Table 1.

At the Filchner Sill, mooring records are available from three locations. The earliest record is from 1977 at FS1 and the latest record covers 2014 to 2016 at FS3. We omit three mooring records in this study. At FS1, we omit the 1987 record, since a large, stranded iceberg caused circulation changes of HSSW in the Filchner region [*Nøst and Østerhus*, 1998; *Grosfeld et al.*, 2001; *Darelius et al.*, 2014b]. At FS2, we omit current records from 2009, where the data set is incomplete, and from 2014, where the current meter is higher up in the water column compared to the other FS moorings. The mooring FS4 is located just south of the Filchner Sill (see map in Figure 1), but is included in the FS group.

Potential densities (σ_Θ) on the continental slope are calculated according to TEOS-10 [*IOC et al.*, 2010], using Absolute Salinity, and Conservative Temperature. Otherwise, we use potential temperatures referenced to surface (θ), since joint salinity measurements

required to calculate Conservative Temperature, do not exist for all measurement depths and records.

2.4 Low pass filtering, correlations, and wavelet analysis

Wind and current data are low-pass filtered using 15 days moving Hanning windows [*Lilly*, 2017]. The data series are zero-padded at each end to display data for the whole time series. We choose to study 15 day low-passed data in order to filter out the high-frequency variability such as tides, continental shelf waves, and short storm events.

Time series of correlation coefficients are calculated using moving windows of low-pass filtered along-slope ERA wind stress, or Halley wind speed, and current speed. For each window we calculate normalized correlation and significance, following *Sciremammano* [1979], while allowing for up to 7 days lag. The method requires more than 10 degrees of freedom (dof). Dof is a function of the auto-correlation of each data series, and is high when the variability within each time series is high. For CS1-3, dof is too low to calculate running correlations. For CC, we obtain $>$ 10 dof using window lengths of 150 days, and for FT1-2 we obtain $>$ 10 dof for window lengths of 120 days. Moorings at ES and FS have higher internal variability and yield $>$ 10 dof for window lengths of 100 days.

Significance levels are denoted by upper superscripts (i.e. $R = 0.6^{99}$ means that R is above the 99% significance level). In Table 1, correlation coefficients which do not exceed the 90% significance level are denoted by NS (Non-Significant).

Complex wavelet transforms, X_ω, are computed for daily low-passed along-slope wind and the along-flow current speed using the Morlet wavelet. The wavelet basis is normalized to have energy power equal to one at all scales, and we apply zero-padding to prevent wraparound effects. The wavelet power is the modulus of the complex wavelet transform, $|X_\omega|$. It shows when energetic oscillations take place, and at what time scales they appear. The wavelet amplitude, which we will study here, is the real part of the wavelet transform, $\mathrm{Re}(X_\omega)$, and is a useful measure when we compare two time series. Whereas the wavelet power only shows when, and at what frequencies energetic oscillations occur, comparison of positive and negative states of the wavelet amplitudes from two time series can tell us when the two oscillations are in or out of phase [*Cooper and Cowan*, 2008].

Table 1. Overview of the mooring records. Original mooring names are given in brackets. Correlation coefficients between the along-slope wind stress upstream of FT (see map in Figure 1) and the along-flow current speed from each mooring are given in column nine. Most current records cover roughly one year of data. In order to compare correlation coefficients between the records, we divide time series from moorings covering more than two years into sets of single years, including 13 months of data, from January to January. The significance level which is exceeded for the normalized correlation coefficients are indicated by superscripts. Non-significant correlations are marked by superscript NS.

Mooring Name	Year	# days	Lat (°S)	Lon (°W)	Dir (°)	Bottom depth (m)	Current depth (m)	R wind/curr.	Lag (days)	Reference
FS1 (S2)	1977	411	74° 40′	33° 56′	314	558	533	0.52^{99}_{a}	1.00	*Foldvik et al.* [1985b]
FS1 (S2)	1985	371	74° 40′	33° 56′	322	545	520	0.33^{95}	0.75	*Foldvik et al.* [2004]
FS2 (S2)	2003	747	74° 40′	33° 28′	294	597	497	0.05^{NS}	7.00	*Darelius et al.* [2014b]
	2004							0.24^{90}	0.00	
FS2 (S2)	2010	364	74° 38′	33° 30′	281	602	577	0.13^{NS}	0.00	*Darelius et al.* [2014b]
FS3 (S2E)	2014	1124	74° 40′	33° 00′	296	593	580	0.28^{90}	2.25	
	2015							0.15^{NS}	0.75	
	2016							0.12^{NS}	0.25	
FS4 (FR1)	1995	837	75° 01′	31° 46′	326	610	484	0.47^{99}	0.75	*Woodgate and Schröder* [1998]
	1996							0.26^{90}	0.00	
	1995	829			336		257	0.34^{99}	0.5	
	1996							0.33^{95}	0.5	
FT1 ($M78_{7E}$)	2013	376	77° 45′	36° 09′	17	705	486	0.32^{NS}	7.00	*Darelius et al.* [2016]
FT2 ($M77_{7}$)	2013	371	77° 00′	34° 28′	35	705	382	0.14^{NS}	7.00	*Darelius et al.* [2016]
ES1 ($M77_{5}$)	2013	371	77° 00′	34° 03′	35	505	434	0.32^{NS}	7.00	*Darelius et al.* [2016]
ES2 (M_{31W})	2014	746	76° 00′	31° 00′	45	457	437	-0.06^{NS}	7.00	*Ryan et al.* [2017]
	2015							-0.17^{NS}	6.50	
CS1 (M1)	2009	386	72° 29′	17° 28′	245	273	224	0.69^{99}	0.50	*Graham et al.* [2013]
CS2 (M2)	2009	386	72° 27′	17° 38′	238	487	224	0.43^{95}	0.75	*Graham et al.* [2013]
					238		400	0.46^{99}	0.50	
CS3 (M3)	2009	361	74° 31′	30° 10′	301	725	220	0.54^{95}	5.50	*Jensen et al.* [2013]
					315		400	0.35^{90}	7.00	
CC (B3)	2003	746	75° 49′	26° 52′	158	392	194	0.60^{99}	3.25	
	2004							0.47^{99}	1.75	*Nicholls* [2005]

[a] Correlation with Halley along-slope (245°) wind speed.

3 Results

In this section we first present the variability in the atmospheric forcing and the SIC (Section 3.1). We then describe the relation between wind and current at different geographic locations, starting with the ISW overflow from the Filchner Sill and Trough, and continuing with the eastern shelf (section 3.3),and the regions upstream of the Filchner area (section 3.5 and section 3.6). The implications of the results are discussed in section 4.

3.1 Atmospheric forcing and Sea Ice Concentration

Figure 3 shows the along-slope wind speed anomalies from ERA and Halley from 1960 to present. The year-to-year variability is large in both data series, with standard deviations of 0.51 $m\,s^{-1}$ for Halley and 0.73 $m\,s^{-1}$ for ERA, from one year low-passed along-slope wind in the period 1979 to 2016. In the Halley data series, which covers more than five decades we also find multi-decadal variability.

The upstream wind (averaged over the region marked by red lines in Figure 1) is mostly directed along the continental slope (toward 245 $^\circ$), but for some years, there is pronounced cross-flow wind (toward NE) during austral summer (Figure 1 in SI).

The upstream region is mostly covered with sea ice (SIC$>$ 0.8) between May and October. There is large interannual variability for the summer (DJF) SIC, ranging from ice-free conditions (SIC $<$ 0.2) to full sea ice cover (SIC $\sim$ 0.8). The mean summer SIC is 0.3, and the minimum SIC is found in mid-February (Figure 3b). In the Filchner region (marked by a yellow line in Figure 1), there is generally higher SIC throughout the year, compared to the upstream region. The period with full sea ice cover lasts longer (April to November), with a mean summer SIC of 0.6.

The variability of the summer SIC in the Filchner region is likely connected to the wind. We find high summer SIC (DJF) following strong along-slope wind in the preceding months (OND), which could indicate sea ice drift into the region. The correlation between the OND wind and the summer SIC in the Filchner region is $R = 0.6^{99}$ (not shown).

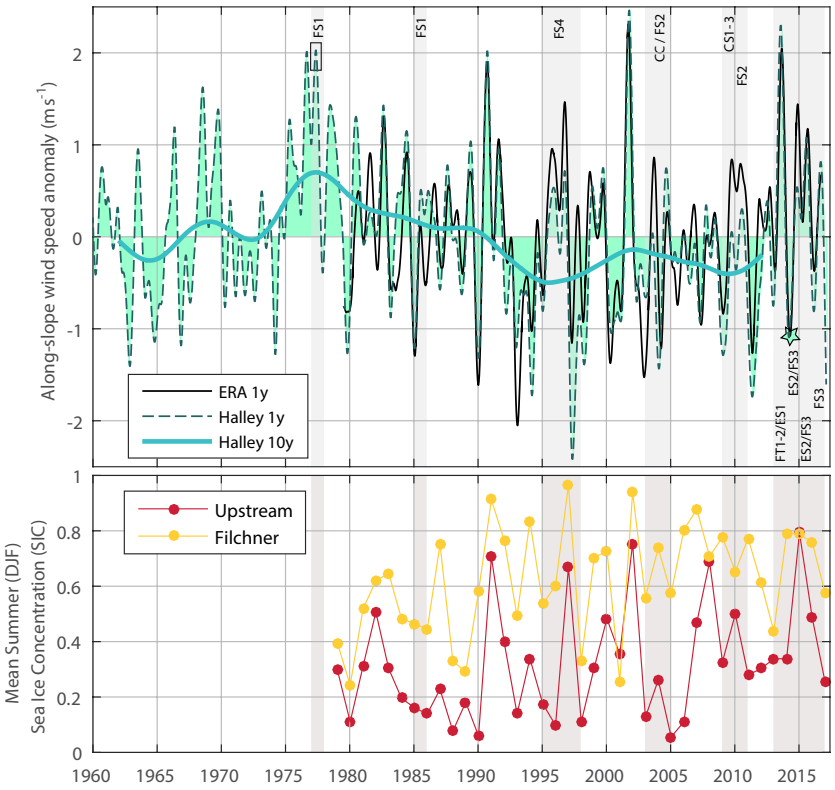

Figure 3. (a) Yearly low-passed wind speed anomaly towards 245° measured at Halley (filled, dashed turquoise) and from ERA averaged in the upstream area (black). The thick turquoise line shows 10y low-passed wind at Halley, where the period after 2012 is omitted due to filter edge effects. (b) Summer Sea Ice Concentration from the Upstream area (red) and the Filchner area (yellow) indicated in Figure 1. Years with available current moorings are indicated by gray shading, and corresponding mooring names. The square marks a period of high Halley wind speed discussed in section 3.2, and the turquoise star marks the low wind speed in 2014 discussed in section 3.3.

3.2 Ice Shelf Water overflow from the Filchner Trough and Sill

Here we present 15 days low-passed time series of ISW overflow from the Filchner Trough and Sill region, starting with the moorings located on the sill (FS1-3), followed by mooring FS4 just south of the sill, and moorings farther south in the FT (FT1-2).

Several current meter records are available between 1977 and 2017. We identify periods of significant positive correlation between upstream along-slope wind and overflow current speed in all records. The correlation varies largely from year to year (Table 1). The ISW overflow speed has also large interannual variability, seen both from consecutive years at one mooring deployment (e.g. FS2 in 2003-2004 or FS3 (Figure 5)), and from different deployments at the same location (FS1 and FS2).

The highest correlation between wind and ISW overflow is found at FS1 in 1977, with a correlation coefficient of $R = 0.52^{99}$ (Table 1). Analysis over 100 days moving windows indicates high correlation from February to August (Figure 4b). In this period we find that (I) the wind is mostly directed along the slope, (II) the overflow speed is high, (III) there is high variability in the 16-64 day period band for wind (Halley) and current wavelet power, and (IV) the along-slope wind speed anomaly is particularly high, compared to other years (see square in Figure 3). The strong wind is persistently directed toward southwest, and agrees with the conditions for recirculation of the slope current in the idealized model results of *Daae et al.* [2017] (Figure 2b). The correlation ceases in September, when the wind direction shifts toward north at Halley (Figure 4a-b), and both wind speed and current overflow speed are reduced.

Wavelet amplitudes from Halley wind speed and FS1 overflow speed (Figure 4c,d) are similar between February and August, with coinciding red and blue patches (positive and negative numbers). When the correlation ceases in September, the energetic oscillations from the Halley wind speed record shift toward longer time scales, and the current variability in the 16-64 day period band weakens.

The characteristics I to III are typical for most periods with high correlation between upstream wind and ISW overflow speed on the Filchner Sill. Figures of each mooring at FS1-2 is presented in the SI.

Mooring FS3 recorded the longest time series from the Filchner Sill, covering three years of data, from early 2014 to early 2017. The vertical extent of the ISW layer ($\theta < -1.9°C$)

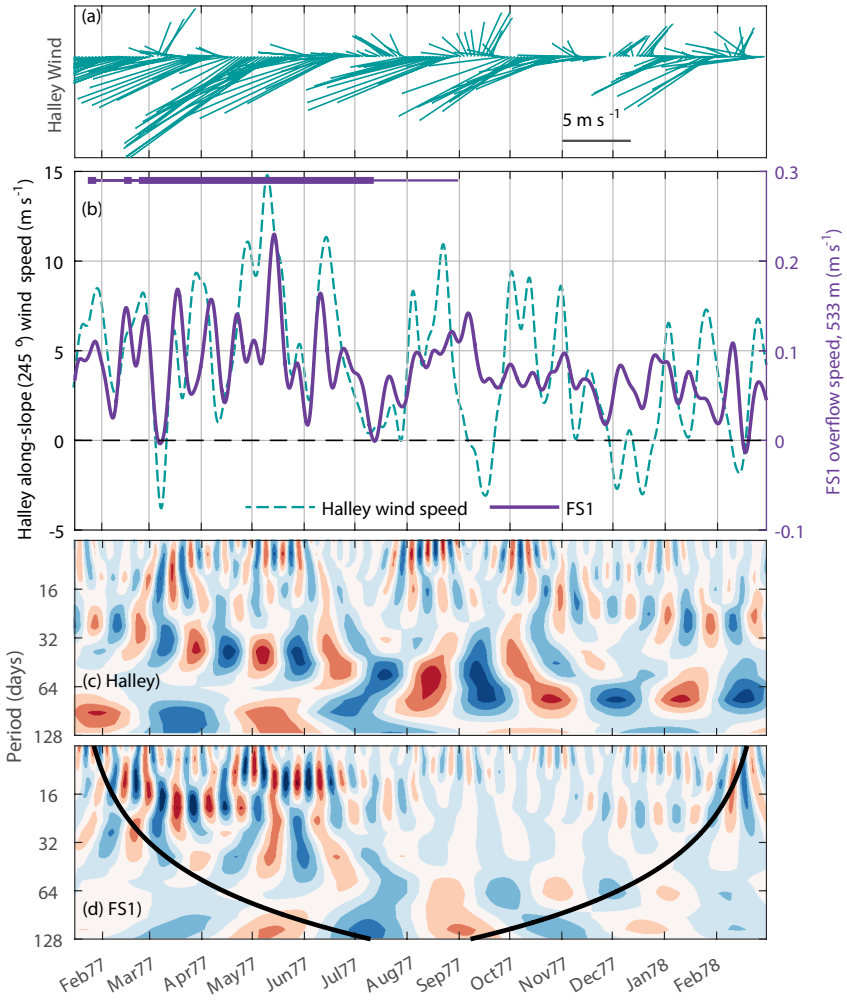

Figure 4. (a) Halley wind vectors, and (b) Halley along-flow wind speed and FS1 overflow speed in 1977. The horizontal bars in b) indicate periods of correlation between wind and current speed above the 95% significance level, identified from 100 days moving windows . The thick bars indicate the center point of each moving window, and the thin lines indicate the time span of the moving windows. Time series of the wavelet amplitudes (real part of the complex wavelet transform ($\mathrm{Re}(X_\omega)$) of (c) along-flow Halley wind speed, and (d) FS1 overflow speed. The color scale ranges from -7 to 7, and the thick black line in (d) show the cone of influence from edge effects. Vertical ticks on the horizontal time axis are placed on the 15th day of the month throughout this manuscript.

at FS3 varies through the year, being thicker from September to January when ISW surrounds both temperature sensors (584 m/485 m, Figure 5c). The depth of the ISW layer does not seem to affect the periods of correlation, as we find significant correlation both during periods of thick ISW layer (e.g. October-December 2014) and thin ISW layer (e.g. April-June 2015, Figure 5b). Similar seasonal variability in the ISW layer thickness is also observed on the shelf east of the FT [*Ryan et al.*, 2017](Figure 7), where it is accompanied by changes in the current direction.

Wavelet amplitudes from FS3 overflow speed and upstream ERA wind stress (Figure 5d-e) show highest agreement in 2014, consistent with the higher correlation coefficient this year (Table 1). From October 2015 to July 2016, there is weak correlation between overflow speed and wind. The wavelet amplitude for FS3 overflow is very low during this period, and the structure differs from the structure of the wind stress wavelet amplitude. From April to July 2016 (austral winter), the overflow speed is very high, and the ISW layer is thick. This could be a result of changes in the flow of ISW from under the FIS, but is not a seasonal feature, as it is not observed in 2014 or 2015. The SIC is anomalously high from December 2014 to January 2015 (austral summer). However, we do not see any changes in the temperature or current records linked to this anomaly.

At FS4, just south of the Filchner sill, a 28 month long record is available. We find an overall agreement between the FS4 overflow speed and the upstream wind stress (Table 1 and Figure 6b). Near the bottom, and up to 378 m, there is ISW ($\theta < -1.9\,^{\circ}\mathrm{C}$) throughout the year [*Foldvik et al.*, 2004]. Analysis over 100 day moving windows shows high correlations between the overflow speed at 484 m and the upstream wind stress in 1995 to 1996. The windows with significant correlation are typically centered in periods with warm water present at 257 m (thick horizontal bars in Figure 6b). The warm water at 257 m, combined with strong along-slope wind, is suggestive of a RSC as sketched in Figure 2b. During periods of high correlation, we also find a good match between positive and negative (red and blue) patches of the wavelet amplitudes for wind stress and overflow speed (Figure 5d-e). Oscillations with 16-64 days periods occur in both time series in 1995, while also longer period oscillations (64-90d) match in 1996.

The running correlation drops below the 95% significance level during austral summer, from December 1995 to February 1996. In this period, there is cold water high up in the water column, and the SIC is low in the upstream area (Figure 6c). Wavelet amplitude patterns

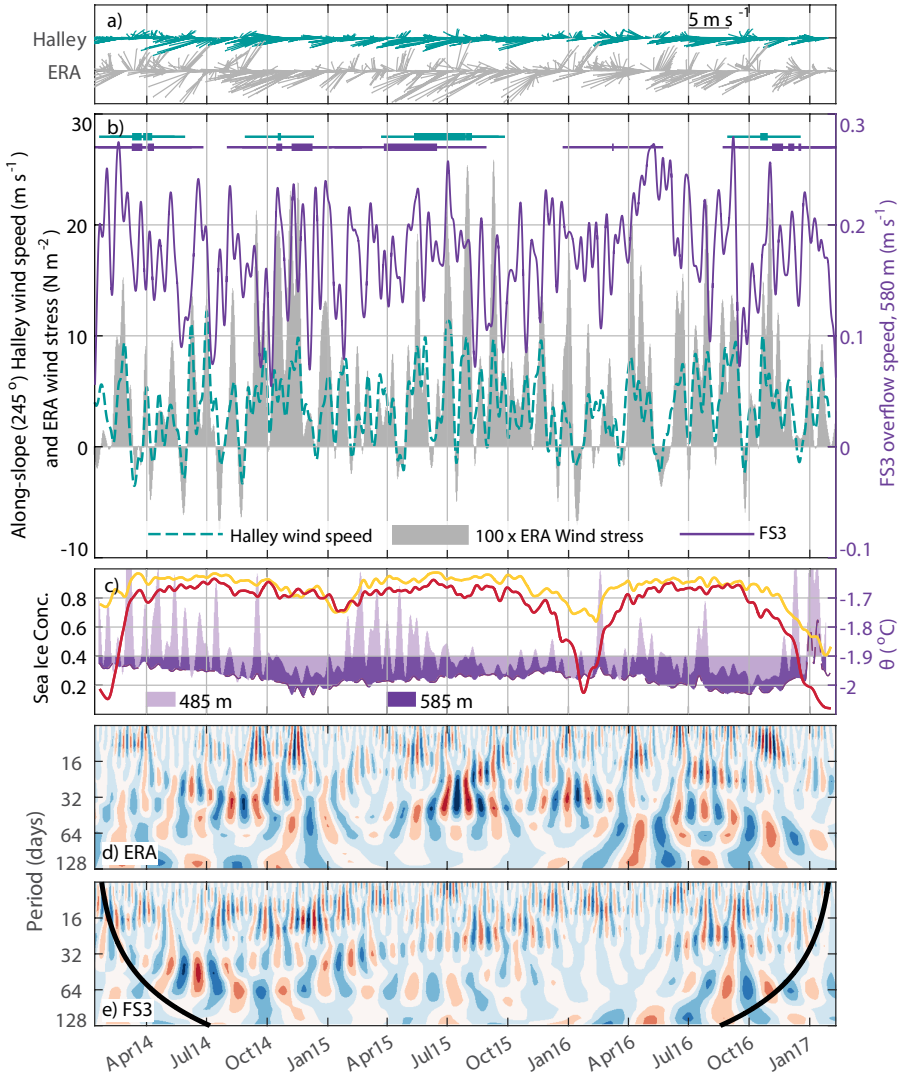

Figure 5. (a) Halley and ERA wind vectors. (b) Along-flow wind speed at Halley (turquoise) and wind stress from ERA (gray shade) together with FS3 overflow speed (purple) in 2014-2017. The horizontal bars in b) indicate periods of correlation between wind and current speed above the 95% significance level, identified from 100 days moving windows. (c) Temperature at 585 m (dark purple) and 485 m (light purple), and SIC averaged over the upstream slope area (red), and the Filchner area (yellow), according to Figure 1. The shading of the temperature curves highlights the freezing point of sea water at atmospheric pressure ($\theta = -1.9$∘C). Time series of the wavelet amplitudes (real part of the complex wavelet transform ($\mathrm{Re}(X_\omega)$) of (d) along-flow ERA wind stress, and (e) FS3 overflow speed. The color scale ranges from -7 to 7, and the thick black line in (e) show the cone of influence from edge effects. We include Halley wind speed to show the similar results.

(Figure 6d-e) indicate that the oscillations in wind stress and overflow speed are out of phase. When the wind stress is weak, the overflow speed is anomalously high, with high variability at the shorter time scales ($<$ 16 days), indicating current variability driven by other mechanisms than we study here. The results are similar to the observations from FS3 during the austral summer from December 2015 to February 2016.

The year 1997 stands out: the temperature maximum at 257 m is missing, suggesting that the seasonal inflow of MWDW was absent that year. Furthermore, we find ISW ($\theta < -1.9\,^{\circ}$C) at all depths, summer SIC are anomalously high in both the upstream and the Filchner area, the wind forcing is weak, and there is no correlation between the upstream wind and the overflow at 484 m (Figure 3 and Figure 6). Weak wind, and cold water at the upper instrument are consistent with the weak wind regime, as illustrated in Figure 2a, where no recirculation of the slope current occurs.

Further south in the FT (FT1-2), correlations between outflow speed and wind stress are not significant for full records (Table 1). At FT1, analysis over 120 day moving windows indicates one longer period of significant correlation from February to May 2013, when warm water ($\theta > -1.9^{\circ}$C) is present, and the wavelet amplitude patterns indicate similar oscillations in the period band 32 to 64 days (Figure 6 in SI). At FT2, there is only a short period with significant correlation (first part of February 2013), when the wavelet amplitudes from ERA wind stress and FT1 outflow are similar in the period band 16 to 32 days (Figure 5 in SI). During the rest of the time series, the wavelet amplitudes appear to be out of phase.

3.3 The eastern shelf

Here we present data from moorings on the upper eastern flank of the FT (ES1) and on the flat shelf, east of the FT (ES2), where a strong seasonality in both hydrography and circulation is observed [*Ryan et al.*, 2017]. Inflow of Modified Warm Deep Water (MWDW) occurs from January to June, when the thermocline at the shelf break is shallow [*Årthun et al.*, 2012; *Darelius et al.*, 2016].

Two moorings on the shelf (green markers in Figure 1) show similar seasonal flow patterns, with presence of warm water during the inflow phase [*Ryan et al.*, 2017] (Figure 7). A thorough discussion of the seasonality on the shelf is given in *Ryan et al.* [2017]. The two mooring records from consecutive years are not co-located (separated by 132 km).

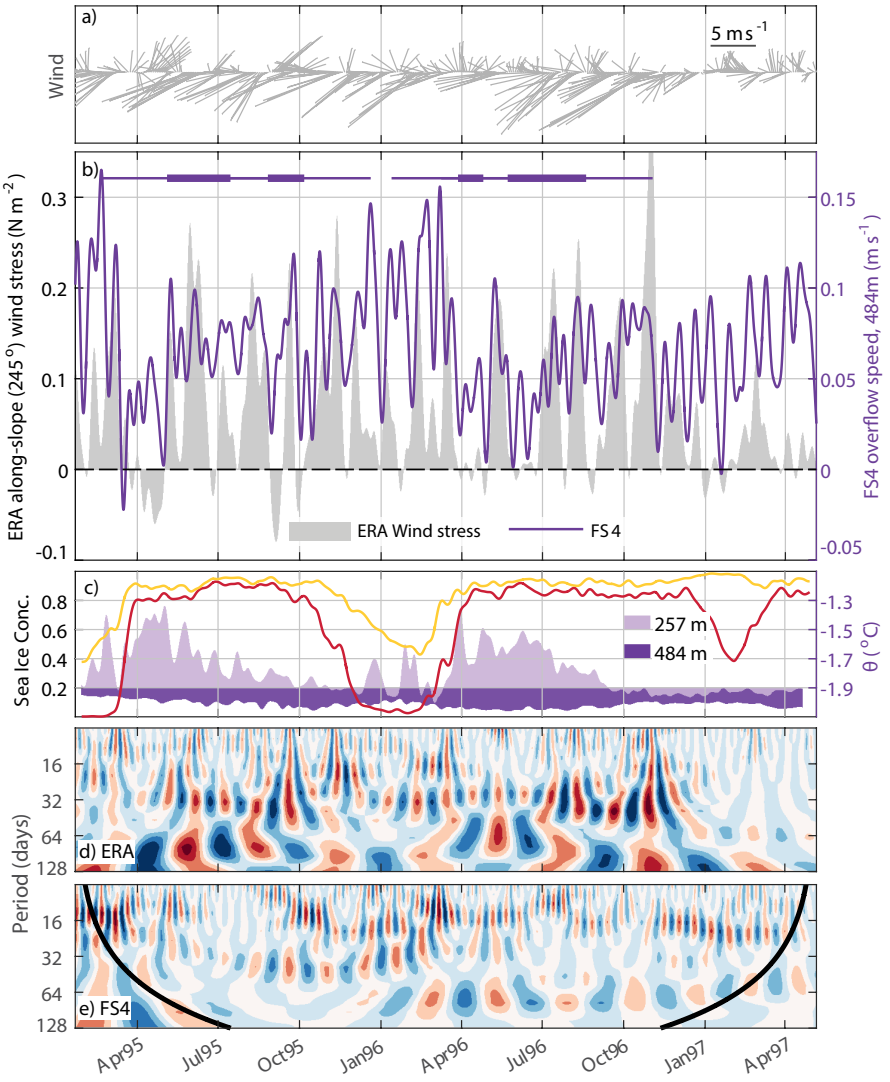

335 **Figure 6.** Same as Figure 5,but for the FS4 overflow speed (purple). Temperatures in c) are from 484 m
336 (dark purple) and 257 m (light purple). We omit wind speed from Halley.

At ES1, the mean current is directed southward from January to July. We find significant ($> 95\%$) positive correlation with wind stress from late March when the SIC reaches 0.8, to July when the current changes direction. In this period, warm water ($\theta > -1.9\,^{\circ}\mathrm{C}$) surrounds the mooring, and correlation between wind and current on shorter (2-5 days) timescales are observed [*Darelius et al.*, 2016]. At ES2 the pattern is similar, although the correlations are weaker in 2014 ($90\% - 95\%$ significance) compared to 2015. The weak correlation can possibly be explained by large variations in wind direction in 2014, compared to 2013 and 2015, and the strong minimum in 1y low-passed wind speed (turquoise star in Figure 3). In 2015, the inflow period extends beyond July, and we find positive correlations both in March to July, when warm water is present, and in September to November when the mooring is surrounded by ISW.

At both moorings, negative correlations occur when the mean current is directed northwards and ISW is present (Figure 7a-b). We also note high along-slope wind speed during spring (OND) 2013 and 2014, and high SIC in the succeeding summers (2014 and 2015), a relation which is described in Section 3.1.

3.4 Recirculation of MWDW in the Filchner Trough

Moorings on the eastern shelf (ES1-2) show flow of MWDW ($\theta > -1.7^{\circ}\mathrm{C}$) toward the FIS cavity during summer and autumn [*Darelius et al.*, 2016; *Ryan et al.*, 2017]. MWDW is also commonly observed in the FT in summer hydrographic sections, typically overlaying the ISW [*Nicholls et al.*, 2009; *Darelius et al.*, 2014a; *Foldvik et al.*, 1985a].

Observations from FT2 and FS4 show that the MWDW observed here flows northward, following the ISW toward the sill (Figure 8). At these locations, the mean velocity has a northward component for all temperature ranges. At FT1, the low-passed temperature at 475 m depth does not exceed the $-1.7^{\circ}\mathrm{C}$ threshold for MWDW. MWDW is found in the upper temperature sensors from 375 to 425 m [*Darelius et al.*, 2016], but current records do not exist in this depth range. However, the warmest water at 475 m flows northward similar to what we find at FT2. At ES1, on the eastern flank of FT, the warmest water flows southward toward the FIS, while water with temperature below $-1.7^{\circ}\mathrm{C}$ is directed toward east and northeast, toward the FT.

The observations suggest that the MWDW flowing southward above the shallower isobaths and on the continental shelf in the east, to some extent recirculates and returns north-

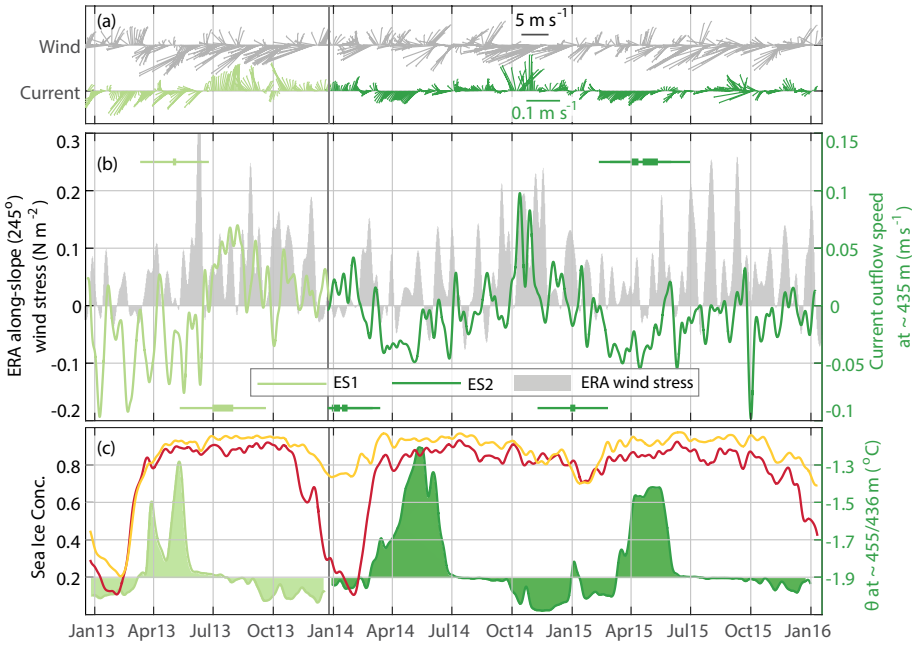

373 **Figure 7.** Same as Figure 6, but for ERA wind stress and current outflow speed at ES1 (light green) in
374 2013, and ES2 (dark green) in 2014-15, both at 435 m depth. In (b), horizontal bars at the top, indicate run-
375 ning windows with positive correlations above the 95% significance level, while horizontal bars at the bottom
376 indicate negative correlations. SIC in (c) is averaged over the upstream slope area (red), and the Filchner area
377 (yellow), according to Figure 1.

ward, away from the ice shelf cavity. The recirculation of MWDW is not to be confused with the RSC, described earlier, but could link the current variability in the FT to the wind and current variability observed over the continental shelf break.

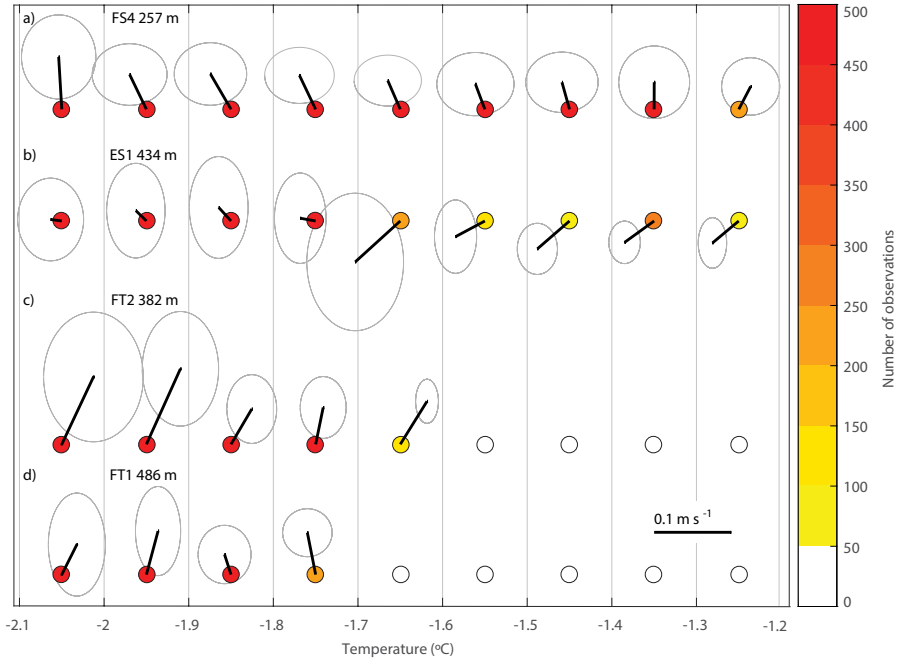

Figure 8. Mean velocity as a function of temperature in bins of 0.1°C intervals) at (a) FS4 257 m depths, (b) ES1 with velocity (θ) from 434 m (455 m) depth, (c) FT2 from 382 m (355 m) depth, and (d) FT1 from 486 m (475 m) depth. The colors indicate number of observations in each temperature bin, and the velocity scale is given in panel (d). The ellipses show the standard deviation of the de-tided velocity in the x- and y-directions.

3.5 Processes along the continental slope

Three moorings (CS1-3) from the continental slope in 2009, are situated within the ASF (red markers in Figure 1). Away from the surface layer, the current is bottom-intensified. Since we are interested in slope-shelf interactions, we select current records from depths roughly corresponding to the shelf depth (approximately 250 m at CS1-2 and 400 m at CS3).

In 2009, the slope current is strongly related to the along-slope wind stress. The highest correlation is found at CS1 ($R = 0.69^{99}$ using full records, Table 1). At CS3, close to the FT opening, the correlation is depth-dependent, with higher correlation at 220 m depth compared to 400 m. At 400 m depth, the correlation is highest during March to July, when the current speed is high, the pycnocline is deep, and the wind and current wavelet amplitudes for oscillations with 16-64 day periods are large, indicating a more energetic driving force (Figure 9).

The SIC in 2009 (not shown) is similar to the SIC in 2003 and 2004 (Figure 10c), with high values (SIC > 0.8) from March to November.

The wavelet amplitudes for wind and current (Figure 9d-f) have similar patterns, with strong power at low frequencies (period, T $>$ 64 days) throughout 2009. The oscillation patterns for $T > 16$ days, and the alternating positive/negative amplitudes (red/blue patches) coincide in time, indicating that the oscillations are in phase. The wavelet amplitudes on the period band 16 to 64 days indicate more energetic oscillations from March to July, when the current speed is high. In this period the slope current is also more barotropic [*Núñez-Riboni and Fahrbach*, 2009] and the volume transport is higher [*Graham et al.*, 2013].

3.6 The Antarctic Coastal Current

The slope current bifurcates around 27°W [*Heywood et al.*, 1998]. The ACoC branch is directed southward, and roughly follows the coast of the Brunt Ice Shelf. Existing current data from CS and CC are from different time periods. Hence, we cannot assess directly how the upstream ASF affects the ACoC. However, the CC current data set comprises more than two years of recorded current, and therefore enables analysis of the year-to-year variability and possible connections to the ASF.

The current variability at CC, is largely wind-driven ($R = 0.57^{99}$, Figure 10, Table 1). The wind and current correlation is higher in 2003 compared to 2004. This is opposite to what we find at FS2, where the correlation with wind is highest in 2004. Correlations obtained from 150 days moving windows exceed the 95% confidence limit continuously from May to December 2003 (horizontal bars in Figure 10b). In 2004, the running correlations are significant in several shorter periods.

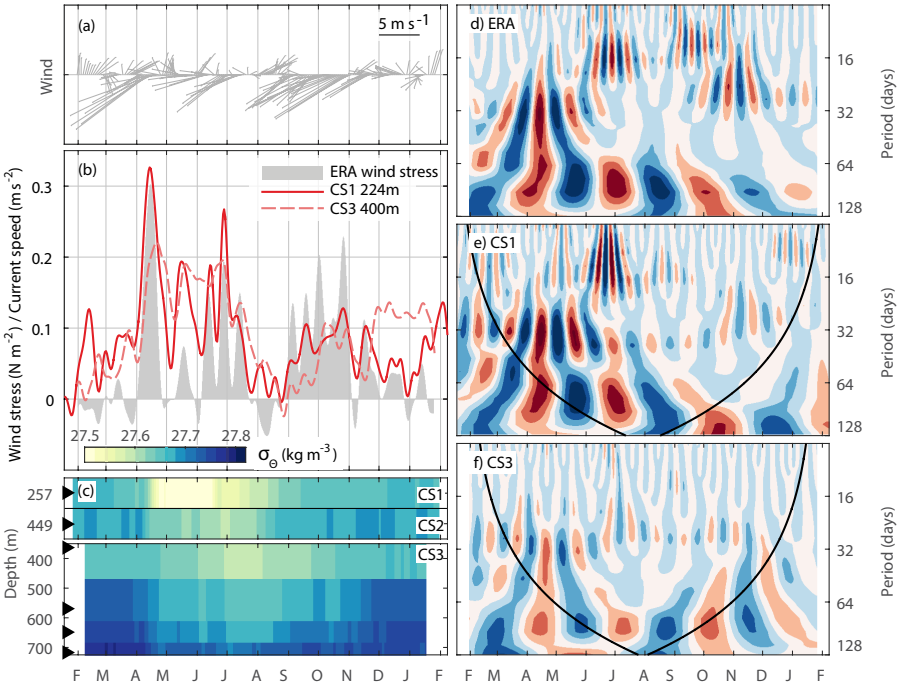

Figure 9. Time series of a) Wind velocity from ERA Interim, b) 15d low-passed along-flow ERA wind stress and along-flow current speed at CS1 (red solid line) and CS3 (red dashed line), and c) Potential density, σ_θ,at CS1-3 in 2009. Time series of the Real part of the complex wavelet transform ($\mathrm{Re}(X_\omega)$) of d) along-slope wind speed, e) along-flow current speed at CS1, and f) along-flow current speed at CS3. The color scale ranges from -7 to 7, and the thick black lines in (e-f) show the cone of influence from the edge effects

Wavelet analyses of current speed and wind stress reveal two differences between the first and the second deployment year (Figure 10d-e). Firstly, the spectral energy is distributed differently. In 2003, the total energy for both wind and current is weaker than in 2004. Most of the energy is at low frequencies (T> 64 days), although power is also seen in the 16-32 day period band around September. In 2004, strong oscillations are found at all displayed frequencies (T$\sim$ 8 $-$ 128 days), and could be the result of strong storm activity. We note a strong storm event in May 2004, associated with high wavelet power at all frequency bands (Figure 10d). The storm event lasts approximately 10 days with associated along-slope wind speed above 10 m s^{-1} throughout the event, and a maximum of 25 m s^{-1}. Secondly, the wavelet amplitudes for wind and current are in phase for all frequencies in 2003, i.e. positive/negative amplitudes (red/blue patches) occur at the same time, while this is only true for oscillations with T $<$ 64 days in 2004. In February 2004, when there is low SIC and a warm surface layer (Figure 10c), low frequency oscillations (T $>$ 64 days) appear in both time series. However, the oscillations are not in phase. This could explain the reduced correlation, despite the strong 16-64 day period oscillations present in both time series.

4 Discussion

The southeastern Weddell Sea is a remote region where observations are scarce. The data set compiled and presented in this study are from moorings deployed at various key locations, but typically in different years. The lack of concurrent sampling limits our ability to link mechanisms of forcing to circulation patterns. Nevertheless, important insight is gained from the analysis with implications on the regional circulation patterns and the response to wind forcing at monthly time scales.

The slope current has previously been shown to respond to the seasonal cycle of the wind forcing along the continental slope [e.g. *Fahrbach et al.*, 1992; *Núñez-Riboni and Fahrbach*, 2009; *Graham et al.*, 2013]. *Sverdrup* [1953] suggested that the on-shore Ekman transport, associated with wind from the east, builds up a pressure gradient toward the coast that leads to a stronger slope current. Here, we show that a similar relation exists on monthly time scales. We find significant positive correlations between the monthly scale along-slope wind variability and the along-flow current variability on both the continental slope and along the Brunt Ice Shelf, in the ACoC pathway (Figures 9-10).

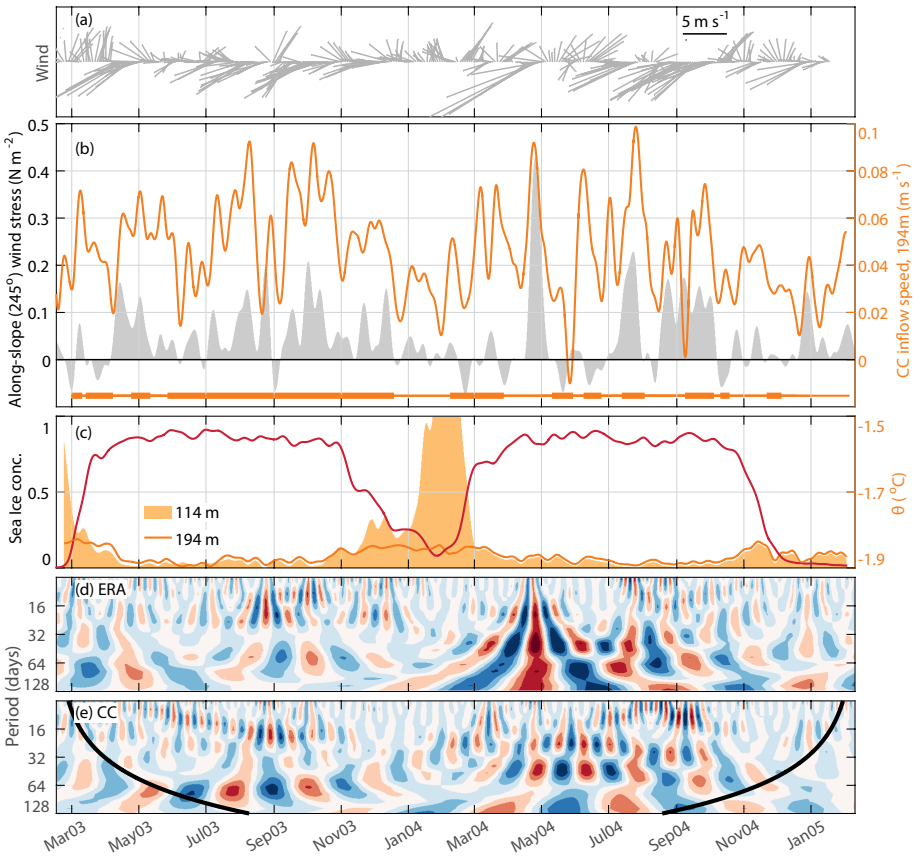

Figure 10. Time series of a) ERA wind velocity, and b) 15 day low-passed along-flow ERA wind stress (gray shade) and inflowing current speed at CC (orange). The horizontal bars in b) indicate periods of correlation between wind and current speed above the 95% significance level identified from moving windows of 150 days. The thick bars indicate the center point of each moving window, and the thin lines indicate the time span of the moving windows. c) Sea Ice concentration from the slope (indicated by red curve on Figure 1) and potential temperature at 194 m (orange line) and 114 m (light orange shade). The temperature axis is cut at -1.5°C to increase the resolution of the lower temperature sensor. The upper temperature reach a peak of -1.26°C during late February 2004. Real part of the complex wavelet transform ($\mathrm{Re}(X_\omega)$) of d) along-slope ERA wind speed, and e) inflowing current speed at CC. The thick black line in (e) shows the cone of influence from edge effects

The ACoC crosses the shelf break where the continental shelf widens up around 27°W (see Figure 1). During periods of high along-flow wind speed, the ACoC speed is also high. This could indicate a higher water exchange between the continental slope and the shelf, but cannot be confirmed with only a single observation point. The amount of heat transported by the ACoC depends on the water masses associated with the transport. The majority of the heat is carried by solar heated surface water that accumulates along the coast [*Sverdrup*, 1953]. At CC, we observe warm water in the upper layer during summer (Figure 10c). However, this water is likely too light and located too high up in the water column to enter the ice shelf cavity. Closer to the bottom at CC (194 m), the temperature increases slightly during summer, and both the current speed and the correlation with wind stress is weaker. This is likely related to a strong cross-flow wind speed component (towards NW). Cross-flow wind is common during summer, but does not occur every year.

The low-frequency wavelet amplitudes for wind stress and CC current shifts out of phase from summer 2004, and throughout the year (Figure 10d-e). During summer, the SIC is low and the wind stress is weak. Although the record at CC do not cover the full summer season in 2003 and 2005, it indicates a seasonal signal in temperature, with higher temperatures during summer in all years. The summer conditions are therefore similar in 2003 and 2004, and can not explain why the low-frequency wavelet amplitudes shift out of phase in 2004, and not in 2003.

Darelius et al. [2016] suggested that the seasonal inflow of MWDW in the FT is a two-step process. Firstly, warm water is lifted onto the shelf, and secondly, warm water present on the shelf can be transported south during favorable wind conditions (wind toward southwest). If MWDW comes into contact with the ice shelf, enhanced basal melting is expected. The MWDW flowing southward along the eastern flank of the FT is observed to recirculate and return northward in the FT (Figure 8). This inflow and recirculation of MWDW occur seasonally, and is not to be confused with the recirculation of the slope current in the sill area. The southward extent of the MWDW inflow recirculation may vary from year to year. MWDW was observed at FT1-2 in 2013, but was absent near the FIS in 2011 [*Darelius et al.*, 2016]. This could be explained by differences in wind forcing in 2011 and 2013. Dense water masses present on the shelf could also affect the southward transport of MWDW. In March to July, when the warm inflow is observed at ES1-2, the ISW layer does not reach the eastern shelf [*Ryan et al.*, 2017]. The thickness of the ISW layer could explain the seasonality of the flow direction in ES1-2. While a thin ISW layer allows southward flow of

warm water, a thick layer could block the southward flow, and aid a westward redirection of the current. In order to quantify and monitor the southward heat flux in the FT and on the eastern shelf, one has to quantify the recirculation of MWDW, or place the moorings so far south that the recirculation occurring south of the mooring array is negligible.

In the FT and over the Filchner sill, we find unexpectedly strong correlation between the dense ISW overflow speed and the along-slope wind stress on monthly time scales. This connection implies that changes in the atmospheric circulation could affect the production rates of Antarctic Bottom Water, through changes in the overflow properties, and associated mixing rates with ambient water masses.

Wang et al. [2012] showed that, on seasonal scales, the Filchner export responds to onshore density anomalies caused by wind-induced variation of the isopycnal depression at the coast, with a lag of about one month. The observed variability of the overflow in the FT and sill reported here, responds to wind variability on the continental slope with no, or very short lags (less than 7 days). The mechanism for this co-variability is different from the one described by *Wang et al.* [2012].

We do not have sufficient data to calculate the volume transport of the ISW overflow. The observed current speed variability could result from changes in the shape and/or position of the overflow current. Since we do not have simultaneous observations from the continental slope and the overflow we cannot verify a link between the slope current and the overflow, or that recirculation of the slope current occurs. However, we do find higher correlations in periods when there is strong along-slope wind, combined with the presence of warm water (MWDW) in the upper water column (e.g Figure 6), which could indicate that recirculation occurs [*Daae et al.*, 2017]. In 1997 (FS4), there is no indication of recirculation when the wind speed and its variability is weak, consistent with the modeled weak wind regime in *Daae et al.* [2017]. At FT1-2 we only find short periods of correlation between wind and outflow speed. This indicates that either (I) the influence of monthly scale wind variability does not reach this far south, or (II) the wind forcing was not sufficient to drive a strong recirculation, as observed at FS4 in 1997. We suggest that (I) is the most likely reason, since the along-flow wind speed was high during most of the year (2013).

At FS1-4 we find large year-to-year variability in the correlation between wind and current speed for both consecutive years from multi-year deployments (FS2 in 2003-2004 and FS3 in 2014-2016), and for deployments at the same location in different years (FS1 and

FS2). In addition to the interannual variability in the wind-forcing (Section 3.1), the Filchner Sill area is affected by several forcing mechanisms such as continental shelf waves [*Middleton et al.*, 1982; *Jensen et al.*, 2013; *Semper and Darelius*, 2017], tides [*Pereira et al.*, 2002; *Fer et al.*, 2015], SIC, and variability in the outflow of cold, dense, shelf water from underneath the FIS. Variability related to these mechanisms could be affecting the recirculation of the slope current. It is therefore likely that recirculation, and hence the link between ISW overflow speed and along-slope wind stress, is strongest in periods when the wind forcing at low frequencies is the dominating source of variability.

In several mooring deployments at FS1-4 we find significant correlation between wind and current speed during autumn, which ceases during winter. Although the results are not conclusive, this could indicate that recirculation of the slope current is strongest when the slope current is strong and barotropic (March to June, Section 3.5, [*Núñez-Riboni and Fahrbach*, 2009]). Other mechanisms such as continental shelf waves, weaker wind forcing, or a cross-flow wind direction could also influence the slope current and recirculation.

The highest correlation between the along-flow wind and outflow speed at the Filchner sill is found at FS1 in 1977. Here, the along-flow wind forcing is strong, and we find high anomalies for both 1 and 10 year low-pass filtered Halley wind speed (Figure 3a). In the past few decades, atmospheric conditions in the southern high latitudes have been changing [*Thompson and Solomon*, 2002]. The Southern Annular Mode (SAM) is thought to be the primary driver of such longterm climate variability [*Thompson and Wallace*, 2000]. The SAM-index is calculated from the difference in mean sea level pressure (mslp) between 40-65°S. A positive SAM-index is connected to a stronger cyclonic wind stress and spin-up of the Weddell gyre. Since the late 1970's, the SAM index has been increasing [*Marshall*, 2003], likely as a result of stratospheric ozone depletion and greenhouse gas emissions [*Gillett and Thompson*, 2003; *Polvani et al.*, 2011]. We find no significant correlation between the SAM-index and the along-flow wind speed (245°) at Halley or in the continental slope region. However, the effect of SAM is most pronounced in multi-decadal time scales, and the period we are studying might be too short to evaluate the effect of SAM directly. We do find a weak longterm wind variability in 1980-90, when the SAM index is close to zero (not shown), but instead of increased wind speed since the 1970's, we note a long-term weakening of the along-flow wind speed from 1977 to 2010 (Figure 3a).

In addition to the SAM, the Semi-Annual Oscillation (SAO) affects the annual cycle of pressure and wind in the high southern latitudes. SAO results from differing annual cycles of temperature in the mid-latitude ocean and the Antarctic regions [*Van Loon*, 1967; *Meehl*, 1991; *Simmonds and Jones*, 1998]. SAO causes a poleward shift of the circumpolar trough in spring (September) and autumn (March), with associated higher meridional pressure gradients and surface wind stress [*Hurrell and Loon*, 1994].The amplitude of SAO is highest between 55 to 65°S [*Large and Loon*, 1988]. Unlike SAM, the phase of SAO is consistent from year to year, and is therefore thought to influence the longterm mslp more strongly than SAM at high latitudes [*Hurrell and Loon*, 1994]. The SAO was particularly strong in the late 1970's, but has since been declining, likely caused by seasonal temperature changes in connection with SAM [*Van Loon et al.*, 1993; *Marshall*, 2003]. The observed longterm negative trend in along-slope wind speed at Halley (Figure 3) is consistent with the reduction of SAO. We speculate that the high correlations between wind and overflow at the Filchner Sill at FS1 in 1977 could be connected to strong SAO, and the reduced correlations found in later records, could partly be caused by decreased effects of SAO. However, the current data set is not sufficient to test whether the wind-current correlation is affected by the variability in SAO.

5 Conclusions

Observations of ocean currents and temperature from 14 moorings in the southeastern Weddell Sea are analyzed. We find significant correlation between the ISW overflow speed in FT and the along-slope wind stress over the upstream continental slope, which could have implications for the production rates of AABW. During strong northeasterly winds, we identified current records consistent with the recirculation of the slope current (RSC) at the mouth of the FT, as shown in the idealized numerical model results of *Daae et al.* [2017]. We suggest that the RSC could explain the correlation between the wind stress and the overflow, however, in order to firmly establish whether recirculation of the slope current occurs, an array of moored instruments is needed over the Filchner Sill, covering both the RSC and the ISW overflow.

The variability in the slope current and the ACoC is strongly wind-driven on monthly time scales. Few measurements of the ACoC exist, and the amount of heat transported onto the shelf by the ACoC is still unknown. Our findings show that an increased wind stress along the continental slope leads to an increased current speed within the ACoC. Strong

wind forcing, coinciding with a thin thermocline could therefore lead to large heat transports onto the shelf and contribute to basal melting of ice shelves. Similarly, the seasonal inflow and recirculation of MWDW to the eastern shelf is partly wind driven. Long-term changes in the atmospheric forcing can alter the present situation characterized by weak and seasonal MWDW inflow, and possibly increase the heat transport onto the shelf region.

Acknowledgments

This work is supported by the Centre for Climate Dynamics at the Bjerknes Centre and by the Norwegian Research councils FRINATEK program through the project WARM (231549) and through the NARE program under the project WEDDELL (211415). For deployment and recovery of moorings, we would like to thank AWI, BAS, NP, and the crew and scientists on RV Polarstern (cruises PS08, PS34, PS82 (Grant no: *AWI_PS*82_02), PS96 (Grant no: *AWI_PS*96_01)), RRS Ernest Shackleton (cruises ES006, ES033, ES052, ES060), RRS James Clark Ross (cruises JR097, JR244, JR16004), M/V Polarsirkel (NARE1, NARE2), K/V Andenes (NARE3) and HMS Endurance. We thank two anonymous reviewers for constructive comments that helped improve the manuscript substantially. The CS1-2 mooring data were provided by Karen Heywood at the University of East Anglia, and were funded by Antarctic Funding Initiative grant R14937 from the Natural Environment Research Council as the UK contribution to the SASSI program for the International Polar Year. A complete list of mooring data availability is given in SI. Wavelet software was provided by C. Torrence and G. Compo, and is available at URL: http://paos.colorado.edu/research/wavelets/

References

Allen, S. E., and X. Durrieu de Madron (2009), A review of the role of submarine canyons in deep-ocean exchange with the shelf, *Ocean Science Discussions*, *6*(2), 1369–1406, doi:10.5194/osd-6-1369-2009.

Andreas, E. L., T. W. Horst, A. a. Grachev, P. O. G. Persson, C. W. Fairall, P. S. Guest, and R. E. Jordan (2010), Parametrizing turbulent exchange over summer sea ice and the marginal ice zone, *Quarterly Journal of the Royal Meteorological Society*, *136*(649), 927–943, doi:10.1002/qj.618.

Årthun, M., K. W. Nicholls, K. Makinson, M. a. Fedak, and L. Boehme (2012), Seasonal inflow of warm water onto the southern Weddell Sea continental shelf, Antarctica, *Geophysical Research Letters*, *39*(17), n/a–n/a, doi:10.1029/2012GL052856.

British Antarctic Survey (2013), UK Antarctic Surface Meteorology; 1947–2013, Database, Version 1.0, Polar Data Centre, British Antarctic Survey.

Carmack, E. C., and T. Foster (1977), Water masses and circulation in the Weddell Sea, in *Proceedings of the Polar Ocean Conference, Montreal, 1974*, pp. 151–165.

Cavalieri, D., P. C.L, P. Gloersen, and H. Zwally (1996), Sea Ice Concentrations from Nimbus-7 SMMR and DMSP SSM/I-SSMIS Passive Microwave Data, Version 1 [NSIDC-0051], doi:https://doi.org/10.5067/8GQ8LZQVL0VL.

Cooper, G. R. J., and D. R. Cowan (2008), Comparing time series using wavelet-based semblance analysis, *Computers & Geosciences*, *34*, 95–102, doi:10.1016/j.cageo.2007.03.009.

Daae, K., T. Hattermann, E. Darelius, and I. Fer (2017), On the effect of topography and wind on warmwater inflow - An idealized study of the southern Weddell Sea continental shelf system, *J. Geophys. Res Ocean*, *122*(3), 2622–2641, doi:10.1002/2016JC012541.

Darelius, E., L. H. Smedsrud, S. Østerhus, A. Foldvik, and T. Gammelsrød (2009), Structure and variability of the Filchner overflow plume, *Tellus A*, *61*(3), 446–464, doi:10.1111/j.1600-0870.2009.00391.x.

Darelius, E., K. Makinson, K. Daae, I. Fer, P. R. Holland, and K. W. Nicholls (2014a), Hydrography and circulation in the Filchner Depression, Weddell Sea, Antarctica, *Journal of Geophysical Research: Oceans*, *119*, 1–18, doi:10.1002/2014JC010225.

Darelius, E., K. O. Strand, S. Østerhus, T. Gammelsrød, M. Årthun, and I. Fer (2014b), On the Seasonal Signal of the Filchner Overflow, Weddell Sea, Antarctica, *Journal of Physical Oceanography*, *44*(4), 1230–1243, doi:10.1175/JPO-D-13-0180.1.

Darelius, E., I. Fer, and K. W. Nicholls (2016), Observed vulnerability of Filchner-Ronne Ice Shelf to wind-driven inflow of warm deep water, *Nature communications*, *7*, 1–7, doi:10.1038/ncomms12300.

Dee, D. P., S. M. Uppala, A. J. Simmons, P. Berrisford, P. Poli, S. Kobayashi, U. Andrae, M. A. Balmaseda, G. Balsamo, P. Bauer, P. Bechtold, A. C. M. Beljaars, L. van de Berg, J. Bidlot, N. Bormann, C. Delsol, R. Dragani, M. Fuentes, A. J. Geer, L. Haimberger, S. B. Healy, H. Hersbach, E. V. Hólm, L. Isaksen, P. Kållberg, M. Köhler, M. Matricardi, a. P. McNally, B. M. Monge-Sanz, J.-J. Morcrette, B.-K. Park, C. Peubey, P. de Rosnay, C. Tavolato, J.-N. Thépaut, and F. Vitart (2011), The ERA-Interim reanalysis: configuration and performance of the data assimilation system, *Quarterly Journal of the Royal Meteorological Society*, *137*(656), 553–597, doi:10.1002/qj.828.

Fahrbach, E., G. Rohardt, and G. Krause (1992), The Antarctic coastal current in the southeastern Weddell Sea, *Polar Biology*, *12*(2), 171–182, doi:10.1007/BF00238257.

Fer, I., M. Müller, and A. K. Peterson (2015), Tidal forcing , energetics , and mixing near the Yermak Plateau, *Ocean Science*, *11*, 287–304, doi:10.5194/os-11-287-2015.

Foldvik, A., T. Gammelsrød, and T. Tørresen (1985a), Hydrographic observations from the Weddell Sea during the Norwegian Antarctic research expedition 1976/77, *Polar Research*, pp. 177–193.

Foldvik, A., T. Gammelsrød, and T. Tørresen (1985b), Physical oceanography studies in the Weddell Sea during the Norwegian Antarctic Research Expedition 1978/79, *Polar Research*, *3*(2), 195–207, doi:10.1111/j.1751-8369.1985.tb00507.x.

Foldvik, A., T. Gammelsrød, S. Østerhus, E. Fahrbach, G. Rohardt, M. Schröder, K. W. Nicholls, L. Padman, and R. A. Woodgate (2004), Ice shelf water overflow and bottom water formation in the southern Weddell Sea, *Journal of Geophysical Research*, *109*(C2), 1–15, doi:10.1029/2003JC002008.

Gill, A. (1973), Circulation and bottom water production in the Weddell Sea, *Deep Sea Research and Oceanographic Abstracts*, *20*(2), 111–140, doi:10.1016/0011-7471(73)90048-X.

Gillett, N. P., and D. Thompson (2003), Simulation of Recent Southern Hemisphere Climate Change, *Science*, *302*(October), 273–276.

Gordon, A. L., B. Huber, D. McKee, and M. Visbeck (2010), A seasonal cycle in the export of bottom water from the Weddell Sea, *Nature Geoscience*, *3*(8), 551–556, doi:10.1038/ngeo916.

Graham, J. A., K. J. Heywood, C. P. Chavanne, and P. R. Holland (2013), Seasonal variability of water masses and transport on the Antarctic continental shelf and slope in the southeastern Weddell Sea, *Journal of Geophysical Research: Oceans*, *118*(4), 2201–2214, doi:10.1002/jgrc.20174.

Grosfeld, K., M. Schröder, E. Fahrbach, R. Gerdes, and A. Mackensen (2001), How iceberg calving and grounding change the hydrography in the Filchner Ice Shelf-Ocean System, *Journal of Geophyscial Research*, *106*(2000), 9039–9055.

Hellmer, H. H., F. Kauker, R. Timmermann, J. Determann, and J. Rae (2012), Twenty-first-century warming of a large Antarctic ice-shelf cavity by a redirected coastal current., *Nature*, *485*(7397), 225–8, doi:10.1038/nature11064.

Hellmer, H. H., F. Kauker, R. Timmermann, and T. Hattermann (2017), The Fate of the Southern Weddell Sea Continental Shelf in a Warming Climate, *Journal of Climate*, *30*(Gill 1973), 4337–4350, doi:10.1175/JCLI-D-16-0420.1.

Heywood, K. J., R. A. Locarnini, R. D. Frew, P. F. Dennis, and B. A. King (1998), Transport and Water Masses of the Antarctic Slope Front System in the Eastern Weddell Sea, *Ocean, Ice, and Atmosphere - Interaction at the Antarctic Continental Margin*, *75*, 203–214.

Hurrell, J. W., and H. V. Loon (1994), A modulation of the atmospheric annual cycle in the Southern Hemisphere, *Tellus A*, *46*(3), doi:10.3402/tellusa.v46i3.15482.

IOC, SCOR, and IAPSO (2010), The international thermodynamic equation of seawater - 2010: Calculation and use of thermodynamic properties. Intergovernmental Oceanographic Commission, Manuals and Guides No. 56, UNESCO (English)., *Tech. rep.*

Jacobs, S. (1991), On the nature and significance of the Antarctic Slope Front, *Marine Chemistry*, *35*(1-4), 9–24, doi:10.1016/S0304-4203(09)90005-6.

Jensen, M. F., I. Fer, and E. Darelius (2013), Low frequency variability on the continental slope of the southern Weddell Sea, *Journal of Geophysical Research: Oceans*, *118*, 1–17, doi:10.1002/jgrc.20309.

Klinck, J. M. (1996), Circulation near submarine canyons: A modeling study, *Journal of Geophysical Research*, *101*(95), 1211–1223, doi:10.1029/95JC02901.

Large, W. G., and H. V. Loon (1988), Large scale, low frequency variability of the 1979 FGGE surface buoy drifts and winds over the south hemisphere, *Journal of Physical Oceanography*, *19*(Feb), 216–232, doi:10.1175/1520-0485(1989)019<0216:LSLFVO>2.0.CO;2.

Lilly, J. (2017), jLab: A data analysis package for matlab, v. 1.6.3.

Marshall, G. J. (2003), Trends in the Southern Annular Mode from Observations and Reanalyses, *Journal of Climate*, *16*(1999), 4134–4143.

Meehl, G. A. (1991), A Reexamination of the Mechanism of Semiannual Oscillation in the Southern Hemisphere, *Journal of Climate*, *4*, 911–926.

Middleton, J., T. Foster, and A. Foldvik (1982), Low-frequency currents and continental shelf waves in the southern Weddell Sea, *J. Phys. Oceanogr*, *12*(7), 618–634.

Nicholls, K. W. (2005), JR097 Cruise Report Autosub Under Ice Cruise to the southern Weddell Sea, *Tech. rep.*, British Antarctic Survey, Cambridge, UK.

Nicholls, K. W., S. Østerhus, K. Makinson, T. Gammelsrød, and E. Fahrbach (2009), Ice-ocean processes over the continental shelf of the southern Weddell Sea , Antarctica: A

review, *Reviews of Geophysics*, *47*(3), 1–23, doi:10.1029/2007RG000250.

Nøst, O. A., and S. Østerhus (1998), Impact of grounded icebergs on the hydrographic conditions near the Filchner Ice Shelf, *Antarctic Research Series*, *75*, 267–284.

Núñez-Riboni, I., and E. Fahrbach (2009), Seasonal variability of the Antarctic Coastal Current and its driving mechanisms in the Weddell Sea, *Deep Sea Research Part I: Oceanographic Research Papers*, *56*(11), 1927–1941, doi:10.1016/j.dsr.2009.06.005.

Pereira, A. A. F., A. Beckmann, and H. H. Hellmer (2002), Tidal Mixing in the Southern Weddell Sea: Results from a Three-Dimensional Model, *Journal of Physical Oceanography*, *32*(7), 2151, doi:10.1175/1520-0485(2002)032<2151:TMITSW>2.0.CO;2.

Polvani, L., D. Waugh, G. Correa, and S. Son (2011), Stratospheric Ozone Depletion : The Main Driver of Twentieth-Century Atmospheric Circulation Changes in the Southern Hemisphere, *Journal of Climate*, *24*(3), 795–812, doi:10.1175/2010JCLI3772.1.

Pritchard, H. D., S. Ligtenberg, H. Fricker, D. G. Vaughan, M. van den Broeke, and L. Padman (2012), Antarctic ice-sheet loss driven by basal melting of ice shelves, *Nature*, *484*(7395), 502–505, doi:10.1038/nature10968.

Rignot, E., S. Jacobs, J. Mouginot, and B. Scheuchl (2013), Ice-shelf melting around Antarctica., *Science*, *341*(6143), 266–70, doi:10.1126/science.1235798.

Ryan, S., T. Hattermann, E. Darelius, and M. Schröder (2017), Seasonal cycle of hydrography on the eastern shelf of the Filchner Trough,Weddell Sea, Antarctica, *J. Geophys. Res Ocean*, *122*, 1–17, doi:10.1002/2017JC012916.Received.

Sciremammano, F. (1979), Suggestion for the Presentation of Correlations and Their Significance Levels, *J. Phys. Oceanogr*, *9*, 1273–1276, doi:http://dx.doi.org/10.1175/1520-0485(1979)009<1273:ASFTPO>2.0.CO;2.

Semper, S., and E. Darelius (2017), Seasonal resonance of diurnal continental shelf waves in the southern Weddell Sea, *Ocean Science*, *13*, 77–93, doi:10.5194/os-2016-36.

Simmonds, I. A. N., and D. A. Jones (1998), The mean structure and temporal variability of the semiannual oscillation in the southern extratropics, *International Journal of Climatology*, *18*, 473–504.

Sverdrup, H. (1953), The currents off the coast of Queen Maud Land, *Norsk Geografisk Tidskrift*, *14*, 239–249.

Thompson, D., and S. Solomon (2002), Interpretation of Recent Southern Hemisphere Climate Change, *Science*, *296*(May), 895–900.

Thompson, D., and J. Wallace (2000), Annular Modes in the Extratropical Circulation . Part I, *Journal of Climate*, *13*, 1000–1016.

Timmermann, R., and H. H. Hellmer (2013), Southern Ocean warming and increased ice shelf basal melting in the twenty-first and twenty-second centuries based on coupled ice-ocean finite-element modelling, *Ocean Dynamics*, *63*(9-10), 1011–1026, doi: 10.1007/s10236-013-0642-0.

Van Loon, H. (1967), The Half-Yearly Oscilations in Middle and High Southern Latitudes and the Coreless Winter, *Journal of Atmospheric Sciences*, *24*, 472–486.

Van Loon, H., J. Kidson, and A. Brett Mullan (1993), Decadal Variation of the Annual Cycle in the Australian Dataset, *Journal of Climate*, *6*, 1227–1231.

Wang, Q., S. Danilov, E. Fahrbach, J. Schröter, and T. Jung (2012), On the impact of wind forcing on the seasonal variability of Weddell Sea Bottom Water transport, *Geophysical Research Letters*, *39*(6), n/a–n/a, doi:10.1029/2012GL051198.

Williams, W. J., G. G. Gawarkiewicz, and R. Beardsley (2001), The adjustment of a shelf-break jet to cross-shelf topography, *Deep-Sea Research Part II: Topical Studies in Oceanography*, *48*(1-3), 373–393, doi:10.1016/S0967-0645(00)00085-0.

Woodgate, R. A., and M. Schröder (1998), Moorings from the Filchner Trough and the Ronne Ice Shelf Front: Preliminary Results, *Filchner Ronne Ice Shelf Programme*, *12*, 85–90.

Zhang, Y., J. Pedlosky, and G. R. Flierl (2011), Cross-Shelf and Out-of-Bay Transport Driven by an Open-Ocean Current, *Journal of Physical Oceanography*, *41*(2004), 2168–2186, doi:10.1175/JPO-D-11-08.1.

Paper IV

Variability and mixing of the Filchner overflow plume descending the continental slope, Weddell Sea

K. Daae, I. Fer, and E. Darelius
Prepared for submission to Journal of Physical Oceanography,

Variability and mixing of the Filchner overflow plume descending the continental slope, Weddell Sea

K. Daae*, I. Fer and E. Darelius

Geophysical Institute, University of Bergen and Bjerknes Centre for Climate Research, Bergen, Norway

Corresponding author address: Geophysical Institute, University of Bergen, Allegt.70, 5020 Bergen, Norway

E-mail: kjersti.daae@uib.no

ABSTRACT

Antarctic Bottom Water (AABW) feeds into the lower limb of the global thermohaline circulation, and is therefore important for the Earth's climate. A large fraction of AABW is produced in the Weddell Sea, where it is formed through mixing between the cold and dense shelf water masses and the warm and saline off-shelf water. We present observations of the Filchner overflow plume from one mooring on the Filchner sill and from two moorings over the continental slope downstream of the Filchner Trough. The monthly scale plume properties at the two sites are related, with high correlation in density. Over the continental slope, the plume thickness fluctuates strongly between less than 25 m and more than 250 m. Observations of elevated temperature variance, high shear, and high Froude numbers at the plume interface imply high mixing rates and entrainment of ambient water masses. Shear spikes are associated with an alignment of counter-rotating oscillations with periods of 24 and 72 hours. The clockwise 24-hour oscillation is related to diurnal, barotropic tidal currents and topographic vorticity waves, while the counter-clockwise 72-hour oscillation is related to vortex stretching or topographic vorticity waves.

1. Introduction

Antarctic Bottom Water (AABW) feeds into the lower limb of the global thermohaline overturning circulation (Orsi 1999), and is therefore an important driver of the Earth's climate. Recent studies indicate that the AABW has freshened during the past 30 years, and that this freshening contributes to a substantial fraction of the global sea level rise (Purkey and Johnson 2013; Jullion et al. 2013). A better understanding of the underlying mechanisms which lead to AABW freshening, could therefore be a key to improved predictions of the global sea level rise.

A large fraction of the AABW originates from the Weddell Sea region (Figure 1), and is formed through processes occurring over the continental shelf, under the Filchner-Ronne Ice Shelf (FRIS) and along the continental slope (Foldvik and Gammelsrød 1988). Over the continental shelf, cold and saline High Salinity Shelf Water (HSSW) is formed through atmospheric cooling and brine rejection from sea ice formation (Nicholls et al. 2009). The HSSW sinks down and enters the deep FRIS cavity, where it interacts with the ice shelf base (melting and mixing) and forms Ice Shelf Water (ISW, $\Theta < -1.9^{\circ}$, Gammelsrød et al. 1994). A plume of ISW flows northward along the eastern flank of the Filchner Trough (FT), and overflows the Filchner sill (Foldvik et al. 2004; Darelius et al. 2014a). We refer to it as the Filchner overflow plume, or just the plume. The Filchner overflow plume veers westward under the effect of rotation and follows the continental slope. A hydrographic transect collected across the continental slope in 1999 illustrates the bottom-attached plume (Figure 2). The transect is indicated by a red line on the map Figure 1, and was originally presented in Foldvik et al. (2004, hereafter F04). In this snap-shot, the plume is roughly 45 km wide and up to 500 m thick, and flows westward along the continental slope. Between the cold surface water and the plume, there is a 500 m thick layer of Warm Deep Water (WDW), a slightly cooler and fresher derivative of Circumpolar Deep Water (Heywood et al. 1998). In addition to the westward flowing plume, two northward and down-slope plume pathways are topographically steered along ridges across the continental slope near 36 and 37°W (F04, Darelius and Wåhlin 2007).

The Filchner overflow plume descends into the deep Weddell Sea. En route, the plume entrains ambient water masses and forms Weddell Sea Bottom Water (WSBW), which is ultimately transformed into AABW (Carmack and Foster 1977) through mixing with WDW. The production rates of WSBW depends on the degree of mixing along the Weddell Sea continental slope. F04 estimated an ISW flux of 1.6 ± 0.5 Sv (1 Sv$= 10^6$ m^3 s^{-1}) over the Filchner sill. Based on an estimated mixing and WDW entrainment factor of 2.7, F04 obtained a WSBW production of 4.3 ± 1.4 Sv along the continental slope.

Several processes contribute to the variability of the ISW overflow. A seasonal signal is observed in the hydrographic properties of the ISW, but not for the overflow velocity (Darelius et al. 2014b).

On monthly time scales, the ISW overflow is influenced by monthly scale atmospheric forcing (Daae et al. 2018). In years with strong wind stress along the continental slope, the Filchner overflow velocity is positively correlated with the along-slope (toward 245°) wind stress, upstream of the FT (area marked by yellow lines in Figure 1).

On shorter time scales (12 hours to one week), internal tides and Topographic Vorticity Waves (TVW) along the continental slope, contributes to enhanced Eddy Kinetic Energy (EKE) and mixing. The upper continental slope is favorable for generation of internal waves (Robertson 2001), and is roughly co-located with the critical latitude for the semi-diurnal internal tidal waves (Daae et al. 2009). High mixing rates are therefore expected in the area, and are confirmed by observations (Daae et al. 2009; Fer et al. 2016).TVW (Platzman et al. 1981), also known as coastal trapped waves, are trapped by a coastal wall or a sloping topography due to conservation of potential vorticity (Rhines 1970; Mysak 1980). In the Weddell Sea, excitation of barotropic TVW at the diurnal frequency leads to enhanced EKE and mixing at the diurnal frequency (Middleton et al. 1987; Foldvik et al. 1990; Semper and Darelius 2017). High EKE is also observed in association with lower frequency (sub-inertial) quasi-regular oscillations over the continental slope (Darelius et al. 2009; Jensen et al. 2013). The properties of these oscillations (with periods of 35 hours, 72 hours and 6 days) are consistent with westward propagating TVW (Jensen et al. 2013). Based on numerical simulations, Marques et al. (2014) show that dense overflows, such as the Filchner overflow plume, may generate TVW with properties agreeing with the observed oscillations.

This study focuses on processes controlling the variability and mixing of the the Filchner overflow plume, and their implications for the production of AABW. We present new datasets of hydrography and current velocity from one mooring located at the Filchner Sill (S2) and two moorings (W2 and W3) located on the continental slope, roughly 80 km downstream of the Filchner sill (Figure 1). We study the characteristics and variability of the Filchner overflow plume from daily to monthly time scales, with focus on the shorter time scales. We show that the monthly scale variability is associated to variability from the Filchner sill region, while shorter term variability is related to energetic oscillations with periods of 24 and 72 hours.

2. Data and Methods

a. Moored Instruments

Yearlong data sets of current, temperature and conductivity from three locations at the continental shelf and slope of the southern Weddell Sea are collected using moored instrument arrays. The moorings were deployed in February 2010 and recovered in February 2011. One mooring (S2) was deployed on the Filchner sill at 602 m depth. Two moorings, W2 and W3, were deployed on

the steep continental slope ($\alpha = 0.03$) at the 1411 and 1844 isobaths. W2 and W3 are separated by 16 km, and are located along the ISW pathway roughly 80 km downstream of S2 (Figure 1).

The moorings were equipped with Sea-Bird Electronics temperature (SBE39) and conductivity and temperature recorders (SBE37 Microcat), single point current meters (Aanderaa recording current meter (RCM-7/8/Seaguard) and acoustic Doppler current profilers (ADCP, RD-Instrument (RDI) 300 kHz Sentinel and 75 kHz Longranger). The details of the moorings are given in Table 1. The RCMs averaged 50 evenly distributed samples per hour. The RDI ADCPs sampled an ensemble of 30 pings collected in burst mode for the first 60 seconds every 20 minutes. The data return from the current profilers varies. We exclude data from depth bins where the data return is below 80%. The current profilers depleted batteries in December 2010. One of the RCM7 instruments (W2 at 84 mab) has a gap in the data series between June 16 and August 11, 2010. It is not clear why the instrument did not return any data in this period, but data before and after this gap is of good quality compared to adjacent instruments. The moorings were relatively stable within the water column, with maximum draw-downs of 7/12/22 m at W2/W3/S2, respectively.

We calculate Absolute Salinity (S_A), Conservative Temperature (Θ) and potential density anomalies referenced to 1000 dbar (σ_1) according to TEOS-10 (IOC et al. 2010). The observations cover the 600 to 1800 m depth range, hence σ_1 is the relevant density. The salinity time series are corrected for sensor drift.The range in salinity is generally small ($\sim 34.65 - 34.88$ g kg^{-1} at W2/W3 and $\sim 34.54 - 34.87$ g kg^{-1} at S2). Salinity measurements at 28 mab at W2 and at 70 mab at W3 are corrected with a small offset of +0.012 and -0.013 g kg^{-1}, respectively, using the records from the adjacent instruments and ISW properties as a reference.

b. Transport density, T_d

Transport estimates of the Filchner overflow plume are sensitive to the threshold values defining the cold water, and to the vertical integration of velocity. The presented data set is limited to one mooring over the Filchner sill, and two moorings across the continental slope. Instead of speculating on the width of the plume at each mooring, we report transports per unit width, also referred to as transport density (T_d).

The current and hydrography data are interpolated to common 5 m vertical bins. The current data from 25 mab is linearly extrapolated to zero at the bottom. T_d is calculated using the along-flow component (following the main current direction) observed at 25 mab (299° at S2, 256° at W2, and 291° at W3).

ISW is the dominating water mass at S2. From $\Theta - S_A$ diagrams (Figure 3a), we find that ISW typically has $\sigma_1 > 32.55$ kg m^{-3}, and we use this value as a threshold for the dense water plume at S2. At W2 and W3 there is a strong temperature gradient across the plume interface. We define

the Filchner overflow plume by a threshold temperature of $\Theta < 0°C$, which is commonly used to define AABW (Foster and Carmack 1976). The plume thickness (H_p) is then the height of the 0° C isotherm. The choice of threshold temperature affects the estimated plume thickness. At W2, a threshold temperature of -0.5°C would give a 40 m reduction of the mean plume thickness, compared to having a threshold of 0°C. However, the plume is generally warmer and thinner at W3 compared to W2. By using a threshold of $\Theta = -0.5°$ C the plume would only be captured at W3 for 50% of the time. In order to capture the plume thickness and plume variability at W3, we therefore choose the $\Theta = 0$°C threshold. With this threshold, the plume is captured 92% of the time , and the plume thickness variability is better resolved.

We exclude the current data from 84 mab at W2 because of a 56 day gap in the current time series (Section 2a). Including this instrument decreases T_d at W2 by approximately 20%. T_d is therefore overestimated, but here we focus on the variability rather than the exact value.

The current profilers at both W2 and W3, stopped recording in December 2010. In order to get rough transport density estimates for the remaining record, we rely on the point current meters, and use the time mean currents from the profilers. A constant upper level current will reduce the variability of T_d. However, a substantial part of the transport variability is related to the bottom current, and this variability is still captured in the time series.

c. Filtering analysis

Most figures and calculations are based on hourly averaged data. In addition, we study variability at different time scales using various low-pass and high-pass filters. Where a filter is applied, the cut-off period is given in the text. Low-pass filters are calculated over moving Hanning windows (Lilly 2017). The monthly scale variability is studied using a 15 days low-pass filter, which removes high-frequency variability such as tides, TVW, and short duration storm events. Shorter filters of 13 hours or 24 hours are used to smooth the time series and reduce the semi-diurnal to diurnal tidal signal. High-frequency temperature anomalies associated with the plume interface at W2 and W3 are obtained from 5 minutes temperature records, high pass filtered at 1 hour cut-off frequency.

d. Bulk shear, S_b

The bulk shear at W2 is calculated from $S_b = \Delta\mathbf{U}/H$, where ΔU is the velocity difference between the upper and lower layer, and H is the vertical distance between the layers. Here, we apply a constant $H = 361$ m. The lower layer velocity is represented by the velocity at 25 mab, and the upper layer velocity is calculated from the vertically averaged current between 376 and 396 mab

from the upper RDI Longranger. To remove semi-diurnal tidal signals, we smooth the velocity data using a 13 h low-pass filter prior to calculation of S_b.

e. Internal Froude number, Fr

The Internal Froude number, Fr$= \Delta \mathbf{U}/\sqrt{g' H_p}$, compares the current speed and the phase speed of a long interfacial gravity wave in a two-layer system. Here, ΔU is the velocity difference between the two layers, H_p is the height of the lower (plume) layer, and $g' = g\Delta\rho/\rho_p$ is the reduced gravity in a two-layer system, where g is the gravitational constant, $\Delta\rho$ is the density difference of the two layers, and ρ_p is the lower layer density.

At W2, ΔU is the same as for bulk shear. At W3, the upper layer velocity is calculated from vertically averaged velocities between 252 to 272 mab. We estimate $\Delta\rho$ from potential density referenced to 1000 dbar (σ_1). σ_1 from the lower layer is represented by observations at 28 mab, while the upper layer density is kept constant with $\sigma_1 = 32.52$ kg m^{-3} at W2 and $\sigma_1 = 32.53$ kg m^{-3} at W3. These values are representative of the ambient water density at each mooring. H_p is defined as the height of the $0^{\circ}C$ isotherm.

3. Results

In this section we first present observations of the Filchner Overflow plume over the Filchner sill and along the continental slope downstream. We look at monthly scale variability at the three moorings and estimates of Filchner Overflow transports density (T_d, Section 3a). We then present shorter time series of variability in the plume thickness at W2 and W3, and describe typical thick plume events (Section 3b). Shear and mixing across the plume interface at W2 is presented in Section 3c. The implications of the results are discussed in Section 4.

a. The Filchner Overflow plume

A thick layer of ISW is observed at S2, on the Filchner sill (Figure 4c).The ISW flows toward 298°, and reaches the upper instrument level (176 mab) 65% of the time. Intrusions of lighter water masses ($\sigma_1 < 32.5$ kg m^{-3}) are observed at 104 and 176 mab (Figure 3 and 4c). The intrusions are often accompanied by low transport values, which could indicate that the flow of ISW over the sill is deflected by the presence of the lighter water masses. The hydrographic properties of the ISW layer at S2 varies seasonally (Darelius et al. 2014b). Minimum temperatures are normally found in September-October, and maximum temperatures in April-May. In 2010, the seasonal signal is different at the upper (176 mab) and lower instruments (25 and 104 mab). While the seasonality at 176 mab agrees with earlier observations, we observe continuous cooling and freshening near the bottom from July 2010 until the record ends in February 2011 (not shown). At low temperatures,

salinity dominates the density. The most dense ISW is observed near the bottom, in April-May, when $S_A > 34.85$ g kg^{-1}. In the same period, warmer and lighter water masses are present higher in the water column, leading to maximum vertical density gradients.

The Filchner overflow plume is observed to flow along the continental slope at both W2 and W3 (Figure 3-4). The mean temperature at 25 mab at W2 (W3) is $-1.35°C$ ($-0.65°C$), and ISW is present 20% (3%) of the time, respectively. A seasonality in bottom temperature is found at both W2 and W3, with minimum in September-October, and maximum temperatures in April-May. The seasonality agrees with earlier observations (F-moorings) from the same region in 1998 (Darelius et al. 2014b). We do not observe a seasonal signal in plume velocity, but the seasonality in temperature leads to a weak seasonality in the plume transports (through change of plume thickness), with an amplitude of 1 m^2 s^{-1}.

WDW ($\Theta > 0°$ C) is the dominant water mass in the upper layer. WSBW is present at all instruments, indicating mixing and entrainment of WDW into the Filchner overflow plume (F04). The mean plume thickness (H_p) is 137 m at W2 and 100 m at W3. The plume reaches the upper instrument at W2 (287 mab) at several occasions (Figure 4b).

F04 estimated the transport of cold water in roughly the same area as our moorings (from 1998 over the continental slope, and from 1985 across the Filchner sill, see the locations on the map in Figure 1). A comparison with our measurements is possible after converting their total volume transports to transports density (T_d), using available parameters in their Table 4. This is necessary because we have fewer moorings, and both the location and the vertical resolution is different. At F04's F2 and F3, located in the vicinity of W2-3 we obtain $T_d = 27$ and $T = 26\,\mathrm{m^2\,s^{-2}}$, respectively, similar to our estimate of $T_d = 24\,\mathrm{m^2 s^{-2}}$ at W2. Over the deeper part of the continental slope, the transport is weaker, with $T_d = 7\,\mathrm{m^2 s^{-2}}$ at W3 (1844 m isobath) and $T_d = 1\,\mathrm{m^2 s^{-2}}$ at F4 (1984 m isobath).

At the sill, T_d from S2 and S3 in 1985 in F04 are 9 and $15\,\mathrm{m^2 s^{-2}}$, respectively. These values are smaller than our estimate of $T_d = 23\,\mathrm{m^2 s^{-2}}$ at S2. However, the location of S2 in this study is 13 km east of that in 1985. The S2 mean current velocity at 25 mab in this study is roughly twice that in 1985 (0.17 m s^{-1} compared to 0.08 m s^{-1}). At S2, the instrumentation and measurement depths are similar in 1985 and 2010. A calculation using the method identical to F04 yields $T_d = 34\,\mathrm{m^2 s^{-2}}$ at S2 in 2010, approximately 50% larger than our estimate based on interpolated currents described in section 2b.

The monthly scale plume variability at W2 is connected to the upstream variability at S2. There is an agreement between the T_d at S2 and W2 (Figure 4d). We compute normalized correlation coefficients following Sciremammano (1979), and denote significance levels by superscripts (i.e. $R = 0.6^{99}$ means that R is above the 99% significance level). The correlation between T_d at S2 and

W2 is $R = 0.32^{95}$. The relation is stronger in March to July ($R = 0.51^{95}$), when the along-flow bottom currents are highly correlated (not shown). The highest correlation between S2 and W2 is found for density, σ_Θ, with $R = 0.63^{99}$ between W2 (25 mab) and S2 (177 mab), with a lag of 4.75 days, which agrees with an advection time scale of 5.5 days, estimated from the mean overflow velocity at S2, and a distance of 80 km. Further downstream, at W3, the density correlation with W2 is high ($R = 0.62^{99}$), but the correlation with S2 is weaker ($R = 0.33^{90}$), indicating substantial mixing between S2 and W2.

b. Thick plume events

At W2, the plume thickness fluctuates between less than 25 m (lowermost instrument) and more than 287 m (uppermost instrument at W2) over typical time scales of 1 to 3 days. We detect 240 events when the plume thickness exceeded 100 m during the 362 day record, yielding an average time interval of $\sim$ 36 hours between subsequent thick plume events. Figure 5 shows details of hydrography and currents in June, when strong variations in the plume thickness were observed at all three moorings. The thickest plume event at W2 occurs on 18-19 June, with a minimum temperature of $\Theta = -1.79^\circ$ C at 287 mab, the uppermost extent of the mooring. A similar cold event occurs two days later at W3, with minimum temperature $\Theta = -1.23^\circ$ C at 190 mab (Figure 5a-b). Elevated temperature variance is associated with the passage of thick plume events, as seen in the high-passed records from multiple levels (Figure 5, red lines), and is suggestive of rapid mixing with the ambient (Cenedese and Adduce 2008). Just before, and during the early stage of the thick plume events, Froude numbers exceed unity (Figure 5d), which indicates entrainment and mixing with the ambient water masses (Turner 1973).

Ensembles of plume events are extracted from the data set as segments of $\pm$ 24-hour records, centered at the time of maximum H_p. Ensembles of the thickest plume events at W2 ($H_p >$250 m) and W3 ($H_p >$160 m), constructed from 20 and 22 events, are shown in Figure 6. At both sites, the plume is skewed. The coldest and densest water near the bottom appears before the time of maximum plume thickness. The plume characteristics are more pronounced at W2 compared with W3. The plume extends higher up in the water column, the plume interface is steeper, and there is a vertical shear between the plume and the upper layer. W2 velocity anomalies tend to rotate clockwise from westward to eastward, with a downslope direction during periods of maximum plume thickness (black vectors in Figure 5b and 6). At W3, current vectors rotate during some distinct plume events (e.g. June 2), but this is not a general feature.

c. Shear across the plume interface at W2

We will now look at details of the plume events and the bulk shear at W2. We focus on the period 20 March to 15 April 2010, when large bulk shear and fluctuations in plume thickness are observed (Figure 7).

We decompose the current velocity into clockwise (CW) and counterclockwise (CCW) rotating components with periods of 24 and 72 hours, using complex demodulation over 7 days moving windows (Emery and Thomson 2001). In the following, we denote the sense of rotation with either CW or CCW followed by a subscript indicating the period in hours, e.g. CW_{24} is the clockwise rotation with a period of 24 hours.

Near the bottom, the Filchner overflow plume flows westward (257°) with a mean speed of $0.27\,m\,s^{-1}$. Above the plume (385 mab), a mean current of $0.11\,\mathrm{m\ s^{-1}}$ is directed northwest (320°). Both layers are strongly influenced by oscillations with periods of 24 hours (diurnal tides) and 72 hours (TVW). On average, approximately 10% and 25% of the total variance is explained by the 24- and 72-hour oscillations, respectively.

The bulk shear, S_b, is dominated by the variability in the bottom current, with a mean bulk shear direction toward 253°. Events with S_b^2 elevated above background values occur in pulses. We define a shear spike event by $\partial S_b^2/\partial t > 1\times10^{-11}\,\mathrm{s^{-3}}$. From March 20 to April 15, we identify 21 spike events associated with a thickening of the Filchner overflow plume (marked by red circles in Figure 7). During the shear spike events, there is a tendency of alignment of two counter-rotating oscillations, the upper layer CW_{24}, and the bulk shear CCW_{72}. Alignment occurs in 16 of the 21 shear spike events shown in Figure 7d. Alignment of CW_{24} and CCW_{72} is expected every 36 hour, and is consistent with the observed time interval between two events. Throughout the full record, we observe 279 shear spike events, and roughly 70% of those show such alignment.

4. Discussion

Here we discuss mechanisms for variability at different time scales, and their implications for the production of AABW. We first discuss the low-frequency variability, and then continue with the short-term variability and possible mechanisms of the 72-hour oscillation.

a. Variability on monthly to interannual time scales

The monthly scale variability of the Filchner overflow velocity is related to the upstream along-slope wind stress (area indicated by yellow lines in Figure 1, Daae et al. 2018). The relation varies from year to year, depending on the wind forcing along the slope. In 2010, when data from W2 and W3 are available, the relation between wind stress and overflow velocity at S2 is weak. However, there is significant correlation between the upstream wind stress and the along-flow

bottom current at W2 ($R = 0.41^{95}$), suggesting a wind influence on the bottom current, similar to what is observed in the slope current, upstream of the FT (Fahrbach et al. 1992; Graham et al. 2013; Daae et al. 2018).

Strong monthly scale variability in both dense water hydrography and T_d is observed at the Filchner sill (S2) and on the continental slope downstream (W2 and W3). The variability in hydrography and T_d at W2 and W3 is linked to the upstream conditions at S2 (Section 3a). The highest correlation is found between σ at 176 mab at S2 and at 25 mab at W2 ($R = 0.63^{99}$). The relation could be a direct result of the internal plume variability. In addition, a similar response to the seasonal heaving of the Antarctic Slope Front thermocline (Årthun et al. 2012; Darelius et al. 2016) at the two sites, could enhance the co-variability of the plume density, and contribute to the observed seasonality of T_d at W2. In a model study, Wang et al. (2012) found a seasonal signal in the Filchner shelf water export rate, resulting from onshore propagating density anomalies related to wind-forced isopycnal depression at the coast. We do not observe such seasonality in T_d or the overflow velocity at S2. However, the total ISW transport is not resolved, as our study is based on only one moored array. Additional observations across the ISW plume is needed to assess the seasonality of the plume.

Wang et al. (2012) show that the seasonality of the Filchner export rate affects the WSBW transports in the western Weddell Sea. However, the Filchner overflow is not the only source of WSBW in the western Weddell Sea. Export of HSSW from the central and western part of the continental shelf contributes largely to the observed WSBW near the South Orkney Islands (Foldvik et al. 1985; Gordon et al. 2010). Gordon et al. (2010) suggest that seasonality of the HSSW export rate, associated with regional winds and Ekman transport, is the main source of the WSBW seasonality observed in the western Weddell Sea.

b. Source of oscillations

Oscillations with periods of 24 and 72 hours dominate the current variability at W2. The 24-hour oscillation is a result of strong diurnal tides and excitation of barotropic TVW (Middleton et al. 1987). The properties of the 72-hour oscillation is also consistent with TVW (Jensen et al. 2013). However, the high energy levels at this frequency could also result either from eddies moving through the region, or from instabilities generated locally within the plume. Laboratory experiments (Lane-Serff and Baines 2000) and idealized numerical model experiments (Wang et al. 2009) suggest that vortex stretching in the Filchner overflow plume, would lead to eddies with periods of about 3 days. Other mechanisms known to induce instability are *(i)* roll waves and *(ii)* baroclinic instability.

(i) Roll Waves: The observed thick plume events resemble the expected signal from internal roll waves. High Froude numbers (FR$>$ 2), which is the necessary criterion the development of roll waves (Fer et al. 2002; Swaters 2003), occur frequently (Figure 5d and 7b), especially in the first part of the records (March to July). However, the period of the plume events are subintertial (1-3 days), while roll waves are expected to occur at superinertial frequencies. Swaters (2003) report roll waves with periods around 2 hours. The role of bottom friction over the Weddell sea continental slope is also smaller than the rotational effect. The bottom friction term $C_D|\mathbf{u_b}|\mathbf{u_b}/H_p$ and the Coriolis term $f\mathbf{u_b}$, calculated using a drag coefficient of $C_D = 0.003$ (a typical value for energetic overflows, calculated from microstructure measurements in the Faroe Bank Channel overflow, Fer et al. 2010), with $\mathbf{u_b}$ the velocity at 25 mab, H_p the height of the 0°C isotherm and f the Coriolis parameter, gives an average ratio of Coriolis to friction terms of approximately 19. Although the value of C_D might be underestimated and the velocity at 25 mab might not be representative for the bottom current, the results indicate that the effect of rotation is more important than the effect of bottom friction. We conclude that the thick plume events are not a result of roll waves.

(ii) Baroclinic instability: Moorings W2 and W3 are located on a steep continental slope, with a slope of 0.03. Over sloping topography, baroclinic instability on a plume interface can lead to development of alternating cyclonic and anticyclonic eddies (Tanaka and Akitomo 2001). The sloping topography has both a stabilizing effect due to the topographic β effect, and a destabilizing effect due to steepening of the inclination of the isopycnal surface. Unstable waves occur more frequently on steep slopes, where the destabilizing effect overcomes the stabilizing effect. However, the eddy transport velocity decreases as the slope steepens (Tanaka 2006) and the duration of the development stage reduces. According to Tanaka (2006), baroclinic instabilities over the Weddell Sea continental slope reach a mature stage after 16 days. We infer a similar time scale using a two-layer linear instability model (Reszka et al. 2002) with a continuously stratified upper layer and parameters representative of the Weddell Sea slope. No combinations of plume thickness, plume width or slope steepness gave periods shorter than 20 days. Furthermore, growing baroclinic instabilities require a substantial vertical phase shift (Spall and Price 1998). Eddies formed from growing baroclinic instabilities are stronger within the dense bottom layer than within the fluid above. Vertical coherence and phase at W2, calculated for three frequency bands (24h, 35h and 3d) show relatively small vertical phase shifts for the cross-slope velocity component ($2-6^\circ/100$ m) for all frequency bands, referenced to 396 mab. Our observations are therefore not suggestive of baroclinic instability, but agree with Darelius et al. (2009) who suggest that TVW or vortex stretching are more likely causes of the 72-hour oscillation.

c. Alignment of oscillations with 24 and 72 hour periods

Shear spiking may trigger the development of shear instabilities and contribute to diapcynal mixing. Shear spiking is a significant source of turbulent kinetic energy production across the seasonal thermocline in shallow stratified shelf seas (Rippeth et al. 2009; Burchard and Rippeth 2009), near the sea bed in Arctic shelf seas (Lenn et al. 2011), and at the base of the oceanic mixed layer (Brannigan et al. 2013). We typically find that the upper layer CW_{24} and the plume layer CCW_{72} are aligned during shear spike events. Associated with these shear spikes, we observe enhanced temperature variances, high Froude numbers, and a thickening of the plume, which indicate strong mixing and entrainment of ambient water (Cenedese and Adduce 2008). The thick plume events following the shear spikes contribute significantly to the dense water transport density, T_d, along the continental slope. By excluding the lower part of the plume in the T_d estimates, we find that the portion of the plume which is thicker than 75/100/150 m contributes with 38/23/7% of the total T_d at W2, and 20/10/2% of T_d at W3, respectively.

Alignment of the CW_{24} and the CCW_{72} oscillations does not explain all the detected shear spikes. In theory, the CW_{24} and the CCW_{72} oscillation are aligned every 36 hour, which agrees with the observed average time interval between two thick plume events. However, along the Weddell Sea continental shelf, presence of TVWs with a similar period ($\sim$ 35 hours) are observed (Jensen et al. 2013). These waves may interfere with the alignment of CW_{24} and CCW_{72} studied here, and could explain why not all shear spikes occur during alignment of CW_{24} and CCW_{72}.

d. Revised transport estimates at the Filchner sill

F04 estimated a cold shelf water transport of 1.6 $\pm$0.5 Sv over the Filchner sill based on two moorings from 1985 (see map in Figure 1). Three year-long records exist from the westernmost mooring site, S2 (1977, 1985, and 1987). The mean overflow velocities are similar in all these records (Darelius et al. 2014b; Daae et al. 2018). The S2 mooring location was shifted roughly 16 km eastward in 2003, 2009, and 2010. The new S2 location is just between the S2 and S3 sites from 1985 (see map in Figure 1). Observations from the new S2 location roughly indicate a doubling of the overflow velocity (Darelius et al. 2014b). The difference in overflow velocity could be explained by increasing ISW transport since 1987. However, it is more likely that the new S2 site is located closer to the core of the ISW flow, and that the velocity therefore is higher. If this is the case, the transport estimates made by F04 could be underestimated, since they do not include the high velocities in the core of the ISW flow. If we estimate the transport of cold water at the new S2 site using the same method as F04, and assigning a width of 65 km (as they do for their S2), we obtain a transport of 2.2 Sv. This is 0.5 Sv more than their estimate from the combined S2 and S3 moorings with a total width of 137 km

Our method for estimating transport densities, T_d (see section 2b), gives significantly lower values compared with F04's method. The discrepancy could be related to the ISW threshold and/or to the vertical extrapolation. Firstly, at cold temperatures, the density mainly depends on salinity. Salinity was not observed in 1985. While we estimate the vertical extent of ISW based on density, F04 were relying on temperature, which could lead to differences. Secondly, we do not extrapolate the currents vertically. We interpolate toward zero velocity at the bottom, and do not include parts of the water column situated above the upper instrument. However, applying the same temperature-based ISW threshold as F04 we found no change in T_d at S2 ($T_d = 23$ m^2 s^{-1} in both cases). We therefore conclude that the vertical interpolation is causing the discrepancy.

The transport estimates across the continental slope (W2 and W3) compare well with those by F04 (F-section). However, keeping in mind the discrepancy in transports estimated from the two methods at S2, we cannot say whether or not the Filchner overflow transport is similar in 1998 and 2010.

e. Formation of AABW in a changing climate

Production of AABW depends both on the source water masses (HSSW and ISW) and on the entrainment of WDW during the descent along the continental slope (Gill 1973; Orsi 1999). The AABW has become fresher since the 1980's (Purkey and Johnson 2013). The freshening is most pronounced in the south Pacific and the south Indian ocean, where the freshening corresponds to roughly half the recent mass loss of the West Antarctic Ice Sheet. Although the freshening of AABW from the Atlantic sector is weaker, freshening of the AABW exported from the Weddell Sea is significant (Jullion et al. 2013). Atmospheric-forced ice shelf collapse, deglaciation, and sea ice changes on the eastern side of the Antarctic Peninsula are suggested to be the main source of AABW freshening (Jullion et al. 2013). Another possible source to freshening is changes in the sea ice production and export over the continental shelf. During the last 30 years, the sea ice production over the Weddell Sea continental shelf has substantially reduced, with subsequent reduction in both formation of HSSW and transport of HSSW under the Filchner-Ronne Ice Shelf (K. W. Nicholls, P. Holland, S. Østerhus and K. Makinson, unpublished manuscript). In turn, this leads to a freshening of the Filchner overflow plume and also fresher AABW.

Our study suggests that high shear and mixing across the Filchner overflow plume interface is related to alignment of counter-rotating oscillations with periods of 24 and 72 hours. This mechanism may be important for the entrainment of WDW and the production of AABW. The sensitivity of this mixing mechanism to ISW freshening is uncertain. While the 24-hour oscillation is related to tides and TVW, which are independent of the ISW density, the 72-hour oscillation is associated with vortex stretching or TVW from the Filchner overflow plume. The amplitude or

frequency of the oscillation may change if the ISW freshens. Given that the ISW freshening is moderate, the 72-hour oscillation can be expected to persist in the future. However, if the Filchner overflow transport is reduced, the thickness and pathway of the plume along the continental slope may change, which could in turn, lead to changes in the mixing mechanisms and production rates of AABW.

5. Conclusions

We present observations of hydrography and current from three moorings located along the pathway of the Filchner overflow plume in the southeastern Weddell Sea. The monthly scale plume variability over the continental slope (mooring W2) is related to upstream conditions over the Filchner sill (mooring S2). A strong variability in plume thickness is observed along the continental slope on shorter time scales (1 to 3 days). The thickness of the plume varies from less than 25 m to more than 287 m. Shear spikes are observed during the early stage of the plume thickening, and may contribute to enhanced mixing and entrainment of ambient water masses. The shear spikes are associated with alignment of clockwise (CW) and counterclockwise (CCW) rotating oscillations with periods of 24 and 72 hours, respectively. CW_{24} is related to diurnal tides and Topographic Vorticity Waves (TVW), while CCW_{72} could either result from vortex stretching of the dense plume (Lane-Serff and Baines 2000; Darelius et al. 2009; Wang et al. 2009) or from westward propagating TVW (Jensen et al. 2013).

In addition to shear spikes, we observe high temperature variance, and high Froude numbers, which also indicate enhanced mixing. Mixing and entrainment are important for the production of WSBW, which is ultimately transformed into AABW. Provided that the suggested mixing mechanism between ISW and WDW is invariant to a moderate freshening of the ISW, future changes in WSBW properties will depend on processes controlling the formation of dense shelf water over the continental shelf.

References

Årthun, M., K. W. Nicholls, K. Makinson, M. a. Fedak, and L. Boehme, 2012: Seasonal inflow of warm water onto the southern Weddell Sea continental shelf, Antarctica. *Geophysical Research Letters*, **39 (17)**, doi:10.1029/2012GL052856.

Brannigan, L., Y.-D. Lenn, T. P. Rippeth, E. McDonagh, T. K. Chereskin, and J. Sprintall, 2013: Shear at the Base of the Oceanic Mixed Layer Generated by Wind Shear Alignment. *Journal of Physical Oceanography*, **43 (8)**, 1798–1810, doi:10.1175/JPO-D-12-0104.1.

Burchard, H., and T. P. Rippeth, 2009: Generation of Bulk Shear Spikes in Shallow Stratified Tidal Seas. *Journal of Physical Oceanography*, **39 (4)**, 969–985, doi:10.1175/2008JPO4074.1.

Carmack, E. C., and T. Foster, 1977: Water masses and circulation in the Weddell Sea. *Proceedings of the Polar Ocean Conference, Montreal, 1974*, 151–165.

Cenedese, C., and C. Adduce, 2008: Mixing in a density-driven current flowing down a slope in a rotating fluid. *Journal of Fluid Mechanics*, **604**, 369–388, doi:10.1017/S0022112008001237.

Daae, K., I. Fer, and E. P. Abrahamsen, 2009: Mixing on the continental slope of the southern Weddell Sea. *Journal of Geophysical Research*, **114 (C9)**, 1–13, doi:10.1029/2008JC005259.

Daae, K., I. Fer, and E. Darelius, 2018: Wind stress mediated variability of the Filchner Trough overflow, Weddell Sea. *J. Geophys. Res Ocean*, **in review**.

Darelius, E., I. Fer, and K. W. Nicholls, 2016: Observed vulnerability of Filchner-Ronne Ice Shelf to wind-driven inflow of warm deep water. *Nature communications*, **7**, 1–7, doi:10.1038/ncomms12300.

Darelius, E., K. Makinson, K. Daae, I. Fer, P. R. Holland, and K. W. Nicholls, 2014a: Hydrography and circulation in the Filchner Depression, Weddell Sea, Antarctica. *Journal of Geophysical Research: Oceans*, **119**, 1–18, doi:10.1002/2014JC010225.

Darelius, E., L. H. Smedsrud, S. Østerhus, A. Foldvik, and T. Gammelsrød, 2009: Structure and variability of the Filchner overflow plume. *Tellus A*, **61 (3)**, 446–464, doi:10.1111/j.1600-0870.2009.00391.x.

Darelius, E., K. O. Strand, S. Østerhus, T. Gammelsrød, M. Årthun, and I. Fer, 2014b: On the Seasonal Signal of the Filchner Overflow, Weddell Sea, Antarctica. *Journal of Physical Oceanography*, **44 (4)**, 1230–1243, doi:10.1175/JPO-D-13-0180.1.

Darelius, E., and A. K. Wåhlin, 2007: Downward flow of dense water leaning on a submarine ridge. *Deep Sea Research Part I: Oceanographic Research Papers*, **54 (7)**, 1173–1188, doi:10.1016/j.dsr.2007.04.007.

Emery, W., and R. Thomson, 2001: *Data Analysis Methods in Physical Oceanography*. 2nd ed., Elsevier Science.

Fahrbach, E., and S. el Naggar, 2001: The Expeditions ANTARKTIS XVI/ 12 of the Research Vessel POLARSTERN" in 1998/1999. *Ber. Polar- und Meeresforsch*, **380**, 177pp.

Fahrbach, E., G. Rohardt, and G. Krause, 1992: The Antarctic coastal current in the southeastern Weddell Sea. *Polar Biology*, **12 (2)**, 171–182, doi:10.1007/BF00238257.

Fer, I., E. Darelius, and K. Daae, 2016: Observations of energetic turbulence on the Weddell Sea continental slope. *Geophysical Research Letters*, 760–766, doi:10.1002/2015GL067349.

Fer, I., U. Lemmin, and S. Thorpe, 2002: Winter cascading of cold water in Lake Geneva. *Journal of Geophysical Research*, **107 (C6)**.

Fer, I., G. Voet, K. S. Seim, B. Rudels, and K. Latarius, 2010: Intense mixing of the Faroe Bank Channel overflow. *Geophysical Research Letters*, **37 (2)**, 2–6, doi:10.1029/2009GL041924.

Foldvik, A., and T. Gammelsrød, 1988: Notes on Southern Ocean hydrography, sea-ice and bottom water formation. *Palaeogeography, Palaeoclimatology, Palaeoecology*, **67**, 3–17.

Foldvik, A., T. Kvinge, and T. Tørresen, 1985: Bottom currents near the continental shelf break in the Weddell Sea. *Antarctic Research Series*, **43**, 21–32.

Foldvik, A., J. Middleton, and T. Foster, 1990: The tides of the southern Weddell Sea. *Deep Sea Research*, **37 (8)**, 1345–1362.

Foldvik, A., and Coauthors, 2004: Ice shelf water overflow and bottom water formation in the southern Weddell Sea. *Journal of Geophysical Research*, **109 (C2)**, 1–15, doi:10.1029/2003JC002008.

Foster, T., and E. C. Carmack, 1976: Temperature and salinity structure in the Weddell Sea. *J. Phys. Oceanogr*, **6**, 36–44.

Gammelsrød, T., and Coauthors, 1994: Distribution of water masses on the continental shelf in the southern Weddell Sea. *Geophysical Monograph*, **84**, 158–176.

Gill, A., 1973: Circulation and bottom water production in the Weddell Sea. *Deep Sea Research and Oceanographic Abstracts*, **20 (2)**, 111–140, doi:10.1016/0011-7471(73)90048-X.

Gordon, A. L., B. Huber, D. McKee, and M. Visbeck, 2010: A seasonal cycle in the export of bottom water from the Weddell Sea. *Nature Geoscience*, **3 (8)**, 551–556, doi:10.1038/ngeo916.

Graham, J. A., K. J. Heywood, C. P. Chavanne, and P. R. Holland, 2013: Seasonal variability of water masses and transport on the Antarctic continental shelf and slope in the southeastern Weddell Sea. *Journal of Geophysical Research: Oceans*, **118 (4)**, 2201–2214, doi:10.1002/jgrc.20174.

Heywood, K. J., R. A. Locarnini, R. D. Frew, P. F. Dennis, and B. A. King, 1998: Transport and Water Masses of the Antarctic Slope Front System in the Eastern Weddell Sea. *Ocean, Ice, and Atmosphere - Interaction at the Antarctic Continental Margin*, **75**, 203–214.

IOC, SCOR, and IAPSO, 2010: The international thermodynamic equation of seawater - 2010: Calculation and use of thermodynamic properties. Intergovernmental Oceanographic Commission, Manuals and Guides No. 56, UNESCO (English). Tech. rep., 196 pp pp.

Jensen, M. F., I. Fer, and E. Darelius, 2013: Low frequency variability on the continental slope of the southern Weddell Sea. *Journal of Geophysical Research: Oceans*, **118**, 1–17, doi:10.1002/jgrc.20309.

Jullion, L., A. C. Naveira Garabato, M. P. Meredith, P. R. Holland, P. Courtois, and B. A. King, 2013: Decadal Freshening of the Antarctic Bottom Water Exported from the Weddell Sea. *Journal of Climate*, **26**, 8111–8125, doi:10.1175/JCLI-D-12-00765.1.

Lane-Serff, G., and P. Baines, 2000: Eddy formation by overflows in stratified water. *Journal of Physical Oceanography*, **(1995)**, 327–337, doi:10.1175/1520-0485(2000)030⟨0327:EFBOIS⟩2.0.CO;2.

Lenn, Y.-D., T. P. Rippeth, C. P. Old, S. Bacon, I. Polyakov, V. Ivanov, and J. Hölemann, 2011: Intermittent Intense Turbulent Mixing under Ice in the Laptev Sea Continental Shelf. *Journal of Physical Oceanography*, **41 (3)**, 531–547, doi:10.1175/2010JPO4425.1.

Lilly, J., 2017: jLab: A data analysis package for matlab, v. 1.6.3. URL http://www.jmlilly.net/jmlsoft.html.

Marques, G. M., L. Padman, S. R. Springer, S. L. Howard, and T. M. Özgökmen, 2014: Topographic vorticity waves forced by Antarctic dense shelf water outflows. *Geophysical Research Letters*, **41 (4)**, 1247–1254, doi:10.1002/2013GL059153.

Middleton, J., T. Foster, and A. Foldvik, 1987: Diurnal shelf waves in the southern Weddell Sea. *Journal of Physical Oceanography*, **17**, 784–791.

Mysak, L., 1980: Recent advances in shelf wave dynamics. *Reviews of Geophysics*, **18 (1)**, 211–241.

Nicholls, K. W., S. Østerhus, K. Makinson, T. Gammelsrød, and E. Fahrbach, 2009: Ice-ocean processes over the continental shelf of the southern Weddell Sea , Antarctica: A review. *Reviews of Geophysics*, **47 (3)**, 1–23, doi:10.1029/2007RG000250.

Orsi, A. H., 1999: Circulation, mixing, and production of Antarctic Bottom Water. *Progress In Oceanography*, **43 (1)**, 55–109, doi:10.1016/S0079-6611(99)00004-X.

Platzman, G. W., G. a. Curtis, K. S. Hansen, and R. D. Slater, 1981: Normal Modes of the World Ocean. Part II: Description of Modes in the Period Range 8 to 80 Hours. 579–603 pp., doi:10.1175/1520-0485(1981)011⟨0579:NMOTWO⟩2.0.CO;2.

Purkey, S. G., and G. C. Johnson, 2013: Antarctic Bottom Water Warming and Freshening : Contributions to Sea Level Rise , Ocean Freshwater Budgets , and Global Heat Gain. *Journal of Climate*, **26**, 6105–6122, doi:10.1175/JCLI-D-12-00834.1.

Reszka, M., G. E. Swaters, and B. Sutherland, 2002: Instability of abyssal currents in a continuously stratified ocean with bottom topography. *Journal of Physical Oceanography*, **32**, 3528–3550.

Rhines, P., 1970: Edge-. Bottom-, and Rossby Waves in a rotating and Stratified Fluid. *Geophysical Fluid Dynamics*, **1 (3-4)**, 273–302.

Rippeth, T. P., P. Wiles, M. R. Palmer, J. Sharples, and J. Tweddle, 2009: The diapcynal nutrient flux and shear-induced diapcynal mixing in the seasonally stratified western Irish Sea. *Continental Shelf Research*, **29 (13)**, 1580–1587, doi:10.1016/j.csr.2009.04.009.

Robertson, R., 2001: Internal tides and baroclinicity in the southern Weddell Sea 1. Model description. *Journal of Geophysical Research*, **106 (C11)**, 27 001–27 016, doi:10.1029/2000JC000475.

Sciremammano, F., 1979: Suggestion for the Presentation of Correlations and Their Significance Levels. *J. Phys. Oceanogr*, **9**, 1273–1276, doi:http://dx.doi.org/10.1175/1520-0485(1979)009⟨1273:ASFTPO⟩2.0.CO;2.

Semper, S., and E. Darelius, 2017: Seasonal resonance of diurnal continental shelf waves in the southern Weddell Sea. *Ocean Science*, **13**, 77–93, doi:10.5194/os-2016-36.

Spall, M., and J. Price, 1998: Mesoscale variability in Denmark strait: The PV outflow hypothesis*. *Journal of Physical Oceanography*, **28 (1969)**, 1598–1623.

Swaters, G. E., 2003: Baroclinic characteristics of frictionally destabilized abyssal overflows. *Journal of Fluid Mechanics*, **489**, 349–379, doi:10.1017/S0022112003005135.

Tanaka, K., 2006: Effects of the Earth's rotation and bottom slope on a density current descending a sloping bottom. *Journal of Geophysical Research*, **111 (C11)**, C11 018, doi:10.1029/2006JC003677.

Tanaka, K., and K. Akitomo, 2001: Baroclinic instability of density current along a sloping bottom and the associated transport process. *Journal of Geophysical Research*, **106 (C2)**, 2621–2638.

Turner, J., 1973: *Buoyancy effects in fluids*. Cambridge University Press, 367 pp.

Wang, Q., S. Danilov, E. Fahrbach, J. Schröter, and T. Jung, 2012: On the impact of wind forcing on the seasonal variability of Weddell Sea Bottom Water transport. *Geophysical Research Letters*, **39 (6)**, doi:10.1029/2012GL051198.

Wang, Q., S. Danilov, and J. Schröter, 2009: Bottom water formation in the southern Weddell Sea and the influence of submarine ridges: Idealized numerical simulations. *Ocean Modelling*, **28 (1-3)**, 50–59, doi:10.1016/j.ocemod.2008.08.003.

Acknowledgments. This work is supported by the Centre for Climate Dynamics at the Bjerknes Centre and by the Norwegian Research council's FRINATEK program through the project WARM (231549) and through the NARE program under the project WEDDELL (211415). For deployment and recovery of moorings, we would like to thank Svein Østerhus and the crew and scientists on RRS Ernest Shackleton (cruise ES052) and RRS James Clark Ross (cruise JR244). Moorings data from W2 and W3 are available at https://doi.org/10.1594/PANGAEA.871146. Mooring data from S2 was provided by Svein Østerhus (Uni Research Climate, and the Bjerknes Centre for Climate Research, Bergen, Norway), and is submitted to the Norwegian Marine Data Centre (NMDC), http://www.nmdc.no

LIST OF TABLES

TABLE 1. Overview of the moorings on the Filchner sill (S2) and over the continental slope downstream (W2-3). Parameter T is temperature, C is conductivity, P is pressure, V is horizontal velocity and W is vertical velocity.

Mooring Name	Time (UTC) (in/out)	Position (lon/lat)	Record days	Bottom Depth (m)	Height (mab)	Parameter	Instrument	Sampling rate (min)
S2	13 Feb 2010	$33^o30'10''W$	362	612	25	T,V	RCM-7	60
	16:13	$74^o38'3''S$	362		26	T,C,P	Microcat	5
			362		104	T,V	RCM-7	60
	11 Feb 2011		362		105	T,C	Microcat	5
	16:43		362		176	T,V	RCM-7	60
			362		177	T,C,P	Microcat	5
W2	17 Feb 2010	$36^o1'13''W$	362	1411	25	T,V	RCM-7	60
	21:00	$74^o21'41''S$	362		28	T,C	Microcat	5
			362		50	T,C,P	Microcat	5
	14 Feb 2011		362		63	T,P	SBE39	5
	08:06		274[a]		84	T,V	RCM-7	60
			362		94	T,C,P	Microcat	5
			362		138	T	SBE39	5
			362		181	T,C,P	Microcat	5
			299-303[b]		198:4:234	T,V,W	RDI Sentinel Down	20
			362		257	T,C	Microcat	5
			362		287	T,C,P	Microcat	5
			319		296:4:396	$T,V,W4$	RDI Longranger Up	20
W3	16 Feb 2010	$35^o55'18''W$	360	1844	25	T,P,V	Seaguard	20
	13:00	$74^o13'6''S$	360		28	T,C	Microcat	5
			360		70	T,C,P	Microcat	5
	14 Feb 2011		360		82	T	SBE39	5
	12:50		360		93	V	RCM-8	60
			360		109	T,C,P	Microcat	5
			360		160	T,C	Microcat	5
			360		190	T,C,P	Microcat	5
			262-304[b]		223.5:4:271.5	T,V,W	RDI Sentinel down	20
			360		277	T,C,P	Microcat	5

[a] Missing data between 16 June 2010 to 11 August 2010. [b] Shorter time series at the deepest cells.

LIST OF FIGURES

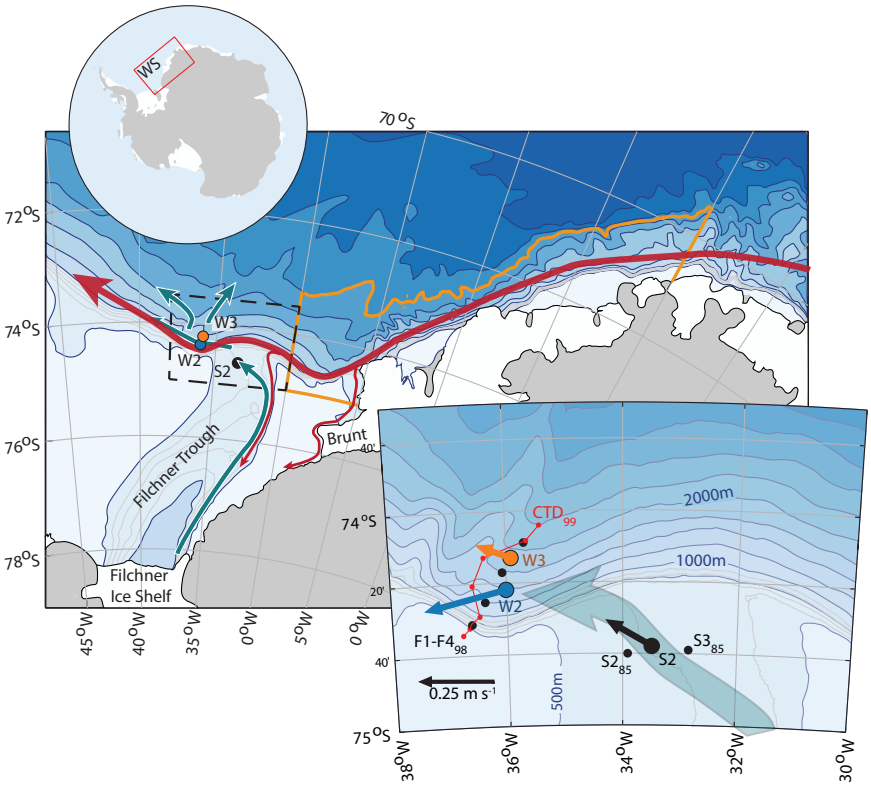

FIG. 1. Map showing the Southeastern Weddell Sea (WS) bathymetry, circulation and the mooring locations. The slope current is indicated by a thick red arrow, where the thinner arrows show the Antarctic Coastal Current and the seasonal inflow into the FT. The turquoise arrows show the overflow of ISW from the FT and possible pathways identified by F04. ERA upstream Wind is extracted from the region bounded by the orange line and the coast. The lower inset shows a zoom-in of the region bounded by black, dashed lines. Colored arrows from each mooring location show vector mean currents at 25 meter above bottom (mab), with a corresponding scale arrow in the lower left corner. Black dots refer to mooring locations in F04, and the red line indicate a Conductivity-Temperature-Depth (CTD) transect obtained in 1999 during the curise ANT XVI/2.

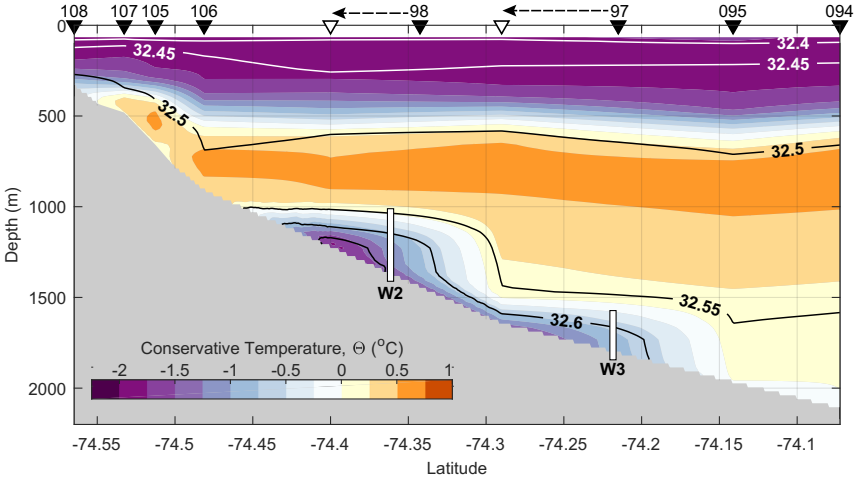

654 FIG. 2. Conservative Temperature (Θ, colors), and density anomalies (σ_1, contours) across the continental
655 slope, obtained from cruise ANT XVI/2 in 1999 (Fahrbach and el Naggar 2001). The transect was originally
656 presented in F04. Here, the temperature is converted to conservative temperature, Θ, and the horizontal axis
657 represent latitude instead of distance. The section (shown in red on the map in figure 1) is obtained roughly
658 along a northeast oriented ridge. However, two profiles (station 97-98) are obtained closer to the ridge, where
659 the isobaths curve toward northwest. To account for the shallower isobaths at these stations, compared to the
660 isobaths along a straight section line, we have shifted their latitudinal position. Station number, and the real
661 latitudes are shown with black annotated triangles. The shifted latitudes of station 97-98 are shown with white
662 triangles. The W2 and W3 moorings are overlain in this snapshot of observations for context.

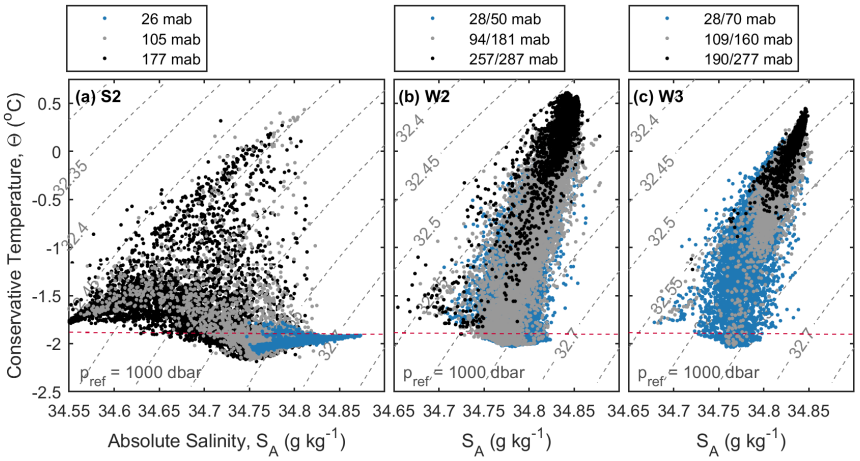

663 FIG. 3. $\Theta - S_A$ diagrams for (a) S2, (b) W2, and (c) W3. Contours of density anomalies are referenced to
664 1000 dbar (σ_1). The red dashed lines indicate the freezing temperature of sea water.

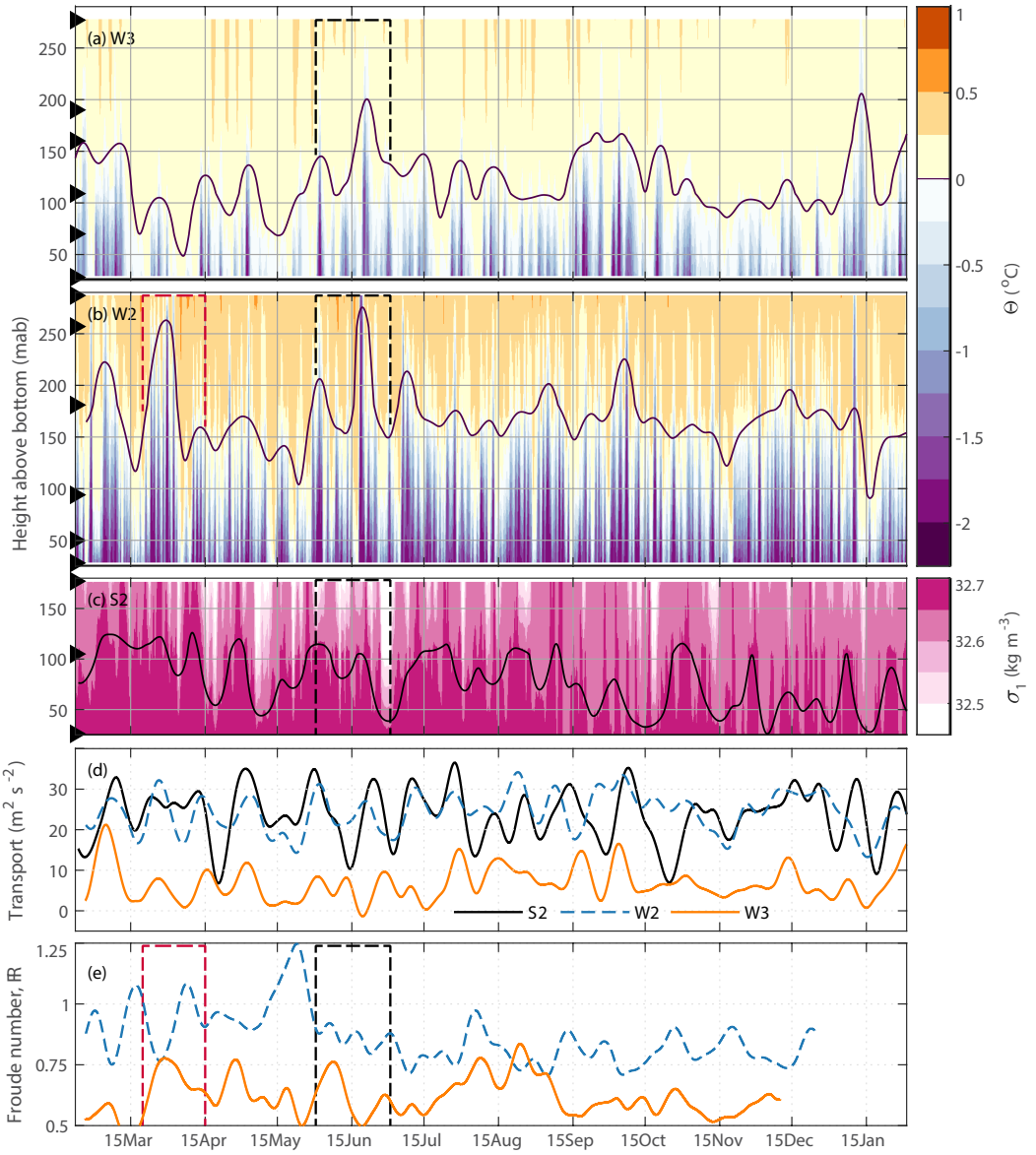

665 FIG. 4. 24 hour low-passed time series of Conservative Temperature, Θ, at (a) W3, and (b) W2, and (c)
666 potential density anomaly referenced to 1000 dbar, σ_1 at S2. Contours of the 15 day low-passed $\Theta = 0°C$
667 isotherms at W2 and W3 (purple lines) and the $\sigma_1 = 32.65$ kg m^{-3} isopycnal at S2 (black line) are drawn on
668 top. Time series of 15 days low-passed (d) plume transport density, T_d, and (e) Froude number at W2 (blue),
669 W3 (orange), and S2 (black). The black dashed boxes indicate the period shown in Figure 5, and the red dashed
670 boxes indicate the period shown in Figure 7.

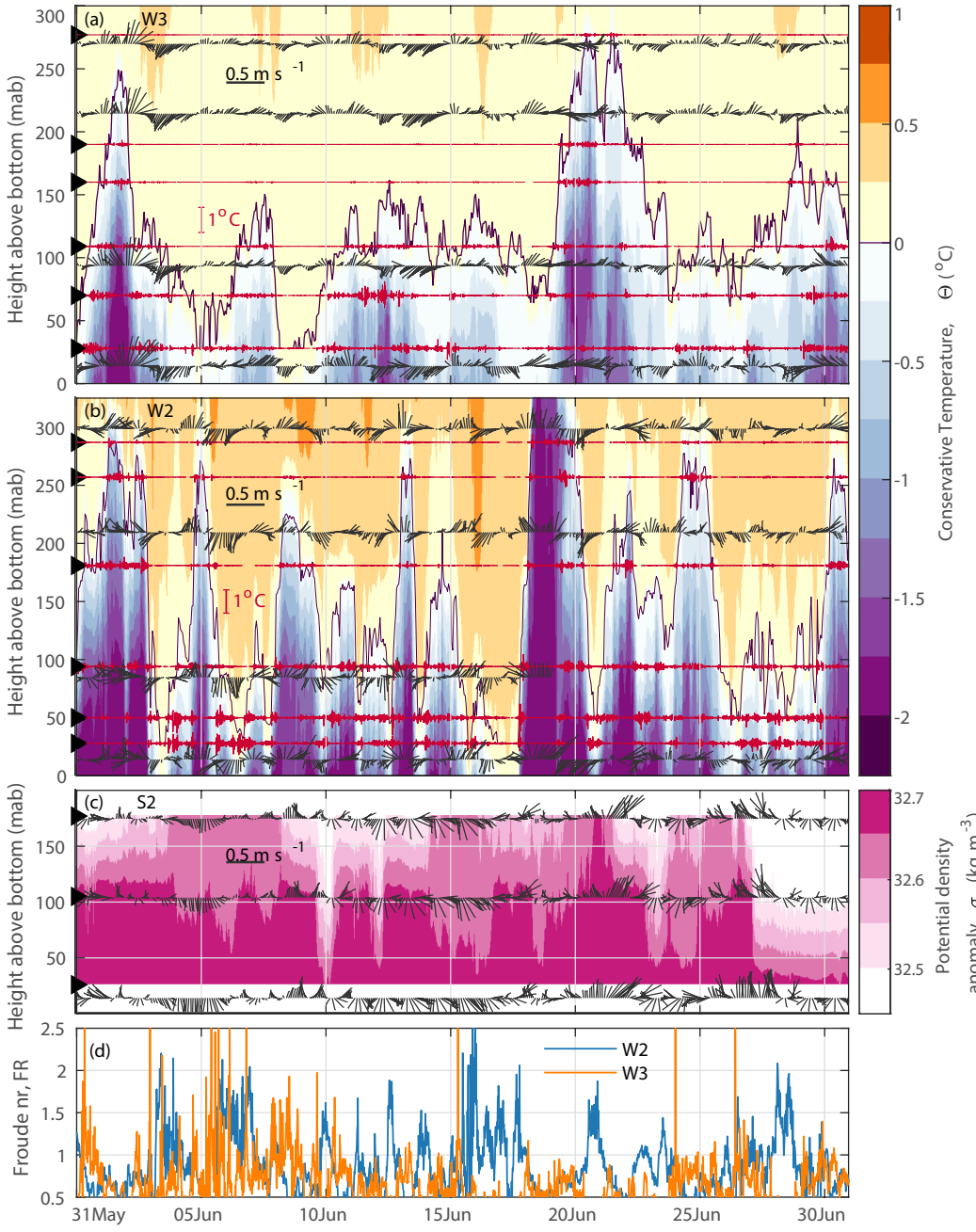

FIG. 5. Time series of hourly averaged Conservative Temperature, Θ, at (a) W3, and (b) W2, and (c) potential density anomaly referenced to 1000 dbar, σ_1 at S2. Vectors of current anomalies (black) are shown from selected depths, with scales indicated by black horizontal bars. High-passed temperature anomalies at (a) W3 and (b) W2 are shown in red, with scales indicated by red vertical bars. (d) Time series of the Froude numbers (Fr), calculated from the along-flow component of the current velocity at W2 (blue) and W3 (orange).

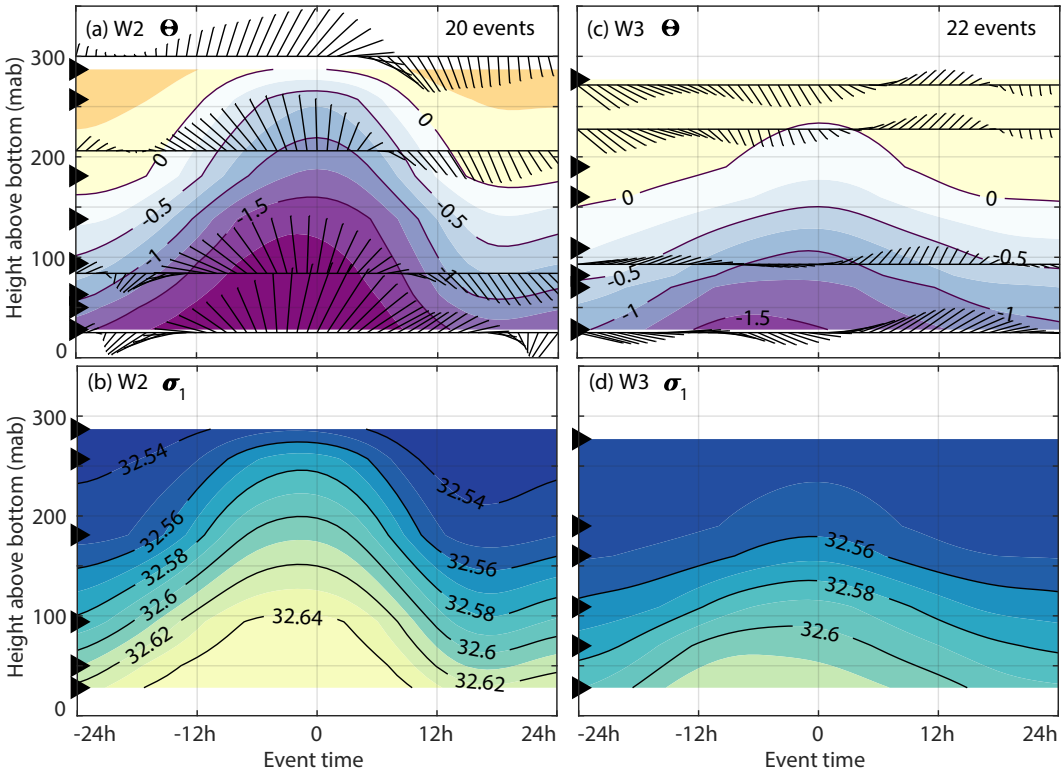

676 FIG. 6. Ensembles of (a,c) Conservative Temperature and (b,d) current anomaly and density during thick
677 plume events at W2 ($H > 250$ m, left panels) and W3 ($H > 160$ m, right panels).

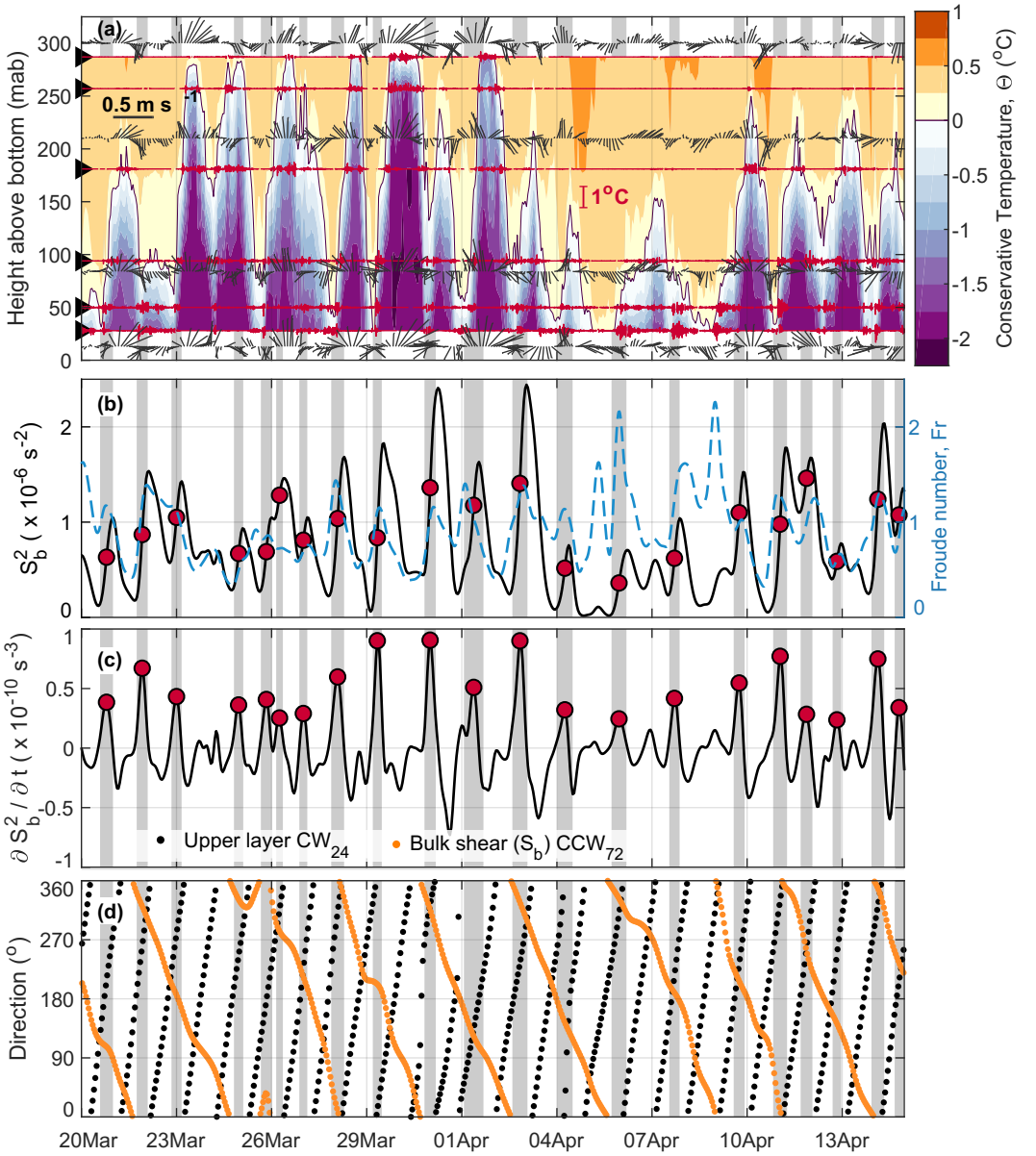

FIG. 7. (a) Time series of Conservative Temperature, Θ, (colors), high-passed Θ anomalies (thin, red lines), and current vector anomalies (black) at W2. (b) Bulk shear squared (S_b^2) between 25 mab and 388 mab. (c) Time derivative of the bulk shear squared, and (d) direction of CW_{24} in the upper layer (black) and the CCW_{72} in the bulk shear (orange). Red circles show peaks in $\partial S_b^2/\partial t$ above a threshold of 2×10^{-11} s^{-3}, and the gray shading indicate the duration (width at half-prominence) of each spike event.

Bibliography

Allen, S. E., and X. Durrieu de Madron (2009), A review of the role of submarine canyons in deep-ocean exchange with the shelf, *Ocean Science Discussions*, *6*(2), 1369–1406, doi: 10.5194/osd-6-1369-2009. 1.2

Allen, S. E., and B. M. Hickey (2010), Dynamics of advection-driven upwelling over a shelf break submarine canyon, *Journal of Geophysical Research: Oceans*, *115*(8), 1–20, doi: 10.1029/2009JC005731. 2.3

Andreas, E. L., T. W. Horst, A. a. Grachev, P. O. G. Persson, C. W. Fairall, P. S. Guest, and R. E. Jordan (2010), Parametrizing turbulent exchange over summer sea ice and the marginal ice zone, *Quarterly Journal of the Royal Meteorological Society*, *136*(649), 927–943, doi: 10.1002/qj.618. 2.2.1

Arneborg, L., A. K. Wåhlin, G. Björk, B. Liljebladh, and A. H. Orsi (2012), Persistent inflow of warm water onto the central Amundsen shelf, *Nature Geoscience*, *5*(12), 876–880, doi: 10.1038/ngeo1644. 1.1

Årthun, M., K. W. Nicholls, K. Makinson, M. a. Fedak, and L. Boehme (2012), Seasonal inflow of warm water onto the southern Weddell Sea continental shelf, Antarctica, *Geophysical Research Letters*, *39*(17), n/a–n/a, doi:10.1029/2012GL052856. 1.3

Årthun, M., K. W. Nicholls, and L. Boehme (2013), Wintertime Water Mass Modification near an Antarctic Ice Front, *Journal of Physical Oceanography*, *43*, 359–365, doi:10.1175/JPO-D-12-0186.1. 4.3

Carmack, E. C., and T. Foster (1975a), On the flow of water out of the Weddell Sea, *Deep Sea Research*, *22*(January), 711–724. 1.4, 2.2.4

Carmack, E. C., and T. Foster (1975b), Circulation and distribution of oceanographic properties near the Filchner Ice Shelf, *Deep Sea Research and Oceanographic Abstracts*, *22*(2), 77–90, doi:10.1016/0011-7471(75)90097-2. 2.2

Carmack, E. C., and T. Foster (1977), Water masses and circulation in the Weddell Sea, in *Proceedings of the Polar Ocean Conference, Montreal, 1974*, pp. 151–165. 1, 1.3, 1.4

Cavalieri, D., P. C.L, P. Gloersen, and H. Zwally (1996), Sea Ice Concentrations from Nimbus-7 SMMR and DMSP SSM/I-SSMIS Passive Microwave Data, Version 1 [NSIDC-0051], doi:https://doi.org/10.5067/8GQ8LZQVL0VL. 2.2.2

Chapman, D. C. (1985), Numerical Treatment of Cross-Shelf Open Boundaries in a Barotropic Coastal Ocean Model, doi:10.1175/1520-0485(1985)015<1060:NTOCSO>2.0.CO;2. 2.3.6

Chavanne, C. P., K. J. Heywood, K. W. Nicholls, and I. Fer (2010), Observations of the Antarctic Slope Undercurrent in the southeastern Weddell Sea, *Geophysical Research Letters*, *37*(13), L13,601, doi:10.1029/2010GL043603. 1.2, 1.3

Daae, K., I. Fer, and E. P. Abrahamsen (2009), Mixing on the continental slope of the southern Weddell Sea, *Journal of Geophysical Research*, *114*(C9), 1–13, doi:10.1029/2008JC005259. 1.5.1

Darelius, E., and J.-B. Sallée (2018), Seasonal outflow of Ice Shelf Water across the front of the Filchner Ice Shelf, Weddell Sea, Antarctica, *Geophys. Res. Lett*, *accepted*. 1.5, 1.4

Darelius, E., and A. K. Wåhlin (2007), Downward flow of dense water leaning on a submarine ridge, *Deep Sea Research Part I: Oceanographic Research Papers*, *54*(7), 1173–1188, doi:10.1016/j.dsr.2007.04.007. 1.4

Darelius, E., K. O. Strand, S. Østerhus, T. Gammelsrød, M. Årthun, and I. Fer (2014a), On the Seasonal Signal of the Filchner Overflow, Weddell Sea, Antarctica, *Journal of Physical Oceanography*, *44*(4), 1230–1243, doi:10.1175/JPO-D-13-0180.1. 2.1

Darelius, E., K. Makinson, K. Daae, I. Fer, P. R. Holland, and K. W. Nicholls (2014b), Hydrography and circulation in the Filchner Depression, Weddell Sea, Antarctica, *Journal of Geophysical Research: Oceans*, *119*, 1–18, doi:10.1002/2014JC010225. 2.2

Darelius, E., I. Fer, and K. W. Nicholls (2016), Observed vulnerability of Filchner-Ronne Ice Shelf to wind-driven inflow of warm deep water, *Nature communications*, *7*, 1–7, doi:10.1038/ncomms12300. 1.1, 1.3, 1.4, 2.1

Deacon, G. (1937), *The hydrology of the Southern Ocean*, vol. 15, 3–122 pp., Inst. of Oceanogr. Sci., Southampton, UK. 1.2

Dee, D. P., S. M. Uppala, A. J. Simmons, P. Berrisford, P. Poli, S. Kobayashi, U. Andrae, M. A. Balmaseda, G. Balsamo, P. Bauer, P. Bechtold, A. C. M. Beljaars, L. van de Berg, J. Bidlot, N. Bormann, C. Delsol, R. Dragani, M. Fuentes, A. J. Geer, L. Haimberger, S. B. Healy, H. Hersbach, E. V. Hólm, L. Isaksen, P. Kållberg, M. Köhler, M. Matricardi, a. P. McNally, B. M. Monge-Sanz, J.-J. Morcrette, B.-K. Park, C. Peubey, P. de Rosnay, C. Tavolato, J.-N. Thépaut, and F. Vitart (2011), The ERA-Interim reanalysis: configuration and performance of the data assimilation system, *Quarterly Journal of the Royal Meteorological Society*, *137*(656), 553–597, doi:10.1002/qj.828. 2.2.1, 2.2.2

Dupont, T. K., and R. B. Alley (2005), Assessment of the importance of ice-shelf buttressing to ice-sheet flow, *Geophysical Research Letters*, *32*(4), 1–4, doi:10.1029/2004GL022024. 1.1

Eriksen, C. C. (1985), Implications of Ocean Bottom Reflection for Internal Wave Spectra and Mixing, doi:10.1175/1520-0485(1985)015<1145:IOOBRF>2.0.CO;2. 1.5.1

Fahrbach, E., and S. el Naggar (2001), The Expeditions ANTARKTIS XVI/ 12 of the Research Vessel POLARSTERN" in 1998/1999, *Ber. Polar- und Meeresforsch*, *380*, 177pp. 1.6, 4

Fahrbach, E., G. Rohardt, and G. Krause (1992), The Antarctic coastal current in the southeastern Weddell Sea, *Polar Biology*, *12*(2), 171–182, doi:10.1007/BF00238257. 1.2

Fer, I., E. Darelius, and K. Daae (2016), Observations of energetic turbulence on the Weddell Sea continental slope, *Geophysical Research Letters*, pp. 760–766, doi:10.1002/2015GL067349. 1.5.1

FISP (2018), The Filchner Ice Shelf Project (FISP), doi:https://www.awi.de/en/science/climate-sciences/physical-oceanography/projects/fisp.html. 4.3

FISS (2018), Filchner Ice Shelf System Project (FISS), doi:https://www.bas.ac.uk/project/fiss/. 4.3

Flather, R. (1976), A tidal model of the northwest European continental shelf, *Mem. Soc. R. Sci. Liege*, *10*(6), 141–164. 2.3.6

Foldvik, A., and T. Gammelsrød (1985), Oceanographic conditions on the Weddell Sea shelf during the German Antarctic Expedition 1979/80, *Polar Research*. 2.2.4

Foldvik, A., T. Gammelsrød, and T. Tørresen (1985a), Hydrographic observations from the Weddell Sea during the Norwegian Antarctic research expedition 1976/77, *Polar Research*, pp. 177–193. 1.3, 2.2.4

Foldvik, A., T. Gammelsrød, and T. Tørresen (1985b), Circulation and water masses on the southern Weddell Sea shelf, *Antarctic Research Series*, *43*. 1.4

Foldvik, A., T. Gammelsrød, and T. Tørresen (1985c), Physical oceanography studies in the Weddell Sea during the Norwegian Antarctic Research Expedition 1978/79, *Polar Research*, *3*(2), 195–207, doi:10.1111/j.1751-8369.1985.tb00507.x. 1.4, 2.1

Foldvik, A., J. Middleton, and T. Foster (1990), The tides of the southern Weddell Sea, *Deep Sea Research*, *37*(8), 1345–1362. 1.5.2

Foldvik, A., T. Gammelsrød, E. Nygaard, and S. Østerhus (2001), Current measurements near Ronne Ice Shelf: Implications for circulation and melting, *Journal of Geophysical Research*, *106*(C3), 4463–4477, doi:10.1029/2000JC000217. 1.1, 1.4

Foldvik, A., T. Gammelsrød, S. Østerhus, E. Fahrbach, G. Rohardt, M. Schröder, K. W. Nicholls, L. Padman, and R. A. Woodgate (2004), Ice shelf water overflow and bottom water formation in the southern Weddell Sea, *Journal of Geophysical Research*, *109*(C2), 1–15, doi:10.1029/2003JC002008. 1.4, 1.4, 1.6, 2.1, 4

Foster, T., and E. C. Carmack (1976a), Temperature and salinity structure in the Weddell Sea, *J. Phys. Oceanogr*, *6*, 36–44. 1, 1.2, 1.2

Foster, T., and E. C. Carmack (1976b), Frontal zone mixing and Antarctic Bottom Water formation in the southern Weddell Sea, *Deep-Sea Research*, *23*(March 1975), 301–317. 1.4, 1.4

Fox, A. J., A. Paul, and C. R. (1994), Measured properties of the Antarctic ice sheet derived from the SCAR Antarctic digital database, *Polar Record*, *30*(174), 201–206, doi:10.1017/S0032247400024268. 1.1

Fox-Kemper, B., R. Ferrari, and J. Pedlosky (2003), On the Indeterminacy of Rotational and Divergent Eddy Fluxes*, *Journal of Physical Oceanography*, *33*(2), 478–483, doi:10.1175/1520-0485(2003)033<0478:OTIORA>2.0.CO;2. 2.3.6

Fretwell, P., H. D. Pritchard, D. G. Vaughan, J. L. Bamber, N. E. Barrand, R. Bell, C. Bianchi, R. G. Bingham, D. D. Blankenship, G. Casassa, G. Catania, D. Callens, H. Conway, a. J. Cook, H. F. J. Corr, D. Damaske, V. Damm, F. Ferraccioli, R. Forsberg, S. Fujita, Y. Gim, P. Gogineni, J. a. Griggs, R. C. a. Hindmarsh, P. Holmlund, J. W. Holt, R. W. Jacobel, a. Jenkins, W. Jokat, T. Jordan, E. C. King, J. Kohler, W. Krabill, M. Riger-Kusk, K. a. Langley, G. Leitchenkov, C. Leuschen, B. P. Luyendyk, K. Matsuoka, J. Mouginot, F. O. Nitsche, Y. Nogi, O. a. Nost, S. V. Popov, E. Rignot, D. M. Rippin, a. Rivera, J. Roberts, N. Ross, M. J. Siegert, a. M. Smith, D. Steinhage, M. Studinger, B. Sun, B. K. Tinto, B. C. Welch, D. Wilson, D. a. Young, C. Xiangbin, and a. Zirizzotti (2013), Bedmap2: Improved ice bed, surface and thickness datasets for Antarctica, *Cryosphere*, *7*(1), 375–393, doi:10.5194/tc-7-375-2013. 1.4, 2.2

Furevik, T., and A. Foldvik (1996), Stability at M2 critical latitude in the Barents Sea, *Journal of Geophyscial Research*, *101*, 8823–8827. 1.5.1

Gammelsrød, T., A. Foldvik, O. A. Nøst, Ø. Skagseth, L. Anderson, F. E., K. Olsson, T. Tanhua, E. Jones, and S. Østerhus (1994), Distribution of water masses on the continental shelf in the southern Weddell Sea, *Geophysical Monograph*, *84*, 158–176. 1, 1.4, 2.2.4

Gill, A. (1973), Circulation and bottom water production in the Weddell Sea, *Deep Sea Research and Oceanographic Abstracts*, *20*(2), 111–140, doi:10.1016/0011-7471(73)90048-X. 1.2, 1.2

Gillett, N. P., and D. Thompson (2003), Simulation of Recent Southern Hemisphere Climate Change, *Science*, *302*(October), 273–276. 1.6

Gordon, A. L. (1998), Western Weddell Sea thermohaline stratification, in *Ocean, Ice, and Atmosphere: Interactions at the Antarctic Continenal Margin*, vol. 75, edited by S. S. Jacobs and R. Weiss, pp. 215–240, AGU, Washington, D. C., doi:10.1029/AR075p0215. 1.4

Gordon, A. L., B. Huber, D. McKee, and M. Visbeck (2010), A seasonal cycle in the export of bottom water from the Weddell Sea, *Nature Geoscience*, *3*(8), 551–556, doi:10.1038/ngeo916. 1.6, 4

Graham, J. A., K. J. Heywood, C. P. Chavanne, and P. R. Holland (2013), Seasonal variability of water masses and transport on the Antarctic continental shelf and slope in the southeastern Weddell Sea, *Journal of Geophysical Research: Oceans*, *118*(4), 2201–2214, doi:10.1002/jgrc.20174. 1.2, 2.1, 4

Grosfeld, K., M. Schröder, E. Fahrbach, R. Gerdes, and A. Mackensen (2001), How iceberg calving and grounding change the hydrography in the Filchner Ice Shelf-Ocean System, *Journal of Geophyscial Research*, *106*(2000), 9039–9055. 1, 2.2.4

Hattermann, T., L. H. Smedsrud, O. A. Nøst, J. Lilly, and B. Galton-Fenzi (2014), Eddy-resolving simulations of the Fimbul Ice Shelf cavity circulation: Basal melting and exchange with open ocean, *Ocean Modelling*, *82*, 28–44, doi:10.1016/j.ocemod.2014.07.004. 1.5.3, 2.3.2, 2.3.4, 2.3.6

Hattermann, T., P. Davis, and S. Østerhus (2017), Field Report , Filchner Shelf Ice, *AWI internal field reports*, (October). 4.3

Hattermann, T., P. Davis, K. W. Nicholls, S. Østerhus, E. Darelius, and H. H. Hellmer (2018), A new look beneath the Filchner-Ronne Ice Shelf, *HE42A-03 presented at 2018 Ocean Sciences Meeting, Portland, OR, 12-16 Feb*. 4.3

Hellmer, H. H., F. Kauker, R. Timmermann, J. Determann, and J. Rae (2012), Twenty-first-century warming of a large Antarctic ice-shelf cavity by a redirected coastal current., *Nature*, *485*(7397), 225–8, doi:10.1038/nature11064. 1.1, 1.2, 4.1, 4.2

Hellmer, H. H., F. Kauker, R. Timmermann, and T. Hattermann (2017), The Fate of the Southern Weddell Sea Continental Shelf in a Warming Climate, *Journal of Climate*, *30*(Gill 1973), 4337–4350, doi:10.1175/JCLI-D-16-0420.1. 1.1, 1.2, 4.1, 4.2

Heywood, K. J., R. A. Locarnini, R. D. Frew, P. F. Dennis, and B. A. King (1998), Transport and Water Masses of the Antarctic Slope Front System in the Eastern Weddell Sea, *Ocean, Ice, and Atmosphere - Interaction at the Antarctic Continental Margin*, *75*, 203–214. 1.1, 1.2

Hurrell, J. W., and H. V. Loon (1994), A modulation of the atmospheric annual cycle in the Southern Hemisphere, *Tellus A*, *46*(3), doi:10.3402/tellusa.v46i3.15482. 1.6

Jacobs, S. (1991), On the nature and significance of the Antarctic Slope Front, *Marine Chemistry*, *35*(1-4), 9–24, doi:10.1016/S0304-4203(09)90005-6. 1.2, 1.2

Jensen, M. F., I. Fer, and E. Darelius (2013), Low frequency variability on the continental slope of the southern Weddell Sea, *Journal of Geophysical Research: Oceans*, *118*, 1–17, doi:10.1002/jgrc.20309. 1.2, 1.5.2, 2.1

Jullion, L., S. C. Jones, a. C. Naveira Garabato, and M. P. Meredith (2010), Wind-controlled export of Antarctic Bottom Water from the Weddell Sea, *Geophysical Research Letters*, *37*(9), doi:10.1029/2010GL042822. 1.6, 4.1

Klinck, J. M. (1996), Circulation near submarine canyons: A modeling study, *Journal of Geophysical Research*, *101*(95), 1211–1223, doi:10.1029/95JC02901. 1.2

Larter, R. D. (2011), Cruise report RRS James Clark Ross JR244, Marine geoscience and physical oceanography, southern Weddell Sea and South Orkney continental shelf, January-March 2011, *Tech. rep.*, technical report number JR244, British Antarctic Survey, Cambridge, U. K. 2.2.4

LeBlond, P. H., and L. A. Mysak (1978), *Waves in the ocean*, Elsevier Science, Amsterdam. 1.5.1

Lefebvre, W., and H. Goosse (2004), Influence of the Southern Annular Mode on the sea ice–ocean system, *Journal of Geophyscial Research*, *109*, 1–12, doi:10.1029/2004JC002403. 1.6, 4.1

Marchesiello, P., J. C. McWilliams, and A. Shchepetkin (2001), Open boundary conditions for long-term integration of regional oceanic models, *Ocean Modelling*, *3*(1-2), 1–20, doi:10.1016/S1463-5003(00)00013-5. 2.3.6

Marques, G. M., L. Padman, S. R. Springer, S. L. Howard, and T. M. Özgökmen (2014), Topographic vorticity waves forced by Antarctic dense shelf water outflows, *Geophysical Research Letters*, *41*(4), 1247–1254, doi:10.1002/2013GL059153. 1.5.2

Marshall, G. J. (2003), Trends in the Southern Annular Mode from Observations and Reanalyses, *Journal of Climate*, *16*(1999), 4134–4143. 1.6, 4.1

Marshall, J., and G. Shutts (1981), A Note on Rotational and Divergent Eddy Fluxes, *Journal of Physical Oceanography*, *11*(12), 1677–1680, doi:10.1175/1520-0485(1981)011<1677:ANORAD>2.0.CO;2. 2.3.6

McDougall, T., and P. Barker (2011), *Getting started with TEOS-10 and the Gibbs Seawater (GSW) Oceanographic Toolbox*, May, SCOR/IAPSO WG127. 1

McKee, D. C., X. Yuan, A. L. Gordon, B. A. Huber, and Z. Dong (2011), Climate impact on interannual variability of Weddell Sea Bottom Water, *Journal of Geophysical Research*, *116*(C5), C05,020, doi:10.1029/2010JC006484. 1.6

Meehl, G. A. (1991), A Reexamination of the Mechanism of Semiannual Oscillation in the Southern Hemisphere, *Journal of Climate*, *4*, 911–926. 1.6

Middleton, J., T. Foster, and A. Foldvik (1987), Diurnal shelf waves in the southern Weddell Sea, *Journal of Physical Oceanography*, *17*, 784–791. 1.5.2

Moffat, C., B. Owens, and R. C. Beardsley (2009), On the characteristics of Circumpolar Deep Water intrusions to the west Antarctic Peninsula Continental Shelf, *Journal of Geophysical Research: Oceans*, *114*(5), 1–16, doi:10.1029/2008JC004955. 1.1

Mysak, L. (1980), Recent advances in shelf wave dynamics, *Reviews of Geophysics*, *18*(1), 211–241. 1.5.2

Nicholls, K. W. (2005), JR097 Cruise Report Autosub Under Ice Cruise to the southern Weddell Sea, *Tech. rep.*, British Antarctic Survey, Cambridge, UK. 1.2, 2.1

Nicholls, K. W., and S. Østerhus (2001), Oceanographic conditions south of Berkner Island, beneath FilchnerRonne Ice Shelf, Antarctica, *Journal of Geophysical Research: Oceans (19782012)*, *106*(C6). 1.4

Nicholls, K. W., and S. Østerhus (2004), Interannual variability and ventilation timescales in the ocean cavity beneath Filchner-Ronne Ice Shelf, Antarctica, *Journal of Geophysical Research*, *109*(C4), 1–9, doi:10.1029/2003JC002149. 1.4, 1.4, 1.6

Nicholls, K. W., S. Østerhus, K. Makinson, T. Gammelsrød, and E. Fahrbach (2009), Ice-ocean processes over the continental shelf of the southern Weddell Sea , Antarctica: A review, *Reviews of Geophysics*, *47*(3), 1–23, doi:10.1029/2007RG000250. 1.1, 1.2, 1.4, 1.4, 2.2.4, 4

Nøst, O. A., and S. Østerhus (1998), Impact of grounded icebergs on the hydrographic conditions near the Filchner Ice Shelf, *Antarctic Research Series*, *75*, 267–284. 2.3.3

Nøst, O. A., M. Biuw, V. Tverberg, C. Lydersen, T. Hattermann, Q. Zhou, L. H. Smedsrud, and K. M. Kovacs (2011), Eddy overturning of the Antarctic Slope Front controls glacial melting in the Eastern Weddell Sea, *Journal of Geophysical Research*, *116*(C11), C11,014, doi:10.1029/2011JC006965. 1.5.3, 2.3, 2.3.4

Núñez-Riboni, I., and E. Fahrbach (2009), Seasonal variability of the Antarctic Coastal Current and its driving mechanisms in the Weddell Sea, *Deep Sea Research Part I: Oceanographic Research Papers*, *56*(11), 1927–1941, doi:10.1016/j.dsr.2009.06.005. 1.2, 4

Nycander, J., and K. Döös (2003), Open boundary conditions for barotropic waves, *Journal of Geophysical Research*, *108*(C5), 1–20, doi:10.1029/2002JC001529. 2.3.6

Orsi, A. H. (1999), Circulation, mixing, and production of Antarctic Bottom Water, *Progress In Oceanography*, *43*(1), 55–109, doi:10.1016/S0079-6611(99)00004-X. 1, 1.4

Orsi, A. H., and C. L. Wiederwohl (2009), A recount of Ross Sea waters, *Deep-Sea Research Part II: Topical Studies in Oceanography*, *56*(13-14), 778–795, doi:10.1016/j.dsr2.2008.10.033. 1.1

Paolo, F. S., H. A. Fricker, and L. Padman (2015), Volume loss from Antarctic ice shelves is accelerating, *Science*, *348*(6232), 327–331. 1.1

Polvani, L., D. Waugh, G. Correa, and S. Son (2011), Stratospheric Ozone Depletion : The Main Driver of Twentieth-Century Atmospheric Circulation Changes in the Southern Hemisphere, *Journal of Climate*, *24*(3), 795–812, doi:10.1175/2010JCLI3772.1. 1.6

Pritchard, H. D., S. Ligtenberg, H. Fricker, D. G. Vaughan, M. R. Van Den Broeke, and L. Padman (2012), Antarctic ice-sheet loss driven by basal melting of ice shelves, *Nature*, *484*(7395), 502–505, doi:10.1038/nature10968. 1.1

Rhines, P. (1970), Edge-. Bottom-, and Rossby Waves in a rotating and Stratified Fluid, *Geophysical Fluid Dynamics*, *1*(3-4), 273–302. 1.5.2

Rignot, E., S. Jacobs, J. Mouginot, and B. Scheuchl (2013), Ice-shelf melting around Antarctica., *Science*, *341*(6143), 266–70, doi:10.1126/science.1235798. 1.1, 1.1

Ryan, S., T. Hattermann, E. Darelius, and M. Schröder (2017), Seasonal cycle of hydrography on the eastern shelf of the Filchner Trough,Weddell Sea, Antarctica, *J. Geophys. Res Ocean*, *122*, 1–17, doi:10.1002/2017JC012916. 1.3, 2.1

Sallée, J.-B. (2017), Cruise report JR16004 24 Jan - 13 Mar 2017, *Tech. rep.*, Locean. 1.5, 4.2, 4.3

Semper, S., and E. Darelius (2017), Seasonal resonance of diurnal continental shelf waves in the southern Weddell Sea, *Ocean Science*, *13*, 77–93, doi:10.5194/os-2016-36. 1.5.2

Shchepetkin, A., and J. C. McWilliams (2009), Computational Kernel Algorithms for Fine-Scale, Multiprocess, Longtime Oceanic Simulations, *Handbook of Numerical Analysis*, *14*, 121–183, doi:10.1016/S1570-8659(08)01202-0. 2.3.1

Simmonds, I., and D. A. Jones (1998), The mean structure and temporal variability of the semiannual oscillation in the southern extratropics, *International Journal of Climatology*, *18*, 473–504. 1.6

Song, Y., and D. Haidvogel (1994), A semi-implicit ocean circulation model using a generalized topography-following coordinate system, *Journal of Computational Physics*, *115*, 228–244. 2.3.1

St. Laurent, P., J. M. Klinck, and M. S. Dinniman (2013), On the Role of Coastal Troughs in the Circulation of Warm Circumpolar Deep Water on Antarctic Shelves, *Journal of Physical Oceanography*, *43*(1), 51–64, doi:10.1175/JPO-D-11-0237.1. 1.5.3, 2.3, 2.3.2

Stewart, A. L., and A. F. Thompson (2015), Eddy-mediated transport of warm Circumpolar Deep Water across the Antarctic Shelf Break, *Geophysical Research Letters*, *42*, 1–9, doi: 10.1002/2014GL062281.1. 1.5.3, 2.3, 2.3.2, 2.3.6

Stewart, A. L., and A. F. Thompson (2016), Eddy generation and jet formation on the Antarctic continental slope, *J. Phys. Oceanogr*, *46*(12), 3729–3750, doi:10.1175/JPO-D-16-0145.1. 1.5.3, 4.2

Sverdrup, H. (1953), The currents off the coast of Queen Maud Land, *Norsk Geografisk Tidskrift*, *14*, 239–249. 1.2, 4

Thompson, D., and S. Solomon (2002), Interpretation of Recent Southern Hemisphere Climate Change, *Science*, *296*(May), 895–900. 4.1

Timmermann, R., and H. H. Hellmer (2013), Southern Ocean warming and increased ice shelf basal melting in the twenty-first and twenty-second centuries based on coupled ice-ocean finite-element modelling, *Ocean Dynamics*, *63*(9-10), 1011–1026, doi:10.1007/s10236-013-0642-0. 1.1, 4.1

Turner, J. (2004), The El Niño-Southern Oscillation and Antarctica, *International Journal of Climatology*, *24*(1), 1–31, doi:10.1002/joc.965. 1.6

Van Loon, H. (1967), The Half-Yearly Oscilations in Middle and High Southern Latitudes and the Coreless Winter, *Journal of Atmospheric Sciences*, *24*, 472–486. 1.6

Van Loon, H., J. Kidson, and A. Brett Mullan (1993), Decadal Variation of the Annual Cycle in the Australian Dataset, *Journal of Climate*, *6*, 1227–1231. 1.6

Vlasenko, V. (2005), *Baroclinic Tides: Theoretical Modeling and Observational Evidence*, Cambridge University Press, Cambridge, UK. 1.5.1

Walker, D. P., M. A. Brandon, A. Jenkins, J. T. Allen, J. A. Dowdeswell, and J. Evans (2007), Oceanic heat transport onto the Amundsen Sea shelf through a submarine glacial trough, *Geophysical Research Letters*, *34*(2), L02,602, doi:10.1029/2006GL028154. 1.1

Wang, D., and C. Mooers (1976), Coastal-trapped waves in a continuously stratified ocean, *Journal of Physical Oceanography*, *6*, 853–863. 1.5.2

WAPITI (2018), The WAPITI project, doi:http://wapiti-project.com/project. 4.3

Weppernig, R., P. Schlosser, S. Khatiwala, and R. G. Fairbanks (1996), Isotope data from Ice Station Weddell: Implications for deep water formation in the Weddell Sea, *Journal of Geophysical Research: Oceans*, *101*(C11), 25,723–25,739, doi:10.1029/96JC01895. 1.4

Williams, W. J., G. G. Gawarkiewicz, and R. Beardsley (2001), The adjustment of a shelfbreak jet to cross-shelf topography, *Deep-Sea Research Part II: Topical Studies in Oceanography*, *48*(1-3), 373–393, doi:10.1016/S0967-0645(00)00085-0. 1.2, 2.3

Woodgate, R. A., and M. Schröder (1998), Moorings from the Filchner Trough and the Ronne Ice Shelf Front: Preliminary Results, *Filchner Ronne Ice Shelf Programme*, *12*, 85–90. 2.1

Zhang, Y., J. Pedlosky, and G. R. Flierl (2011), Cross-Shelf and Out-of-Bay Transport Driven by an Open-Ocean Current, *Journal of Physical Oceanography*, *41*(2004), 2168–2186, doi: 10.1175/JPO-D-11-08.1. 1.2

Graphic design: Communication Division, UiB / Print: Skipnes Kommunikasjon AS

uib.no

ISBN: 978-82-308-3739-9